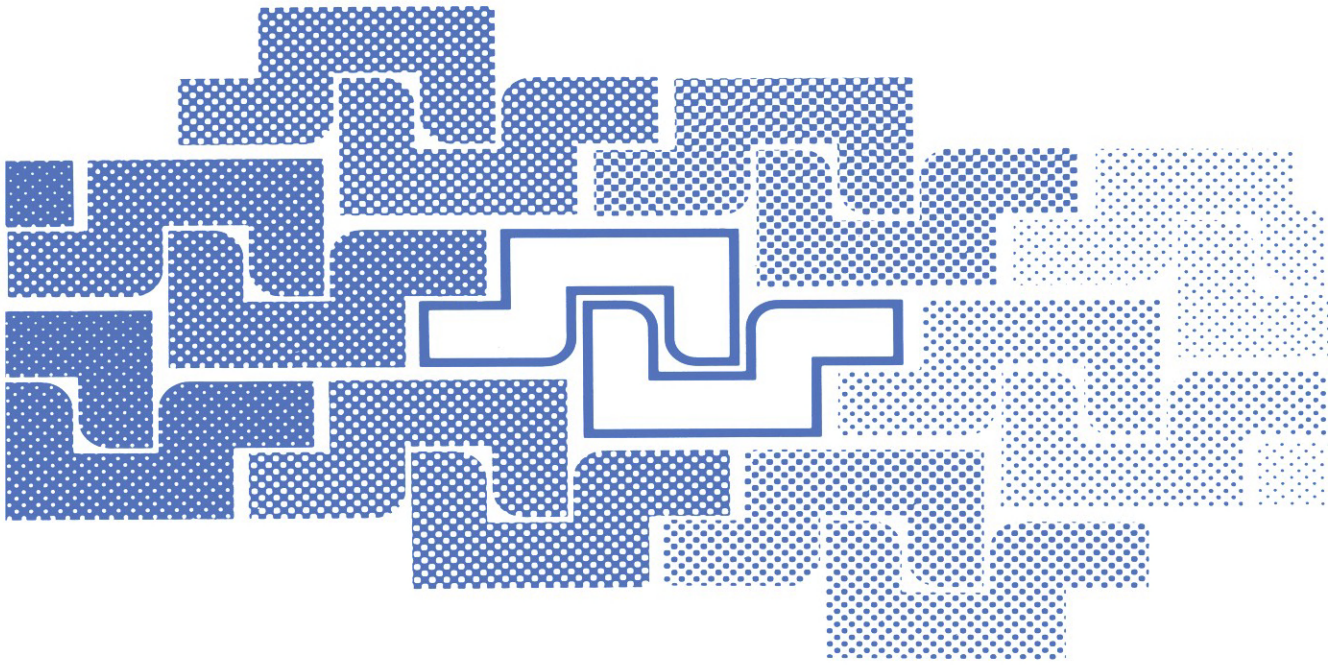

Examining the Submicron World

Edited by
Ralph Feder
J. Wm. McGowan and
Douglas M. Shinozaki

NATO ASI Series

Series B: Physics Vol. 137

Examining the Submicron World

NATO ASI Series

Advanced Science Institutes Series

A series presenting the results of activities sponsored by the NATO Science Committee, which aims at the dissemination of advanced scientific and technological knowledge, with a view to strengthening links between scientific communities.

The series is published by an international board of publishers in conjunction with the NATO Scientific Affairs Division

A Life Sciences **B Physics**	Plenum Publishing Corporation New York and London
C Mathematical and Physical Sciences	D. Reidel Publishing Company Dordrecht, Boston, and Lancaster
D Behavioral and Social Sciences **E Engineering and Materials Sciences**	Martinus Nijhoff Publishers The Hague, Boston, and Lancaster
F Computer and Systems Sciences **G Ecological Sciences**	Springer-Verlag Berlin, Heidelberg, New York, and Tokyo

Recent Volumes in this Series

Volume 130—Heavy Ion Collisions: *Cargèse* 1984
edited by Paul Bonche, Maurice Lévy, Philippe Quentin, and Dominique Vautherin

Volume 131—Physics of Plasma-Wall Interactions in Controlled Fusion
edited by D. E. Post and R. Behrisch

Volume 132—Physics of New Laser Sources
edited by Neal B. Abraham, F. T. Arecchi, Aram Mooradian, and Alberto Sona

Volume 133—Scaling Phenomena in Disordered Systems
edited by Roger Pynn and Arne Skjeltorp

Volume 134—Fundamental Processes in Atomic Collision Physics
edited by H. Kleinpoppen, J. S. Briggs, and H. O. Lutz

Volume 135—Frontiers of Nonequilibrium Statistical Physics
edited by Garald T. Moore and Marlan O. Scully

Volume 136—Hydrogen in Disordered and Amorphous Solids
edited by Gust Bambakidis and Robert C. Bowman, Jr.

Volume 137—Examining the Submicron World
edited by Ralph Feder, J. Wm. McGowan, and Douglas M. Shinozaki

Series B: Physics

Examining the Submicron World

Edited by

Ralph Feder

IBM Research Laboratory
Yorktown Heights, New York

J. Wm. McGowan

National Museum of Science and Technology
Ottawa, Ontario, Canada

and

Douglas M. Shinozaki

The University of Western Ontario
London, Ontario, Canada

Plenum Press
New York and London
Published in cooperation with NATO Scientific Affairs Division

Proceedings of a NATO Advanced Study Institute on
Improved Methods for Examining the Submicron World,
held July 28–August 11, 1984,
in Nova Scotia, Canada

Library of Congress Cataloging in Publication Data

NATO Advanced Study Institute on Improved Methods for Examining the Submicron World (1984: Nova Scotia)
Examining the submicron world.

(NATO ASI series. Series B, Physics; v. 137)
"Proceedings of a NATO Advanced Study Institute on Improved Methods for Examining the Submicron World, held July 28–August 11, 1984, in Nova Scotia"—T.p. verso.
Includes bibliographies and index.
1. Electron microscopy—Congresses. 2. X-ray microscope—Congresses. 3. Ultrastructure (Biology)—Congresses. I. Feder, Ralph. II. McGowan, J. William (James William), 1931– . III. Shinozaki, Douglas M. IV. Title. V. Series.
QH212.E4N37 1984 502′.8′25 86-9442
ISBN-13: 978-1-4612-9297-5 e-ISBN-13: 978-1-4613-2209-2
DOI: 10.1007/978-1-4613-2209-2

Softcover reprint of the hardcover 1st edition 1986
A Division of Plenum Publishing Corporation
233 Spring Street, New York, N.Y. 10013

PREFACE

An Institute like ours cannot help but lend credence to the notion of the late Derek J. de Solla Price of Yale University that "the scientific revolution was largely the improvement, invention and use of a series of instruments .... that expanded the reach of science in innumerable directions". Most of science today and in years gone by depends on the experimental observation of structure on the small scale with microscopes, and on the large scale with telescopes. The first instruments to expand the observational range of the human eye were simple optical systems, designed in the case of microscopes and telescopes to magnify the image. The big breakthrough in the 17th century was not when Galileo first turned his telescope to the heavens, but when improvements in lens-grinding techniques allowed eyeglass makers to make the first telescope.

Early microscopy revealed new and previously unsuspected microstructures in biological and non-biological materials and thus helped to enlarge on the understanding of the relationship between structure and properties. The natural inclination of all microscopists, the desire to observe ever smaller structures, was satisfied by the construction of higher quality optical systems which reduced the aberrations limiting the usable magnification. The modern optical microscope is the result of this evolution in design and construction, and it can be operated easily to achieve close to the theoretical resolution. Different methods of examining the microscopic world, many of which are considered in this Institute, are at various stages of instrumental development. In each method, the quality of the image depends upon instrument engineering and as Dr. Price argues, it is still the maker of the tools who opens the way for mankind to advance in his understanding of nature.

The evolution of the modern electron microscope is a recent example of the effect of instrument development in our understanding of the structure of matter and of biological processes. Early experimental instruments were difficult to use, but subsequently many improvements were incorporated into the

production of instruments. Modern electron microscopes are easily switched between standard modes of operation from conventional TEM to scanning TEM and to SEM, with energy dispersive x-ray analysis and even electron energy loss spectroscopy included. The operation and alignment of these instruments to achieve quite high resolution has been developed to such an extent that even an inexperienced operator can obtain quite remarkable images.

Other tools for the examination of microstructures are not nearly as well developed. The essential driving force behind the improvement of new instruments is "to see" small structures, that is, to improve instrument resolution. Resolution has a variety of meanings, depending upon the instrument being considered - one can "see" things with one instrument that one cannot "see" with another. The secondary ion mass spectrometer is one example. It has good chemical sensitivity but relatively poor lateral spatial resolution. In some applications, for example in measuring depth distribution of small concentrations in semiconductor devices, it is ideal; while it is not nearly as suitable for measuring concentration profiles across the surface in the plane perpendicular to the beam direction.

The instruments used in SIMS, scanning x-ray microscopy, Auger spectroscopy and so on, are in general difficult to operate, partly because they lie lower in the evolutionary ladder of instrumentation. However, in spite of the different stages of development for different instruments, it is clear that significant advances in understanding of biological and non-biological mechanisms and structure can be made by using a variety of microscopic tools in concert. For example, the correlation of microstructure and distribution of chemical species within the structure might involve the use of electron microscopy, SIMS and even microradiography using soft x-ray imaging. Any one tool is sufficiently different from another that scientists today are hard pressed to become skilled in the use of the wide variety of tools. Indeed, specialization in science is such that one working in a given area of microscopy is often unfamiliar with the basic capabilities and limitations of other techniques.

An interesting "spin-off" or an example of intellectual cross-fertilization is that instruments designed for analysis such a scanning transmission electron microscopes are now used to synthesize or build submicron structures. Ten nanometer lines and complex topographic structures can now be "written"onto substrates such as silicon using ultra-fine electron beams. The drive for the development of this technology comes from many VLSI semiconductor microfabrication groups. Also, grainless polymer films which were developed by the semiconductor industry for the production of integrated circuits are now used in high resolution contact x-ray imaging to study biological materials *in vivo* and *in vitro*. New soft x-ray radiation sources and the image recording

media are tools which after their invention have allowed scientists to look at samples which could not previously be examined.

There is no doubt that modern instruments developed by today's equivalent of the eyeglass maker now allow us to examine the old world in new ways and with greater resolution. Many examples of this symbiosis were identified at our Institute and many more will no doubt evolve out of the interactions which will follow.

The variety of techniques used today or that are under development was appropriately summarized by Professor Kirz, and the table he presented concisely illustrates the breadth of the techniques covered in this Institute.

Probe	Method	Specimen Resolution	Chemical Thickness	Comments
Xrays	contact	$\geq$ 100Å	100Å – 10μ	stereo flash
	Zone plate imaging	500Å→200Å?	" "	
	Scanning	2000Å→200Å?	" "	
	XPS	100μ→0.1μ?	surface	see Caudano
electrons	CTEM	~ 3Å	5 – 2000Å	(materials sci)
	dark field	~ 3Å	5 – 300Å	(biology)
	STEM	~ 3Å	5 – 600Å	micromachining
	EELS	3 – 5Å	5 – 300Å	30-50 atoms!
	STM	3Å	surface	0.1Å surface topography
	SAM	300Å	surface	see Caudano
	HREELS	1mm	surface	see Caudano
ions	SIMS	0.5μ→100Å	surface or dynamic	see Caudano

With the development of new tools like the x-ray microscope and the improvement of older ones like the electron microscope, scientists in biology, physics and materials science are rapidly using them in concert to understand mechanisms, processes and structure. It is our hope that this Institute has made a contribution to helping them understand the potential of some of these diverse methods.

Ralph Feder
Bill McGowan
Doug Shinozaki

ACKNOWLEDGEMENTS

The success of the meeting was found not only in the lectures and scientific discussions, but also in the informal gatherings and social interaction outside the formal presentations. A wide variety of organizations and individuals contributed to all aspects of the Institute. Among them we must thank the granting agencies and other institutions which made it possible. These are listed below. The invited speakers of course provided the essential scientific core of the whole meeting and the speakers who took part in the discussions made the intellectual content lively and interesting; these are too numerous to mention individually. The preparation of the manuscript was helped by P.C. Cheng, who generously spent long hours reformatting many pages of script, and in addition helped considerably during the meeting. His enthusiasm was contagious.

However the bulk of the difficult, odious and generally unrecognized toil was accomplished with remarkable facility and good humour by Marilyn Adams, who acted as administrator, secretary, complaint bureau and mother confessor. The failings of the the directors of the Institute were mostly hidden behind her competence.

Supporting Agencies:

Alexander Graham Bell National Historic Park (Parks Canada)
Cape Breton Development Corporation
Duplicom Business Products Ltd.
Fortress Louisbourg (Parks Canada)
Inverary Inn
Medical Research Council of Canada
NATO
Natural Science and Engineering Research Council of Canada
National Science Foundation (U.S.)

Nova Scotia Department of Tourism
Office of Naval Research (U.S.)
St. Francis Xavier University
T.J. Watson Research Center, IBM, Yorktown Heights
United States Air Force Office of Scientific Research
University College of Cape Breton

CONTENTS

SCANNING TUNNELING MICROSCOPY

S. Chiang and R. J. Wilson

IBM Research Laboratory
San Jose, California 95193

ABSTRACT

The scanning tunneling microscope is a new tool for determining surface topography on a sub-atomic scale. It uses the measurement of the quantum mechanical tunneling current from a sharp tip to a sample through a vacuum gap in order to plot a topographic map of the surface with vertical resolution as high as 0.1Å and horizontal resolution as high as 2Å. We will discuss the technique and its instrumentation as developed by Binnig et al.[1-5] at IBM Zurich Research Laboratory. We will also discuss the instrument which is presently operating at ~2Å vertical resolution in our laboratory. The technique has been shown to apply to samples consisting of metals, semiconductors, and adsorbates on metals. Examples of high resolution surface profiles from published results of the Zurich group, including gold, silicon, and oxygen on nickel, will be shown. Applications to rougher surfaces in poor vacuum, such as gold sputtered on silicon and silver evaporated on mica, will also be demonstrated.

INTRODUCTION

The knowledge of the structure of a surface is extremely important to the fundamental understanding of the chemical reactions which occur there. Low energy electron diffraction (LEED), atom diffraction, and ion channeling are some of the common experimental methods for studying surface structure. These methods are all indirect because calculations must be performed for model structures in order to fit the data. Periodic surface structures are also required in order to measure structures using diffraction techniques. Other methods of measuring surface structure, such as

photoemission and vibrational spectra, may be even less direct and more difficult to interpret. The measurement of the real space image of a surface with atomic resolution is clearly very desirable for improved understanding of the surface structure.

Real space atomic resolution of surfaces is possible for special types of samples by well known microscopic techniques. The advent of the high energy transmission electron microscope (TEM) has recently permitted the real space imaging of individual atoms in very thin samples with high mass contrast. The field ion microscope (FIM) is also able to image individual atoms at the edges of each layer of a very sharp tip using very high electric fields. While these microscopes have atomic scale lateral resolution, comparable vertical resolution is not readily attainable.

The scanning tunneling microscope (STM) is a tool for measuring surface topography on an atomic scale which was recently developed by Binnig et al.[1-5] at the IBM Zurich Research Laboratory. The highest vertical resolution which has been attained with the technique to date is 0.1Å, with a lateral resolution of 2 to 5 Å. The technique uses the quantum mechanical tunneling of electrons between two electrodes through an insulator, typically vacuum. The electrodes consist of the sample under study and a sharp tip to obtain high spatial resolution. As the tip is scanned over the surface, the measurement of the tunneling current allows the plotting of a "topographic" map of the surface in real space in all three dimensions. The technique can be used to measure both periodic and non-periodic surface features on both metals and semiconductors.

Because the tunneling current depends on the overlap between the electronic wavefunctions of the sample and the tip, the STM images also depend on the chemical properties of the sample and tip. Therefore, the STM has the potential for studying these chemical properties. In addition, with sufficient stability against mechanical vibrations, inelastic tunneling spectroscopy[6] to give information on the vibrational modes of molecules on the surface may be possible in the future.

DESCRIPTION OF TUNNELING AND PRINCIPLE OF STM

The tunneling of electrons from one conductor to another through an insulator is a purely quantum mechanical phenomenon known for over 50 years.[7] Although classically the electrons involved do not have enough energy to surmount the potential energy barrier of the insulator, quantum mechanically they have a small probability of reaching the other side of the barrier if the height and width of the barrier are sufficiently small. If two conductors are placed within a few Ångstroms of each other, the

exponentially decaying electronic wavefunctions of the two conductors can overlap sufficiently that the electrons then have a probability of "tunneling" from one conductor to the other. If a potential is applied between the two conductors, the resulting tunneling current can be measured. For two flat, parallel electrodes, this tunneling current, I_T, has an exponential dependence on the distance s between the two conductors:[7]

$$I_T \propto (\frac{V_T}{s}) \cdot \exp (- A\phi^{1/2}s).$$

Here $A \approx 1.025\ (eV)^{-1/2}\text{Å}^{-1}$ for a vacuum gap, ϕ is the average of the two electrode work functions, s is the distance between the electrodes, and V_T is the applied voltage. With work functions of a few eV, I_T changes by an order of magnitude for every Ångstrom change of s.

A schematic diagram of the STM is shown in Fig. 1. The tunneling tip is mounted on three orthogonal piezodrives, P_X, P_Y, and P_Z, which are made of commercial piezoelectric ceramic material. An electronic feedback circuit keeps I_T constant by applying a voltage V_Z to piezodrive P_Z. For a *constant work function*, this circuit thus keeps the tip a constant distance s from the surface as it is scanned along the x and y directions. The plotting of the voltages on the three piezodrives, $V_Z(V_X,V_Y)$ thus directly gives the surface topography z(x,y) in this case. By running the instrument with the tunneling current constant, an actual *change* in the work function will appear in the tunneling scan as a change in the distance s of the tip from the surface. For the case of flat, parallel electrodes, the work function can be separately measured by modulating Δs while scanning, since the logarithmic derivative of the tunneling current with respect to the electrode separation is

$$\frac{\Delta(\ln I_T)}{\Delta s} \approx \phi^{1/2} + \frac{s}{(2\phi^{1/2})} \frac{\delta\phi}{\delta s}.$$

From this equation, one can estimate ϕ far away from the surface, as well as the potential barrier change as the tip approaches the sample. Recent experiments show that $\Delta(\ln I_T)/\Delta s$ is nearly constant and approximately equal to the square root of the average work function ϕ_o, despite the lowering of the actual tunneling barrier by the image potential.[8] Since this average work function is equal to the barrier height at large distances, this logarithmic derivative directly measures the work function independently of the tip to surface distance.

The simple interpretation of STM measurements of surface topography given above results from a local approximation which is valid only when

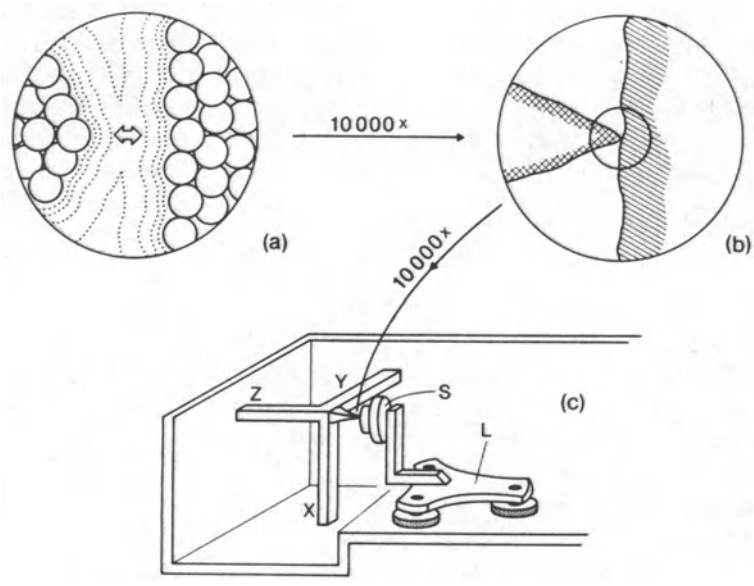

Fig. 1. Schematic of the physical principle and technical realization of STM. (a) shows apex of the tip (left) and surface (right) at a magnification of about 10^8. The solid circles indicate atoms, the dotted lines electron density contours. The path of the tunnel current is given by the arrow. (b) Scaled down by a factor of 10^4. The tip (left) appears touching the surface (right). (c) STM with rectangular piezodrive X, Y, Z of the tunnel tip at left and "louse" L (piezoelectric "walker" with electrostatic clamping) for rough positioning (μ to cm range) of sample S. After Ref. 5.

the radii of curvature of the sample and the tip are large compared to other relevant distances[9], i.e.,

$$r_s, r_t >> s, (A\phi^{1/2})^{-1}.$$

Since the sample and tip are not parallel on an atomic scale, the interpretation of high resolution STM scans requires more complicated theoretical analysis.

The STM scans actually give the shape of the electronic wavefunctions near the Fermi level, roughly in the middle of the vacuum gap, rather than the positions of the atomic cores.[3] To make the quantitative correspondence between the electron wave functions and the atomic cores, one requires a tunneling theory on an atomic scale. In principle, the detailed understanding of the tunneling process of electrons from the tip to

the sample, or *vice versa*, requires the solution of the Schrödinger equation for the many-body charged-particle Hamiltonian. Since the full problem is too complicated to solve, one must simplify and separate it into three parts:[10] (1) the effective potentials and electronic band structure of the tip and the sample, (2) the changes in these properties due to the influence of the surface, and (3) the tunneling process. In the past year, several model calculations for the three dimensional tunneling problem as applied to the STM have been performed. Baratoff[11] and Tersoff and Hamann[12] both used a perturbation theory approach to tunneling which is useful for connections to the electronic structure of specific materials. On the other hand, Garcia et al.[13] and Stoll et al.[14] consider the transmission of plane waves through a rectangular potential barrier with corrugated boundaries, an approach which is not restricted to low transmissivity.

INSTRUMENTATION OF THE SCANNING TUNNELING MICROSCOPE

In order to obtain high resolution from a scanning tunneling microscope, in which the tip is maintained within a few Å of the surface, it is clear that the suppression of vibrations is extremely important. The vertical resolution of the instrument depends upon the stability of the tip to sample distance. In order to obtain high resolution from the instrument, this distance must remain stable within 0.1Å. In the high resolution models in Zurich,[3] the vibrations were successfully suppressed by supporting the microscope from two sets of spring stages, reducing most of the vibrations to frequencies <1 Hz. Viton spacers are used to damp the high frequency vibrations propagating along the springs. Additional damping of the low frequency vibrations is provided using the magnetic eddy currents induced in pieces of copper on the support and on the inner stage by SmCo permanent magnets mounted on the intermediate stage. These very simple measures work surprisingly well in permitting the ultrahigh vacuum (UHV) instrument in Zurich to operate with vertical resolution in the sub-Ångstrom range. In our laboratory, we are currently operating an instrument with the same type of vibration isolation in a 10^{-6} torr vacuum evaporator. This instrument has both vertical and horizontal resolution of ~2Å.

Another integral part of the tunneling microscope allows the positioning of the sample close to the tip without coupling in external vibrations. To obtain the tunneling current the sample must be within a few Å of the tip. Since the piezodrives on which the tip is mounted are rigidly fixed to the inner stage of the microscope and can extend a maximum length of a few microns, some mechanism must be provided to move the sample towards the tip until the sample is within the range of the z piezodrive motion. The step size of the motion of the sample towards the

tip must be smaller than the range of the z piezodrive in order to be useful. Therefore, Binnig et al.[3,4] developed a piezoelectric walker which they call the "louse" to carry the sample and move it towards the tip. (See Fig. 1.) The louse has a body made from a plate of piezoelectric ceramic with 3-fold symmetry and three metal feet attached to the body. By applying a voltage between a foot and ground across an insulator with a high dielectric constant, such as $SrTiO_3$, a foot can be clamped electrostatically to a ground plane. By varying the pattern of clamping voltages on the feet while expanding and contracting the body of the louse appropriately, the louse can walk in a two dimensional plane, carrying the sample with it.

To carry the sample in our microscope, we have developed a reliable one dimensional piezoelectric walker, which we call a "micropede." (See Fig. 2.) Its operation is similar to that of Zurich's louse, except that it is uses frictional clamping of the feet instead of electrostatic clamping. The piezoelectric micropede body is divided into three electrodes, which effectively act as a body with a foot at each end. A piece of metal, currently aluminum, is machined so that the piezoelectric plate can rest on a flat surface between two rails. The tension of the rails against the piezoelectric can be adjusted with two screws and springs. The feet of the micropede are then lapped into the piece of metal so that there is less than 1μ tolerance between the two pieces. Thus, the application of voltage to a foot can cause its sideways expansion, clamping that end of the micropede. Alternately clamping the feet and extending and contracting the body of the micropede causes it to advance along the railing. With a step size which can be varied from 0.3μ to 1.0μ, the micropede can walk at a speed of ~2mm/min.

In our instrument, the tip is scanned using small piezoelectric tubes, 1.25 mm diameter with 0.25 mm walls, which have a sensitivity of 100Å/V. Three orthogonal tubes are soldered to a small block of stainless

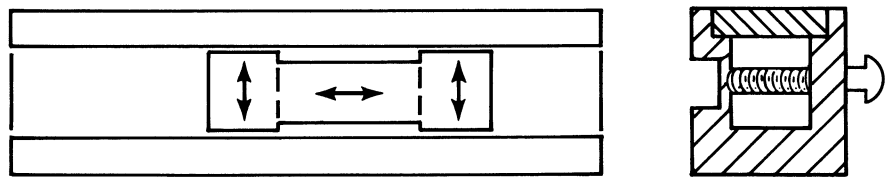

Fig. 2. Schematic diagram of the "micropede," a one-dimensional piezoelectric "walker" with frictional clamping. The piezoplate is divided into three electrodes consisting of a body in the center and two feet which clamp on the metal rails on both sides. Two screw and springs adjust the tension of the rails before the piezoplate is lapped into the metal holder.

steel which holds the tunneling tip. Voltage is applied between the inner and outer walls of the tubes, causing the linear expansion of the tube as it conserves its volume. With these high sensitivity tubes, it is possible to scan the surface in the x and y directions over several microns with a few hundred volts. A feedback loop controls the extension of the z piezodrive so as to keep the tunneling current between the tip and sample constant.

Feedback circuitry is required to control the tip motion so as to keep the current constant as the tip is scanned laterally across the surface. Our circuit has a low noise FET preamplifier to amplify the current. Since the tunneling current is an exponential function of the distance between the tip and sample, a logarithmic amplifier is the next stage. This is followed by two amplifiers in parallel with different frequency rolloffs so that the time constant of the circuitry can be adjusted. Finally, these outputs are summed in another amplifier and then amplified by a high voltage operational amplifier, which can produce the ± 150 V needed to drive the z piezodrive over $\pm 1.5\mu$. The scanning electronics in its simplest form can be just two ramp generators, one about an order of magnitude faster than the other, which control the motion of the x and y piezodrives which move the tip.

An obvious problem is to prevent the collision of the tip with the surface as the micropede moves the sample towards the tip. We observe the motion of the micropede walking towards the tip with a Volpi TV-microprobe, which is an optical microscope with a working distance of 50 mm connected to a television camera so as to give an overall magnification of ~100. When observing the tip and its reflection in the sample surface, it is possible to observe a relative motion of the tip and sample as small as 2μ with this system. Nevertheless, caution is still required so as not to cause a collision between the sample and the tip, since there may well be structures on the end of the tip which cannot be observed with this magnification.

The "approach" is the process by which the sample and the tip move close enough to each other so that we can measure a tunneling current. This process involves several steps. Using the optical microscope, the sample is moved within $\sim 20\mu$ of the tip by walking the micropede. Then the amplifier feedback loop is switched on so that the z-piezodrive moves the tip towards the sample until the circuit senses a tunneling current of 10 nA. If the z-piezodrive reaches its maximum extension without obtaining tunneling current, an override switch is thrown to cause it to contract to its minimum length so as to move the tip as far as possible from the sample. Then the micropede takes another step, and the entire process is repeated. Since the motion of the micropede is already controlled by an

IBM Personal Computer, this entire approach process will be fully automated shortly.

Analog data acquisition can be conveniently performed on an x-y recorder, as in Zurich, or on a storage oscilloscope, depending on the speed of the feedback electronics and the desired scan speed. In our laboratory, we are currently using a storage oscilloscope. In this case, we trigger the oscilloscope from one of the scan oscillators. The voltage on the z piezodrive is then applied to the oscilloscope and added to the voltage from the slow ramp so that the traces from subsequent scans are displaced on the oscilloscope screen. The resulting image is then a topographic map of the surface under study.

TECHNOLOGICAL DEVELOPMENT OF A SCANNING TUNNELING MICROSCOPE

Since scanning tunneling microscopy is still a relatively young technique, some difficulties with reliability and reproducibility of high resolution operation remain. Here we will discuss some improvements to the STM which is under development in our laboratory. Similar developments are in progress in Zurich and elsewhere.

To correctly interpret the STM scans on an atomic level, one must be sure of the surface characterization and cleanliness. Therefore, we are currently building an STM in an ultrahigh vacuum system which will contain a set of reverse view LEED optics. The STM chamber will be connected through a transfer system with multiple radial ports and a rotatable rack and pinion mechanism to a Vacuum Generators Escalab. The Escalab is a commercial instrument equipped with 500Å resolution scanning Auger microscopy (SAM), scanning electron microscopy (SEM), X-ray photoemission spectroscopy (XPS), argon ion cleaning, and an airlock for fast entry of samples into the vacuum system. Using this system, we hope to have *in situ* exchange of tips or samples, completely in ultrahigh vacuum conditions, from the STM to the Escalab. We hope that studying the properties of the tunneling tips with the facilities in the Escalab will permit us to learn to make a more reproducible high resolution instrument. The combination of surface analysis capabilities with the STM will enable us to study clean and adsorbate covered metal surfaces and thin films.

The influence of thermal drift on the STM scans is also an important problem. When studying features on the sub-Ångstrom level, a small amount of temperature change in the environment of the sample can cause a large change in the observed scans. In fact, in Zurich, where the sample is heated by an oven on the louse, a common mode of operation is to use the

scanning electronics only to scan the tip along the x-direction while the slower thermal drift, caused by the sample's cooling after cleaning, is used to scan the tip along the y-direction.[15] Our current instrument, which is mostly composed of aluminum, has thermal drifts of ~30Å/min. We hope to reduce this substantially by changing many of the materials in our STM to invar and quartz, which have extremely low thermal expansion coefficients compared to most metals.

An important problem in tunneling microscopy is the fabrication of suitable tips. To obtain extremely high sub-atomic resolution from the microscope, the end of the tip closest to the surface must consist essentially of a single atom. In Zurich, Binnig et al.[3,4] have successfully used very crudely ground tips which have a radius $<1\mu$. Their tips have small minitips. Since the tunneling current depends so strongly on the distance between the tip and sample, the current will select the minitip which is closest to the sample surface. The tip can be sharpened by applying an electric field of 10^8V/cm to it for approximately half an hour. Unfortunately, these very sharp tips are not stable, so that extremely high resolution can be difficult to attain and maintain for long periods of time.

We have recently been using sharp field emission tips[16] in our tunneling microscope. These tips are electrochemically etched from tungsten wire 0.13 mm in diameter in 2N NaOH solution. Since the etching occurs preferentially at the meniscus of the solution, a special controller circuit is used to stop the etching process when the etching current suddenly decreases, as the bottom part of the wire drops off. Using this method, we can reproducibly fabricate tips with a radius of ~1000Å, as observed by scanning electron microscopy (SEM). In SEM photographs with a resolution of ~90Å, no whiskers are observed. Auger spectroscopy indicates that the surface of the tip is mostly carbon; no tungsten is observed until after the tip is sputtered.

By fabricating sharper tips, we hope to make the tips more reproducible, as well as making them have a smaller included angle at the end. This is important for scanning along relatively rough surfaces, with features on the scale of thousands of Ångstroms. The lateral resolution of the STM depends not only on the radius of curvature and the included angle of the end of the tip, but also on the size of the structures on the surface.[17] If the surface is flat on an atomic scale, the lateral resolution of the instrument will depend on the size of the single atom or cluster of atoms at the end of the tip. If the surface topography is very rough, the tip dimensions must be small compared to the surface structure in order to follow the contours of the surface reliably. In addition, the scanning speed must be slow enough that the feedback loop has time to move the tip away from the large hills before the tip bumps into them.

The use of these sharp tips allows us to measure field emission current from the tip to the sample when the voltage applied to the tip is increased to about 20V. In field emission mode, the electrons tunnel from the tip into the vacuum and then propagate as free electrons until they are collected by the sample. When the microscope operates in this mode, with 20V applied to the tip, the tip is about 2000Å farther from the surface than it is in the tunneling mode. This mode of operation thus gives us the possibility of measuring surface topography while the tip is several thousand Å from the surface, with concomitant degradation of lateral resolution. We do not yet know, however, how the field emitted electrons from the tip may change the surface. This type of field emission scanning microscope has been used before by Young et. al.[18].

Finally, we are currently working on software to control our tunneling microscope using an IBM Personal Computer. This software will use two digital to analog converters to control the scanning piezodrives, and then will measure the z piezodrive voltage with an analog to digital converter. The scans will be displayed in real time on the IBM color graphics display and plotted later. For further analysis of the tunneling scans, data can be shipped to an IBM mainframe computer for more sophisticated data transformations and graphics.

TOPOGRAPHY OF CLEAN SURFACES STUDIED BY STM

The STM has been demonstrated to yield atomic scale information on surface topography on reconstructed metal surfaces,[15,19] semiconductor surfaces,[20,21] and adsorbates on metal surfaces.[22] In this section, we will discuss some of the more impressive results obtained with this new technique on Au(110), Au(100), Si(111) 7x7, and O adsorbed on Ni(110).

Au(110)

The STM has been used to study the reconstruction of Au(110).[19] Fig. 3 shows an STM picture of the surface, which appears to consist of ribbons of (111) facets along the $[1\bar{1}0]$ direction. This facetting is believed to be the driving mechanism behind the reconstruction of the surface. The 1x2 missing row reconstruction is due to (111) facets with two free rows, while three row facets produce the 1x3 reconstruction. Locally random combinations of two and three row facets cause disorder. Since corrugations deeper than 1x3 and 1x4 channels were not observed, the lowest energy surface appears to consist of ≤ 3 free rows of (111) facets along the $[1\bar{1}0]$ direction.

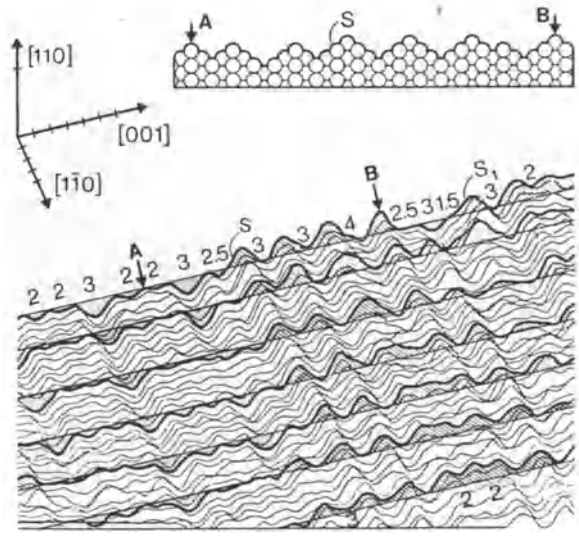

Fig. 3. STM picture of a section of the Au(110) surface. Divisions on the crystal axes are 5Å. The straight lines help visualize the terraced structure with monolayer steps (e.g., at S); below each line the missing rows, and above each line the remaining rows are enhanced. The numbers on the top scan give distances between maxima in units of the bulk lattice spacing. The inset shows the proposed structural model for the observed corrugation between A and B. After Ref. 19.

Au(100)

High resolution STM micrographs of the 1x5 reconstruction of Au(100) are shown in Fig. 4,[15] with tip sharpening performed between the measurements of parts (a) and (b) of the figure. The applied voltage was V_T=800 mV. Along the[01$\bar{1}$] direction, we observe alternating sequences of double-maxima, double minima and single-maxima, single-minima structures with ribbons of smooth corrugation in between. The pseudo unit cell is large and slightly irregular. The measured data are consistent with a buckled hexagonal top layer, which is isotropically contracted by 3.82% and rotated by 0.1°, forming an incommensurate Au on Au structure.

Si(111) 7x7

Fig. 5 shows two complete rhombohedral unit cells of the famous 7x7 reconstruction of the Si(111) surface,[20] which has been an intriguing surface problem for twenty years. The 7x7 unit cell is bounded by lines of

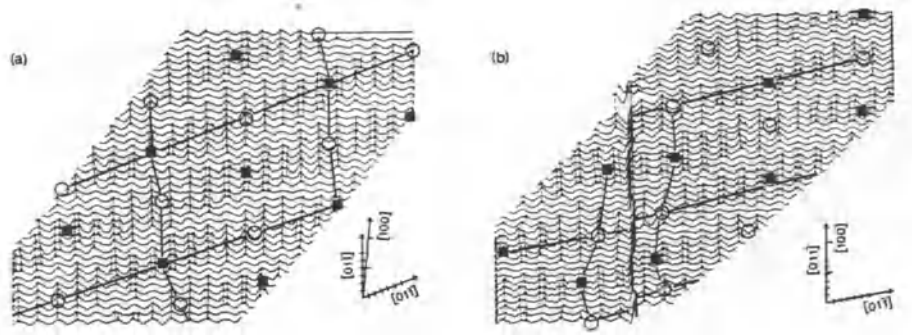

Fig. 4. High resolution micrographs of Au(100) showing large pseudo unit cells indicated by broken lines. (b) contains a meandering step line running in the [001] direction. The dots on the scans locate maxima with a curvature above a certain threshold. The alternating sequences of double-maxima, double-minima and single-maxima, single- minima structures in the $[01\bar{1}]$ direction with ribbons of smooth corrugation in between are clearly evident. The lines connecting maxima are drawn by eye for better visibility of the two typical structures forming the large pseudo unit cell. Shearing of the latter in the $[01\bar{1}]$ direction is also clearly visible. Divisions on the axes correspond to 5Å. After Ref. 15.

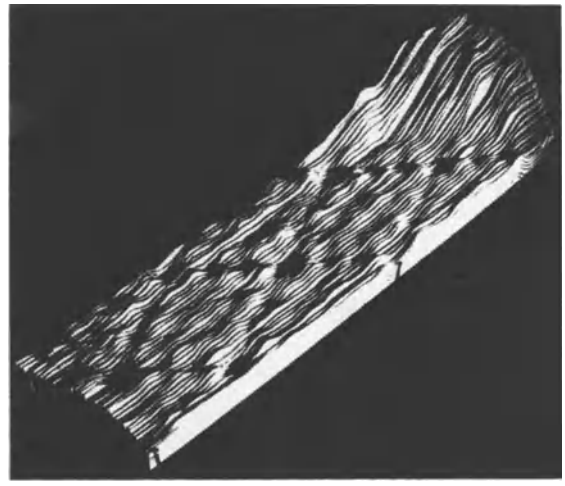

Fig. 5. Relief of two complete 7x7 unit cells on Si(111), with nine minima and twelve maxima each, taken at 300° C. Heights are enhanced by 55%; the hill at the right grows to a maximal height of 15Å. The $[\bar{2}11]$ direction points from right to left, along the long diagonal. After Ref. 20.

minima with deep corners and twelve maxima in each cell. These maxima are interpreted as 12 Si adatoms sitting on top of the Si(111) surface in distinct sites. The different depths of the minima are attribute to non-uniform relaxation of the top layer. The STM scans of the Si(111) 7x7 surface have stimulated much interest in further models of the structure. Recently, these experiments have been repeated on highly doped p-type material and show very similar structural features to the earlier work.[21]

O Adsorbed on Ni(110)

The STM was used to determine the real space three dimensional image of an ordered structure of chemisorbed atoms, using the oxygen induced 2x1 reconstruction on Ni(110).[22] For this experiment, a clean Ni(110) surface was prepared by ion bombardment and annealing cycles. After exposure to >1 Langmuir of oxygen, the 2x1 LEED pattern was observed. The STM micrograph was made using a gold tip with a gap voltage of ~10mV (tip positive) and a tunneling current of 5 nA. Fig. 6 shows a

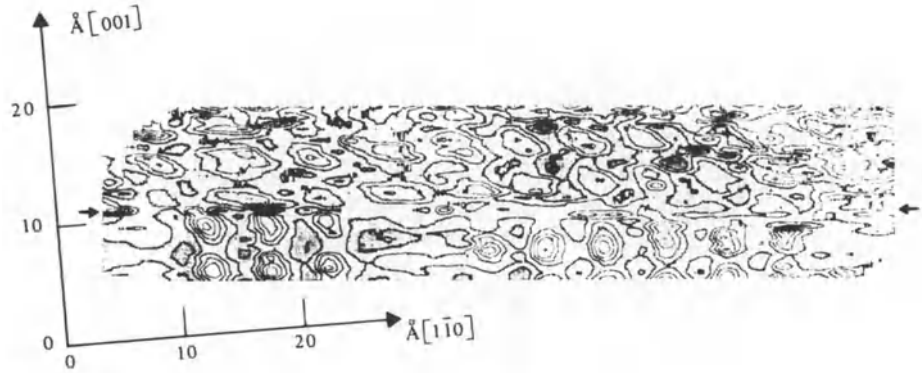

Fig. 6. Top view of STM micrographs of oxygen adsorbed on Ni(110). Compression along the [001] direction has been artificially introduced. The contours of equal corrugation height are spaced 0.1Å apart in the lower, and 0.05Å apart in the upper part. The brightness scale goes from white for maxima to gray for minima. The change of the tip condition is marked by the arrows. They also locate a narrow domain wall in the [1$\bar{1}$0] direction which might have induced the change. After Ref. 22.

contour map made from the STM micrograph. The top part of the contour map shows reduced resolution due to an inadvertent change in the tip condition, probably due to tunneling through two atoms at the end of the tip instead of one. The maxima in the lower half of the figure form domains with 2x1 structures separated in the [1$\bar{1}$0] direction by wide domain walls. The sharp maxima are associated with individual oxygen atoms and the intervening flat regions with uncovered unreconstructed Ni(110). The shape of the corrugation and the registry in the [001] direction of the oxygen atoms with respect to uncovered nickel atoms and to steps in the [1$\bar{1}$0] direction are consistent with a sawtooth model of the reconstructed nickel, with oxygen atoms in long bridge sites. (See Fig. 3 of Ref. 22.)

ROUGH SURFACES STUDIED BY STM

We have used our little STM, which operates in 10^{-6} torr vacuum, to study some fairly rough, dirty surfaces. The highest resolution which we have attained with this instrument is ~2Å, both vertically and horizontally. The scans from this instrument yield information on surfaces which is complementary to that from an SEM. Its vertical resolution is comparable to that of a good stylus profilometer, but its lateral resolution can be better by about three orders of magnitude. We will discuss some of our data on an etched Ag(111) crystal, 100Å of Au sputtered onto Si(111), and 2500Å of Ag epitaxially grown on mica.

Etched Ag(111)

On an etched, dirty Ag(111) crystal, we scanned across the surface to find a fairly flat area, like that shown in Fig. 7, where the hills are about 5Å high and 3Å wide. The dotted lines in the figure show structural features, while the smaller periodic ripples are 60 Hz noise which was not filtered out of the signal and thus appear on the scans. On other parts of the same sample, we observed 500Å hills as we scanned over an area of 3000Å x 3000Å. We can also easily magnify the area under study to scan areas of 300Å x300Å or 30Å x 30Å.

Au Sputtered on Si(111)

Fig. 8 shows our STM scans on two areas of the same sample consisting of 100Å Au sputtered onto Si(111). In the top part of the figure, we observe a single hill 200Å high and 1000Å wide. On another part of the sample, shown in the bottom part of the figure, we see many asperities 100Å high, 100Å wide, and about 500Å apart. The ability to observe

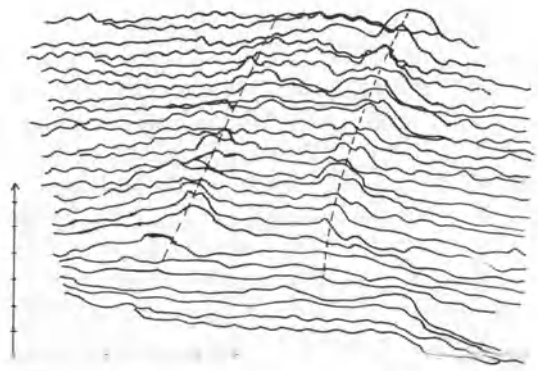

Fig. 7. STM graph of an etched Ag(111) crystal. The dotted lines guide the eye along the structural features. Most of the smaller periodic ripples are due to 60 Hz noise which was not filtered out of the signal. Divisions on the x and z axes correspond to 5Å while thermal drift caused the scan in the y direction, which is uncalibrated. Scan speed was 1 sec. per scan.

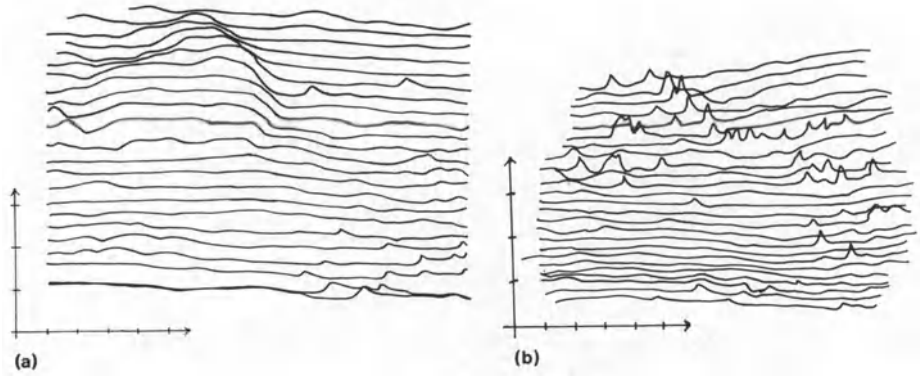

Fig. 8. STM scans for two different areas on the same sample of consisting of 100Å of gold sputtered onto Si(111). (a) shows a large hill which is 200Å high and 1000Å wide. (b) shows many asperities which are 100Å high, 100Å wide, about 500Å apart. The scale is 200Å/division on x and z, with ~120Å along y between scans, scan speed of 2 sec. per scan, V_T=-1.0V, J_T=1nA.

asperities of this size on such a rough surface indicates that our field emission type STM tip must be very small close to its end.

Ag on Mica

Fig. 9 shows STM scans on two different samples of 2500Å of silver epitaxially grown on mica. X-ray analysis shows that the bulk of the silver is primarily oriented along the (111) direction.[23] The top part of the figure shows a sample with larger hills, about 500Å high and 700Å wide. This corresponds well with the size of features observed by SEM. The bottom part of the figure shows a more recent sample, grown on a smoother and thinner piece of mica. Here the STM showed features on some parts of the sample which were 100Å high and 100Å wide. SEM photographs are mostly featureless except for occasional very small spots. We see that the STM scans correspond well with what we expected from the SEM photographs. These samples show that the STM not only works but also easily observes large features even on a relatively rough surface.

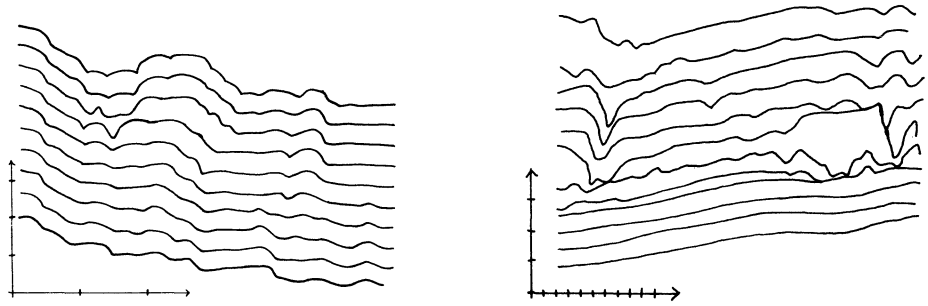

Fig. 9. STM scans of two different samples consisting of 2500Å of silver grown epitaxially on mica. (a) shows hills which are 500Å high and 700Å wide. SEM photographs showed structures of approximately this size. The scale is 500Å/division on x and z, with 30Å along y between scans, and a scan speed of 10 sec. per scan. (b) Another sample, grown on a smoother, thinner piece of mica. In some areas, features are about 100Å high and 100Å wide. The bottom of the figure shows an area which is flat to within 10Å. The scale is 100Å/division on x and z, with ~30Å along y between scans, scan speed of 10 sec. per scan, V_T=-0.55V, J_T=10nA.

FUTURE APPLICATIONS OF THE STM

The scanning tunneling microscope has been shown to be capable of measuring surface topography on an atomic scale on both periodic and non-periodic structures. The technique applies to both reconstructed metal and semiconductor surfaces. It is also able to observe rough surfaces fairly easily, still with better resolution than most other types of microscopes. The experiment on oxygen chemisorbed on nickel shows that the technique also gives useful information on adsorbed molecules. Other types of chemical analysis of surfaces on an atomic scale, such as tunneling spectroscopy, may also follow from the improvements in the technique. Obvious applications include the study of nucleation and growth of islands on adsorbate systems, thin films, and alloys. Other possible problems include the electronic structure of surfaces and the electrical properties of thin insulating layers. Biological applications are also possible. Many groups are building scanning tunneling microscopes all around the world. Nevertheless, at the present time, more research problems than instruments exist. We look forward to an exciting future with this technique.

ACKNOWLEDGMENTS

We would like to thank H. Rohrer, G. Binnig, and R. Feenstra for helpful and stimulating discussions. We would also like to thank A.M. Baro, A. Baratoff, G. Binnig, Ch. Gerber, H. Rohrer, E. Stoll, and E. Weibel for permission to reproduce figures from their publications. We are grateful to J. G. Gordon, G. Borges, and F. O. Sequeda for the samples of silver epitaxially grown on mica and to D. J. Auerbach for the loan of the Ag(111) crystal.

REFERENCES

1. G. Binnig, H. Rohrer, Ch. Gerber, and E. Weibel, *Appl. Phys. Lett.* **40**, 128 (1982).

2. G. Binnig, H. Rohrer, Ch. Gerber, and E. Weibel, *Phys. Rev. Lett.* **49**, 57 (1982).

3. G. Binnig and H. Rohrer, *Helv. Phys. Acta* **55**, 726 (1982).

4. G. Binnig and H. Rohrer, *Surf. Sci.* **126**, 236 (1983).

5. G. Binnig and H. Rohrer, "Scanning Tunneling Microscopy," Hewlett-Packard Prize Lecture at EPS Meeting, The Hague, Netherlands, March, 1984, to be published in *Physica B*.

6. Paul K. Hansma, ed., *Tunneling Spectroscopy; Capabilities, Applications, and New Techniques*, Plenum Press, New York (1982).

7. R. H. Fowler and L. Nordheim, *Proc. R.Soc. London*, **A119**, 173 (1928).

8. G. Binnig, N. Garcia, H. Rohrer, J. M. Soler, and F. Flores, to be published.

9. A. Baratoff, "Theory of Scanning Tunneling Microscopy--Methods and Approximations," Condensed Matter Division, Conference of EPS, The Hague, Netherlands, March 1984, to be published in *Physica B*.

10. E. Stoll, "Scanning Tunneling Microscopy," Proceedings AVCP Meeting, March 11-17, 1984, Saas Fee Switzerland. Note: These are very comprehensive lecture notes summarizing both the experimental and theoretical aspects of scanning tunneling microscopy.

11. A. Baratoff, *Europhysics Conference Abstracts*, **7b**, 364 (1983).

12. J. Tersoff and D. R. Hamann, *Phys. Rev. Lett.*, **50**, 1998 (1983).

13. N. Garcia, C. Ocal, F. Flores, *Phys. Rev. Lett.*, **50**, 2002 (1983).

14. E. Stoll, A. Baratoff, A. Selloni, and P. Carnevali, *J. Phys. C.*, **17**, 3073 (1984).

15. G. Binnig, H. Rohrer, Ch. Gerber, and E. Stoll, "Real-Space Observation of the Reconstruction of Au(100), to be published in *Surf. Sci.*

16. R. Gomer, *Field Emission and Field Ionization*, Harvard University Press, Cambridge, Mass., (1961).

17. E. Stoll, "Resolution of the Scanning Tunneling Microscope," to be published in *Surf. Sci.* Letters.

18. Russell Young, John Ward, and Fredric Scire, *Rev. Sci. Instrum.* **43**, 999 (1972).

19. G. Binnig, H. Rohrer, Ch. Gerber, and E. Weibel, *Surf. Sci.* **131**, L379 (1983).

20. G. Binnig, H. Rohrer, Ch. Gerber, and E. Weibel, *Phys. Rev. Lett.* **50**, 120 (1983).

21. A. Baro, G. Binnig, H. Rohrer, F. Salvan, and Ch. Gerber, to be published.

22. A. M. Baro, G. Binnig, H. Rohrer, Ch. Gerber, E. Stoll, A.Baratoff, and F.Sylvan, *Phys. Rev. Lett.* **52**, 1304 (1982).

23. J. G. Gordon and G. Borges, private communication.

APPLICATIONS AND LIMITATIONS OF SIMS

J.D. Brown

Faculty of Engineering Science and The Centre for Interdisciplinary Studies in Chemical Physics
The University of Western Ontario
London, Canada N6A 5B9

ABSTRACT

Secondary ion mass spectrometry is one of the most sensitive techniques for determining dopant profiles in semiconductors. Depth resolutions of less than 10 nm can be achieved with sensitivities down to 1×10^{16} atoms/cm^3 for the important dopant elements. The lateral resolution of the technique under ideal circumstances can be better than 0.5 μm. Practical and theoretical limitations in three-dimensional depth profiling are discussed.

INTRODUCTION

Secondary ion mass spectrometry (SIMS) is one of the most sensitive and versatile methods of materials analysis. A primary ion beam of a few kilovolt energy bombards the surface of a solid specimen. In the resulting collision processes, secondary particles are emitted which can be atoms, molecules or ions. The number of total atoms released per incident ion, Y, the total sputter yield is typically 2-5 (1) but can be as large as 20-30 (2). The secondary ions formed can be sorted according to m/e ratio in a mass spectrometer. Since individual ions can be detected and counted and since the efficiency of secondary ion extraction can be as high as 10% and of ion formation 0.01 to almost 100%, the technique offers high sensitivity for measurement of almost all elements in the Periodic Table. One consequence of the high sensitivity for secondary ion detection is that at almost every mass number in a simple mass scan, a peak is seen. This is illustrated in the case of a relatively pure GaAs specimen (Figure 1) in which

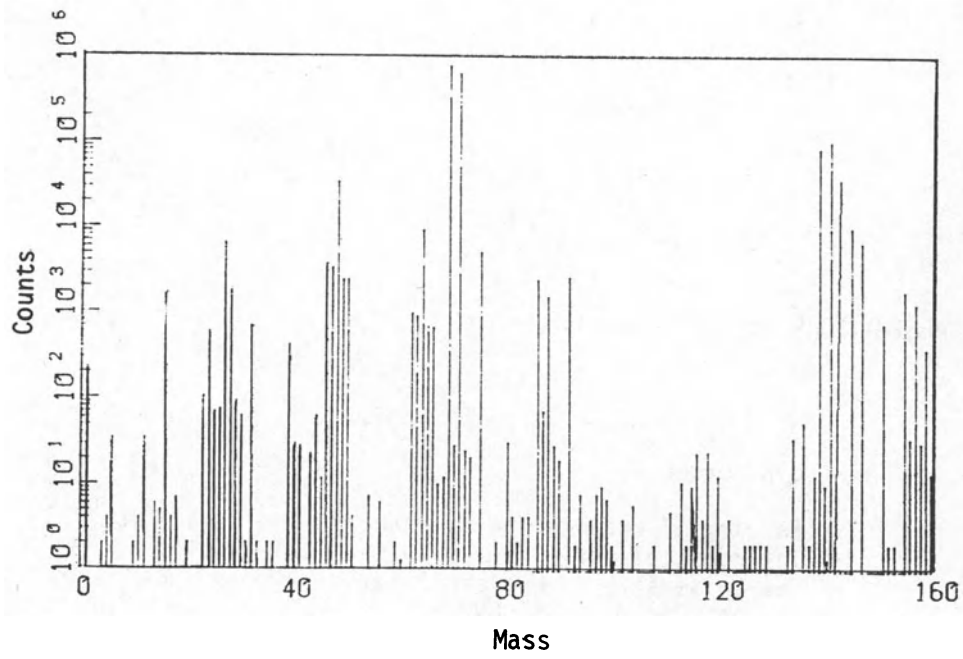

FIG. 1 Mass Spectrum From GaAs, O_2^+ Primary Ion Beam

one can see not only peaks for Ga and As alone but also molecular ions such as oxides, hydrides and clusters. The result is a very complex spectrum even for this almost pure compound. This points to one of the difficulties in SIMS, that of mass interference usually due to molecular ions. Only rarely do two isotopes of neighbouring elements result in an interference which must be deconvoluted on the basis of known natural abundance ratios. However, almost always some molecular peak interferes with measurement of atomic peaks at the same nominal mass number. There are two methods for removing these molecular mass interferences. A small but significant mass difference exists between the interfering molecular ions and the atomic ions so that they may be separated in a mass spectrometer which has sufficient mass resolution. An example is the mass spectrum at mass 28 for a specimen of GaAs which contains a small concentration of silicon (Figure 2). The interfering species of CO, N_2 and C_2H_4 while all possessing a nominal mass of 28, can be separated at a mass resolution of 2800. The second method of resolving these mass interferences utilizes the observed fact that molecular ions are emitted with a kinetic energy distribution which is at lower energy and has a much sharper cut off at higher energies than the energy distribution for atomic ions (Figure 3). Thus by admitting ions of only high energy to the mass spectrometer, the interference due to molecular ions can be suppressed. This technique can be used with quadrupole mass spectrometers in which the mass resolution is insufficient to discriminate by differences in mass. Recently, Metson et al. (3) have reported

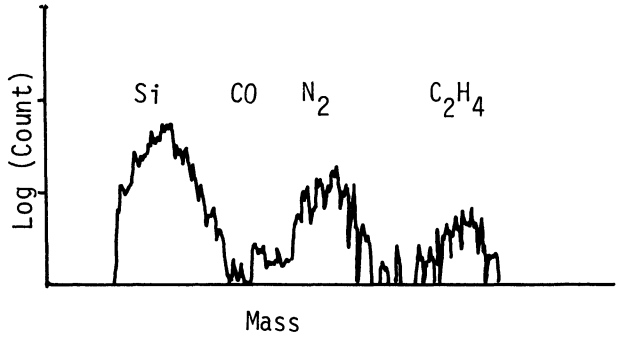

FIG. 2 Mass Spectrum of Mass 28 At High Mass Resolution ($M/\Delta M \approx 2800$)

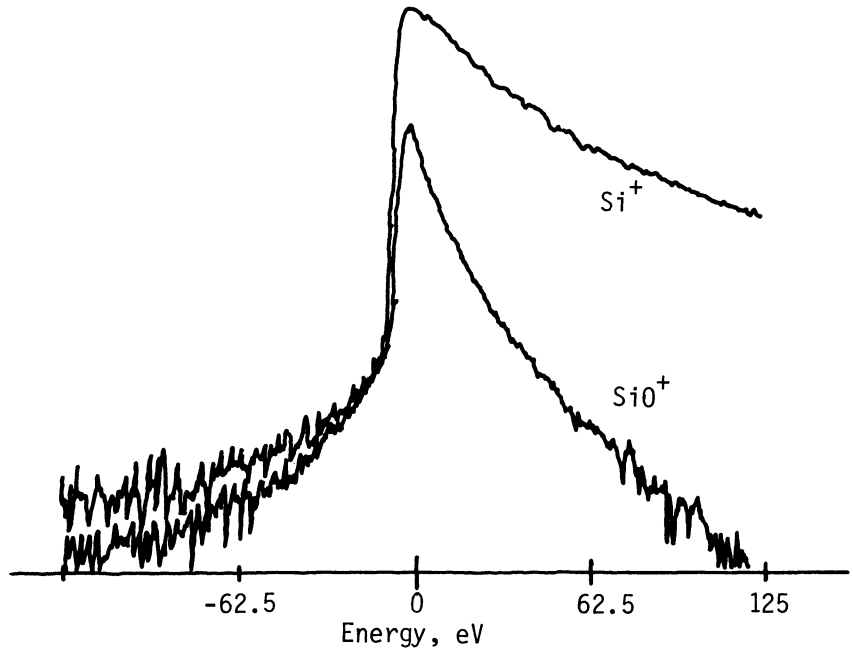

FIG. 3 Energy Distribution of Secondary Ions Measured Using Voltage Offset in a Cameca IMS 3f

a specimen isolation technique which can be used with a Cameca ion microscope which suppresses molecular interferences several orders of magnitude beyond that which can be achieved by simple energy discrimination. Whether this technique which depends on a very broad, high energy band pass in the secondary mass spectrometer to maintain high sensitivity, can be applied to quadrupole instruments has yet to be attempted.

Since ion detection is by a mass spectrometer, isotope abundance studies and isotopic tracer experiments are natural applications of SIMS. In the geological sciences particularly, the ability to measure isotopic abundances is invaluable for isotopic dating measurements as well as mass fractionation during rock formation.

Several modes of analysis are possible in SIMS instruments depending on the manner of operation. With normal primary beam current densities of a few milliamperes per square centimetre, the specimen erodes away as a function of time at the rate of a few Angstrom units per second. By following the intensity of several secondary ion species as a function of time, variations of intensity (and hence concentration) can be measured as a function of depth. On the other hand, if the current density is reduced to a few nanoamperes per square centimetre, so-called static SIMS results in which only the outer layer is sampled. For thin organic layers, a large fraction of secondary ions has a mass equivalent to the parent organic molecule with or minus a hydrogen (4).

ION FORMATION AND SECONDARY ION YIELDS

When an ion of KeV energy strikes the surface of a specimen, energy is transferred through collisions to atoms in the solid. This has been very graphically modelled by Harrison et al. (5) who have shown that an almost liquid-like state exists in the volume surrounding the entrance point of the incident particle. Enough energy is transferred to a few surface or near surface atoms or clusters of atoms for them to escape from the surface. Some of the escaping particles are ionized to form positive or negative ions by a mechanism or mechanisms which are still the subject of much debate. Some of the characteristics of ion emission are well established, for example that positive ion emission depends on the mean ionization potential while negative ion emission depends on the electron affinity (6). One consequence of this is that secondary ion yields vary over many orders of magnitude from element to element. For example, the ion yield of $^{27}Al^+$ from aluminum is at least 6 orders of magnitude greater than for $^{179}Au^+$ from gold when bombarded with an oxygen primary ion beam (7). Further, it is well established that the presence of oxygen either as primary ion species or as a consequence of vacuum conditions or oxygen flooding

enhances the production of both positive and negative ions (8) while negative ion emission is significantly increased by the presence of caesium (9).

ION BEAM MIXING AND SELECTIVE SPUTTERING

Several physical effects change the measured depth profiles from the actual composition distribution in the original specimen. Two of the most important of these are ion beam mixing and selective sputtering. When the ion beam strikes the sample, energy is transferred to the atoms of the specimen, which can then be moved as a consequence of their acquired kinetic energy, at times some distance in the specimen. Although secondary ions are always emitted from the top few layers of the specimen which would imply that a depth resolution of a few Angstrom units should be achieved, ion beam mixing can reduce the expected depth resolution to the range of the primary ions which could be several hundred Angstrom units. A particularly severe form of ion beam mixing is knock-on, in which the primary ion drives a specimen atom deeper into the specimen as a consequence of an almost head-on collision. The consequence of ion beam mixing is always a smearing out of any concentration gradient, both to deeper and shallower depths.

Selective sputtering can also distort depth profiles. For almost any system in which different kinds of atoms are present on the surface of the specimen, the probability of an atom escaping from the surface will be mass dependent. As a consequence, some species will have increased concentrations on the surface above the bulk concentration while others will have smaller concentrations. If a specimen which is uniform in composition is being sputtered, the sputtered composition will accurately reflect the bulk composition after a short transient. On the other hand, if the composition is changing as a function of depth, then a smearing of the depth change of composition will result. In extreme cases, a thin layer of one element deposited on the surface of a second element may sputter away very slowly (10). This could be interpreted by the unwary as a deep diffusion of the one element into the other.

A third phenomenon which can limit depth resolution is preferential sputtering. This can occur when one part of a specimen sputters away more quickly than another. An obvious example is the case of inclusions which may sputter more slowly than the bulk material. The result is that as sputtering proceeds, the specimen surface becomes rougher, resulting in the loss of depth information. Even for quite pure specimens, different crystallographic planes will sputter at different rates (particularly if inert gas primary ion beams are used) with the result that a smooth polished surface can become faceted. The use of oxygen as primary ion beam has been shown to minimize these effects (11).

ION MICROPROBES

The ion microprobe consists of an ion source and primary ion optics to produce an ion beam of a few micrometers in diameter. This small diameter beam falls on the specimen and secondary ions are released. The secondary ions are extracted into a mass spectrometer with appropriate detection circuits so that individual ions can be detected. Normally, the primary beam can be scanned over the surface of the specimen, and secondary ion intensities can be impressed on the z-electrode of an oscilloscope to obtain secondary ion images. An example of this kind of instrumentation is the ARL ion microprobe. A schematic diagram of this instrument is shown in Figure 4. A duoplasmatron is used as ion source and the primary ions are mass selected using a magnetic mass spectrometer of moderate mass resolution. In this way, neutrals cannot bombard the specimen. The primary ion column is capable of focussing the primary ion beam to a diameter of a few micrometers with a beam current of 1 nanometer.

A particularly attractive ion source for use in ion microprobes is the liquid metal ion source (12). Ions are pulled off the surface of a liquid metal by an electrostatic field, in some ways similar to the electron field emission sources. With such a source beam sizes of less than 0.1 micrometer have been reported (13). Such a small diameter source has great potential as the demands for more localized analyses increase. However, the limitations on sensitivity as dimensions shrink which are outlined below may make such sources less attractive.

THE ION MICROSCOPE

The ion microscope (Figure 5) consists of a primary ion source and primary ion optics so that the focussed primary ion beam strikes the surface of the specimen. Secondary ions are extracted with an extraction lens, then through transfer optics which permits the choice of acceptance angle, to the entrance slit of the electrostatic sector of the mass spectrometer. After passing through the mass spectrometer, the ions are incident on a channel plate, with the area of impact being controlled by a projection lens. Ions in passing through the entire instrument maintain their spatial relationship so that an image can be seen on the fluorescent screen in which dark and light areas represent positions of lesser and greater ion emission. Alternately, the secondary ions can be deflected into an electron multiplier or Faraday cup so that total secondary ion intensities can be measured.

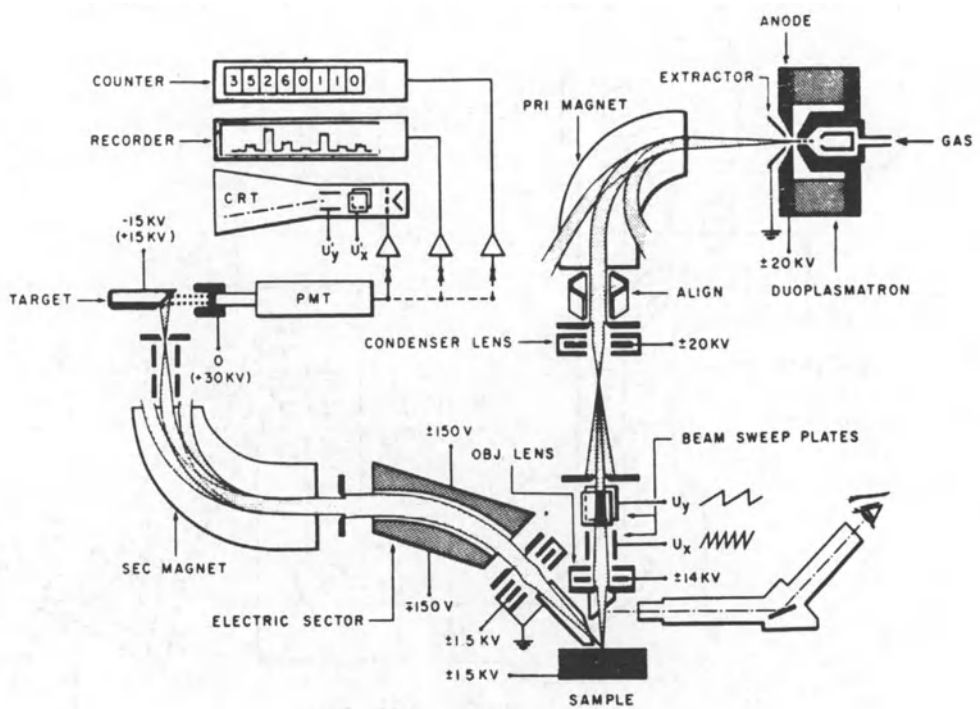

FIG. 4 Schematic Diagram of the Applied Research Laboratories Ion Microprobe Mass Analyser (IMMA)

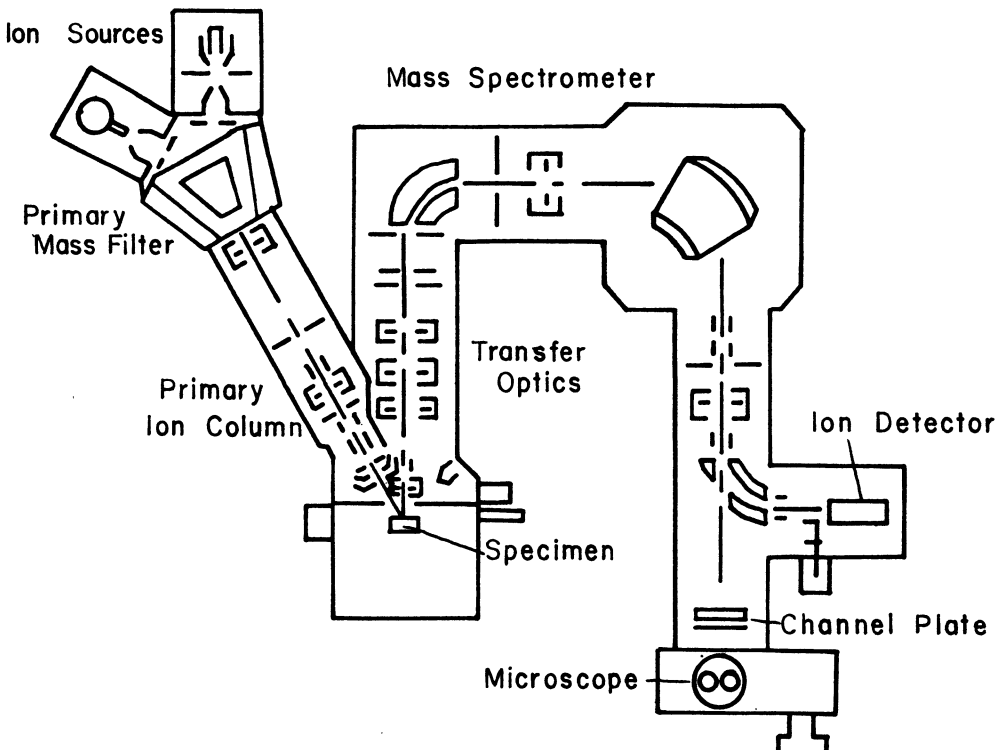

FIG. 5 Schematic Diagram of the Cameca Ion Microscope IMS 3f

ION IMAGING

Two methods have been developed for the formation of ion images in which three-dimensional information can be obtained about a specimen. This is the result of knowing not only the secondary ion intensities as a function of time and hence depth in a specimen but also as a function of position in the specimen which provides information about the other two dimensions. While the depth resolution can be as small as approximately 10 Angstrom units, the lateral resolution of ion images is limited to 0.1 to 1 micrometer.

The first method for obtaining ion images utilizes an ion microprobe in which a finely focussed primary ion beam bombards the specimen and intensity is recorded as a function of ion beam position as the primary ion beam is scanned across the surface of the specimen. This is entirely analogous to the process of obtaining x-ray images in an electron probe microanalyser. However, because secondary ion emission is a very localized phenomenon, the resolution in the secondary ion image is almost completely the result of the primary ion beam diameter, the smaller the beam, the better the resolution. Examples of secondary ion images photographed directly from the face of an oscilloscope tube can be seen in Figure 6. In this example of an electrolytic iron specimen, a hole was drilled with subsequent oxidation of the iron around the hole. The oxides are seen in cross-section on a polished specimen. The lower left corner of the image is unoxidized iron while next to the iron is FeO, then Fe_3O_4 in the upper left. A very important characteristic of ion images is illustrated in the mass 56 image, namely the inversion of intensities, i.e., a higher secondary ion intensity from a phase containing a lower concentration of an element than from the phase containing the higher content. Note in the iron image the oxide phases which contain 50 atomic percent iron or less have a greater brightness than the pure iron which has double the concentration even though these images were obtained using a primary oxygen beam. This is not an uncommon phenomenon and makes the simple interpretation of images in terms of the higher the brightness the higher the concentration an extremely dangerous assumption. The need for a means for matrix correction in these images becomes obvious indeed.

Since these kinds of ion images are obtained point by point in sequence as the ion beam is scanned over the surface of the specimen, quantitative accumulation and storage of the image information consists simply of storing sequentially in a memory the intensity data as a function of beam position (14). Once data has been stored in this manner for a number of elements as a function of position and time, corrections for matrix effects can be applied and images reconstructed as a function of composition rather than simply intensity (15). Further, with appropriate data manipulation, concentrations can be displayed or plotted of any section through the analytical volume.

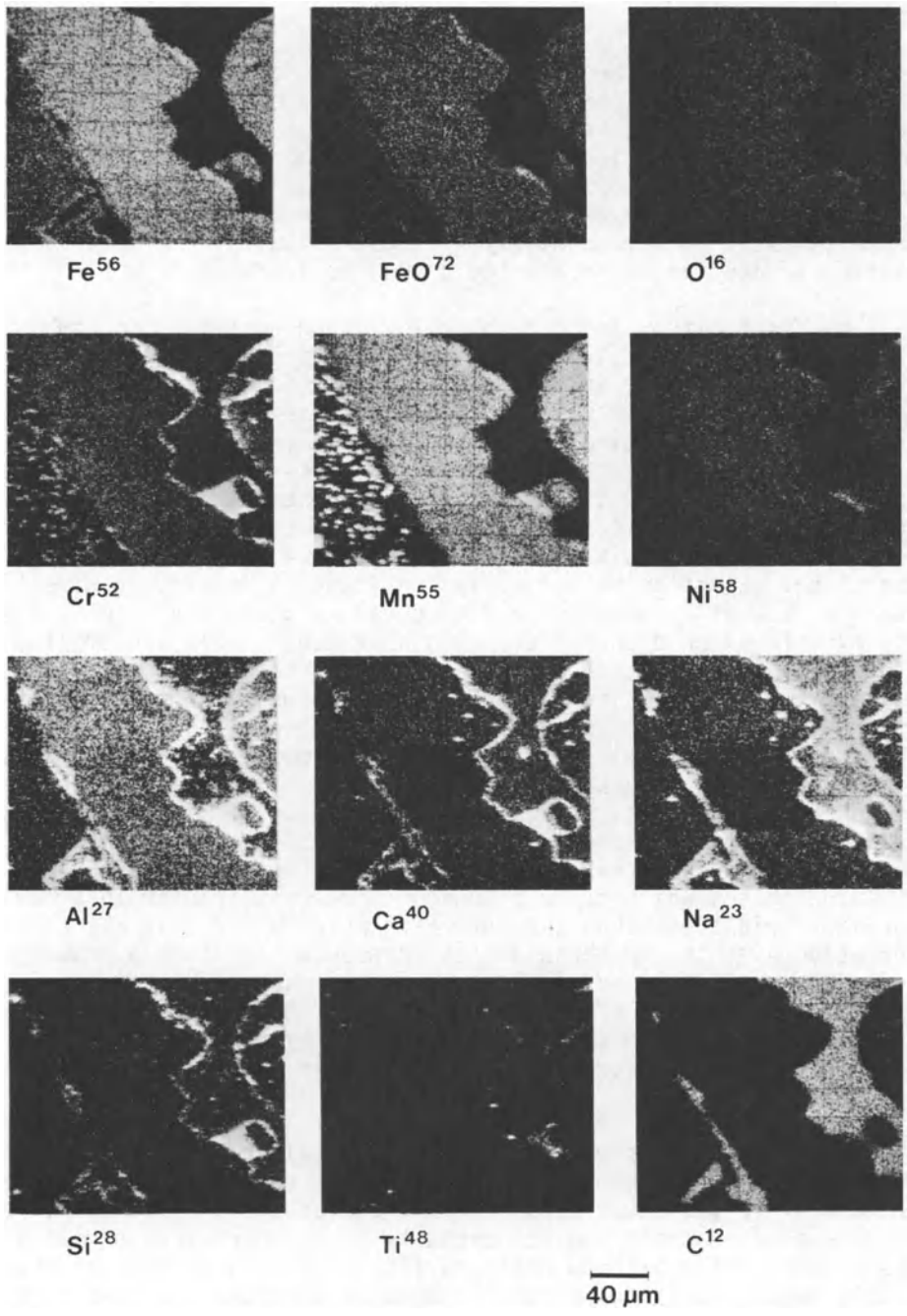

FIG. 6 Scanning Ion Images From an Iron Oxide Specimen. Typical Exposure Times 10-600 Seconds

The second method of ion imaging is typified by the ion optics used in the Cameca ion microscope. The spatial relationship of the secondary ions leaving the surface of the specimen is maintained in passing through the instrument so that when the secondary ion beam is magnified and spread out to strike the channel plate, a magnified image of the specimen in terms of ion intensity is seen on the fluorescent screen. Figure 7 shows such an image from an integrated circuit chip for both $^{27}Al^+$ and $^{28}Si^+$ ions. An important fact to realize about images formed in this manner is that the resolution in the image is a function of the secondary ion optics only, and the primary ion beam diameter is unimportant in the definition of such an image. Further, the entire image is present on the screen at all times provided the primary beam is sufficiently defocussed. The specifications for the Cameca IMS 3f state that the resolution in secondary ion images can be as small as 0.5 micrometers. Such images as are seen in Figure 7 are only qualitative in nature, again with the limitation in interpretation imposed by inversions in the intensity-concentration relationship which was discussed above. For quantitative measurements, it is necessary to convert the secondary ion image to quantitative numerical data. Several systems have been constructed to carry out this measurement based on either a T.V. camera which views the channeltron image (16) or a resistive anode placed behind the channel plate to replace the

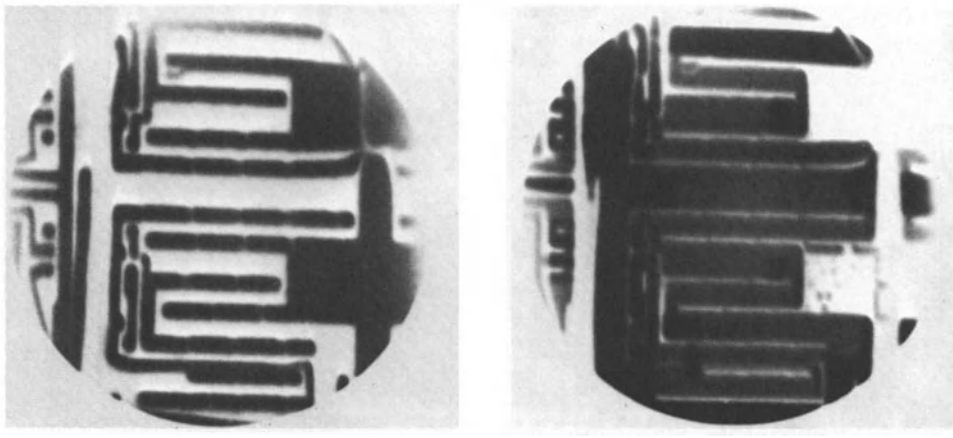

FIG. 7 Ion Microscope Images of an Integrated Circuit Chip. Field of View 150 μm. Exposure 0.1 Seconds. Contrast Reversed.

fluorescent screen (17). In either case, the objective is to obtain a quantitative measurement of ion intensity as a function of pixel location in the image. Once ion intensities have been digitized, the procedure for image analysis is fundamentally the same as with the images obtained with a probe type instrument.

LIMITATIONS IN ION IMAGE ANALYSIS

As the dimensions decrease laterally to the order of a few micrometers, then the concentrations which can be detected within the small volume must by necessity increase. A relatively simple calculation based on the sensitivity which can be achieved from blanket implants can reveal the ultimate detection limits to be expected in more limited volumes. In Figure 8 is seen a depth profile for a boron implant in silicon at 50 KeV with a total dose of 1.0×10^{15} atoms per square centimetre. The measurement was made with the primary beam rastering over an area of 250 x 250 micrometers with secondary ions being extracted and measured from an area 60 micrometers in diameter. The area under the curve, corrected for measurement time, corresponds to the total number of ions which are extracted from and measured from the 60 micrometer diameter area which contained a total number of boron atoms equal to the total dose times the area. For the profile of Figure 8, the total integrated area under the boron curve is 5.65×10^6 counts and the

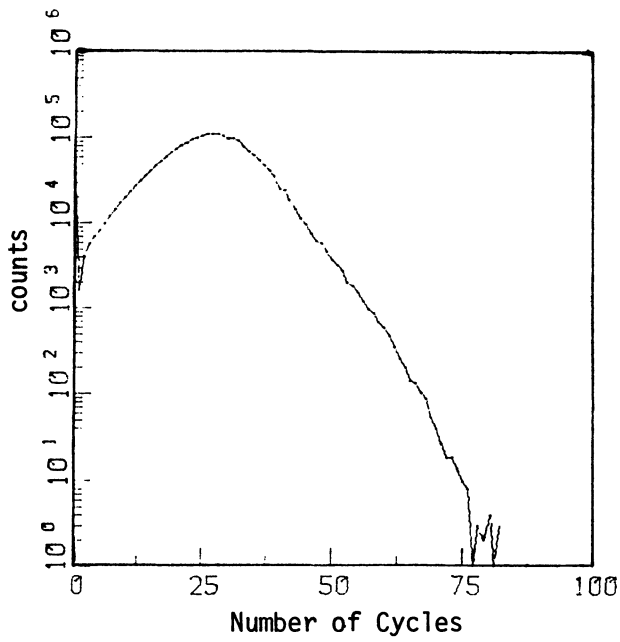

FIG. 8 Depth Profile for $1x10^{15}a/cm^2$ 50 KeV B Implant in Silicon Measured Using an O_2^+ Primary Ion Beam

total number of atoms in the volume analyzed is 2.83×10^{10} atoms. Thus for each measured boron secondary ion, approximately 5000 boron atoms must be sputtered. Applying these numbers to the case of a 50 Angstrom thick layer in a 1 square micrometer area, the total number of atoms contained in such a volume is 2.5×10^{9}. If we place the detection limit as 10 counts, then this corresponds to a limiting concentration of about 20 ppma. This limit can be pushed down only by increasing the analysis volume or the efficiency of ion measurement and detection. Since the Cameca IMS 3f already has high transmission for secondary ions, the prospects for greatly improved sensitivity are not great.

Similar considerations apply to the ion probe type instruments as well. However, the demands for maintaining the spatial integrity of the secondary ions in the ion microscope which should limit collection angles because of lens aberrations, are not a consideration in an ion probe. Thus in principle, increased collection efficiency should be possible in a probe type instrument (18). To this date, no probe instrument to my knowledge can match the sensitivities obtained with the Cameca IMS 3f.

CONCLUSIONS

SIMS is a very sensitive analytical technique capable of giving three-dimensional compositional information about solid specimens. Many applications particularly to semiconductor analysis require the extreme sensitivity of SIMS which can detect parts per billion atomic of most of the common semiconductor dopants. More localized analysis in small volumes demands that detection limits be relaxed as the inevitable consequence of reduction in the available sample in this destructive analytical technique.

REFERENCES

1. H.F. Winters. "Physical Sputtering: A Discussion of Experiment and Theory", in "Radiation Effects on Solid Surfaces" M. Kaminsky, ed. American Chemical Society, Washington, D.C. (1976), p. 1.
2. J.D. Brown, M.J. Higatsberger, F.G. Rüdenauer and W. Steiger. "Comparison of Oxygen and Indium Primary Ion Beams for SIMS Depth Profiling" in "Secondary Ion Mass Spectrometry, SIMS IV" A. Benninghoven et al., eds. Springer Verlag, Berlin (1984), p. 302.
3. J.B. Metson, G.M. Bancroft, H.W. Nesbitt and N.S. McIntyre. "Molecular Ion Suppression in the Secondary Ion Mass Spectra of Minerals" in "Secondary Ion Mass Spectrometry, SIMS IV" A. Benninghoven et al., eds. Springer Verlag, Berlin (1984), p. 466.

4. A. Benninghoven, D. Jaspers and W. Sichtermann. "Secondary Ion Emission of Amino Acids" Appl. Phys. 11: 35 (1976).
5. D.E. Harrison, Jr., W.A. Mason and R.P. Webb. "Molecular Dynamics Computer Simulation Study of the Damage Produced in Metal Target Surfaces During Ion Bombardment" in "Secondary Ion Mass Spectrometry, SIMS IV" A. Benninghoven et al., eds. Springer Verlag, Berlin (1984), p. 24.
6. C.A. Andersen, J.R. Hinthorne. "Thermodynamic Approach to the Quantitative Interpretation of Sputtered Ion Mass Spectra" Anal. Chem. 45: 1421 (1973).
7. C.A. Andersen. "Analytic Methods for the Ion Microprobe Mass Analyser Part II" Int. J. Mass Spectrom. Ion. Phys. 3: 413 (1970).
8. C.A. Andersen. "Progress in Analytic Methods for the Ion Microprobe Mass Analyser" Int. J. Mass Spectrom. Ion. Phys. 2: 61 (1969).
9. H.A. Storms, K.F. Brown and J.D. Stein. "Evaluation of a Cesium Positive Ion Source for Secondary Ion Mass Spectrometry" Anal. Chem. 49: 2023 (1977).
10. P. Williams. "Anomalous Sputter Yields Due to Cascade Mixing" Appl. Phys. Lett. 36: 758 (1980).
11. C.A. Andersen and H.J. Liebl. "Analysis by Bombardment With Chemically Reactive Ions" U.S. Patent No. 3508045, July 12, 1968.
12. R. Clampitt. "Advances in Molten Metal Field Ion Sources" Nucl. Instrum. and Methods 189: 111 (1981).
13. R. Levi-Setti. "Heavy Ion Probes Play Significant Role in SIM Development" Ind. Res. and Dev., Sept. 1982, p. 124.
14. F.G. Rüdenauer. "Instrumental Aspects of Spatially 3-Dimensional SIMS Analysis" in "Secondary Ion Mass Spectrometry, SIMS III" A. Benninghoven et al., eds., Springer Verlag, Berlin (1982), p. 2.
15. G.H. Morrison and M.G. Moran. "Image Processing SIMS" in "Secondary Ion Mass Spectrometry, SIMS IV" A. Benninghoven et al., eds., Springer Verlag, Berlin (1984), p. 178.
16. B.K. Furman and G.H. Morrison. "Direct Digitization System for Quantification in Ion Microscopy" Anal. Chem. 52: 2305 (1980).
17. R.W. Odom, D.H. Wayne and C.A. Evans, Jr. "A Comparison of Camera-Based and Quantized Detectors for Image Processing on an Ion Microscope" in "Secondary Ion Mass Spectrometry, SIMS IV" A. Benninghoven et al., eds., Springer Verlag, Berlin (1984), p. 186.
18. H. Liebl. "The Ion Microprobe - Instrumentation and Techniques" N.B.S. Spec. Publ. 427, K.F.J. Heinrich and D.E. Newbury, eds., (1975), p. 1.

ANALYTICAL ION MICROSCOPY OF CELLS AND TISSUES

P. Galle and J.P. Berry

Laboratoire de Biophysique, Faculté de Médecine de Créteil

8, rue du Général Sarrail 94000 Creteil, France

INTRODUCTION

With the introduction 40 years ago of electron microscopy in biomedical research, a new submicron world has been observed and the ultrastructure of normal and pathological cells has been described with a remarkable precision. However, some new investigations are now needed for a better understanding of the function of subcellular organelles.

In cell biology, the aim being to establish a relation between a given structure and a function, one important point is to know the chemical composition of these organelles. New microanalytical methods have been developped for the chemical analysis of microscopic or submicroscopic volumes in a solid sample, and these methods can be applied to the study of biological tissues. The first method, Electron probe X ray analysis proposed by Castaing (3) is now very well known. These instruments equipped with electron microscopes are of particular interest in biology. More recently new methods have been developped and applied to different fields of research. Among these methods, Analytical Ion Microscopy (AIM) proposed by Castaing and Slodzian (4) offers the biologist new possibilities. The main advantage of this method is its very high sensitivity which makes possible for the first time analysis of elements at a trace concentration (0.1 ppm or less) in a microvolume. Isotopic analysis is also possible and images of distribution of most stable or radioactive nuclides are easily obtained in a tissue section with a resolution of 0.5 μm.

The aim of this paper is to present the potentiality of AIM in cell biology and cell pathology.

PRINCIPLES OF THE METHOD

An ion beam of several KeV energy (primary ions) is focused onto a relatively large area (30-400 µm in diameter) of the tissue section. As a result of this ion bombardment, the atoms of the upper atomic layers of the section are sputtered (fig. 1) and some of them are in a ionized form (positive or negative secondary ions). These secondary ions characteristic of the surface of the section are accelerated and focused into a beam carrying the image of the sputtered atoms. These secondary ions are filtered by a mass spectrometer and the selected ions are imaged on a detection display system.

As a result of the sputtering process, the specimen is progressively eroded at the rate of about one atomic layer per second and the analysis is performed at the cost of the destruction of the specimen.

INSTRUMENTATION

The instrument consists of four different part : a primary ion source, an electrostatic optics to accelerate and focus the secondary ions emitted from the tissue section, a mass spectrometer for the selection of secondary ions and a detection display system (figure 2).

1) Primary ion source

Two varieties of primary ion sources can be used : a duoplasmatron or a Cesium gun. The duoplasmatron gun produces either a noble gas (A_r^+) or a reactive gas (O_2^+, O^-, N^-). The primary ions are accelerated (12 KeV) and focused with a double condenser lens system onto the surface of the specimen at approximatively 45°. The diameter of the bombarded surface varies from 30 to 400 µm depending on the area to be imaged. The cesium gun produces cesium positive ions which are accelerated and focused onto the sample.

2) Electrostatic optics

The secondary ions emitted from the surface of the sample are collected, accelerated by a potential of 4.5 KV and focused into a beam by electrostatic lenses. This beam carries the global image of all secondary ions emitted from the specimen. This non analytical image is not formed and the beam enters the mass spectrometer where the ions will be selected.

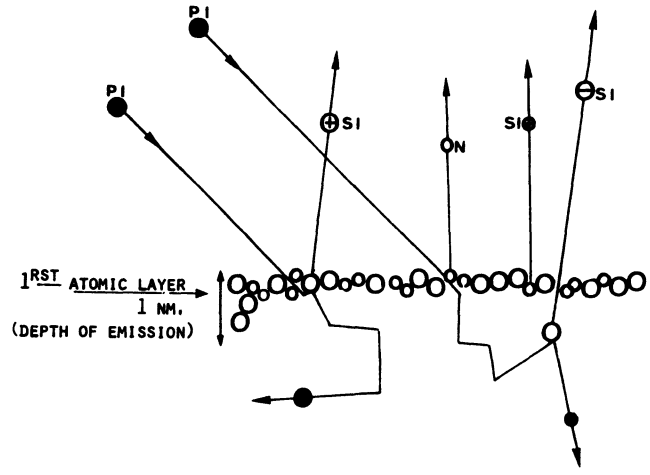

Figure 1. Emission of secondary ions SI from the surface of a specimen bombarded with primary ions PI. N = Neutral atoms.

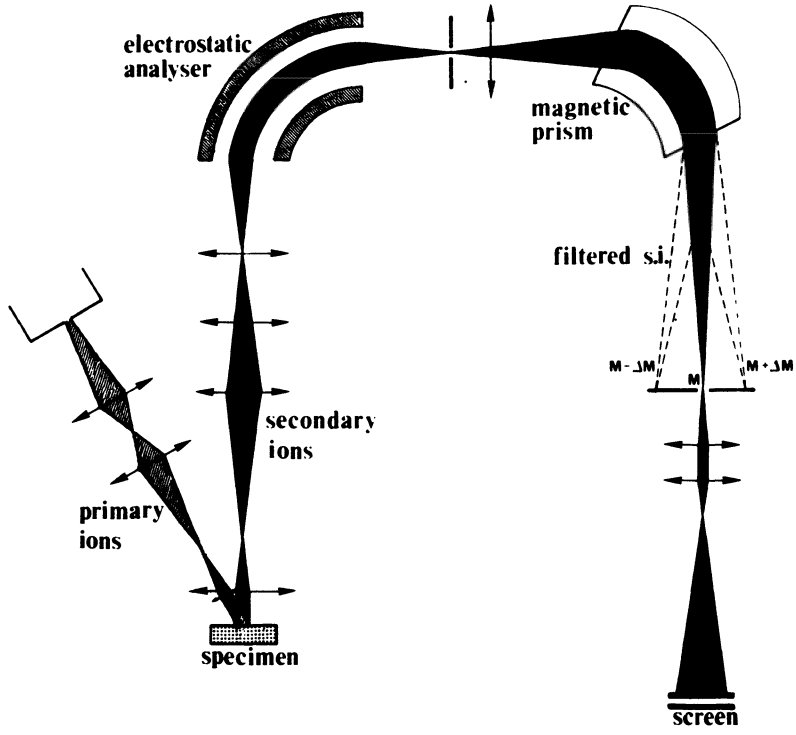

Figure 2. Schema of the Ion Microscope

3) Mass spectrometer

In the mass spectrometer, the secondary ion beam is first deflected by an electrostatic field where the ions are selected according to their energy and then by a magnetic field where the ions are selected according to their specific charge $\frac{e}{m}$ (e = electrostatic charge, m = mass of the charged particle). The mass spectrometer has been designed as to preserve the quality of the final selected image. Finally the role of the mass spectrometer is to split the initial beam carrying the global, non analytical image, into as many secondary beams as there are ions of a given specific charge $\frac{e}{m}$. Each of these beams carries the image of a given variety of ion. One of these beams can be selected with a suitably selected aperture and imaged on the detection display system. By changing the setting of the mass spectrometer, it is possible to observe successively on the screen images of the different varieties of ions emitted from the specimen.

4) Detection display system

The selected ion image carryied by the beam cannot be directly imaged on a fluorescent screen or a photographic plate because of the very weak response of these receptors to ions. The detection display system used in the new instruments is a microchannel plate where ions are converted into electrons which can be displayed on a fluorescent screen.

SPECIMEN PREPARATION

The surface of the specimen must be perfectly flat and equipotential. In addition, the specimen must be prepared so that the in vivo distribution of the elements present in the different cellular and intracellular compartments is not changed. Subsequently the specimen preparation is depending on the elements, diffusible or non diffusible, to be studied.

1) Study of non diffusible elements in a tissu section

Tissue sections embedded in resins currently used in electron microscopy technics (epon, araldite, methacrylate) can be studied by AIM. However, these resins of low electrical conductivity may become irregularly charged during bombardment by the primary ions with a resultant loss of the image. This difficulty is avoided if the section is thin enough (less than 2 μm) and deposited on a conductive metallic support. Pure gold is generally used. In this condition, the tissue section acts like a sheet with parallel surfaces and the support like one of the plates of a condenser charged to a given potential. The two faces of the section (especially the

free surface which will be used for the analysis) correspond to an equipotential surface, charges can flow along the metallic support and the analytical images are obtained without difficulty. With thicker sections, charging effects make impossible the obtention of good quality images.

Paraffin sections deposited on a gold specimen holder can also be studied after removing of the paraffin. However in this case, the surface of the section is not perfectly flat and the resolution is not so good.

2) Study of non diffusible elements in a cell smear

A smear of different varieties of cells deposited on a perfectly metallic support can be easily studied. Of particular interest is the study of cells cultured on a gold specimen holder (cancerous cells, neurones, keratinocytes, macrophages).

3) Study of diffusible elements

In this case, the conventional technics of tissue fixation (chemical fixation) and embedding cannot be used. The only valid method should be a quick freezing of the tissues followed by cryosectionning. However, even in these conditions, it is very difficult to avoid a diffusion of very soluble elements such as sodium, potassium, chloride through cell membranes 7 nm. thick. These applications are limited by the difficulty of the specimen preparation and not by the microanalytical method.

FUNCTIONNING OF THE ION MICROSCOPE

1) Sputtering process

With a primary ion beam density of 0.1 $\mu A/cm^2$ or 10^5 ions/μm^2/sec., the erosion rate of a biological epon section is 1-10 atomic layers/sec. In these conditions, a section 1 µm thick is generally completly eroded in 300 - 3000 sec. However, the erosion rate varies with the chemical and physical state of the matrix and experience shows that the nuclei of the cells are more rapidly eroded thant the cytoplasm. The sputtering yield S is defined as :

$$S = \frac{N_o}{Np}$$

where N_o is the total number of atoms sputtered from a given surface of the specimen and Np is the total incident primary ions during the same time onto the same surface. During the sputtering process, most of the secondary ions are emitted from the two or

three first atomic layers of the surface although the primary beam produces perturbations to a deepth of approximately 10 nm (30 atomic layers).

2) Ionization ratio

All sputtered atoms are not emitted as monoatomic mono-charged particles. Some atoms are emitted in a neutral form and some atoms are emitted as poly atomic, charged or neutral, particles. Since every atoms or particles emitted in a neutral form are lost for analysis, an important factor influencing the sensitivity is the ionization ratio τ defined for the element A emitted as positive ion as

$$\tau (A^+) = \frac{N (A^+)}{N (A)}$$

where N (A^+) is the number of atoms A emitted as a monoatomic positive ion and N (A) the total number of atoms A emitted from the same surface during the same time.

3) Collection efficiency and transmission of the instrument

All ions emitted from the surface of the specimen do not reach the detection display system. Some of them are not collected by the objective lens and other ones are eliminated by the diaphragms of the mass spectrometer resulting in a loss in sensitivity. The transmission of the instrument or collection efficiency η is defined for positive ions A as

$$\eta = \frac{n (A^+)}{N (A^+)}$$

where N (A^+) is the number of ionized atoms A^+ emitted from a given area of the sample and n (A^+) the number of ions A^+ collected by the detector.

4) Practical ion yield or useful yield

Finally the important parameter to be considered to appreciate the sensitivity is the useful yield τ_u defined for positive ions of atoms A as

$$\tau_u (A^+) = \tau (A^+) \times \pi$$

CHARACTERISTICS OF THE ION MICROSCOPE

1) Spatial resolution

Analytical images of an epon tissue section are obtained with a resolution of 0.5 µm for an imaged area from 30 to 400 µm in diameter. The resolution in depth varies from 1 to 1000 nm depending on the volume to be sputtered to obtain the image. For an element of high τ_u and in a concentration of the order of 1 % - 1 ‰, the images are obtained in a few seconds corresponding to the sputtering of only 1 - 10 atomic layers. More important volumes have to be sputtered for elements at a trace concentration or of low τ_u.

2) Mass resolving power of the mass spectrometer

The mass resolving power P is defined as

$$P = \frac{M}{\Delta M}$$

where M is the mass of the ion and Δ M is the smallest difference of mass that can be distinguished. With P = 300 every mass unit from 1 to 300 can be separated. However such a resolving power is not sufficient to separate a given monoatomic ion from a cluster ion or multicharged ions. A given atom A may be emitted either as a monoatomic ion A^+ or as multicharged ion A^{++}, A^{+++}, or as cluster ions A_n^+, AB^+, ABC^+... In a biological tissue, many of these cluster ions are formed of $C_n H_m^+$, with n and m = 1, 2, 3... With P = 300 many interferences may be observed. For example Al^+ and $C_2 H_3^+$ have the same mass unit 27. Fe^+ and CaO^+ have the same mass unit 56. A better mass resolving power of 5000 which is obtained on most modern instruments is generally sufficient to resolve most mass interferences. For example the true masses of Iron, calcium and oxygen are respectively ^{56}Fe = 55,934932, ^{40}Ca = 39,962589 and ^{16}O = 15,994915. The true mass of the cluster ion ^{56}CaO is 55,957504. The mass resolving power required for the separation of ^{56}Fe from ^{56}CaO is $P = \frac{56}{0,027572} = 1800$

3) Sensitivity

Ultimate sensitivity should be achieved if all atoms emitted from the specimen were collected, detected and localized by the detector. However, some atoms are lost for analysis, and the sensitivity is given by the ratio R

$$R = \frac{\text{number of atoms detected and localized in a given area}}{\text{total number of atoms sputtered from the same area of the sample.}}$$

The atoms lost for analysis are : 1) atoms emitted as a neutral form or as cluster ions, 2) secondary ions eliminated by the diaphragms and 3) secondary ions not detected by the detection display system. R is dependant on three factors : the ionization ratio τ of the element, the collection efficiency η of the instrument and the quantum yield Q of the detector. The value of R is given by

$$R = \tau \times \eta \times Q = \tau_u \times Q$$

η and Q are depending on the characteristics of the instrument. When the detector is a microchannel plate, Q is of the order of 30 % ; for a good resolution on the image (1 µm), small diaphragms must be used and η is of the order of 3 ‰.

Minimum detectable concentration

The minimum detectable concentration is obtained for elements of highest ionization ratio. Taking the example of an element such as Sodium in a specimen bombarded by oxygen primary ions. In these conditions τ $(Na^+) \simeq 100$ % and

$$R(Na^+) = \tau (Na^+) \times \eta \times Q$$

$$R(Na^+) = 1 \times 3.10^{-3} \times 30.10^{-2} \simeq \frac{1}{1000}$$

For sodium, one light point is observed on the screen, and the element is detected and localized with a precision of 1 µm when 1000 sodium atoms are emitted from 1 μm^2 of the surface of the specimen.

The minimum detectable concentration is depending on the number of sputtered atoms under 1 μm^2 of the surface of the specimen.

The number of atoms in a monoatomic layer of 1 μm^2 is approximately 10^7. By sputtering one monoatomic layer, the minimum detectable concentration is

$$Cm = \frac{10^3}{10^7} = 10^{-4}$$

For the detection of sodium at a lower concentrations, a larger amount of material has to be eroded : by sputtering 1000 atomic layers (a thickness of about 0.3 µm), the minimum detectable concentration is given by

$$Cm = \frac{10^3}{10^{10}} = 10^{-7} = 0.1 \text{ ppm}$$

by sputtering the whole thickness of a section 1 μm thick, the minimum detectable concentration should be Cm = 30 ppb.

Variation of sensitivity with the ionization ratio

For most elements, τ is not 100 % and the sensitivity is lowered. τ is very depending on the chemical characteristics of the element of its chemical bonds in the matrix and of the nature of primary ions. Under bombardment by non reactive gaz such as argon, τ for positive ions is high for elements of low ionization potential (groups 1, 2A, 3A of the periodic classification) and for negative ions, τ is high for elements of high electron affinity (groups 6A, 7A). For a given element, the effect on τ of the chemical bonds in the matrix has been described by Slodzian (6). For example, under argon bombardment, τ (Al^+) is almost 100 times higher in $Al_2 O_3$ than in pure Al.

For a given element and a given matrix τ may vary very much with the nature of primary ions. By using electronegative elements such as oxygen ions (1), the ionization ratio of positive ions is greatly enhanced and advantage can be taken of this effect for a better sensitivity. A similar effect can be obtained by introducing oxygen at low pressure at the surface of the target (7). For elements preferentially emitted as negative ions, enhancement of negative ion emission is obtained by using an electropositive element such as Cesium (Cs^+) as primary ions (5). The same effect is observed by Cesium flooding of the surface of the specimen (2). This enhancement of τ may be very high, up to 5 orders of magnitude for elements such as gold or copper and advantage can be taken from this effect to improve the sensitivity for all elements preferencially emitted as negative ions.

COMPARISON OF ANALYTICAL ION MICROSCOPY WITH OTHER MICROANALYTICAL METHODS

In electron probe X ray microanalysis (EPMA), the minimum detectable concentration is of the order of 100 ppm for most elements of $Z > 11$ (sodium). For elements of Z between 5 and 11 the sensitivity is low and elements of $Z < 5$ are not detectable. In comparison, in Ion Microscopy all elements can be studied, the sensitivity is generally 1000 - 10 000 times better than in EPMA and isotopic analysis is possible. On the other hand, observations of the specimen at the ultrastructural level is not possible.

In Electron energy loss microanalysis, very small volumes, of the order of a few nanometers is diameter can be studied; however, in these volumes only elements at a relatively high concentration can be detected.

In Raman spectrometry using laser probes for microanalysis, some molecular informations can be obtained but the sensitivity is low.

In time of flight mass spectrometry using laser probes (LAMMA) the sensitivity is of the same order of magnitude as in Ion Microscopy. However, the mass resolving power of the mass spectrometer is not sufficient to eliminate mass interferences with cluster ions.

In Microautoradiography (MAR), an method of microlocalization very often used in biological reserach, the spatial resolution is of the order of 0.5 μm and the sensitivity may be very high. However only some radioactive isotopes are convenient in M.A.R. for a good resolution and a good sensitivity and three factors have to be considered : the percentage of atoms useful for the detection, the quantum yield of the detector and the background.

The percentage of atoms useful for the detection

In MAR, the collection efficiency of the detector (photographic emulsion) is 50 % (2 π sterads). However, the number of atoms A really useful for detection are only those which decay during the contact of the section with the photographic emulsion. That means that for both long-lived or short-lived isotopes, the sensitivity may be much lowered. Taking the example of plutonium ^{239}Pu (T 1/2 = 24.400 years), during a 3 month's exposure, less than two decays (1.8) are observed in 10^{-16} g of ^{239}Pu (250.000 atoms) in 1 μm^3. Since 50 %of the α particles are detected, the probability to observe one α track is 1/250.000 for a 3 months exposure. In comparison, with Ion Microscopy the detection of this amount of ^{239}Pu should be obtain in several seconds only for the same spatial localization. On an other hand, for an isotope such as ^{125}I (T 1/2 = 2 months) the sensitivity should be much higher in MAR than in AIM.

The quantum yield of the detector

In MAR, the emission of a single particle is sufficient to produce a reduction of a silver bromide grain : one single radioactive atom may be detected and localized with a precision of 0.5 μm. For a β particle of low energy (10 - 20 KeV) the quantum yield of the detector may be 100 %. However for a β particle of higher energy, the probability of a silver bromide grain to be reduced may be much lower (less than 1 %) : the sensitivity and the resolution decrease. In AIM, the quantum yield of a detector such as microchannel plate is of the order of 30 %.

The background

In MAR, the background is very depending on the characteristics of emission of the radionuclide. For isotopes emitting γ radiations or β particles of high energy, the background may be very important with a resulting loss in sensitivity. In AIM, the background may be considered as almost negligeable.

A comparison between MAR and AIM is presented on Table 1.

Table 1

	MAR	AIM
Range of study	Onlysome radionuclides	Every stable or radioactive nuclide
Exposure time	1 day to 6 months	1 sec to 1000 sec
Specimen observation	Light and electron microscopy	Ion microscopy
Resolution	Depending on the nuclide $\simeq$ 0,5 μ	= 0,5 μ
Local isotopic ratio	not possible	possible
Background	yes	no
Sensitivity	Depending on the characteristics of the nuclide : radioactive period.β energy.	Depending on the practical ion yield of the element

EXAMPLES OF APPLICATIONS

Gallium is a tracer used in nuclear medicine for the detection of tumors. Figures 3a and 3b are two analytical images obtained from the same area of a kidney tissue section of a rat after injection of gallium. The specimen is a section 1 μm thick of the tissue embedded in epon. In this section, most of the sodium, a very diffusible element has been removed from the tissue during the preparation of the specimen (fixation, embedding). However, the concentration of sodium remains sufficient to obtain an image (fig. 3a) repre-

senting the histological structure of the tissue. Figure 3b shows the distribution of gallium which appears as bright points corresponding to the tubules. These bright points correspond to intracellular lysosomes.

Figure 4b shows the distribution of gallium in cancerous cells cultured on a gold specimen holder. Fgure 4a is the sodium image obtained from the same area of the sample.

Figure 5b shows the distribution of uranium in a tissue section of a rat kidney. The animal was sacrified 24 hours after an intravenous injection of soluble uranyle acetate. Uranium is focally concentrated and appears as bright points corresponding to the cytoplasm of some tubules. Histological structure of the section is observed on the sodium image (Fig. 5a).

Figure 6b shows the distribution of Selenium in a tissue section of a rat kidney. After injection of selenium, this element is concentrated in the basement membranes. Histological structure of the same area of the section is observed with the cluster ion $^{26}CN^-$ image (figure 6a).

Figures 7a and 7b show the distributionof nitrogen obtained with the cluster ion $^{26}CN^-$ and of phosphorus obtained with the cluster ion $^{79}PO_3^-$. These cluster ions are more emissive than the corresponding monoatomic ions.

Figures 8a and 8b show the distribution of two isotopes of iodine obtained from the same area of a thyroid section. The animal was sacrified 24 hours after injection of a radioactive isotope of iodine $^{129}I^-$. The distribution of the two isotopes are different. Natural stable iodine $^{127}I^-$ is observed both in the follicules in large homogeneous areas and inside the cells surrounding the follicules where it appears as bright points corresponding to intracellular secretion vacuoles. These vacuoles contain the hormonal iodine although the follicules contain the storage iodine fixed to a protein, the thyreoglobulin. 24 hours after injection of $^{129}I^-$, this isotope is only observed inside the follicules.

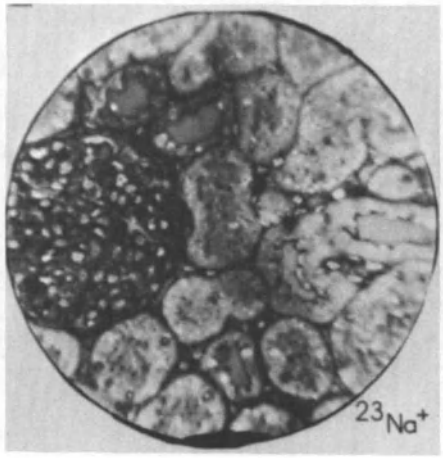

Figure 3a. Sodium image obtained from the surface of an epon section of a rat kidney. Histological structures of a glomerulus an several tubules are observed.

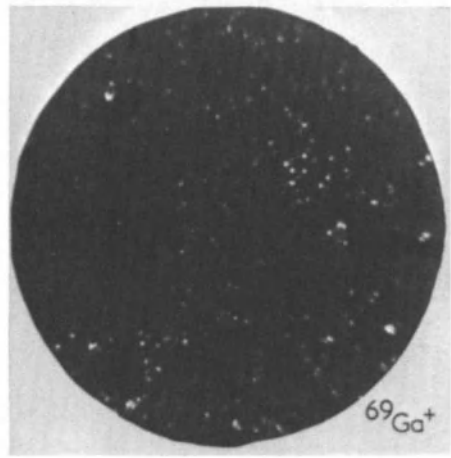

Figure 3b. Gallium image obtained from the same area as figure 3a.

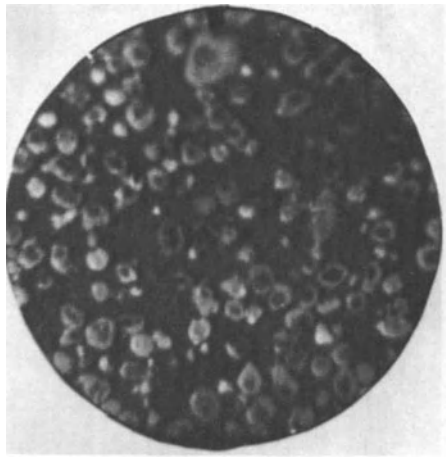

SODIUM $^{23}NA^{+}$

Figure 4a. Sodium image of cancerous cells cultured on a gold specimen holder.

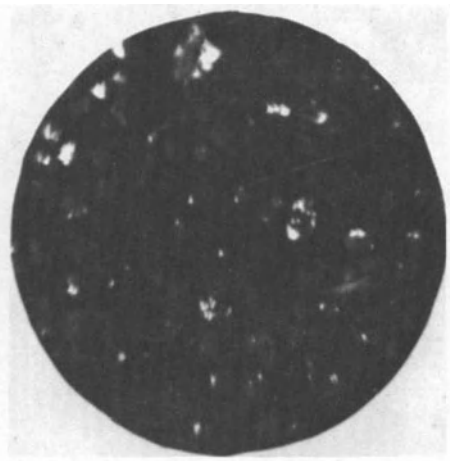

GALLIUM $^{69}GA^{+}$

Figure 4b. Distribution of gallium obtained from the same area as figure 4a.

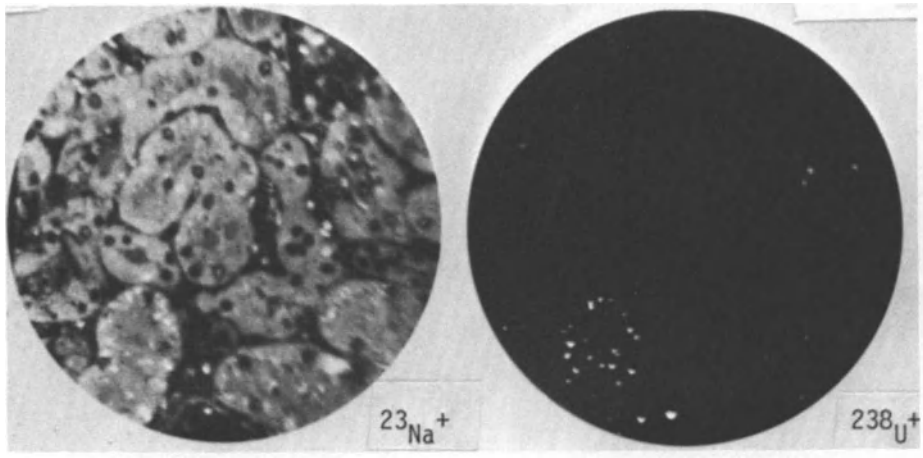

Figure 5a. Sodium image obtained from the surface of an epon section of a rat kidney. Histological structure of several tubules is observed.

Figure 5b. Uranium image ($^{238}U^{+}$) obtained from the same area as figure 5a.

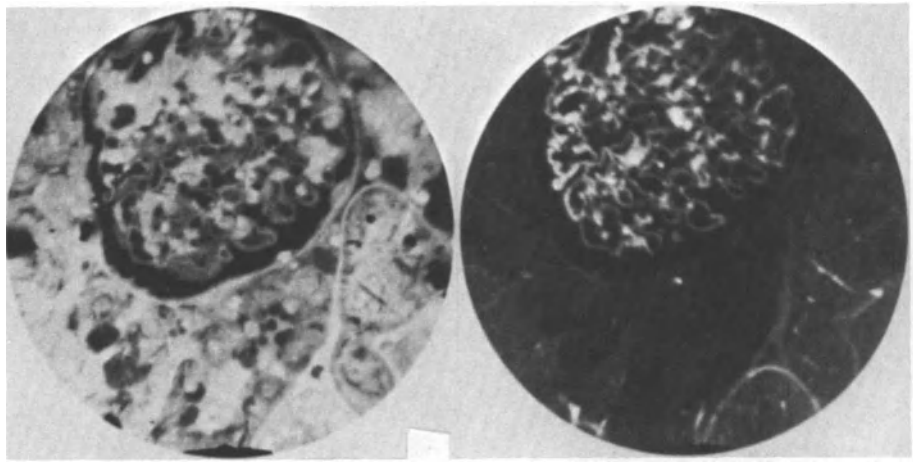

Figure 6a. Distribution of nitrogen obtained with the emission of a cluster ion $^{26}CN^{-}$ from the surface of the section of a rat kidney. Histological structures of a glomerulus and several tubules are observed.

Figure 6b. Selenium image ($^{80}Se^{-}$) obtained from the same area as figure 6a. Selenium is localized in the basement membranes of the glomerulus and in the basement membranes of the tubules.

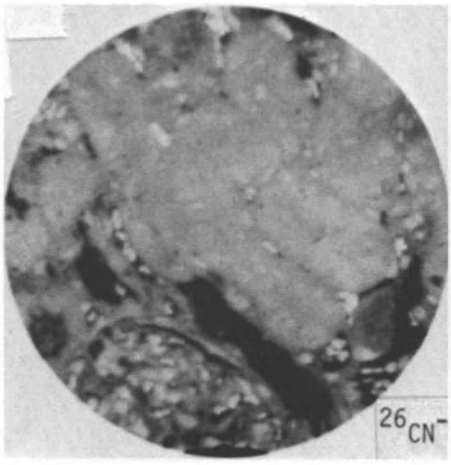

Figure 7a. Distribution of nitrogen obtained with the cluster ion $^{26}CN^-$ from the surface of the section of a rat kidney.

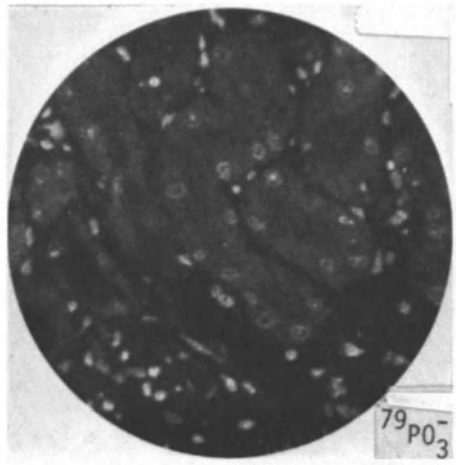

Figure 7b. Distribution of phosphorus obtained with the cluster ion $^{79}PO_3^-$ from the same area as figure 7a. An intense emission is observed from the nuclear chromatin.

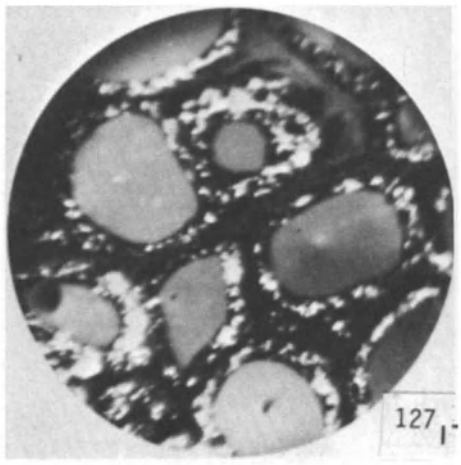

Figure 8a. Distribution of natural isotope of iodine $^{127}I^-$ from the surface of a thyroid section of a rat. ^{127}I is observed in the follicules (storage iodine) as large homogeneous areas and around the follicules as light points (hormonal intracellular iodine).

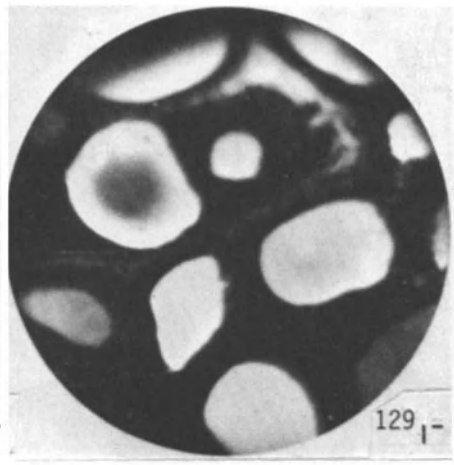

Figure 8b. Image of a radioactive isotope of iodine $^{129}I^-$ obtained from the same area as figure 8a. $^{129}I^-$ is only observed in the follicules.

REFERENCES

1. C.A. Andersen, 1973, Analytic methods and applications of the ion microprobe mass analyser. Microprobe analysis. J. Wiley and Sons NY, USA, 531-553.

2. M. Bernheim and G. Slodzian, 1977, Emission d'ions négatifs en présence de Caesium. J. Microsc. Spectr. Electr. 2, 291-292.

3. R. Castaing, 1961, Application des sondes électroniques à une méthode d'analyse ponctuelle chimique et cristallographique. Thèse Sci. Paris ONERA ed. Chatillon S/Bagneux France

4. R. Castaing et G. Slodzian, 1960, Microanalyse par émission ionique secondaire. J. Mcroscopie 1:395.

5. V.E. Krohn, 1962, Emission of negative ions from metal surfaces bombarded with cesium ions. J. Appl. Physics. 33:3523.

6. G. Slodzian, 1963, Etude d'une méthode d'analyse locale chimique et isotopique utilisant l'émission ionique secondaire. Thesis Sci. Paris, Masson ed. Paris.

7. G. Slodzian, 1975, Some problems encountered in secondary ion emission applied to elemental analysis. Surface Science, 48:1961.

ELECTRON SPECTROSCOPIES FOR STUDYING CHEMICAL BONDINGS AT SURFACES

R. Caudano, J.J. Pireaux and P.A. Thiry

Laboratoire de Spectroscopie Electronique
Institute for Research in Interface Sciences
Facultés Universitaires Notre-Dame de la Paix
61, rue de Bruxelles, B-5000 Namur, Belgium

INTRODUCTION

The general topic of these lectures being the sub-micron world, it seems pretentious to try to demonstrate the importance of a group of analytical techniques that has just recently grazed the area of 10 microns lateral resolution. The situation is even worse if one realizes that most of the corresponding instruments are still one or two orders of magnitude above that last figure. This could summarize the unfortunate (?) present status of the group of electron spectroscopies that will be reviewed here, namely : XPS (X-ray Photoelectron Spectroscopy, also known as ESCA for Electron Spectroscopy for Chemical Analysis), UPS (Ultra-violet Photoelectron Spectroscopy, the UV radiation being extracted from a conventional discharge lamp or a synchrotron) EELS and HREELS (Reflection Electron Energy Loss Spectroscopy at respectively Low and High Resolution). However, they share the important quality of being very sensitive to the surface chemical bondings and this quality makes them unsurpassed so far.

Indeed, their spectra show, in a way or another, "chemical shifts". Moreover, we will demonstrate that they complement very much each other in order to dig out different chemical informations from the surfaces.

Nowadays, the Scanning Auger Microscope (SAM) is the most successfull analytical microscopy that is able to image the elements of very small objects (currently 30 nm). At this level, the serious drawback of the method is a severe radiation damage of the sample.

In the near future, SIMS (Secondary Ion Mass Spectrometry) will also be able to achieve as good a lateral resolution, thanks to the development of liquid metal field emission sources. In such a case, it will be at the expense of a rapid erosion of the specimen. Photoelectron spectroscopies and low energy (few eV) electron energy loss spectroscopy are certainly much less harmful to the sample. It becomes a most relevant quality if one has to deal with organic, and particularly biological materials. This is another strong motivation to try to improve their spatial resolution.

Photoelectron spectroscopies achieve already a better lateral resolution by a conventional approach in which the size of the beam is decreased and its density increased. Position sensitive lenses are simultaneously developed, which will allow, in principle, a direct imaging of the afterwards energy selected photoelectrons. The most promising results in imaging the emitted photoelectrons, with a possibility of subsequent energy analysis, was obtained recently by means of a diverging magnetic field [1-6].

Sometimes, the physical principles underlying the scattering and excitation processes involved in these methods can also characterize a local configuration or a film thickness. There are thickness and size dependent spectral changes in XPS and HREELS. By varying the primary electron beam energy in reflection EELS, one is able to probe the electronic structure and depth of an interface in a non destructive way. Consequently, in the case of depth resolution and non destructive depth profile these spectroscopies can also be at their best.

In résumé, this lecture will give a general perspective about the specific and complementary chemical information given mainly by XPS and HREELS, less accent will be put on UPS and EELS. When relevant, the spectroscopies will be discussed from the standpoint of lateral and depth resolution.

GENERAL CONSIDERATIONS

Numerous monographs and review articles on electron spectroscopies have been published and we refer just a few edited volumes[7-10] as a start to get more detailed information and references on this subject.

Analytical electron spectrometers are based on the arrangement shown on Fig. 1. Under the impact of a monochromatized photon beam of energy $h\nu$ (photoemission) or of an electron beam of energy E_k (the energy range refered to the different techniques on Fig. 1 being indicative and not restrictive), electrons are emitted from the sample into some type of electrostatic electron energy analyzer

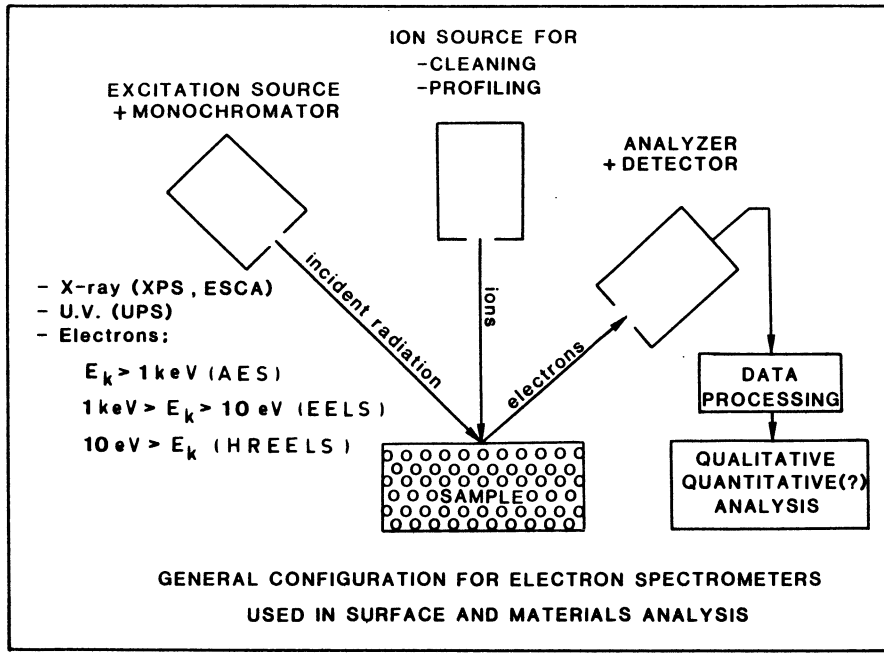

Figure 1

after which they are detected and the corresponding information is stored and eventually on-line processed.

Most of these spectrometers perform a surface analysis integrated over a few mm^2 of the sample area, which corresponds to the diameter of the incident beam. On the other hand, they have an excellent depth resolution in the order of 1 nm, the typical escape depth[11] for outgoing electrons within the kinetic energy range of 20 to 1000 eV.

Regarding the diameter of the incident beam and the subsequent analysis performed on the outgoing electron (Fig. 2) these technological methods lead to a pure surface analysis or to a microscopy, or better, to a combination of both.

PHOTOELECTRON SPECTROSCOPIES (XPS, UPS)

In order to understand clearly what will be developed later, one has to remember a few simple facts. In the photoelectric process, the energy conservation law includes the kinetic energy E_k of the detected photoelectron and the total energy of the solid sample, before (E_i) and after (E_f) the photoionization.

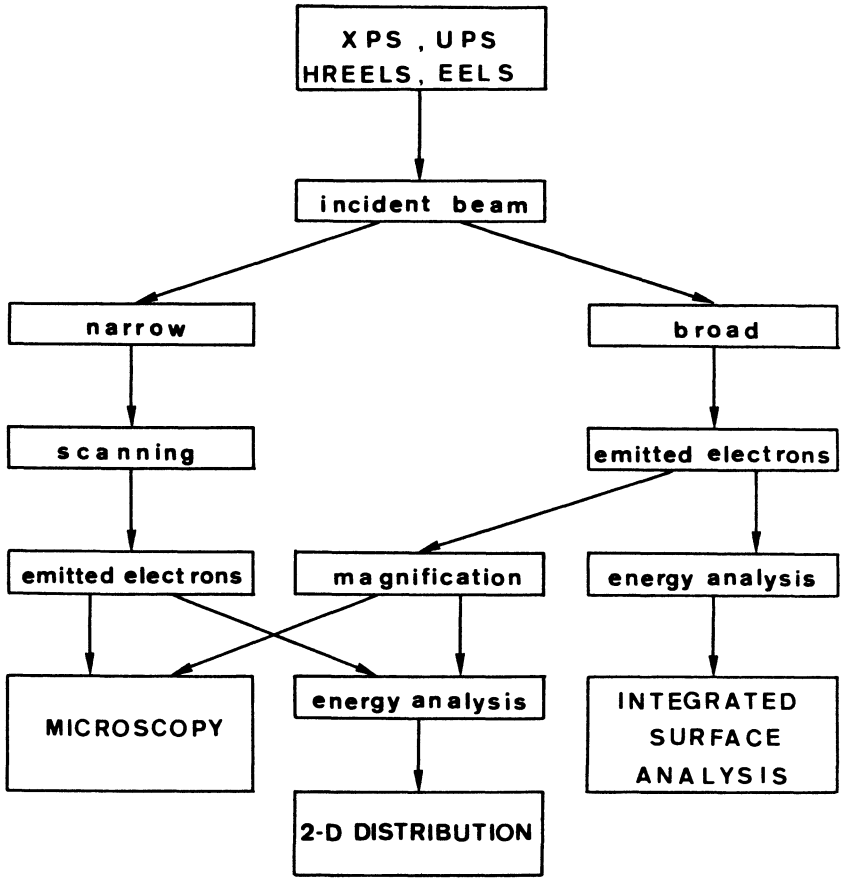

Figure 2

The energy conservation can then be written :

$$E_i + h\nu = E_f + E_k + \Delta\phi$$

where :

$$\Delta\phi = \phi_{sp} - \phi$$

ϕ = work function of the solid ;
ϕ_{sp} = work function of the analyzer ;
since the emitted electrons have to overcome the contact potential in order to penetrate within the analyzer of the spectrometer, which is supposed to be in thermodynamical equilibrium with the sample.
Then :

$$E_B = E_f - E_i = h\nu - \Delta\phi - E_k$$

E_B is now the so-called "binding energy" of the photoelectron within the solid. In photoelectron spectroscopies the binding energies are refered to the Fermi level and therefore, the "binding energy" becomes :

$$E'_B = E_f - E_i - \phi$$

In XPS, the energy distribution $N(E_k)$ of the photoelectrons emitted is related to the initial electron population (or the density of occupied states) in the system, as a function of their "binding energy",E'_B. In fact, it is only when the electron energies would not rearrange themselves within the system, after the positive core hole creation, that E'_B would correspond to the real binding energy of the photoelectron before the process. This situation is called the frozen orbitals approximation. Actually, there is a relaxation within the system which plays a most fundamental role when one looks at very small objects (about one nanometer).

A first straightforward example of what this spectroscopy could observe with such small dimension systems is an experimental illustration of the formation of a band structure in a solid (Fig. 3). It is based on the structures analysis of the valence band spectra of a series of molecules with increasing length, the linear normal alkanes (C_nH_{2n+2}, where $1 \ll n \ll \infty$). It shows how a single atomic electronic level (C2s) evolves to molecular orbitals, and then to a band, as the number n of carbon atoms increases in the molecule and simulates at the end a 1-D solid [12-14].

This experiment illustrates (Fig. 4) also that the increasing size of the molecule allows more possibilities for electrons to flow towards the positive core hole and therefore the relaxation and the corresponding final energy depends on the size of the molecule. It recalls us that E'_B is not formally a binding energy because of the final state effects. The effect is called the relaxation shift as opposed to the "true" chemical shift, which is as we will see an initial state effect. It is strongly dependent on the size of small dimension systems and this has originated a tremendous interest in the study of small metallic clusters [15,16], supported by insulating layers such as oxides as it occurs in heterogeneous catalysis, or more generally in metal-insulator and metal-semiconductor interfaces [17].

One cannot write about photoelectron spectroscopy without remembering briefly the property which made its original success : the chemical shift. The binding energies of the core electron levels are not only dependent on the nature of the atomic element to which they belong but also to the "chemical" environment of this atom. The electronic states are indeed influenced by the chemical bondings of the atom within the molecule or solid and the corresponding charge

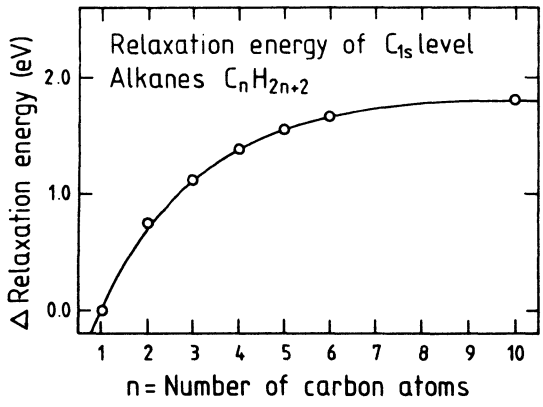

Figure 3

Figure 4 : X-ray induced photo-electron of some alkanes measured in the gas phase.

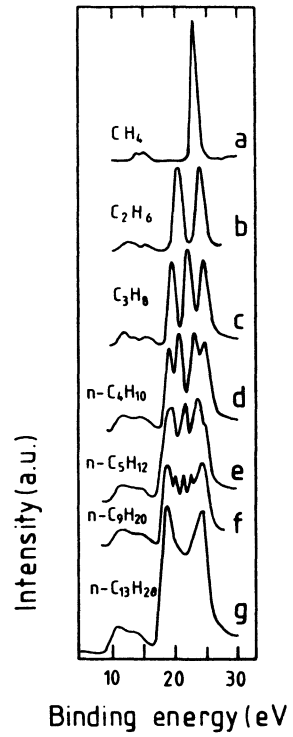

Figure 4

transfer which results from it. If we remove any, one, or even a fraction of an electron out of the valence band, the apparent positive charge of the nucleus will increase for all the other electrons, even for the most inner shells. The reason is that the wave function of any removed, or partially removed, electron extends initially within the whole distribution of the electronic core levels, bringing with it a negative density of charges which screens the positive charge of the nucleus. As a result the corresponding binding energies of the electronic levels are increased, consequently to the charge transfer(s) in the bonding(s).

It explains that the $4f_{7/2}$ and the $4f_{5/2}$ lines of gold, respectively with E_B^i at 84.0 and 87.7 eV for the metal [18] (see Fig. 5,D) are shifted by 1.5 eV towards higher binding energies for the aurous oxide (Au_2O : see Fig. 5, B and C), and are 2.1 eV more binded for the surface covered with auric oxide (Au_2O_3 : Fig. 5, A).

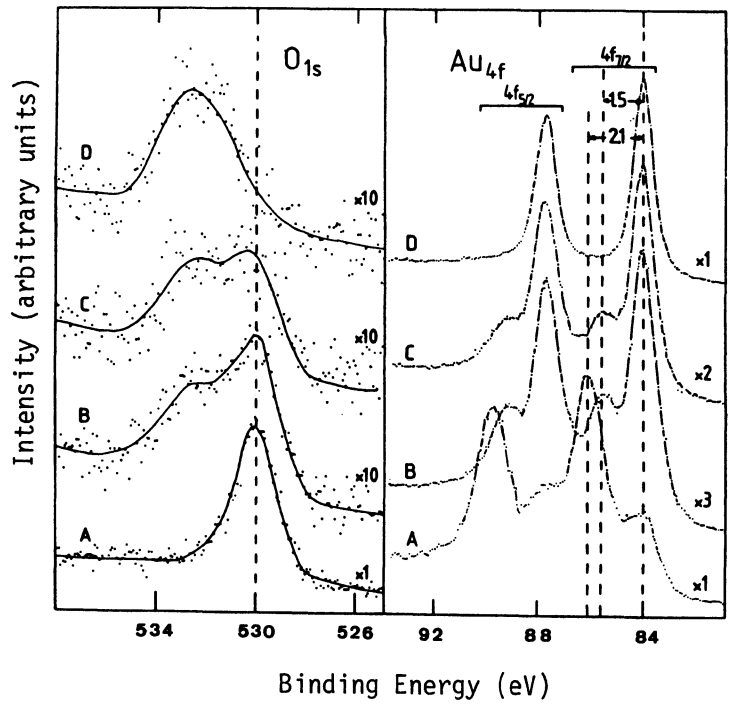

Figure 5 : Photoelectron spectra recorded on a Au(111) crystal treated fifteen minutes by DC reactive sputtering in oxygen.
A. As measured at 300 K directly after the transfer to the spectrometer.
B. After half a day in UHV, under X-ray bombardment, at 320 K.
C. Same as B, at 340 K.
D. Sample heated to 360 K.

Of course, the opposite argument holds for the O_{1s} level of the same samples. The binding energies observed for the two O_{1s} peaks are consistent [18] with the existence of true oxides in which the O_{1s} electrons are less binded (530 eV) than within oxygen or hydroxyl radicals (532.5 eV), on the surface.

This discrimination of different oxides is extremely difficult and very often impossible in Auger spectroscopy, because of the complex and broad levels within the corresponding Auger spectra. Let us note that photoelectron spectroscopy has now reached enough

sensitivity and resolution ($\sim$ 0.2 eV) [19] in order to measure "chemical shifts" related to surface states (for instance, d or f levels of transition metals in a lower coordination site at their surfaces)[20].

However, XPS is unsensitive to hydrogen and as a matter of fact, we cannot solve unambiguously the problem related to the presence of OH groups on the surface ; later we will show that HREELS can clarify this situation.

The use of ultra-violet radiation will of course restrict the emitted photoelectrons to the valence band. In the direct transition model it appears that the presence of the joint density of states in the photoionization probability is responsible for a major difference between the low energy (UPS) and the high energy (XPS) regime. Indeed, when the final empty state is relatively close to the Fermi level (i.e. $\ll$ 100 eV) the transition probability will be strongly dependent on the corresponding finite final density of states into which the electron is ejected. Whereas in the high energy regime there is a continuum of final states, making the transition probability only dependent on the initial density of states. If one accounts also for the presence of the surface, the overlap of the initial and final state wave functions can favour local surface transitions [7].

The measurements of an additional parameter, the direction of the photoelectron emission, combined with the knowledge of its energy, determine the final wave vector $\vec{k}_f$ of the electron. If we can relate this $\vec{k}_f$, ejected electron wave vector, with $\vec{k}$, the one the electron had initially in the solid, we are then able to measure the dispersion curves (E, k) of the band structure. This experimental method is known as "angular resolved photoemission" or ARUPS (Angular Resolved UPS : since it is mainly in the low energy range, nowadays with synchrotron radiation, that this method is used).

The problem is very complex, but, by chance regarding to our present concern, is much easier in the case of low dimensional solids. Indeed, in the case of 2-D systems (lamellar solids, growing interfaces, surface states) one can often neglect the dispersion along the perpendicular direction and obtain the dispersion of the energy bands within the two dimensional Brillouin zone [20] ; in the case of 1-D systems (1-D conductors) the same argument holds, the dispersion is neglected perpendicularly to the solid direction leading to the one dimensional Brillouin zone [21].

INSTRUMENTAL PROGRESS

Although X-ray Microscopy can perform some elemental microanalysis and that SAM is excellent at it, neither of them has as much potentialities as the combination of the two photoelectron spectroscopies to probe locally the elements and their chemical bondings, or the electronic structure. Unfortunately, considerable technical problems hinder the progress of any conventional approach of what could be a true "chemical" microanalysis. Original ideas will be necessary to take a short cut to avoid the tedious way of progressive technical improvements towards the micron-world resolution.

In order to analyse a very small area without destroying the photoelectron flux, the first requirement is to increase the photon beam density. Apart from the synchrotron radiation performances, the most significant step forward was made recently by the group of K. Siegbahn [19] with the aid of a fast rotating anode followed by a double focusing multicrystal X-ray monochromator. A flux of about 10^{13} monochromatic photon/s is expected onto a solid sample within a 200 μm diameter spot. This would be almost two orders of magnitude better than what can be achieved nowadays with synchrotron radiation in this energy region with the same degree of monochromacy. Further exciting improvements in the field of microanalysis can be extrapolated with such an instrument.

Another group [23] is able to focus a monochromatic X-ray beam onto a 150 μm diameter spot. Of course, the absence of a rotating anode and a small number of crystals in the monochromator cut down the intensity.

Other type of selected area XPS instruments without scanning facilities are developed [24,25] but they all perform no better lateral resolution than 200 μm and at the cost of a much lower beam density. As a first improvement the entrance to the transfer lens was collimated in front of the selected area [24], about 500 μm resolution was obtained in this manner. A further progress was the design of a transfer lens which images and magnifies the area of analysis onto the analyzer entrance aperture [25], bringing the resolution down to 200 μm.

For evident optical reasons, spherical condensors analysers (SCA) perform the photoelectron energy selection in all these instruments. Based upon the focusing properties of the SCA and the use of a two-dimensional electron detector, an interesting experi-

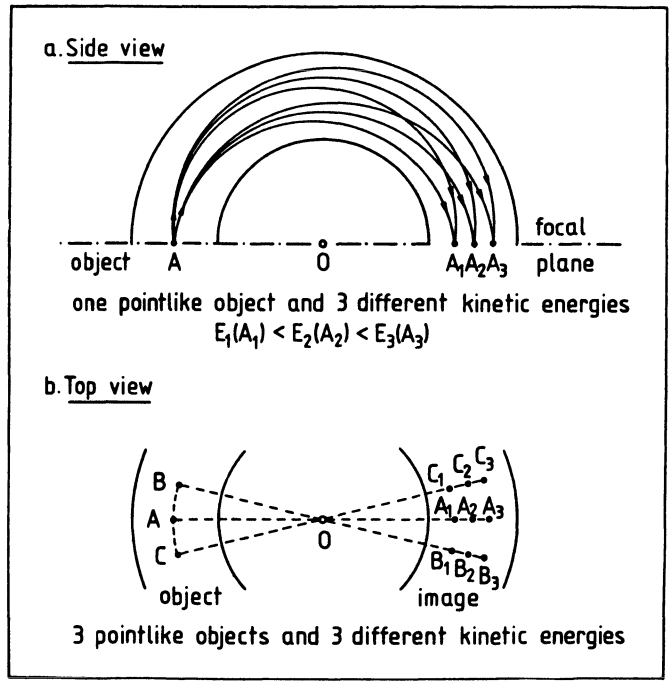

Figure 6 : 180° spherical condensor analyser.

mental arrangement for a true XPS imaging was suggested recently [26]. The specimen image after the transfer lens and the detector are positioned in the conjugate planes (Fig. 6 shows the specific situation of an 180° hemispherical analyser). Consequently, the photoelectrons emitted with different energies from the object point A will be focused along the radial lines AO (Fig. 6a), the most energetic ones being deviated outwards. Also all monoenergetic photoelectrons emitted from a line parallel to the spheres are depicted into an inverted image, at a $\sim$ 1:1 scale (Fig. 6b). This property was already used more than twelve years ago in the Hewlett-Packard ESCA system [27], in order to provide a two-dimensional image (position x energy) of the photoelectrons emitted from the X-ray beam line focused onto the sample ($\sim$ 1 x 5 mm^2).

It is easy to imagine that a strip-like area can be at once analysed by the spectrometer and its image restored for a given energy or energy width. Therefore, the X-ray beam is line shaped either by focusing or shielding. Another possibility is to collimate the sample image with a slit at the entrance of the spherical condensor. Finally, these authors [26] suggest a mechanical translation of the sample so that its image is scanned on the conjugate

plane perpendicularly to the strip direction. With the aid of an on-line computer a two-dimensional image of the specimen could be built up simultaneously at different photoelectron energies, or within a range of energy in order to increase the sensitivity. Again, resolution of the order of 200 μm may be possible and could be improved in the future with a higher magnification and aberration-free transfer lens.

The focusing and scanning of an X-ray photon beam would be an extremely difficult operation. Therefore, a completely different approach of scanning XPS microanalysis which avoids this problem was conceived by J. Cazaux [28,29] and C.T. Hovland [30] (Fig. 7). An electron beam is focused and scanned over a metal foil (Al, Mg, etc.), just thick enough (nowadays ∿ 25 μm) to stop completely the electrons, in order to generate the X-rays. The sample has to be very thin also (between 0.01 and 10 μm) and is deposited at the back face of the foil where the X-rays will emerge. This set-up produces a quite high X photons flux within a very small spot : ∿ 10^{13} photons/s x mm^2. The photoelectrons ejected from the outside surface of the specimen are analysed and detected in a conventional electron spectrometer. Up to now a spatial resolution of ∿ 25 μm is achieved by this method. It could be improved by one order of magnitude, reaching its intrinsic physical limit, with a thinner metallic foil (1 μm) and a better focused electron microprobe [29].

By using heavier metals (Mo, Ag), continuous X-ray induced Auger electron spectroscopy (CXAES) could also be performed with such a system [31], allowing Auger analysis of biological materials with much less radiation damage as it is in a SAM instrument. The drawback is the appreciable heating from sample support due to the electron beam hitting the back side of it. Also the sample is limited in thickness.

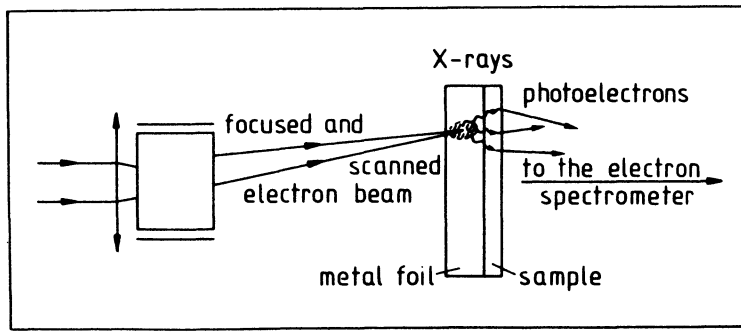

Figure 7. Principle of thin film XPS microanalysis.

The most original and promising prospect of improved spatial resolution appears through the direct imaging method initiated in the group of D.W. Turner at Oxford University [1-5]. It is based on the collimating and magnifying properties of an axially symmetric diverging magnetic field and the principle of operation is remarkably straightforward, it is an image projection method which has some similarity with the field ion microscopy. The photon beam irradiates the whole sample surface which is at the center of an intense magnetic field created by a superconducting magnet (Fig. 8). The photoelectrons ejected are confined to move along the direction of the field lines. Since the magnetic field diverges the electrons are spread out in a controlled way and when they reach the phosphor screen they form an enlarged projection of the specimen surface. The magnification is linearly proportional[1] to $(B(2)/B(1))^{1/2}$, B(1) is here the magnetic field at the sample surface and B(2) at the phosphor screen.

So far the system works as a photoelectron microscope, a feature that has already been developped by other methods not reviewed in this lecture. The outstanding advantage of the present technique is that a simultaneous energy analysis can be performed. To understand how it is achieved one has to refer to the analysis of G. Beamson et al. [1,2] about the electron motion along a solenoid axis.

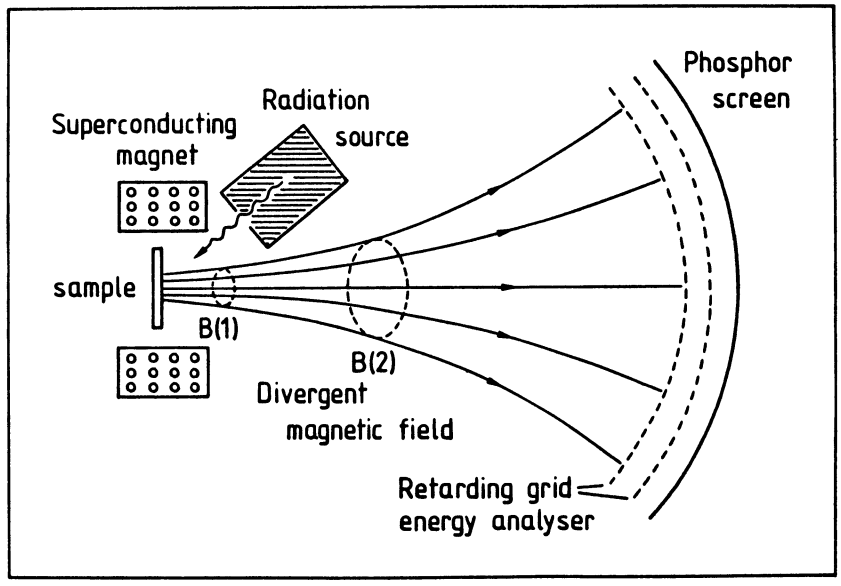

Figure 8. Principle of the magnetic photoelectron spectromicroscope.

First, let us consider what happens in a magnetic mirror at the bottleneck. The electrons arrive in a region of high field and their axial motion is converted into transverse one until they are axially stopped and eventually reflected. The opposite effect occurs in this photoelectron microscope, the electrons move from a high to a weak field region and transverse energy is converted into axial in proportion to the ratio of the field strength [1] :

$$E_{/\!/} = E_0 - E_{0\perp} \frac{B(2)}{B(1)} \qquad \text{(Fig. 8)} \ ;$$

where E_0 is the total energy of the electron (which is always conserved), $E_{/\!/}$ is its axial motion energy along the field line and $E_{0\perp}$ is the transverse energy of the photoelectron when it is emitted from the surface. It is a consequence of the angular momentum conservation which implies that $E_\perp^2/B$ is an invariant.

These authors conclude that the measurement of the axial component will give an accurate approximation of the total energy after a sufficiently large change of the magnetic field. They also predict an effective lateral resolution which results from the distribution of the spiralling motions (cyclotron orbits) of the electrons along the field lines. They demonstrate that it should be about one tenth of the maximum cyclotron orbits radius that is given by the approximate expression [6] :

$$\rho \simeq 7 \, E_0^{1/2} / B_0 \ \mu m$$

where E_0 is expressed in eV and B_0 is the peak field in Tesla (currently $B_0 \sim 7$ Tesla). One should also notice that there is no focusing of the electrons and the depth of field is in principle infinite (practically a few mm).

Therefrom, an efficient microscopic energy analysis will be performed at the level of the phosphor screen either in two ways :

1° with an electron field parallel to the magnetic field lines. It is easily obtained with two grids acting as a retarding field analyser and achieving a high pass energy filter before an image intensifier. A classical modulation technique can also be used in order to obtain the differentiated signal [6] . In the UPS regime (with He I radiation : 21.2 eV photons) an energy resolution down to 20 meV was reported [2] and the lateral resolution was limited at that time to $\sim$ 2 µm. Striking pictures of microelectronic devices and even biological objects were obtained at different photoelectron energies in that manner ;

2° with an uniform electric field perpendicular to the magnetic field lines, made also uniform in that region, it performs a trochoidal energy analysis which results in a band pass analyser. In this case, the function of imaging and energy analysis are combined by using a slit (or a hole) at the image level, which corresponds

to a strip (or to a spot in the case of the hole) onto the sample. It produces a 2-D image on which the photoelectron intensity is distributed as a function of energy versus position along the strip. Corresponding image strip dispersed XPS spectra were obtained [5] with a C(K) X-ray source (275 eV). An elemental distribution was infered with a resolution of about 15 μm along the chosen strip.

In résumé, many advantages can be associated with this technique. First, there are few physical constraints imposed to the sample due to the large depth of field. Moreover, the effective solid angle of the collected photoelectrons being 2 π, it compensates partly the loss of intensity resulting from the magnification. By switching the radiation source one can perform successively UPS and XPS analyses on the same spot. One can also simultaneously image the sample in the corresponding photoelectron energy range. Therefore, such an instrument is labelled as a photoelectron spectromicroscope (PESM).

But there are limitations. The performances of the energy analyser are still to be improved. We also mentioned the physical limitation in lateral resolution, where the situation is presently the most worrying in the XPS regime. For a reasonable central magnetic field (8 T), a final spatial resolution of 0.1 μm is expected [2] with photoelectrons having a kinetic energy of 5 eV, it degrades to 1 μm when their energy increases up to 500 eV. Hopefully, these limits could be half cut if the magnetic field intensity is doubled.

Undoubtedly, PESM has brought a realistic hope to the photoelectron spectroscopists to explore in a near future the sub-micron world. The coupling of such an improved spectromicroscopy with synchrotron radiation could end up into one of the most powerful analytical technique.

ELECTRON ENERGY LOSS SPECTROSCOPIES (EELS, HREELS)

In both EEL and HREEL spectroscopies, a monochromatic electron beam is focused onto the sample surface and the number of scattered electrons in one direction is recorded as a function of their kinetic energy.

The two names refer implicitely to the type of excitation which generates the inelastic energy losses. The vibrational excitations (adsorbates vibrations, phonons) range from a few meV up to a few hundreds of meV. Consequently, the incident beam will have only a few eV energy, but a very high resolution is needed for the monochromator and the analyzer (typically $\sim$ 5 meV). In the case of

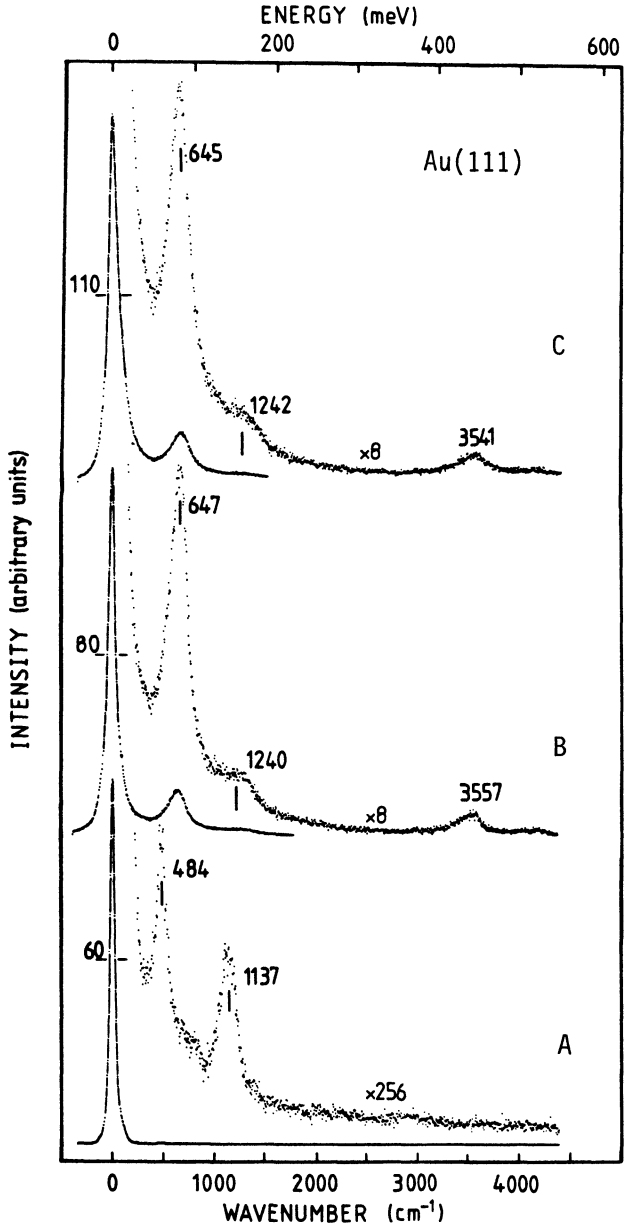

Figure 9 : HREELS spectra measured on a Au(111) crystal at room temperature :
A. "as cleaned" sample (see ref. 18)
B. sample treated five minutes by DC reactive sputtering in oxygen
C. sample treated fifteen minutes.

electronic excitations (electronic transitions, plasmons, etc.), they range from a tenths up to a few tens of eV and need consequently higher incident energy and lower resolution ($\sim$ 0.1 eV).

HREELS is a vibrational spectroscopy extremely efficient to study surface vibrations on metals and semiconductors [7,10], but also unexpectedly on insulators as it was shown recently [32]. The dipole theory shows that for a metal, or a semiconductor, only the adsorbates at or near the surface are probed. (However, under peculiar circumstances, impact scattering events can be detected which originate from a few deeper atomic layers [33,34]). HREELS is therefore considered as extremely surface sensitive.

Hence, this technique will contribute to identify adsorbates, or light contaminants, present at the surface. The interpretation of the spectrum will be inspired from infrared spectroscopy : number and energy of the excited vibrations, symmetry consideration, etc.

As an example, Fig. 9 shows the HREEL spectra from similar gold samples as discussed previously on Fig. 5. It was demonstrated [18] that spectrum A shows the presence of SiO_2 contaminant, since the bands at 484 and 1137 cm^{-1} (1 meV = 8.066 cm^{-1}) are the typical O-Si-O deformation mode and asymmetric stretching vibration respectively. When the gold surface was oxidised by DC reactive sputtering in oxygen (spectra B and C), two intense vibrational bands appeared at about 647 and 1240 cm^{-1}, attributed to the gold oxygen stretching vibration and the corresponding overtone. From these values, it would be extremely difficult to deduce the oxidation state of gold, but XPS has already given the answer. However, the presence of molecular oxygen would be detected through its characteristic O-O stretching vibration, as it is on silver for instance[35]. Moreover, hydroxyl contaminants are fingerprinted at 3557 and 3541 cm^{-1}, suppressing the previous ambiguity in the attribution of the O_{1s} XPS peak at 532.5 eV.

A last example will show clearly how HREELS can complement XPS as an analytical technique. Therefore, an aluminium crystal was exposed to a glow discharge in hydrogen (Fig. 10b) or in deuterium (Fig. 10a). The vibrational bands can be attributed as follow :

Energy loss (cm^{-1})	420	790	1387	1895	2912	3315
Vibrational band	δ(Al-D)?	ν(Al-O) + δ(Al-H)?	ν(Al-D)	ν(Al-H)	ν(C-H)	ν(O-H)

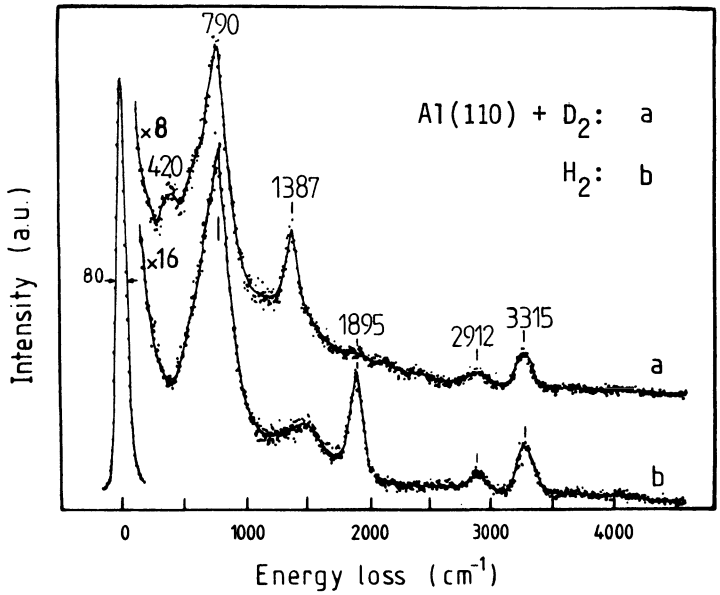

Figure 10 : HREELS spectra measured on a Al(110) crystal treated 30 seconds by DC reactive sputtering :
a : in deuterium
b : in hydrogen

As we know XPS would not be able to reveal the chemical bondings involving hydrogen. The isotopic shift observed here is often used in HREELS to label some chemical bondings at surfaces involving light elements. A further study of such a spectrum would give the adsorption site and in some cases (presence of a true overtone) the bonding energy of a molecule.

In the case of pure dielectric materials, the infrared optical constants are determined by measuring surface phonons [32]. If a HREEL spectrometer could be developed with a sufficiently dense focused beam (and this is questionable in this range of energy) it could be of prime interest to study optoelectronic integrated devices.

Because of its principle, the EEL spectroscopy potentialities are, to a much lower extent, comparable to UPS but have been poorly exploited. Moreover, by tuning the electron beam energy and therefore the mean escape depth of the electrons, one is able to probe an interface in a non destructive manner. Such an experiment has already been performed, for instance in the case of Si/SiO_2 [36].

Since electron beams of 100 eV and 2.10^{-10} Amperes are now focused onto a 100 nm spot [37], it could become a powerful method in the thin film technology.

CONCLUSION

Chemical bonding and electronic structure characterization of a surface are not only relevant to one spectroscopy. From an analytical point of view, XPS is the unique technique which can achieve simultaneously an elemental and a "true" chemical analysis. If necessary, HREELS is complementary because of its sensitivity to vibrations involving chemical bonds with hydrogen. Adsorption sites, bonding energies, infrared optical constants are amongst a few other parameters infered eventually from this spectroscopy. UPS, particularly with synchrotron radiation, is nowadays irreplaceable to characterize the valence bands, even their dispersion.

There is a need to dig out on a very local scale such a chemical bonding information. Unfortunately, until recently, the area probed by these spectroscopies was at least of a mm^2 order. In the last three years, exciting progress was made with "conventional" XPS instruments, pushing the limit of lateral resolution down to 150 μm, but hey are probably close to their final limitation. The most dramatic advance in spatial resolution can be expected from the magnetic photoelectron spectromicroscope which reaches already 2 μm in UPS and 20 μm in XPS. One order of magnitude improvement can be expected in the near future, bringing the photoelectron spectroscopies at the edge of the sub-micron world.

ACKNOWLEDGEMENTS

We thank Drs A. Dixon and K. Gehring of Thor Cryogenics for discussions and information on the development of the magnetic photoelectron spectromicroscope. J.J. Pireaux is indebted to the Belgian NFSR for financial support.

REFERENCES

1. G. Beamson, H.Q. Porter and D.W. Turner, J. Phys E : Sci. Instrum., 13, 64-66 (1980)
2. G. Beamson, H.Q. Porter and D.W. Turner, Nature 290, 556-561 (1981).
3. D.W. Turner, Liversedge Lecture, R. Soc. Chem., London (1982).
4. I.R. Plummer, H.P. Porter and D.W. Turner, J. Mol. Struct. 79, 154-162 (1982).
5. I.R. Plummer, H.Q. Porter, D.W. Turner, A.J. Dixon, G. Gehring and M. Keenlyside, Nature 303, 599-601 (1983).

6. A.J. Dixon, Scanning Electron Microscopy I, 55-66 (1984), SEM Inc., AMF O'Hare (Chicago, USA).
7. H. Ibach (Ed.) : "Electron Spectroscopy for Surface Analysis" (Springer Verlag, Berlin 1977).
8. L. Fiermans, J. Vennik, W. Dekeyser (Eds.) : "Electron and Ion Spectroscopy of Solids" (NATO ASI, Plenum Press, New-Yprk 1978).
9. C.R. Brundle, A.D. Baker (Eds.) : "Electron Spectroscopy Theory, Techniques and Applications", Vol 1-4 (Academic Press, New-York 1977, 1978, 1980, 1981).
10. H. Ibach and D.L. Mills : "Electron Energy Loss Spectroscopy and Surface Vibrations" (Academic Press, New-York 1982).
11. C.J. Powell, Surf. Sci. 44, 29 (1974).
12. J.J. Pireaux, S. Svensson, E. Basilier, P-A. Malmqvist, U. Gelius, R. Caudano and K. Siegbahn, Phys. Rev. A14, 2133 (1976).
13. J.J. Pireaux and R. Caudano, Phys. Rev. B15, 2242 (1977).
14. J.J. Pireaux, R. Caudano, E. Basilier, P-A. Malmqvist, U. Gelius and K. Siegbahn, J. Physique 38, 1213 (1977).
15. J. Colbert, A. Zangwill, M. Strongin, S. Krummacher, Phys. Rev. B27, 1378 (1983).
16. M.G. Mason, Phys. Rev. B27, 748 (1983).
17. H. Roulet, G. Dufour, A. Masson, G. Colomer, Le Vide, les C. Minces, 216, 171 (1983).
18. J.J. Pireaux, M. Liehr, P.A. Thiry, J.P. Delrue and R. Caudano, Surf. Sci. 141, 221 (1984).
19. U. Gelius, L. Asplund, E. Basilier, S. Hedman, K. Helenelund and K. Siegbahn, Nucl.Instr. Meth. 229, 85 (1984).
20. J. Lecante, C. Guillot, Helvetica Phys. Acta 56, 427 (1983).
21. F.J. Himpsel, Adv. Phys. 32, 1-51 (1983).
22. C. Binns, C. Norris, S.J. Gurman, J. Phys. C : Solid State Phys. 16, 417 (1983).
23. R. Chaney, M.A. Kelly and C. Bryson, Appl. Surf. Sci., to be published.
24. D.J. Keast and K.S. Downing, Surface and Interface Analysis 3, 99-101 (1981).
25. K. Yates and R.H. West, Surface and Interface Analysis 5, 217-221 (1983).
26. N. Gurker, M.F. Ebel and H. Ebel, Surface and Interface Analysis 5, 13-19 (1983).
27. K. Siegbahn, D. Hammond, H. Fellner-Feldegg and E.F. Barnett, Science 176, 245 (1972).
28. J. Cazaux, Rev. Phys. Appl. 10, 263 (1975).
29. J. Cazaux, Analusis 11, 55-64 (1983).
30. C.T. Hovland, Appl. Phys. Lett. 30, 274 (1977).
31. J. Cazaux and Tran Minh Duc, J. Electron Spectrosc. Relat. Phenom. 31, 13-23 (1983).
32. P.A. Thiry, M. Liehr, J.J. Pireaux and R. Caudano, Phys. Rev B29, 4824 (1984).

33. S. Lehwald, J. Szeftel, H. Ibach, T.S. Rahman and D.L. Mills, Phys. Rev. Letters 50, 518 (1983).
34. M. Rocca, S. Lehwald and H. Ibach, Surf. Sci. 138, L123-L128 (1984).
35. C. Backx, C.P.M. de Groot and P. Biloen, Surf. Sci. 104, 300 (1981).
36. T. Ito, M. Iwami and A. Hiraki, Solid State Commun. 36, 695-699 (1980).
37. T. Ichinokawa, in these NATO ASI proceedings (Baddeck, 1984).

HIGH RESOLUTION ELECTRON MICROSCOPY IN MATERIALS SCIENCE

S. Amelinckx

University of Antwerp (RUCA)
Groenenborgerlaan 171, B 2020-Antwerp (Belgium)
(Also at S.C.K.,B 2400-MOL(Belgium))

PART I : GENERAL CONSIDERATIONS

INTRODUCTION

In recent years solid state electron microscopy has become a separate branch of electron microscopy based on principles which are quite different from those underlying the biological applications. Roughly speaking one can say that solid state electron microscopy is essentially based on diffraction phenomena in crystals and to a much smaller extent on absorption effects; the reverse is true for the imaging of biological material. In both cases "phase contrast" effects play an important role as well.

In discussing the observations of "sub-micron" features in solids by means of electron microscopy and electron diffraction one has to distinguish between **diffraction contrast** observations, where only one beam is used and **multiple beam imaging** methods where the interference effects between a number of beams is important. The different operating modes are shown schematically in fig.1 In fig.1,a only the direct beam is admitted through the objective selector aperture; the image is in this case a magnified map of the intensity distribution in the diffraction spot due to the transmitted beam; this is called a **bright field image**. One can also select a diffracted beam and magnify the intensity distribution in the spot due to a diffracted beam; this is called a **dark field image** (fig.1,b).

It is important to realize in this context that Bragg angles are very small in electron diffraction. Electrons can thus be assumed to travel down the crystal specimen along narrow columns.

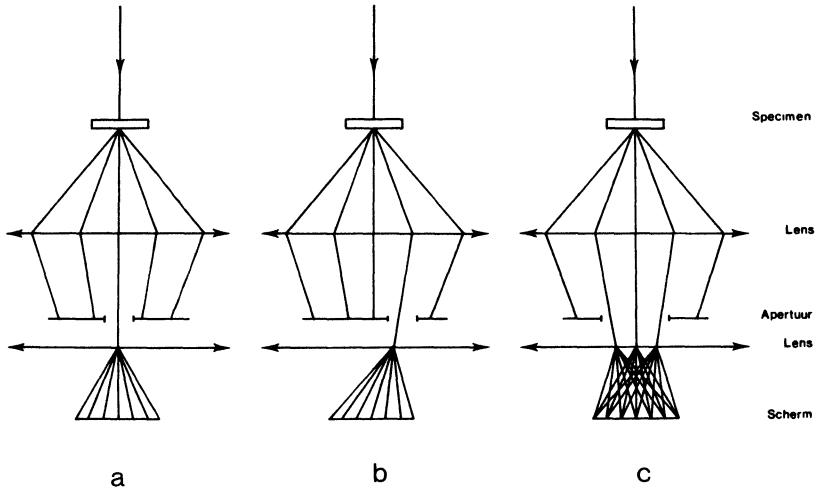

Fig.1. Different operating modes of the electron microscope.
a) B.F diffraction contrast, b) D.F.diffraction contrast
c) Multiple beam lattice fringe imaging.

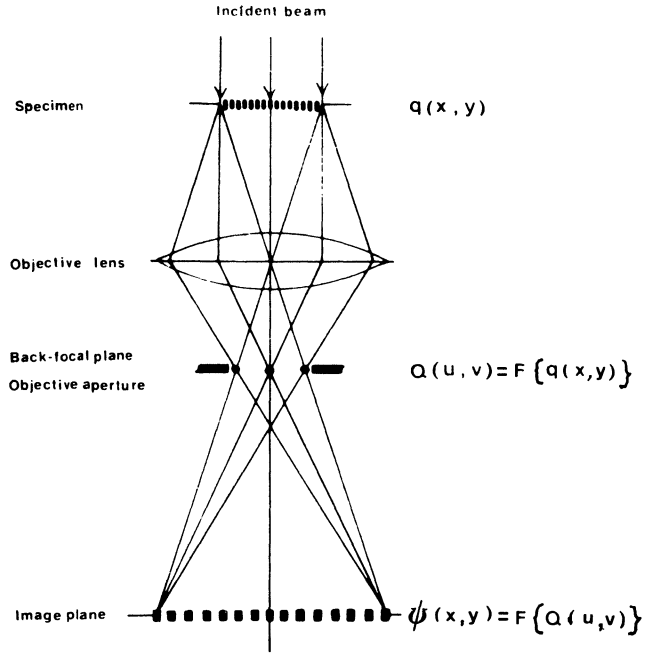

Fig.2. Image formation in an ideal microscope. The diffraction amplitude is the Fourier transform of the object, the image amplitude is the F.-transform of the diffraction pattern.

The intensity map formed by the electron distribution in the exit face of the specimen, is now the object.

Diffraction contrast is used in the study of crystal defects, such as dislocations and planar interfaces, since the local electron intensity is very sensitive to local orientation changes as a result of strain fields or as a result of changes in the orientation of the lattice. Differences in structure amplitude also give rise to contrast (so called structure factor contrast). Phase changes in the scattered beam due to a relative translation of two crystal parts leads to fringe contrast along inclined interfaces.

Quantitative studies such as the determination of Burgers vectors of dislocations or displacement vectors of stacking faults or of antiphase boundaries are usually made under two-beam conditions i.e. with only one scattered beam strongly excited next to the transmitted beam. Under such conditions only one diffraction vector is active i.e. the electron beam "sees" only one set of lattice planes. No information can be gained on lattice or structure. We shall not discuss this imaging mode any further; we refer for further reading to Hirsch et al (1965), Amelinckx (1964,1978) and Thomas and Goringe (1979). We shall limit ourselves to a survey of methods which give at least a rudimentary image of the lattice and therefore make use of at least two interfering beams. Special attention will be given to images which also carry structural information and therefore imply the use of many beams.(fig.1,c).

We shall discuss the underlying theory, following Van Dyck (1978), Spence (1981) and Cowley (1976) and then illustrate this by means of a number of recent case studies.

IMAGE FORMATION IN AN IDEAL MICROSCOPE (fig.2)

Let the incident electron beam be described by a plane wave of amplitude 1 and let the object be characterised by a two-dimensional transmission function q(x,y). Diffraction occurs in the object and electrons emerge from the exit face; the back surface of the object can then be considered as being a planar assembly of point sources of spherical wavelets in the sense of Huyghens. The interference between these wavelets generates in fact the diffracted beams in the case of a crystalline specimen, and produces a diffraction pattern in the back focal plane of the objective lens. This diffraction pattern can to a good approximation be described by Fraunhofer diffraction, because of the relative dimension of the lenses and the electron wavelength and because of the paraxial nature of most of the diffracted beams. This is a consequence of the fact that in electron diffraction Bragg angles are very small because of the short wavelength of electron beams (~0.04Å at 100 kV). The diffraction amplitude is then the Fourier transform of the function

q(x,y). In turn the diffraction pattern in this back focal plane acts as a source of Huyghens spherical wavelets, which interfere to produce an enlarged image of the transmission function. This image is again the Fourier transform of the diffraction pattern. We can thus conclude that the **ideal** microscope acts as an analogue computer and performs a double Fourier transformation apart from a linear magnification,and thus reproduces the object. Unfortunately ideal microscopes are not of this world and the actual situation is somewhat more complicated.

IMAGE FORMATION IN A REAL MICROSCOPE

Real microscopes are subject to a number of limitations which induce deviations from the ideal imaging conditions described above.

Spherical Aberration

In real magnetic lenses the paraxial approximation which leads to point-to-point representation in the Gaussian focal plane (i.e. the focal plane considered in geometrical optics) breaks down. This is due to the fact that the value of $\sin\beta$, which enters in the expression for the Lorentz force on a moving charge, can no longer be approximated by the angle β, but higher order terms, up to the third power in β, are required. This is analogous to approximating $\sin\beta \simeq \beta$ in Snell's law for paraxial rays in ordinary optics.

The radius of the disc of confusion in object space resulting from this lens aberration is then given by : (Glaser, 1952)

$$\rho_S = C_S \beta^3$$

where C_S is the spherical aberration constant, which has a value somewhere between 1 and 10 mm. A typical high resolution microscope operating at 200 kV has a value C_S = 1.2 mm.

As a result of spherical aberration electron beams inclined at an angle with the optical axis suffer a phase shift with respect to the beam at β =0, given by

$$\chi_S = 2\pi \Delta/\lambda$$

where Δ is the path difference caused by the fact that the beam does not pass along the axis. From fig.3,a it can be concluded that $\Delta = \rho_S \sin\beta \simeq \rho_S \beta$ and hence $d\Delta = \rho_S d\beta$ and $d\chi_S = 2\pi\rho_S d\beta/\lambda = 2\pi C_S \beta^3 d\beta/\lambda$. After integration from 0 up to the angle β

$$\chi_S = \tfrac{1}{2}\pi C_S \beta^4/\lambda \quad \text{(Scherzer, 1949)} \qquad (1)$$

Aperture

The microscope contains an objective aperture which eliminates beams which enclose an angle β with the optical axis, exceeding an

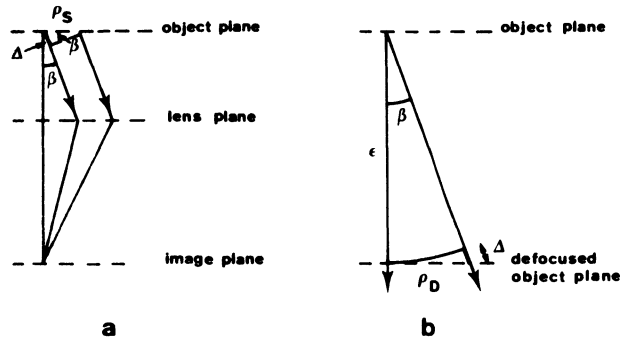

Fig. 3. (a) Derivation of the spherical aberration phase shift
(b) Phase shift due to defocusing.

angle β_A in order to reduce the spherical aberration. This imposes a limit to the theoretically achievable resolution called the **Abbe** limit.A geometrical point is imaged as a circle (the disc of confusion) with the radius

$$\rho_A = 0.61\ \lambda/\beta_A \qquad (2)$$

which means in practice that only points separated by at least this distance in the object can be observed as separate points in the final image.

Defocus

Most high resolution images are automatically made under conditions where visual contrast is best. It turns out that in the exact Gaussian focal plane the contrast is smallest, at least for a phase object. One therefore usually works under somewhat defocused conditions. Also defocusing causes "phase shifts" and a disc of confusion which we can estimate with reference to fig.3,b.

When defocusing the electron microscope by an amount ε leaving the plane of observation unchanged, the object being situated near the first focal plane, results in an apparent displacement ε of the object plane (fig.3,b). One clearly has

$$\rho_D = \varepsilon \sin\beta \simeq \varepsilon\beta$$

and for the value of Δ

$$\Delta = \frac{\varepsilon}{\cos\beta} - \varepsilon = \left[\varepsilon/(1-\tfrac{1}{2}\beta^2)\right] - \varepsilon = \varepsilon(1+\tfrac{1}{2}\beta^2) - \varepsilon = \varepsilon\,\frac{\beta^2}{2}$$

and hence $\chi_D = 2\pi\Delta/\lambda = \pi\varepsilon\beta^2/\lambda$; (3)

$\varepsilon>0$ means lens strengthening; $\varepsilon<$ means lens weakening.

Chromatic Aberration

As a result of instabilities in the high voltage of the microscope the incident electron beams exhibits a wavelength spread since λ is related to the acceleration potential E by the non-relativistic relation

$$\lambda = h(2meE)^{-1/2} \qquad (4)$$

Moreover variations in the lens currents $\Delta I/I$ also cause aberrations which are of the same nature.

A third origin of aberration is the inelastic scattering in the specimen which is equivalent to a change in energy of the electrons entering the lens system : $\Delta E/E$. The net effect of all these phenomena on the image formation is to cause a spread Δf on the focal distance f of the objective lens. The latter is proportional to EI^{-2}, hence assuming ΔE and ΔI to be uncorrelated, Δf is given by

$$\Delta f = C_c[(\Delta E/E)^2 +_4(\Delta I/I)^2]^{1/2} \qquad (5)$$

The corresponding disc of confusion in object space has a radius

$$\rho_c = \beta \, \Delta f \qquad (6)$$

The constant C_c is called the chromatic aberration constant. Since the instabilities in high voltage and in lens current can be reduced to smaller than 10^{-6}, Δf takes a typical value of 100 Å which corresponds with a C_c value smaller than 10 mm.

Beam Divergence

Because of the finite dimensions of the electron source and of the condensor lense aperture the incident beam is somewhat divergent. Under the intense illumination conditions used in high resolution imaging the apex angle of the illumination cone may reach a value of the order of $\simeq 10^{-3}$ radians.

The influence of incoherent beam divergence on the image can be described as being due to the superposition of independent images (i.e. intensities) corresponding with different incident directions within the divergence cone.(Hibi, 1962; Spence, 1981).

Ultimate Resolution

Apart from the lens imperfections discussed above and which lead to image blurring and phase shifts, a number of other imperfections occur, but these are unimportant as compared to the ones we discussed. Furthermore resolution also depends on mechanical stability (vibration, drift,..); these effects can be eliminated to a large extent by a proper microscope design; they will not be discussed any further here.

The ultimate resolution is thus limited mainly by three up to the present, inevitable phenomena : finite aperture, spherical aberration and chromatic aberration.

The final disc of confusion has a radius given by :

$$\rho = (\rho_A^2+\rho_S^2+\rho_C^2)^{1/2}$$

Because of the difference in angular dependence of the different aberrations it turns out that in present day high resolution electron microscopes, chromatic aberration has only a relatively smaller influence. The limiting factor at small angles ($\beta<5\times10^{-3}$rad) is the aperture, whereas in the range $\beta>5\times10^{-3}$ rad the limiting factor is the spherical aberration. (This is true for E=100 kV; C_S=8.2 mm and C_C=3.9mm).

The curves ρ_A and ρ_S versus β have opposite slopes. There is therefore a minimum value for ρ which occurs for $\partial\rho/\partial\beta=0$ where $\rho=(\rho_A^2+\rho_S^2)^{1/2}$. This minimum, which corresponds to the optimum compromise β_0 between spherical aberration and aperture effects, occurs for $\beta=(0.61\lambda/C_S\sqrt{3})^{1/4}$. The corresponding radius of the confusion disc is then $\rho_0=0.9\lambda^{3/4}C_S^{1/4}$ (6,bis).Representative values are $\beta_0=5\times10^{-3}$ rad; $\rho_0\simeq0.5$ nm). This expression makes it clear that one gains more in resolution by decreasing the wavelength (i.e. by increasing the accelerating voltage) than by decreasing C_S.

Phase Shift

We have pointed out that spherical aberration and defocus cause phase shifts of the non-axial electron beams with respect to the axial beam. These phase shifts depend on β in the following manner:

$$\chi(\beta) = (\tfrac{1}{2}\pi C_S\beta^4+\pi\varepsilon\beta^2)/\lambda \qquad (7)$$

Note that $\chi=0$ for the defocus value

$$\varepsilon= -\tfrac{1}{2}C_S\beta^2$$

This value still depends on β and can thus only be satisfied approximately in a limited range of β values. It is thus necessary to take the phase shifts into account when performing image calculations. For negative ε-values the function $\chi(\beta)$ presents stationary points where $\partial\chi/\partial\beta=0$; there is a minimum for $\beta^2=-\varepsilon/C_S$ and a maximum for $\beta=0$. The corresponding values of $\chi(\beta)$ are respectively $\chi_{min}=-(1/2)\pi\varepsilon^2/\lambda C_S$ and $\chi_{max}=0$. The general aspect of the curve is then as presented in fig.4.

The phase shift can also be expressed in terms of a coordinate system (u,v) in the back focal plane of the objective lens. The axis u and v are parallel respectively with the x and y axis in the object plane, ignoring the image rotation, which is inherent to magnetic lenses. We have the relations :

$$u = \beta_x/\lambda \text{ and } v = \beta_y/\lambda$$

where β_x and β_y are the angles enclosed with the optical axis (the diffraction angles) in the x and y directions respectively. One has the relation

$$\beta^2 = \beta_x^2 + \beta_y^2 = (u^2 + v^2)\lambda^2$$

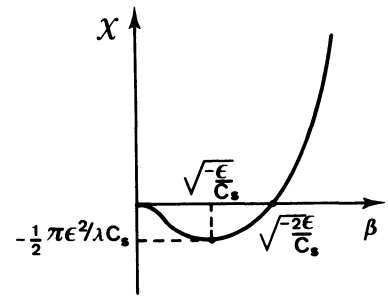

Fig.4. Total phase shift due to spherical aberration and defocus as a function of the angle β.

MATHEMATICAL FORMULATION

General

The amplitude distribution in the back focal plane of the objective lens is given by the Fourier transform (F) of the object function. In the case of a crystalline specimen the object function is in fact the electron wave function at the exit face of the thin foil, i.e. $q(x,y)=\Psi(x,y)$. The amplitude distribution in the diffraction pattern is then :

$$Q(u,v) = \underset{u,v}{F}\, q(x,y)$$

The final image amplitude is in turn the Fourier transform of the diffraction amplitude. However, the electrons are now moving in a lens system and thus undergo the phase shifts $\chi(u,v)$ discussed above. Moreover an aperture is limiting the number of beams transmitted through the system. This can be taken care of by introducing an aperture function A(u,v) in the plane of the diffraction pattern. This function is 1 over the surface of the aperture and zero outside of this. The amplitude of the final image can then be represented by the truncated Fourier transform of the diffraction pattern :

$$U(x,y) = \underset{x,y}{F}\, A(u,v)e^{-i\chi(u,v)}Q(u,v) \qquad (8)$$

In which the expression for the phase shift χ is given above as :

$$\chi(u,v) = \tfrac{1}{2}\pi C_S\lambda^3(u^2+v^2)^2 + \pi\varepsilon\lambda(u^2+v^2) \qquad (9)$$

The intensity in the image is then $I = UU^*$.

It has been shown that the blurring effect due to beam divergence and chromatic aberration can to a first approximation be simulated by using a smaller effective radius of the aperture in the calculation thereby eliminating the beams with the largest Bragg angles (Fejes, 1977).

Phase Grating Approximation (Grinton and Cowley, 1971)

We shall now illustrate the image calculations in the simple case where the specimen can be assimilated with a **phase grating**, i.e.the specimen only causes phase changes in the electron beam.

The phase change introduced by a local potential $V(\bar{r})$ in a slice of thickness dz can be estimated as follows :

$$d\chi(\bar{r}) = 2\pi(1/\lambda' - 1/\lambda)dz$$

where λ and λ' are the electron wavelengths, respectively in a field free region and in regions with electrostatic potential $V(\bar{r})$. One has

$$\lambda'(\bar{r}) = h / \left[2me(E+V(\bar{r}))\right]^{1/2}$$

whereas $\lambda(\bar{r}) = h/(2meE)^{1/2}$.

The phase shift is thus given by

$$d\chi(\bar{r}) = (2\pi/\lambda\{\left[E+V(\bar{r})\right]^{1/2} / \left[E^{1/2}\right]-1\}dz$$

Since V/E is a small quantity (V of the order of volts; E ≃ 100 kV) it is a good approximation to write

$$d\chi(\bar{r}) = (2\pi/\lambda)\left[(1+\frac{V}{E})^{1/2}-1\right]dz$$
$$\simeq (2\pi/\lambda)(V/2E)dz = \sigma V dz$$

with $\sigma = \pi/\lambda E$. The total phase shift on propagating through the slab is then obtained by integration over the thickness of the sample

$$\chi(x,y) = \sigma \int_{\text{thickness}} V(x,y,z)dz = \sigma\phi(x,y)$$

where $\phi(x,y)$ represents the **projected potential**, along the z-direction. The object function can then be written as

$$q(x,y) = \exp\left[i\sigma\phi(x,y)\right] \qquad (10)$$

The object clearly only introduces a phase shift.
In reality the sample also causes some absorption, which can be accounted for by introducing an exponential damping factor. The same factor takes into account a position dependent apparent "loss"" of electrons due to all kinds of processes which cause electrons to be intercepted by the finite aperture. The object function then becomes

$$q(x,y) = \exp\left[i\sigma\phi(x,y) - \mu(x,y)\right]$$

Two extreme models will now be discussed : the weak phase object" model and the "thick" object model, but assuming ε to be small.

Weak Phase Object (Cowley and Iijima, 1972)

In very thin foils, i.e. in weakly scattering objects, this exponential can be expanded up to the first order:
$q(x,y) \simeq 1 + i\sigma\phi(x,y) - \mu(x,y)$
The Fourier transform then becomes
$Q(u,v) = \delta(u,v) + i\sigma\Phi(u,v) - M(u,v)$
where $\delta(u,v)$ is the Dirac function.

The image amplitude then becomes

$$U(x,y) = F_{x,y}\, Q(u,v)e^{-i\chi(u,v)}$$
$$= F_{x,y}\, [\delta(u,v)+i\sigma\Phi(u,v)-M(u,v)][\cos\chi(u,v)-i\sin\chi(u,v)]$$
$$= F_{x,y}\, \{[\delta(u,v)+\sigma\Phi(u,v)\sin\chi(u,v)-M(u,v)\cos\chi(u,v)] + i[\sigma\Phi(u,v)\cos\chi(u,v)+M(u,v)\sin\chi(u,v)]\}$$

We note that an image which is directly related to the object will be obtained for $\sin\chi(u,v) = \pm 1$ for all u and v; in this case $\cos\chi=0$. Let us consider in particular the case $\sin\chi = -1$. One then obtains

$$U(x,y) = F_{x,y}\, \{\delta(u,v)-\sigma\Phi(u,v) - iM(u,v)\}=1-\sigma\phi(x,y)-i\mu(x,y)$$

The image intensity then reads up to first order terms:
$I(x,y)=UU^*=[1-\sigma\phi(x,y)-i\mu(x,y)][1-\sigma\phi(x,y)+i\mu(x,y)] \simeq 1-2\sigma\phi(x,y)$
The image intensity has thus clearly a direct relation with the object represented by $\phi(x,y)$. The intensity will be smaller the larger the projected potential. The image contrast i.e. $(I-I_0)/I_0=-2\sigma\phi(x,y)$, where $I_0=1$, is directly proportional with the projected potential ϕ.

In case one could make $\sin\chi = +1$, one would obtain
$I(x,y) = 1 + 2\sigma\phi(x,y)$
The intensity is now **larger** for larger projected potential. The situation is somewhat like **positive** and **negative** phase contrast. The lenses have introduced phase shifts of $\pi/2$, similar to what the quarter wavelength ring does in optical phase contrast microsopy. The lens aberrations are in fact exploited to produce "phase" contrast which would be absent otherwise.

Optimum Defocus Images

If we wish the image to be a "faithful" representation of the projected potential we must thus require that $\sin\chi\approx\pm1$, not just for a single beam but for as many diffracted beams, contributing to the image, as possible.

The value of $\sin\chi$ will not vary rapidly in the vicinity of a stationary point of χ, i.e. a minimum or a maximum. We have found above that χ adopts such a stationary value $\chi=-\pi\varepsilon^2/2\lambda C_S$ for $\beta=(-\varepsilon/C_S)^{1/2}$. Since this value of χ is essentially negative we cannot satisfy simultaneously the requirement $\sin\chi=+1$(i.e.$\chi=\pi/2$) but we can do so for $\sin\chi=-1$(i.e.$\chi=-\pi/2$). It is sufficient to choose the defocus ε in such a way that $-\pi\varepsilon^2/2\lambda C_S=-\pi/2$, i.e. $\varepsilon_S=-(\lambda C_S)^{1/2}$(11). Since the $\sin\chi$ function is in turn stationary around $\chi=\pm\pi/2$, the $\sin\chi$ versus β curve will present a flat part in the region of $\beta=(-\varepsilon/C_S)^{1/2}$ provided $\varepsilon=\varepsilon_S$.The defocus value $\varepsilon_S=-(\lambda C_S)^{1/2}$ which corresponds to the optimum imaging conditions of a phase grating, is called Scherzer defocus and the quantity $(\lambda C_S)^{1/2}$ is used as a unit of defocus. A more complete expression is $\varepsilon_S=-[(4/3)\lambda C_S]^{1/2}$.(see e.g. Thomas and Goringe, 1979).

The dependence of $\sin\chi(u,v)$ on the diffraction angle $\beta=\lambda(u^2+v^2)^{1/2}$ is represented in fig.5 for a typical situation close to the Scherzer defocus (Scherzer,1949). It is a rapidly oscillating function; it is thus not possible to fullfil the required condition for all β-values. The curve of fig.5, which was drawn for the Scherzer defocus value of -2100Å, in this particular case, does exhibit a region where $\sin\chi$ is approximately -1 as expected. Beams which are diffracted in this angular range thus give rise to an image which is a direct representation of the object. If not enough beams can be passed through this "window" in the $\sin\chi$ curve the image may be rudimentary of course in the sense that it can only give true detail up to some maximum spatial frequency. This limiting frequency corresponds roughly with the β angle for which $\sin\chi$ goes the first time through zero at Scherzer focus, i.e. $\beta_{max}=(-2\varepsilon/C_S)^{1/2}$ for $\chi(\beta_{max})=0$ with $\varepsilon=\varepsilon_S$ this becomes $\beta_{max}=2(\lambda/3C_S)^{1/4}$ and the radius of the corresponding disc of confusion is $\rho=(\lambda/3)^{3/4}C_S^{1/4}$ to be compared with the expression given above (6bis). Fig.5,b and 5,c show two image transfer functions for two different instruments; the advantage of high voltage becomes quite apparent from the width of the window.

It is worth noting that the image , i.e. the positive or the negative deviations from the background, is in fact proportional to the **projected potential $\phi(x,y)$.**

Projected Charge Density Approximation or "Thick"Phase Object
Lynch and O'Keefe,1972; O'Keefe,1973; Lynch and Moodie, 1975)

Let us now consider a situation where the spherical aberration and the effect of the aperture can be neglected. The image amplitude is then given by

$$U(x,y) = F_{x,y} \exp\left(-i\frac{\pi\varepsilon\beta^2}{\lambda}\right) Q(u,v) \qquad (13)$$

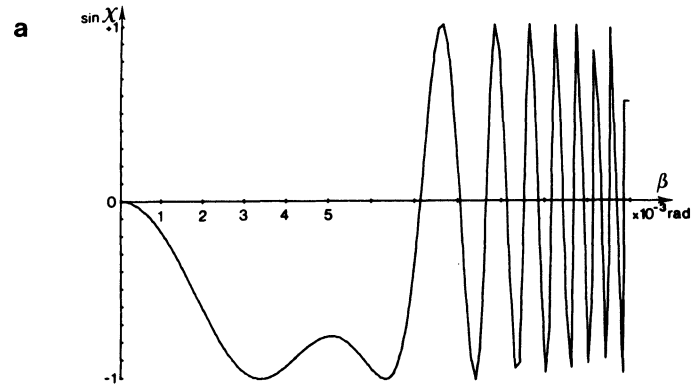

Fig.5. Theoretical image transfer function.
(a)sin χ as a function of β:C_S = 8.2 mm; ε_S=-2100Å 100kV
The effect of chromatic aberration and beam divergence would be to damp the oscillations beyond the window by an envelope function (not shown)

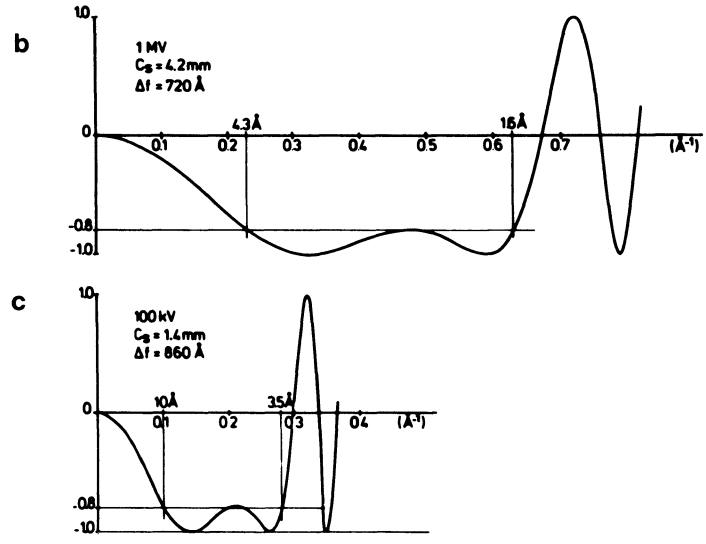

Fig.5. Theoretical image transfer functions: sinχ versus ($\bar{g}$).
Comparing the image transfer function for two different accelerating voltages illustrating the advantages in using high voltage (1MV).
(b) 1MV (c) 100 kV

For small defocus values ε the exponential can be expanded, retaining only the first order term, and writing $\beta^2=\lambda^2(u^2+v^2)$ one finds :

$$U(x,y)\simeq \underset{x,y}{F}\left[1-i\pi\varepsilon\lambda(u^2+v^2)\right]Q(u,v)=q(x,y)-i\pi\varepsilon\lambda \underset{x,y}{F}(u^2+v^2)Q(u,v)$$

The Fourier transform can be written explicitely as

$$\underset{x,y}{F}(u^2+v^2)Q(u,v) =\int(u^2+v^2)Q(u,v)\exp\left[2\pi i(ux+vy)\right]dudv$$

It is easy to show that

$$\frac{\partial^2}{\partial x^2}\int Q(u,v)\exp\left[2\pi i(ux+vy)\right]dudv =-4\pi^2\int u^2Q(u,v)\exp\left[2\pi i(ux+vy)\right]dudv$$

and a similar expression is valid for the second partial derivative with respect to y. We can thus write

$$U(x,y)=q(x,y)+\frac{i\pi\varepsilon\lambda}{4\pi^2}\left(\frac{\partial^2}{\partial x^2}+\frac{\partial^2}{\partial y^2}\right)\int Q(u,v)\exp\left[2\pi i(ux+vy)dudv\right.$$

$$=\left[1+\frac{i\varepsilon\lambda}{4\pi}\Delta\right]q(x,y)$$

where Δ is the Laplace operator in two dimensions $(\partial^2/\partial x^2)+(\partial^2/\partial y^2)$

We note that in the case of the phase grating approximation $q(x,y) = \exp\left[i\sigma\phi(x,y)\right]$ and that

$$\Delta\exp(i\sigma\phi) =\left\{i\sigma\Delta\phi - \sigma^2\left[\left(\frac{\partial\phi}{\partial x}\right)^2+\left(\frac{\partial\phi}{\partial y}\right)^2\right]\right\}\exp(i\sigma\phi)$$

In this special case one thus obtains for the image amplitude

$$U(x,y)=\left\{1-\frac{\varepsilon\lambda\sigma}{4\pi}\Delta\phi - \frac{i\varepsilon\lambda\sigma^2}{4\pi}\left[\left(\frac{\partial\phi}{\partial x}\right)^2+\left(\frac{\partial\phi}{\partial y}\right)^2\right]\right\}\exp(i\sigma\phi)$$

Up to the first order in ε the image intensity is thus given by

$$I(x,y) = UU^* = 1 - \frac{\varepsilon\lambda\sigma}{2\pi}\Delta\phi$$

We know from electrostatics that the Laplacian of the potential ϕ is related to the charge density ρ by Poisson's equation

$$\Delta\phi = -4\pi\rho$$

We thus finally obtain

$$I(x,y) = 1 + 2\varepsilon\lambda\sigma\rho(x,y) \qquad (14)$$

From this expression it becomes clear that the image contrast is now proportional to the **projected charge density** $\rho(x,y)$ and to the defocus ε. In the Gaussian image plane $\varepsilon = 0$ and all contrast disappears; the contrast reverses with the sign of defocus ε, i.e. bright becomes dark and vice versa. The same phase object,e.g. a column of atoms may thus appear bright or dark depending on the defocus.

The theory presented here is of course strictly speaking only valid if spherical aberration can be neglected; it was shown that it can be generalized so as to take the latter effect into account. Since the specimen is assumed to be a pure phase grating the theory is only applicable to very thin crystals; it still works surprisingly well for a range of thicknesses.

HIGH RESOLUTION IMAGES

One Dimensional Lattice Fringes (Amelinckx,1964; Hashimoto et al,1961; Cowley, 1959)

Two-beam fringes. We shall first consider the simplest possible case the so called two-beam case (Menter, 1956). It is assumed that next to the transmitted beam only one diffracted beam is excited. According to the two beam dynamical theory (ignoring absorption) the amplitudes of the transmitted and of the diffracted beam are given by (Amelinckx,1978)

$$T = (\cos\pi\sigma z - \frac{is}{\sigma}\sin\pi\sigma z)e^{\pi isz}$$

$$S = \frac{i}{\sigma t_g}\sin\pi\sigma z\, e^{\pi isz} \qquad (15)$$

where s is the excitation error (or the deviation from the exact Bragg position), z is the distance from the entrance face of the specimen, t_g is the extinction distance of the excited reflection with diffraction vector $\bar{g}$ and

$$\sigma = \frac{1}{t_g}[1+(st_g)^2]^{1/2}$$

The wave function of the electrons at the exit surface of the specimen is then

$$\Psi(\bar{r}) = e^{2\pi i.\bar{K}.\bar{r}}\,[T+Se^{2\pi i\bar{g}.\bar{r}}] \qquad (16)$$

where $\bar{K}$ is the wave vector of the incident beam.

In an ideal microscope the amplitudes in the diffraction pattern, i.e. the Fourier transform of Ψ would be :

$$F\Psi(\bar{r}) = T\,\delta(\bar{K})+S\,\delta(\bar{K}+\bar{g})$$

i.e. the diffraction pattern consists of two spots : the spot at the origin with intensity $I_T=TT^*$ and a second one at $\bar{g}$, with intensity $I_S=SS^*$. A second Fourier transformation, using the two spots, yields the original expression back(16) which therefore also represents the image amplitude. The image intensity is then

$$I=\Psi\Psi^*=TT^*+SS^*-2(TT^*SS^*)^{1/2}\sin(2\pi gx+\phi) \qquad (17,a)$$

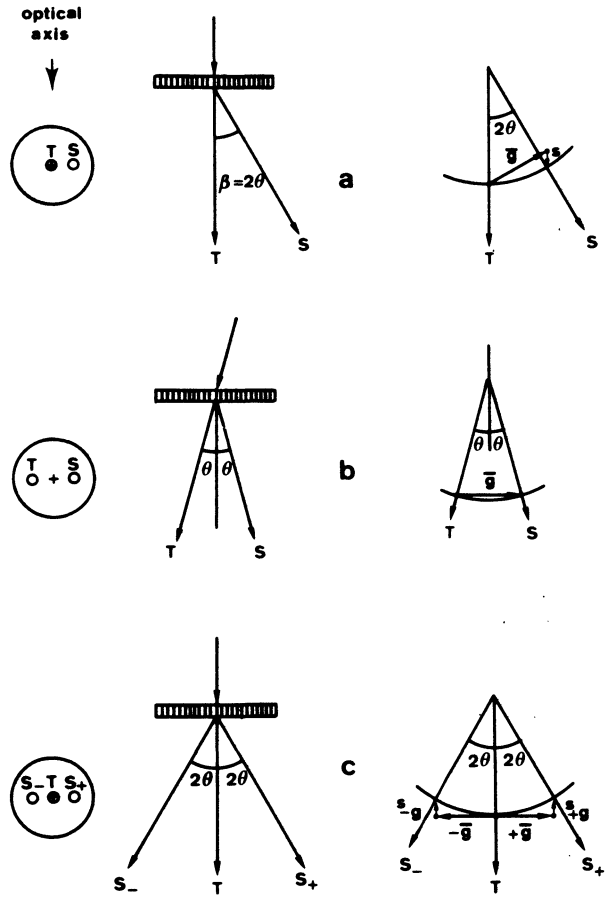

Fig. 6. Different modes for producing lattice fringes
(a) Two-beam normal incidence
(b) Two-beam tilted incidence
(c) Symmetrical three beam case
For each mode the geometry is shown in direct space (center) and in reciprocal space (right). The positions of the objective selector aperture is represented schematically for each case (left).

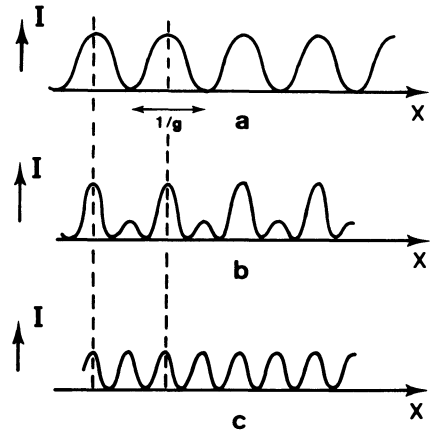

Fig.7. Different types of lattice fringes
(a) Simple sinusoidal two-beam fringes
(b) Three beam fringes exhibiting two different periods 1/g and 1/2g
(c) Three beam fringes exhibiting only the 1/2g period.

with $tg\phi=(s/\sigma)tg\pi\sigma t$ (17,b) where t = thickness of the specimen and where $x=\bar{r}.e_x$, with $\bar{e}_x$ parallel with $\bar{g}$. This can be rewritten as

$$I = I_T+I_S-2(I_TI_S)^{1/2}\sin(2\pi gx+\phi) \qquad (18)$$

This expression clearly represents a set of sinusoidal fringes perpendicular to $\bar{g}$ and with a period 1/g (fig.7,a). The position of the fringes depends on ϕ,i.e. on s (specimen orientation) and on t (specimen thickness). However, in a real microscope the scattered beam will suffer an additional phase shift due to the lens aberration and to defocus. The amplitude of the scattered beam will thus be multiplied by a factor $\exp(i\chi)$.

The expression for the image intensity will then become :

$$I = I_T+I_S-2(I_TI_S)^{1/2}\sin(2\pi gx+\phi+\chi) \qquad (19)$$

The sinusoidal fringe pattern will thus be shifted by an additional amount, which depends on the instrumental constants and on the diffraction angle β. Since χ changes with focus the lattice fringes move on changing the focus; this demonstrates clearly that the lattice fringes are not localized with respect to the specimen lattice. They provide nevertheless a rudimentary image of the crystal which consists in the period of a given set of lattice planes.

If χ changes by a multiple of 2π, i.e. $2m\pi$ (m:integer) the expression (19) clearly does not change. From (7) follows that a change in defocus $\Delta\varepsilon=m(2\lambda/\beta^2)$ or (using Bragg's law $d\beta=\lambda$) $\Delta\varepsilon=m(2d^2/\lambda=m(2/\lambda g^2)$ does not affect the fringe profile. There are then several defocus values leading to the same profile (Fourier images)

If a planar interface with displacement vector $\bar{R}$ is crossed by the set of lattice fringes the latter will suffer a fractional shift given by $\bar{g}.\bar{R}$. This can be deduced from the fact that the amplitude of the transmitted beam is the same in both crystal parts, whereas the scattered beam will have a different phase. If the expression for S in the first part of the crystal is given by (15), the corresponding expression for S in the second part of the crystal is multiplied by a factor $e^{i\alpha}$ with $\alpha = 2\pi\bar{g}.\bar{R}$. As a result the fringes in this second part will be described by

$$I=I_T+I_S-2(I_TI_S)^{1/2}\sin[2\pi g(x+\bar{R}.\bar{e}_x)+\phi+\chi] \qquad (20)$$

i.e. the interface clearly causes an additional shift in the fringe positions and hence a relative lateral shift of the fringes on crossing the interface. Lattice fringes can thus provide some information on the displacement vector of planar interfaces.

Note that the fringe contrast C, defined as $(I_{max}-I_{min})/(I_{max}+I_{min})$ is given by

$$C = 2(I_S/I_T)^{1/2}/\left[1 + (I_S/I_T)\right]$$

it will be maximum for $I_S = I_T$. For the exact Bragg orientation (s=0) this occurs for $\cos\frac{\pi t}{t_g}=\sin\frac{\pi t}{t_g}$ i.e. for $t = (1/4)t_g$.

The best contrasted two-beam lattice fringes (for s=0) are thus observed in a crystal thickness which is about 1/4 of the extinction distance. The condition $I_S=I_T$ can be satisfied for larger thicknesses also (i.e. for $t = (n+1/4)t_g$; n=integer), but then absorption effects become more pronounced also.

If s=0 and the beam is tilted over the Bragg angle (fig.6,b) the expression for I(x) becomes extremely simple; $T=\cos(\pi z/t_g)$ and $S=i\sin(\pi z/t_g)$ and from (17,b) also $\phi=0$ and hence $I(x) = 1 + \sin 2\pi gx \sin^2\pi t/t_g$.
It is independent of χ because the same shift occurs for both interfering beams T and S. By eliminating the aberrations to some extent fringe spacings which are smaller than the point resolution of the microscope may thus be obtained. It is by the use of this technique that Menter (1956) succeeded in obtaining the first 0,9nm lattice fringe in platinum phtalocyanide (1956). The positions of the diffraction spots with respect to the objective selection aperture are shown in fig.6 for the two beam cases discussed so far:two-beam

fringes at normal incidence (fig.6,a) and two-beam tilted incidence fringes (fig.6,b). The situation in reciprocal space is shown as well.(Dowell, 1963).

Many beam one-dimensional fringes. When several beams belonging to a systematic row collaborate to the image formation, more and more details can be resolved since higher order harmonics contribute to the one-dimensional Fourier synthesis.

The wave function at the exit face of the specimen is now schematically of the form

$$\Psi(\bar{r}) = e^{2\pi i\bar{K}.\bar{r}}(T+\sum_n S_n e^{2\pi i n\bar{g}.\bar{r}}) \qquad (21)$$

here T is the amplitude of the transmitted beam and S_n are the amplitudes of the scattered beams with diffraction vectors $\pm n\bar{g}$. The explicit expression for T and S_n can be derived from dynamical diffraction theory. Analytical expressions are only available in the very simplest cases e.g. -g,0,+g.The wave function is then of the form

$$\Psi(\bar{r}) = e^{2\pi i\bar{K}.\bar{r}}(T+S_+e^{2\pi i\bar{g}.\bar{r}} + S_-e^{-2\pi i\bar{g}.\bar{r}})$$

The intensity can then be written as

$$I(x) = TT^*+S_+S_+^* + S_-S_-^* + (S_-T^*+S_+^*T)\exp(-2\pi igx) + (S_+T^*+S_-^*T)\exp(2\pi igx) + S_+S_-^*\exp 4\pi igx + S_-S_+^*\exp(-4\pi igx)$$

This can be transformed into an expression of the form

$$I(x) = I_0+A\sin(2\pi gx+\phi_1)+B\sin(4\pi gx+\phi_2) \qquad (22)$$

where $I_0=I_T+I_g+I_{-g}$ and A,B,ϕ_1 and ϕ_2 are complicated expressions of the excitation errors, of the crystal thickness and of the Fourier coefficient V_g and V_{-g} of the lattice potential.

It is quite clear that now a second harmonic term with period 1/(2g) appears in the intensity distribution. One observes primary fringes with period 1/g and subsidiary fringes with period 1/(2g).

Since the beams +g and -g are off-axial beams it is necessary to introduce additional phase shifts due to lens aberration and defocus.The final amplitude distribution in the image is then of the form

$$\Psi(\bar{r})=e^{2\pi i.\bar{K}.\bar{r}}(T+S_+e^{2\pi i\bar{g}.\bar{r}}e^{i\chi(g)}+S_-e^{-2\pi i\bar{g}.\bar{r}}e^{i\chi(-g)})$$

In the symmetrical three beam case (fig.6,c) with $s_g=s_{-g}$ some simplification is possible since, because of symmetry, $\chi(g)=\chi(-g)=\chi$.

For the image amplitude one finds

$$\Psi(\bar{r})=\phi_0+\phi_g e^{2\pi i\bar{g}.\bar{r}+i\chi}+\phi_{-g}e^{-2\pi i\bar{g}.\bar{r}+i\chi}$$

Because of the symmetry one can put

$$\phi_g=S_g e^{i\varepsilon};\ \phi_{-g}=S_{-g}e^{i\varepsilon};\ S_g = S_{-g}$$

The intensity distribution is then finally of the form

$$I(x)=\Psi\Psi^*=I_T+I_g+I_{-g}+2S_gS_{-g}\cos(4\pi gx)+2TS_g\cos(2\pi gx+\chi+\varepsilon)+$$
$$+2TS_{-g}\cos(2\pi gx-\chi-\varepsilon)$$
$$=(I_T+2I_S)+2I_S\cos(4\pi gx)+4(I_TI_S)^{1/2}\cos(2\pi gx)\cos(\chi+\varepsilon) \quad (23)$$

From this expression it finally follows that the resulting fringes are of the type shown in fig.7,b. In the case where $\chi+\varepsilon=\pi/2$ the fringes look like fig.7,c.

For certain crystal thicknesses I_T may be zero. Also in this case one obtains sinusoidal fringes with half the lattice period (fig.7,c).

Two-Dimensional Multiple Beam Images

General Considerations. When a large number of beams corresponding with a two-dimensional array of diffraction spots is admitted through the objective selector aperture a correspondingly large number of Fourier components form the image. Each diffraction vector contributes one Fourier component, i.e. a system of parallel sinusoidal fringes perpendicular to $\bar{g}$ and with period $1/g$, to the final image. The larger the number of Fourier components the better the resolution in the image, the fine details are carried by the high order components. However, it is important to stress that the Fourier components should interfere with the correct phase relationship; relative phase shifts of some of the components cause spurious features to appear in the image and destroy the simple relationship between object and image. The image is then no longer the projected lattice potential or the projected charge density.

Unfortunately, with increasing order of the Fourier components correspond beams enclosing increasing angles with the optical axis. As long as we only make use of beams which pass through the "window" or "plateau" in the image transfer function (i.e. the sin χ versus β curve) the different components interfere with approximately the correct phase relationship and hence produce a directly interpretable image for a properly chosen defocus value (~ Scherzer defocus). For high resolution studies it is thus important to have an instrument with a wide plateau in the image transfer function and to eliminate the beams outside of it by an aperture. From fig.5,b the advantages of the use of high voltage become apparent in this respect.

One can use also beams corresponding with β angles outside of the window, but then the resulting image is in general no longer directly interpretable except in very special cases, such as in the "Aberration free focus method". For simple crystals (e.g. Si) with a small unit cell and using a small number of beams it is possible, by choosing defocus and an appropriate C_S-value, that a number of reflections, outside of the plateau still keep the correct phase. An image is then obtained which represents the true structure with a resolution which may exceed the point resolution (Hashimoto et al, 1978-79).

The interpretation usually proceeds by the "trial and error" method which consists in comparing the calculated image for a given structural model with the observed image. In this calculation the phase shifts introduced by the lens system have to be properly taken into account. Usually the calculation is made for different defocus values and for different specimen thicknesses; since we know that these parameters affect strongly and differently the phases of the different Fourier components and hence the final image.

A number of computational methods are used; for a survey of these methods we refer to Spence (1981). A fully dynamical direct space method has been formulated by Van Dyck.(1980,1983). Examples of the application of this method have been reproduced in fig.13. The calculated images have been plotted on a cathode ray screen, simulating in this way images of the same nature as the ones observed in the microscope.

Imaging modes. One-dimensional images. If only a one dimensional representation of the structure is required, for instance because the structure is a long period one-dimensional superstructure, one can use the following imaging techniques (fig.8):
Mode 1 : One can select two neighbouring superstructure reflections belonging to the same basic spot in a row of spots passing through the origin, i.e. in a central row. One uses only one Fourier component and consequently the image only reveals the long spacing
Mode 2 : If all superstructure reflections belonging to a central row are used, excluding the basic reflections in the row, one obtains the distribution of long spacings.
Mode 5 : One can also use a sequence of superlattice reflections from a non-central row. This is a useful mode if one wants to reveal polysynthetic sub-unit cell twinning.
Mode 3 : If one selects basic reflections as well as superlattice reflections in a central row (3) or a non-central row (5) one images also the set of lattice planes of the basic structure which is parallel with the periodic interfaces that produce the super-

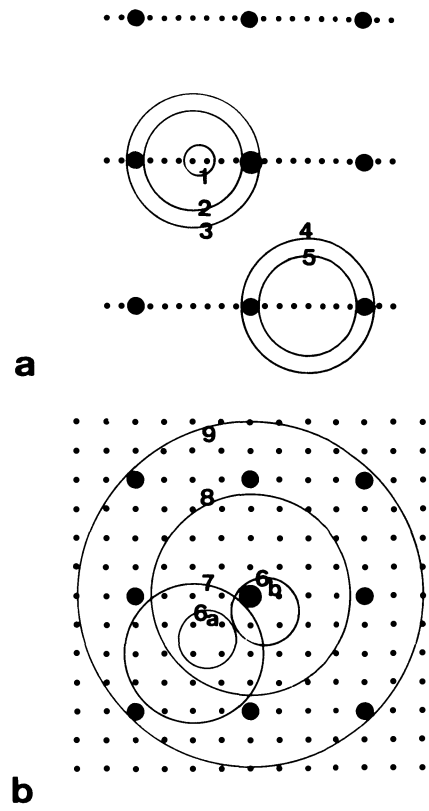

Fig.8. Imaging modes.
(a) One-dimensional fringes
(b) Two-dimensional images
The position and size of the objective selector aperture is shown for 9 different modes. The incident beam in assumed to pass through the central black dot.

structure. Any variability of the long spacing is now imaged in terms of the spacing of the basic lattice.

Two-dimensional images

Mode 6 : If only the superlattice needs to be imaged it is sufficient to include only pairs of neighbouring superlattice spots in two directions. This can be done either in the dark field (6,a) or in the bright field (6,b). In the latter case the image is formed by the direct beam and the first shell of superlattice reflections around it; the contrast is usually lower than for 6,a.

Mode 7 : All superlattice reflections are selected which are present within one mesh of the reciprocal lattice of the basic structure, excluding the direct beam and the basic reflections. This is clearly a multiple beam dark field image. The Fourier components contributing to the image are in general just sufficient to locate the positions of the minority atoms.

Mode 8 : Except for the direction beam all other basic reflections are excluded but as many shells of superlattice reflections as feasible are admitted. The number of Fourier components required to image the columns of minority atoms is now redundant, however such columns will therefore be imaged as sharper dots than in the previous mode 7.

Mode 9 : All beams originating from the basic as well as from the superstructure reflections are selected, provided they do not correspond to spacings which are smaller than the instrumental resolving power of the microscope. For most current instruments this means that up to the first or possibly up to the second shell of reflections, due to an FCC matrix, can usefully be included.

PART II : CASE STUDIES

INTRODUCTION

In this second part we shall demonstrate the use of high resolution imaging for a wide variety of problems. Although this survey is far from exhaustive, each of the main aspects is covered by one or two examples. The selection has to a large extent been determined by the accessibility of the illustration material, which

is an essential ingredient of a paper of this nature. Emphasis is therefore inevitably on work performed in our laboratory.

All applications are based on the assumption, to be supported by computer simulation in each case, that atom positions can be observed directly in crystal structures. We shall not discuss the observations of isolated atoms, which is more of a "tour de force" , without many applications, at least at the present time.

The experimental techniques are still in evolution, but a number of recommendations can be made in this respect. Very thin specimens are required (10-20 nm). They can be prepared by a variety of techniques depending on the material : crushing, cleaving, electrolytic polishing, ion beam milling, etc. The thinned material has to be deposited on a stable support, which is usually a holey carbon film. The best specimens are crystal flakes protruding over the edges of a hole. A goniometer stage is very helpful in orienting the specimens along the chosen zone axis. The diffraction pattern has to reflect very accurately the crystal symmetry along this zone axis. The objective aperture must be accurately centered on the optical axis and be chosen of the appropriate size to admit the beams wanted for the selected imaging mode. The magnification has to be sufficiently high to allow direct observation of the structural detail (this means at least 400.000x for a 3Å detail. Focus and astigmatism should be corrected by successive approximations using Fresnel fringes along the edge of the supporting carbon film.

Finally the image should be focused for optimum contrast. For this operation an image intensifier is particularly helpful since it allows to choose visually the proper underfocus. In the absence of such equipment a through focus series should be recorded. Last but not least the microscope should of course be capable of resolving the structural detail looked for and have, under the optimum defocus conditions the required "window" in the image transfer function.

BASIC ALLOY STRUCTURES

General Considerations

The spatial separation of minority atoms in binary alloys is in many cases at least of the order of 2-3 Å, a distance which can conveniently be resolved. A number of these structures is represented in fig.9.

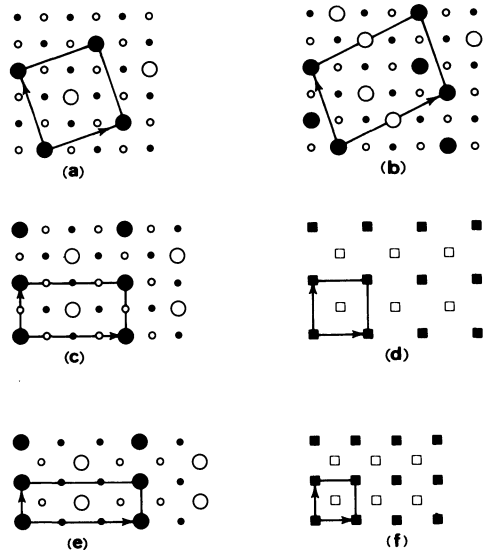

Fig.9. Schematic representation of different ordered structures derived from the FCC and BCC structures. Large dots represent minority atoms.

(a) Au_4Mn structure viewed along the tetragonal c-axis

(b) Monoclinic Au_5Mn_2 structure viewed along the two-fold axis

(c) Tetragonal DO_{22} structure (Au_3Mn) as viewed along the c-axis

(d) The same DO_{22} structure viewed along the tetragonal c-axis

The three structures are derived from the FCC structure.

(e) Tetragonal Cr_2Al structure viewed along the c-axis (Au_2Mn has the same structure

(f) The same structure viewed along the c-axis. This structure is based on a BCC lattice

Along certain zones the structures consist of columns, which contain only one atomic species, i.e. minority and majority atoms occur in separate columns. We shall say that the structure is a "column structure" along such zones. The distance between columns of minority atoms is then relatively the largest and it determines the unit mesh of the reciprocal lattice of the superstructure along this zone. Such zones are the most informative ones; along these it is possible to image only the minority atom columns by collecting only superlattice reflections in the objective aperture (mode 8). (fig.8,b). Once the positions of the minority atoms are determined in a binary alloy based on a known lattice the structure is completely known.

The Ni_4Mo structure (Van Tendeloo and S.Amelinckx,1978a;Van Tendeloo, De Ridder and Amelinckx,1978;Van Tendeloo and Amelinckx,1978b,1981)

The alloy Au_4Mn which is isomorphous with Ni_4Mo(fig.9,a) is a particularly suitable object for high resolution electron microscopy, using the dark field superlattice mode (mode 7). The reciprocal lattice as viewed along the c-direction, is shown in fig.10,a for a single variant. The diffraction conditions can then

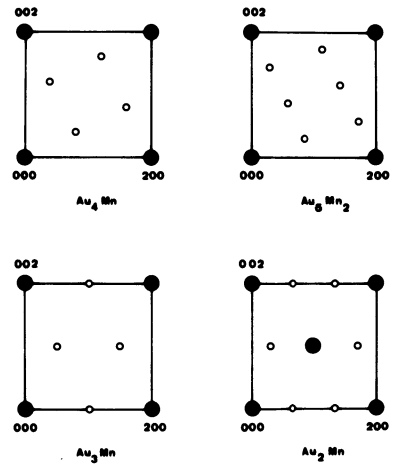

Fig. 10. Reciprocal lattice sections of the structures represented in fig.9. In all cases a cube zone is shown. The full dots represent basic reflections, the open dots superstructure reflections.

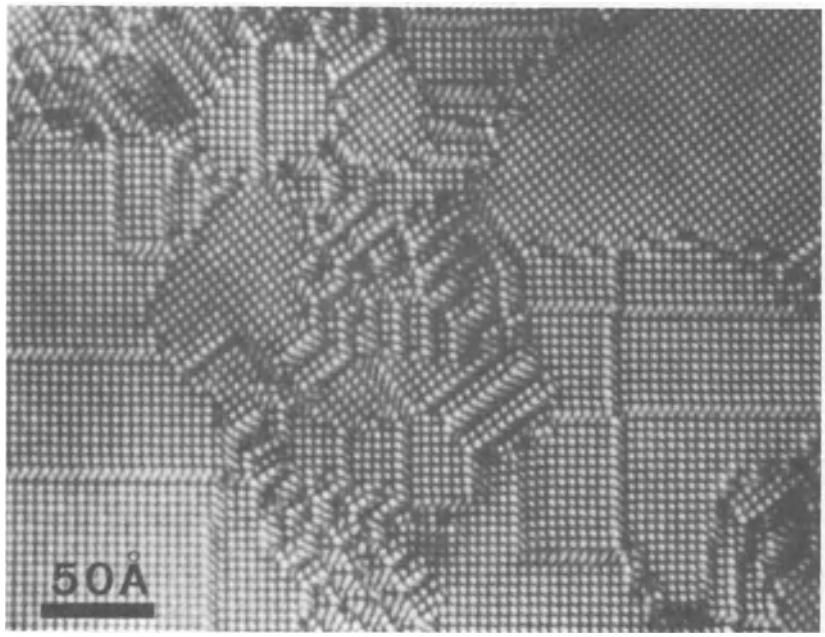

Fig.11. High resolution image of Au_4Mn made in the dark field superlattice mode (mode 7)

be chosen in such a manner that the projection of the centre of Ewald's sphere coincides with the centre of the octagon of superstructure reflections produced by the two coaxial variants (mode 7). Under these conditions all beams contributing to the images of coaxial variants enclose the same angle with the optical axis of the microscope and thus aberration induced phase differences cancel. Particularly well defined and to some extent defocus independent images result under these conditions. The four beams collected in each variant provide the minimum number of Fourier components that allow to generate the pattern of minority atoms, without any redundant information. Fig.11 and 12,a show examples of the Au_4Mn structure observed in this mode (mode 7); along the [001] zone, the Au_4Mn structure is a column structure.

We have also used the bright field basic lattice mode (mode 9). We now collect all beams within four unit meshes of the basic FCC reciprocal lattice, as well as the basic reflections themselves. The image now clearly contains information on the basic FCC structure, as well as on the superstructure. An image of a wedge shaped crystal obtained using this mode, is reproduced in fig.12,b. It is clearly seen that in the thin part of the wedge the basic FCC structure is revealed. In the thicker parts on the other hand strikingly bright dots reveal the positions of manganese columns. It is thus possible

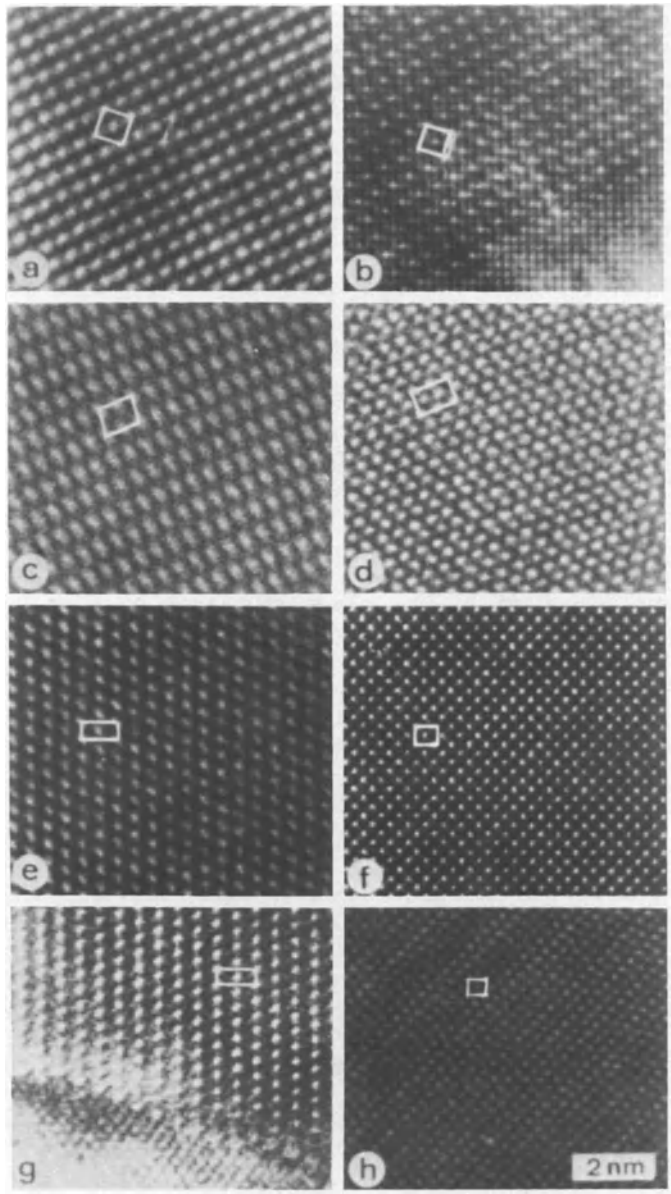

Fig.12. Images of basic ordered structures (cfr.fig.9).(a) Au_4Mn; (b) Au_4Mn+FCC in thin part;(c) Au_5Mn_2 ("low" resolution); (d) Au_5Mn_2("high"resolution);(e) $Au_3Mn(DO_{22})$:a-zone (f) Au_3Mn:c-zone (g) Cr_2Al;(a-zone); (h) Au_2Mn:c-zone.

to verify directly that the manganese columns occupy the positions with respect to the FCC lattice represented in the model of fig.9,a. The interpretation of the bright dots as marking the positions of the manganese columns is justified on the basis of computer simulated images, using the method described further.

The DO_{22} structure (Van Tendeloo, Van Landuyt and Amelinckx,1982)

A model of the DO_{22} structure is represented in fig.9,c and fig.9,d which are views along the a-axis and the c-axis respectively. It is clearly a tetragonal superstructure of the FCC superstructure with an ideal c/a ratio of 2, its ideal composition is A_3B. The reciprocal lattice as viewed along the a-direction is represented in fig.10,c.

In specimens with nominal composition Au_3Mn we obtained extensive regions of DO_{22} structure as judged from the diffraction pattern. Images were obtained using the imaging mode 8. A view along the a-direction is reproduced in fig.12,e whereas an image taken along the c-direction is shown in fig.12,f. From the two projections the structure can be determined unambigeously.

Like Au_4Mn viewed along the c-direction, the DO_{22} structure is a column structure when viewed along the a-direction, but not along the c-direction. The bright dots in fig.12,e have the geometry and scale of the configuration of manganese columns in fig.9,c viewed along the a-zone. Along this zone there are in fact two types of manganese columns which differ in level by a/2; they are imaged in the same way however, suggesting that the projected charge density is to a good approximation all that matters in determining the image. The gold columns are not imaged at all.

Along the c-direction on the other hand the structure is not a column structure; all manganese containing columns are mixed and have the composition AuMn. Apart from a relative shift of c/2 in the c-direction they are all identical. One finds in fact that all such columns are imaged in the same way; the observed configuration of bright dots in fig.12,f can be compared with the scheme of fig.9,d.

The Au_5Mn_2 structure (Van Tendeloo and Amelinckx, 1979)

The Au_5Mn_2 structure is a monoclinic superstructure of the FCC structure; it is represented in projection of fig.9,b; whereas the [010] section of the reciprocal lattice is shown in fig.10,b.

When viewed along the twofold axis it is a column structure; the configuration of manganese columns is shown in fig.9,b. The distance between the components of a pair is only 0,25 nm. In our most recent

instrument we have been able to image the two columns in a pair as clearly separated bright dots (fig.12,d) whereas in an earlier instrument we have only obtained elongated bright dots imaging a column pair (fig.12,c).

Image simulation of alloy Structures

In this paper we have mostly used images which allowed a direct interpretation in terms of structure models. Such images can be obtained by making through focus series, but also more efficiently with an appropriately adapted microscope. Our instrument is equipped with an image intensifier system, making it possible to see the image on a television monitor at a magnification of 10^7X. Under these conditions it is possible to observe visually the bright dot pattern of minority atoms. This makes it possible to select systematically focusing conditions and thicknesses which produce this type of patterns, avoiding the need for through focus series.

In all cases so far studied, we could produce images such that the pattern of bright dots had the same scale and geometry as the arrangement of columns of minority atoms. Along zones where all columns have the same but mixed composition, i.e. the macroscopic composition, all columns are represented by bright dots of the same intensity.

All these observations strongly suggest that the bright dots do represent columns of minority atoms along zones where minority and majority atoms occur in separate columns (so called column structure). Nevertheless it is desirable to verify this interpretation by means of computed images, following a "trial and error" scheme. This is in any case required if we want to make sure that the bright dots occur at the sites of the minority atom columns and are not merely reproducing the correct configuration at a shifted position however. It is perhaps an academic question if we want to obtain information on the perfect structure or even on translation interfaces; this is no longer so if we study the interface between orientation variants or other defect structures such as dislocations.

In order to make this verification it is necessary to produce computed images and compare these with the observations. The computation method used here is an improved version of the multislice method originally proposed by Cowley and Moodie (1957) and further developed by D. Van Dyck(1978). It takes fully into account multiple beam dynamical scattering in the crystal, as well as the phase shifts introduced by the aberration of the electron optical system and by defocusing (C_s = 1,1mm in our microscope). The final result of the calculation is plotted on a cathode ray

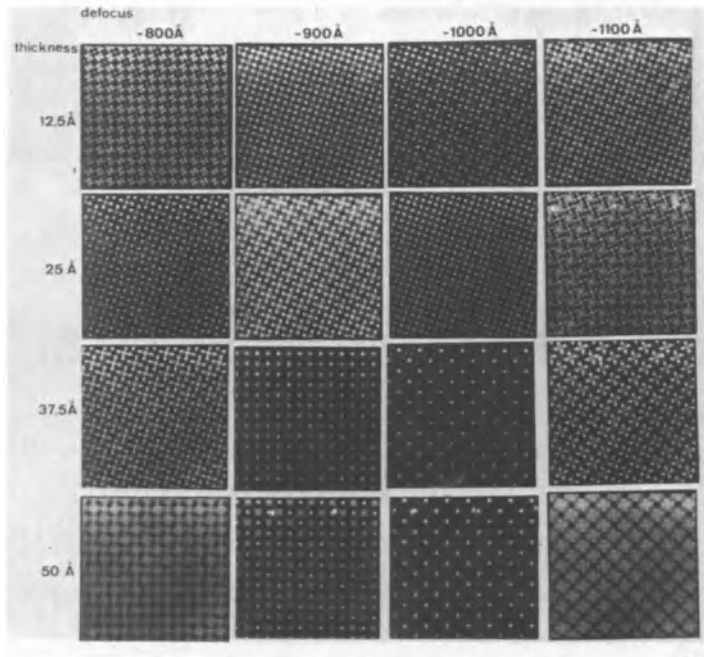

Fig.13. Computer generated images of Au_4Mn for different thicknesses and different defocus values (indicated on the photograph).

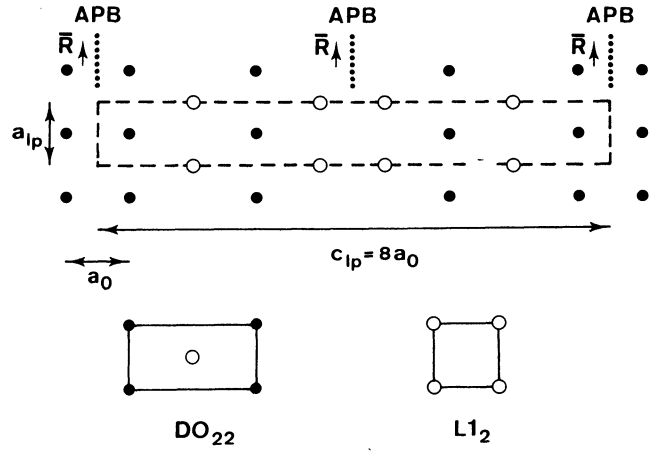

Fig.14. Schematic representation of long period anti-phase boundary structure in Pt_3V.

screen and photographed, producing in this manner an image of the same nature as the electron micrograph.

We have computed a number of images of different basic structures, viewed along different directions, for a number of thicknesses and defocus values (Van Dyck, Van Tendeloo and Amelinckx,1982). We shall discuss here briefly one example Au_4Mn (fig.13). The images were calculated on the assumption that the incident beam is parallel with the atom columns and that superstructure spots as well as the first shell of basic spots are admitted through the objective aperture (mod.9). For easy reference the left bottom corner of the frame was occupied in the model by a manganese column. The brightest dots clearly occur at the sites where manganese columns are located according to the model at least for a defocus value of -1000 Å to -1200 Å and a thickness in the range of 50 Å.

At small thicknesses the sites of the gold atoms are marked by weaker dots; at larger thicknesses the gold images become vanishingly weak (fig.13). This thickness behaviour is in agreement with the observation (fig.12,b). Qualitatively the contrast behaviour as a function of thickness can be understood by noting that the intensity of the superstructure beams builds up much more slowly as a function of thickness than the intensities of the beams due to the basic structure. Stated otherwise the depth variation of the intensities of the basic reflections is different from that of the superstructure reflections. At certain thicknesses the intensities of the basic beams may thus be weak whilst the superstructure beams may be relatively strong. A semi-analytical treatment of the image formation in alloy systems with column structures is given by Van Dyck, Van Tendeloo and Amelinckx (1982).

LONG PERIOD ANTI-PHASE BOUNDARY STRUCTURES

Introduction

Many alloy systems exhibit long period anti-phase boundary modulated structures. Most of these are based on a FCC basic lattice; some are based on a HCP lattice. These structures are usually stable in a limited temperature range only. Their occurrence is often favoured by deviations from a simple chemical composition; the excess of one of the components may then be incorporated in the crystal along non-conservative anti-phase boundaries, it determines in this way their separation and possibly their orientation. In other systems the anti-phase boundaries are conservative; their spacing then seems to be related to the electron/atom ratio.

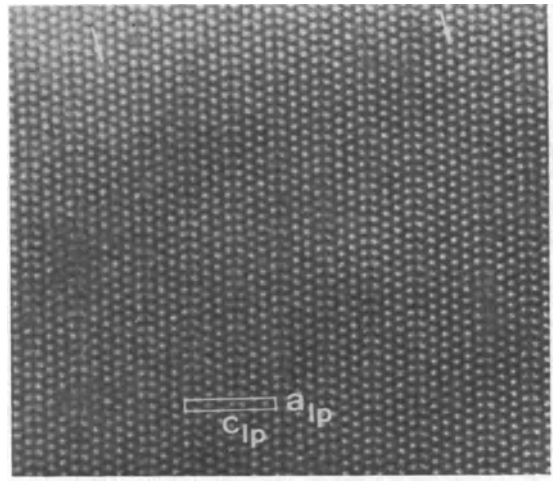

Fig.15. Long period anti-phase boundary structure in Pt_3V; this image can be compared with fig.14.

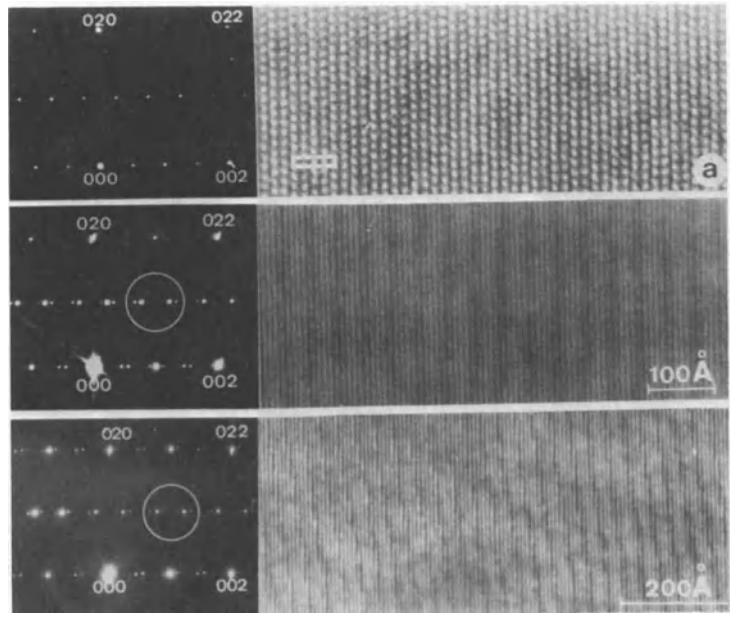

Fig.16. Long period superstructures in $Au_{3+}Zn$.
(a) $2\bar{2}$ superstructure of Ll_2 and corresponding diffraction pattern; (b) Superstructure $2\bar{2}2\bar{3}$ and its corresponding pseudo-incommensurate diffraction pattern; (c)region of $2\bar{2}2\bar{3}$ structure; note the orientation anomaly.

One-dimensional long period anti-phase Boundary Structures

Based on a FCC lattice. Pt_3V has the Ll_2 structure at high temperature (>1000°C) and the DO_{22} structure at lower temperature (<900°C)(Maldonado and Schubert,1964). In the intermediate temperature range (~900°C) it was recently found to exhibit a long period superstructure which includes structural elements of the high and low temperature structures (Schryvers and Amelinckx,1984). This structure is represented schematically in fig.14 and the high resolution image, in which the bright dots image vanadium columns, is shown in fig.15.The structure is best described as body centered tetragonal with lattice parameters $a=a_0$; $c=8a_0$.

A different tetragonal one-dimensional long period superstructure of Au_3Zn, also derived from the Ll_2 structure is shown in fig. 16,a together with the corresponding diffraction pattern. It consists of slabs of Ll_2 structure, two unit cells wide, shifted one with respect to the next over a vector $\frac{1}{2}[110]$. The resulting structure is body centered tetragonal with $a=a_0$ and $c=4a_0$. (Schryvers, Van Tendeloo, Van Landuyt and Amelinckx, 1983)

Based on a HCP lattice. The structure of Cu_3Sn is a periodic anti-phase boundary structure derived from an orthorhombic superstructure which is itself based on the hexagonally close packed structure (Bernal,1928; Van Sande et al, 1978;Carlsson and Hagg, 1932, Schubert et al,1955). The lattice parameters of the long period superstructure a_s,b_s and c_s are given in terms of the lattice parameters of the basic orthorhombic structure by the relation $a_s = 2\ a_o$, $b_s = 4$ to $10\ b_o$, $c_s = c_o$.

The observations prove that the b_s parameter may be varied by the addition of aliovalent impurities such as Ni and Zn.

The structure is represented in fig.17; it was assumed that $b_s = 10b_o$. The APB's are in (010) planes and the displacement vector is $\vec{R} = 1/2\ [100]$. The observations on this alloy illustrate how the selection of an appropriate set of beams affects the final image and allows to obtain the information best adapted to specific purposes. A typical diffraction pattern is reproduced in fig.18,a and represented schematically in fig.18,b, after omission of double diffraction spots.

A rudimentary lattice image is obtained by collecting a sequence of satellite spots of the row h = 1 in the objective aperture. Such dark field images only reveal the APB's as fine straight lines (fig.19,a)). Apart from occasional isolated faults the spacing is quite constant in well-annealed specimens. In nominally stoichiometric specimens the line spacing is $5b_o$; we shall represent the long period structure by the symbol 5 $\bar{5}$,

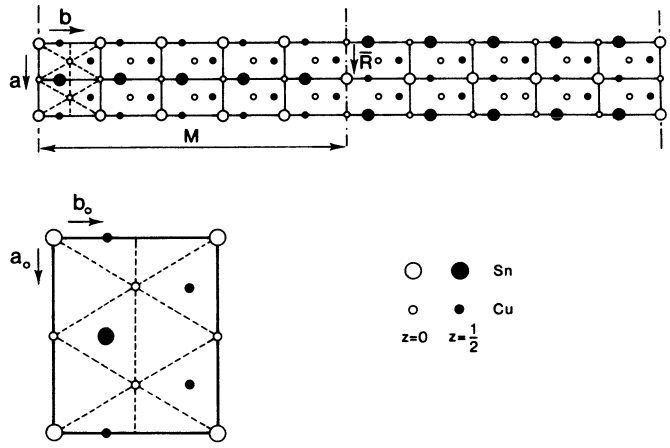

Fig.17. Schematic representation of the basic structure and the long period anti-phase boundary structure in Cu_3Sn.

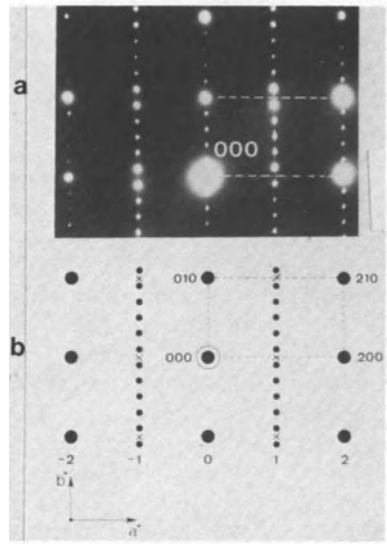

Fig.18. (a) Diffraction pattern of the long period anti-phase boundary structure in Cu_3Sn and its schematic representation (b). The spots along h=even rows are due to double diffraction.

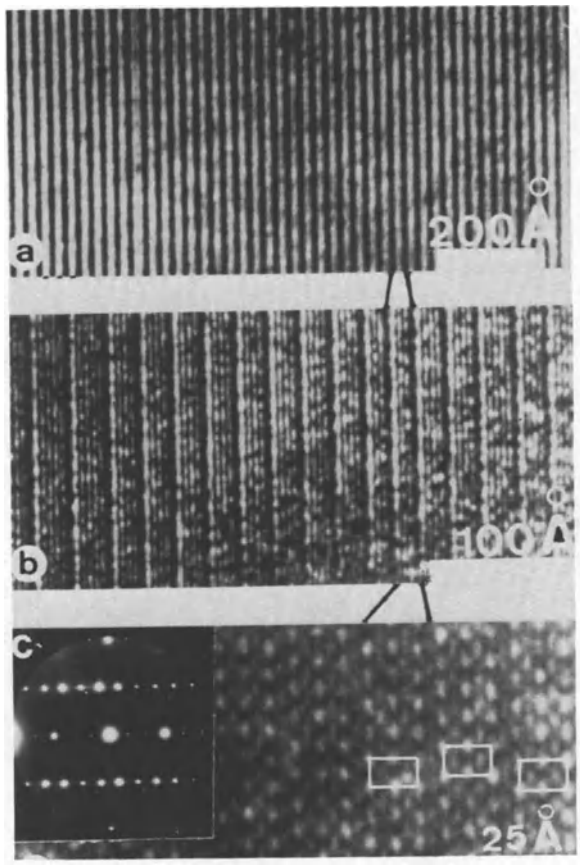

Fig.19. (a) Two-beam fringes of the long period superstructure in Cu_3Sn (mode 1)
(b) One-dimensional many beam fringes, including basic reflections (mode 3)
(c) Two-dimensional many-beam images including the reflections visible in the inset.

(the minus sign means displaced; the numbers indicate the width of the strips). In crystals containing Zn the structure may become $2\bar{2}$.

When collecting in the objective aperture also the basic spots along the linear arrays of superlattice spots, lattice fringes due to the basic structure can be revealed as well. It is then possible to observe directly the width of the domain strips in terms of unit cells of the basic structure (fig. 19,b).

When collecting beams belonging to at least two neighbouring arrays of satellite spots, as shown in the inset of fig. 19,c, one obtains a two-dimensional representation of the structure such as the one reproduced in fig. 19,c Darker bands now mark the APB's. The scale and configuration of the white dots within the domains are the same as those of the minority atoms (Sn). The shift of the structure along the APB's is quite evident and in agreement with the model of fig. 17.

The different levels of resolution have been used for different purposes. The simple superlattice fringes have been used to study orientation variants; since the fringe orientation reveals directly the three possible directions of the b-directions with respect to the hexagonal basic structure. The lattice fringes of the basic structure have been used to study the changes in superperiod in alloys with addition of zinc and nickel; in particular the distribution of superlattice spacings becomes immediately evident. The diffraction pattern allows on the other hand to determine the average spacing. In quenched specimens the distribution is found to be quite irregular. The "atomic" resolution image finally exhibits directly the configuration of atoms along APB's, and reveals the shift of the structure along them.

Two-dimensional periodic APB structures

A number of alloy systems exhibit long period structures derived from a basic structure by the introduction of a crossed grid of anti-phase boundaries. The same alloy system may exhibit, under slightly different conditions, either one or two-dimensional APB structures.

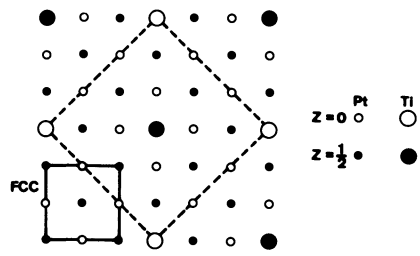

Fig.20. Schematic representation of the structure of Pt_8Ti and Pt_8V

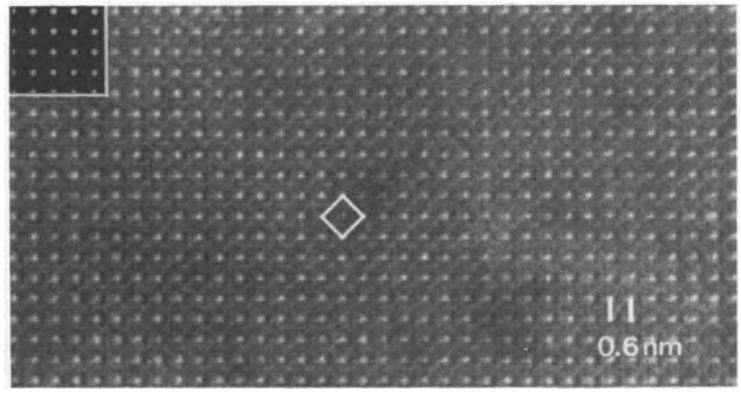

Fig.21. Ordered structure of Pt_8V; the bright dots image V-columns. The inset shows a computer generated image.

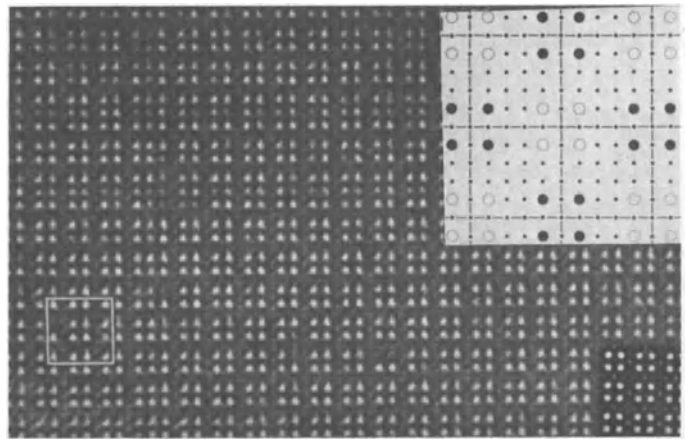

Fig.22. Two-dimensional periodic anti-phase boundary superstructure of Pt_8Ti. Alternatively it can also be considered to be derived from the $L1_2$ structure (Pt_3Ti). The left top inset shows a simulated image of the model shown in the lower left inset.

We shall present here only one recent example observed in Pt_8Ti. (Schryvers, Van Landuyt, Van Tendeloo and Amelinckx,1983). The structures of Pt_8V and Pt_8Ti are tetragonal superstructures of the FCC structure (fig 20). The unit cell is only one FCC unit cell thick,i.e. $a=(3\sqrt{2})a_0$; $c=a_0$ along the $[001]$ zone the structure is a "column structure". An image of Pt_8V along this zone is shown in fig.21, quite similar images have been obtained from Pt_8Ti specimens (Schryvers, Van Landuyt and Amelinckx,1983). In specimens containing

an excess of Ti structures such as that imaged in fig.22 have been obtained; the corresponding structure model is represented in the inset of fig.22.It consists of a regular patchwork of unit cells of Pt_8Ti structure and unit cells of Ll_2(Pt_3Ti structure)(Schryvers, Van Landuyt, Van Tendeloo and Amelinckx, 1983).

IMAGING OF MIXED LAYER COMPOUNDS AND POLYTYPES

General Considerations

A number of materials such as SiC and ZnS with layer structures crystallize in different structures which differ only in the stacking of the same layers, usually close-packed, or of the same lamella (e.g.CdI_2) but having the same composition.

Another class of materials have structures consisting of a mixture of layers or lamella differing in composition as well as in structure and occurring in varying proportions. In this case not only the stacking but also the compositions are different. Such materials are called mixed layer compounds.

High resolution electron microscopy is a powerful tool for elucidating the often complicated stacking sequences in such structures. In some cases the stacking sequence can be inferred from one-dimensional lattice images; in other cases two-dimensional images are required to derive the stacking sequence. Depending on the information searched for a variety of imaging modes is used, we shall refer to fig.8 to designate them. A number of examples will now be discussed.

A mixed layer compound : Barium Ferrite (Van Landuyt, Amelinckx, Kohn and Eckart, 1974)

The structure of barium ferrite is based on the close-packed stacking of oxygen ions. The two basic stackings are shown in fig.23b and c, where the lower case letters represent close-packed oxygen layers and the capital letters mixed barium oxygen layers the structure of which is represented in fig.23(a)(Braun, 1957).

The hexagonal M structure (fig.23,b) has the composition $BaFe_{12}O_{19}$; it contains two blocks with a thickness of 11.6Å per unit cell. The blocks M_1 and M_2 are rotated with respect to each other by an angle of 180° about the c-axis. The barium-containing layer is in fact a mirror plane for the structure. The subdivision into blocks is of course arbitrary; however, the choice made here emphasizes the symmetry within a single block and shows that only two positions are used in each block, for the oxygen layers.

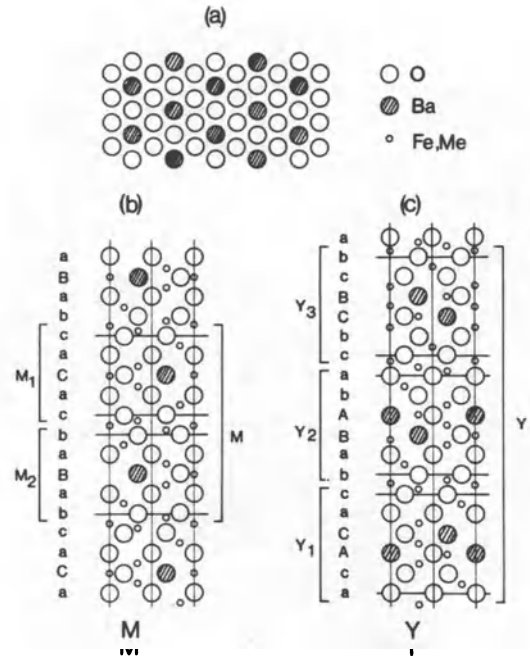

Fig.23. Structure of barium ferrite. In (a) the arrangement within the mixed O-Ba layers is shown. The M-structure (b) has the composition $BaFe_{12}O_{19}$ and the Y-structure (c) has the composition $Ba_2Me^{II}Fe_{12}O_{22}$(Me^{II}=Zn).

The rhombohedral Y structure has the composition $Ba_2Me^{II}Fe_{12}O_{22}$ (Me^{II} = Zn). It contains three blocks with a thickness of 14.52 Å per unit cell. The choice of blocks made here, again emphasizes the fact that in each block only two positions are used for the oxygen layer. In both structures the contact between blocks, as defined above, is realized by means of two triplet layers in the cubic arrangement. This seems to be a general building principle which is obeyed in all known mixed-layer compounds of the type M_nY_m.

The central row dark field lattice images(mode 3 in fig.8) for a number of mixed-layer compounds of the series M_nY_m are reproduced in fig.24. The most striking feature is the occurrence of dark lines with two different spacings closely corresponding to 11.6 and 14.5Å. It is therefore very tempting to associate the pairs

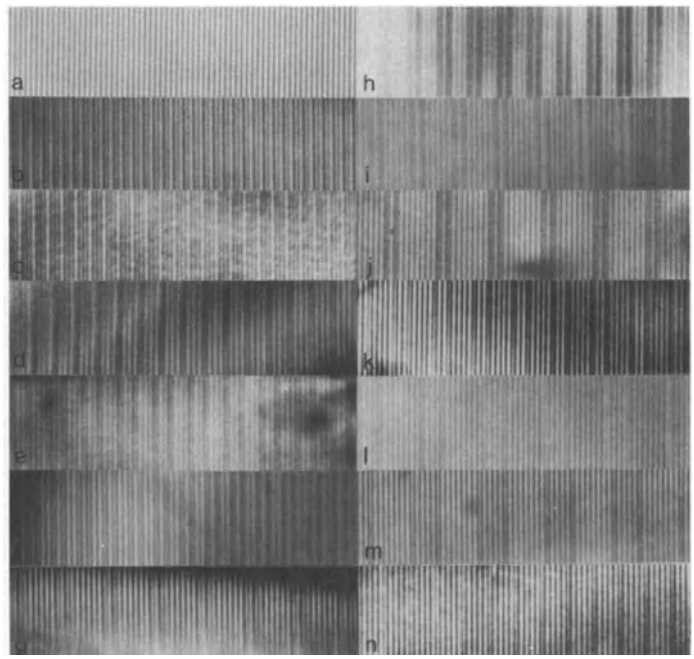

Fig.24. One-dimensional multiple beam lattice fringes of different Bariumferrites realized in a central row. The narrow spacing corresponds to a M-block; the wider spacing to a Y-block. The corresponding structure symbols are given in table I.

of more closely spaced lines with M blocks and the pairs of more widely spaced lines with Y blocks. This very simple imaging code allows one to explain consistently the structures of those compounds for which the structure was known from X-ray diffraction. It therefore seems justifiable to extend this interpretation to compounds the structure of which has not been previously determined. Table I summarizes the interpretation of the line sequences of fig.24. Note that in all these sequences the M blocks appear isolated, whereas the Y blocks form bands.

With non-central row dark field images(mod.4 in fig.8) used, successive Y bands separated by an M block exhibit different shades, showing that these mixed-layer compounds are in fact polysynthetic twins (fig.25) and allowing an easy interpretation of these structures in terms of non-conservative subunit cell level twinning.

In the present case the polysynthetic twinning can be considered as a means of accomodating different O:Ba ratios in the structure. A schematic representation of the twinned structure is given in fig.26.

Table I

M:Y	Stacking Sequence	Figure
1:∞	Y	24a
2:1	MMY	24c
2:2	MYMY	24b
2:3	$MYMY_2$	24f
2:4	$MYMY_3$	24h
2:5	MY_2MY_3	24e
2:6	$MYMY_5$	24i
	MY_2MY_4	24k
	MY_3MY_3	24d
2:7	$MYMY_6$	24g
2:8	$MYMY_7$	24j
	Y_4MY_4	24n
2:10	MY_3MY_7	24l
2:11	MY_4MY_7	24m

We have also produced two-dimensional images of the MY_2MY_3 compound in which M and Y blocks can clearly be recognized (fig.27); structural detail now becomes visible within the blocks.(see also Anderson and Hutchinson, 1975; Hutchinson, 1978-79)

Polytypes of SiC and ZnS (Van Landuyt, Van Tendeloo and Amelinckx, 1983)

The fundamental building unit in all SiC and ZnS polytypes is a tetrahedron in which each silicon atom (zinc atom) is surrounded by four carbon atoms (sulphur atoms) and similarly each carbon atom (sulphur atom) is surrounded by four silicon atoms (zinc atoms). The bonds are primarily covalent. The tetrahedra are stacked in such a way that atoms of the same chemical species occupy parallel planes (fig 28). By analogy with the symbolism used to designate the stacking of close packed planes of spheres one can describe the structure of the cubic phase by the symbol aαbβcγaαbβcγ
where the latin letters represent for instance silicon and the greek letters carbon. The symbol for the hexagonal polytype 4H is similarly aαbβaαcγaαbβaαcγ.

One often denotes a double layer by a single symbol aα→A,bβ→B and cγ→C. Using this notation the 4H polytype is represented by the

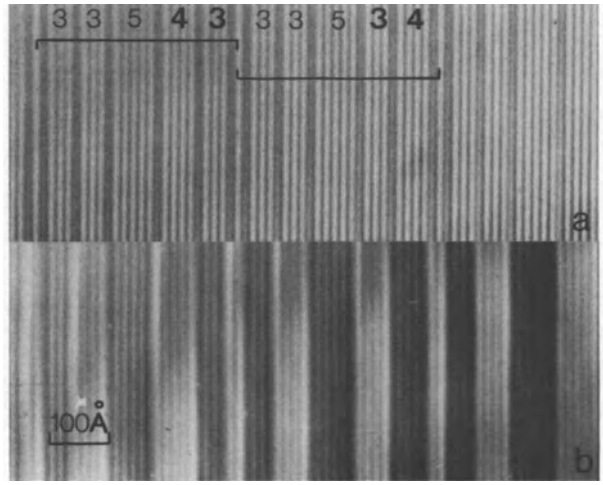

Fig.25. (a) Central row dark field image (mode 3, fig.8)
(b) Off central row dark field image (mode 4, fig.8) of the same crystal area. The image in (b) reveals that the crystal consists of polysynthetically twinned Y lamella seperated by a layer of M-structure. Note the good correspondance between the two images.

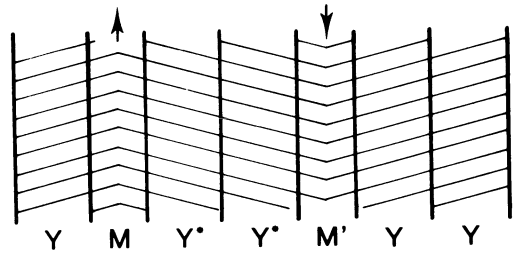

Fig.26. Schematic representation of the polysynthetic twin structure of barium ferrite.

stacking symbol ABACABAC... and the common polytype 15R by the symbol ACBAB/CBACA/BACBC.... Some of these polytypes are drawn schematically in fig.28.

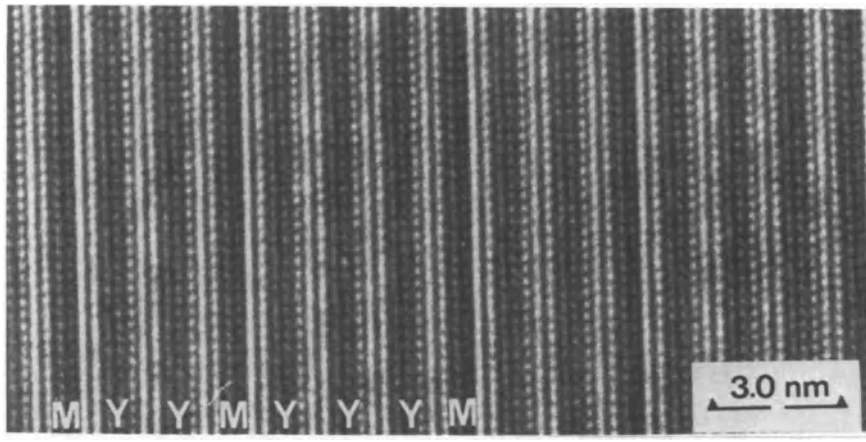

Fig.27. Two-dimensional multiple beam images of Bariumferrite MY_2MY_3.

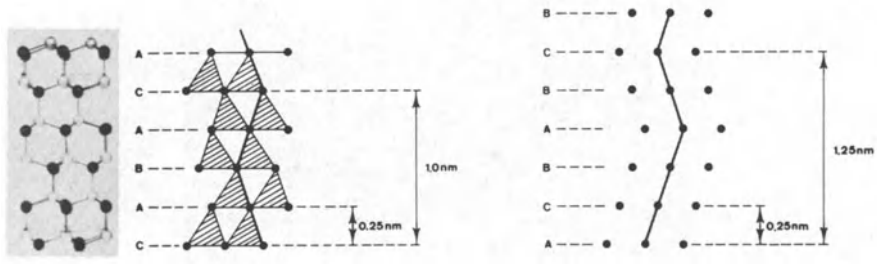

Fig.28. Structures of polytypes of SiC and ZnS.
(a) Ball model for the 4H ($a\alpha b\beta c\gamma$) structure of SiC and ZnS.
(b) Schematic representation of the 4H structure; the projected tetrahedra are cross-hatched. The stacking symbol is simplified to ABAC.
(c) Schematic representation of the 15R polytype of SiC with stacking symbol ACBA/BCBACA/BACBC.

Fig. 29 shows high resolution micrographs of 15R silicon carbide made with the use of three different imaging modes(J.Van Landuyt, Van Tendeloo and Amelinckx, 1983). In each case the viewing zone is $[11\bar{2}0]$. In fig.29,a the central beam and the first reflection adjacent to it have been used. Only the 5-layer long period is revealed (i.e.c/3). In fig.29,b which is also a bright field image

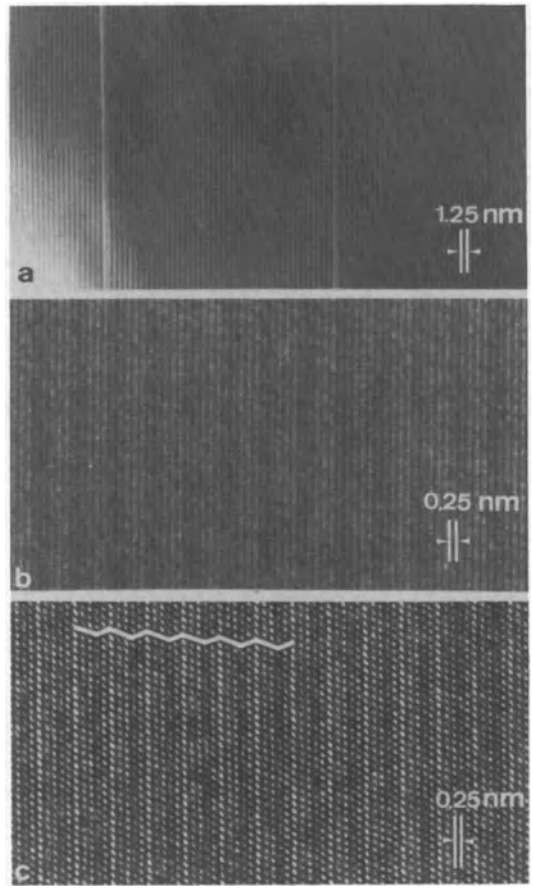

Fig.29. High resolution images of 15R-SiC using three different imaging modes.
(a) Only the five layer spacing is revealed. Note two deviating spacings at stacking faults
(b) The 00.15 reflection is included in the aperture (mod.3). The interlayer spacing is revealed.
(c) Two-dimensional image using reflections from adjacent rows. The stacking is now clearly revealed.

a larger aperture was used accepting up to the 00.15 reflection, i.e. the reflections corresponding with the interlayer spacing; the individual layers in a five layer lamella are now imaged. In fig.29,c a still larger objective aperture, including spots from adjacent rows, was used. One can now deduce not only the layer spacing, but also the stacking sequence, when assimilating a bright

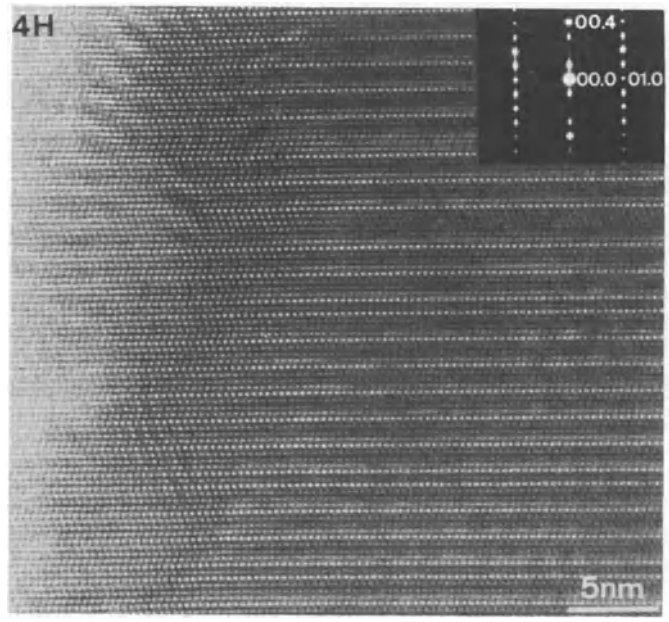

Fig.30. High resolution image of the 4H polytype of ZnS. The inset shows the reflections used for imaging. The stacking sequence is clearly somewhat irregular; note the occurrence of prominently bright rows of dots in the thicker part of the specimen.

dot with a pair of atoms aα,bβ or cγ. This interpretation is justified by image simulation. It should further be noted that such atom pairs could not be resolved in the microscope.

ZnS is not quite as prolific in forming different polytypes as SiC nevertheless a large number of polytypes is known as well. Above 1150 °C the 2H-polytype (wurzite) is the stable form, whereas at room temperature sphalerite, i.e. the cubic form is the stable phase. At intermediate temperatures other stackings are formed, often being faulted. The 4H stacking is rather common. Fig. 30 shows the high resolution image of a 4H crystal with stacking ABCB taken along the $[11\bar{2}0]$ zone. Depending on the focus one can obtain bright as well as dark dot images. Image simulation shows that the bright dots represent atom pairs, whereas dark dots image the open channels in the structure (Bender et al, to be published).

High resolution images make it possible to derive directly complicated stacking sequences and to study partly disordered crystals (Dubey et al, 1977).

INCOMMENSURATE AND PSEUDO-INCOMMENSURATE MODULATED STRUCTURES

Pseudo-incommensurate $Au_{3+}Zn$ (Van Tendeloo and Amelinckx, 1977, 1978c, Schryvers et al, 1983)

The interpretation of incommensurate diffraction patterns may cause a problem because the incommensurability may either find its origin in a "quasi-regular" mixture of commensurate spacings or in a genuine deformation or composition modulated structure with an incommensurate q-vector. High resolution electron microsocopy can be of great help in the interpretation of such diffraction patterns.

In the alloy $Au_{3+}Zn$ one often observes diffraction patterns of the type shown in fig.16,b or c, as compared to the simple pattern of fig.16,a. The superlattice spots have acquired satellites at incommensurate positions, (fig.16,b) and often also the direction of the linear sequences of satellites deviates slightly from the [001] direction (fig.16,c). The one-dimensional lattice fringes, corresponding with (b), are parallel with the (001) plane and exhibit a regular sequence of two different spacings; every fourth interfringe distance being somewhat larger. In (c) their average orientation deviates moreover somewhat from the (001) plane.

The ideal Au_3Zn structure produces the diffraction pattern in (a). Assuming the bright dots in the corresponding image to represent the minority (i.e. zinc) atoms it clearly shows that the structure is a long period anti-phase boundary derivative of the $L1_2$ structure, with stacking symbol $2\bar{2}$. This symbol means that a strip of this structure two unit cells wide and limited by (001) planes alternates with a displaced strip of the same structure also two unit cells wide; the displacement vector being $\frac{1}{2}[110]$. The image of (b) suggests that the structure in this case is represented by the symbol $2\bar{2}23$ leading to an average period of 2,25 times a_0, the lattice parameter of the underlying FCC lattice. In the case of fig.16,c the anti-phase boundaries are moreover systematically ledged, leading to an average orientation which encloses a small angle with the (001) planes. It is evident that without the images the interpretation of the diffraction patterns would have been difficult and ambigeous.

Chimney Ladder Structures : $MnSi_{2-x}$

The diffraction pattern of the compound $MnSi_{2-x}$ consists of closely spaced composition dependent linear sequences of satellite

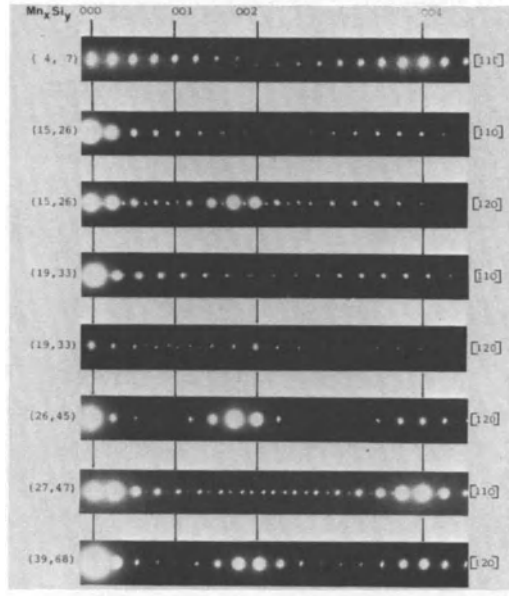

Fig.31. Central rows of diffraction patterns of different manganese silicides $MnSi_{2-x}$. The Mn/Si ratio, as derived from the diffraction pattern, is indicated on the left. The zone-axis is indicated on the right. Note the presence of orientation and spacing anomalies.

reflections, associated with basic reflections, which are the same in all diffraction patterns (fig.31). Where the sequences of satellites meet orientation as well as spacing anomalies usually result, producing an incommensurate diffraction pattern (De Ridder, Van Tendeloo and Amelinckx, 1976). The structures of this class of compounds were determined using X-ray diffraction (Jeitschko and Parté, 1967). Hereby the existence of very long unit cells had to be assumed in order to be able to index all reflections present. Two of these structure are represented in fig.32; they consist of a framework of manganese atoms (black circles) the silicon atoms (open circles) being positioned along a double helix arrangement. The origin of the incommensurability is in fact that the period of the double helix need not be commensurate with that of the manganese sublattice. In fact the two sublattices have periods which are not simply related; the c-parameter of the structure is the smallest common multiple of the two subperiods.

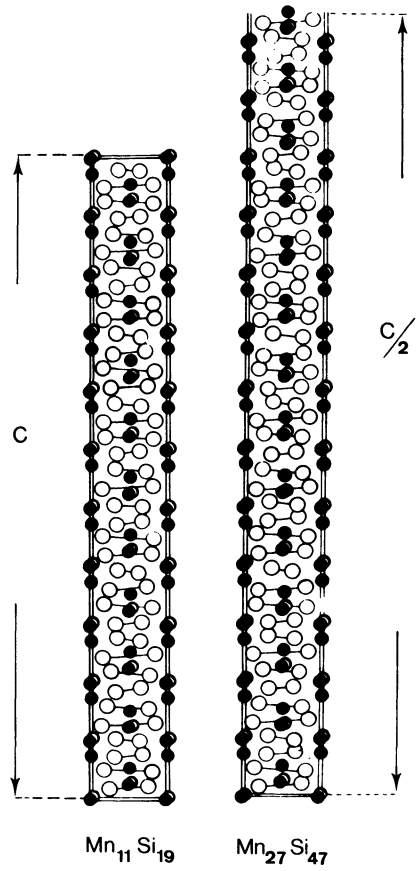

Fig.32. Structure of two manganese silicides. The black dots represent manganese; the open dots silicon.

High resolution images of such compounds (fig.33) viewed along the [110] zone reveal the two periods separately (Ye and Amelinckx, 1983). In fig.33 a dark field as well as a bright field image of the same area is represented. The widely spaced pronounced fringes mark the period of the silicon arrangement, whereas the rows of dots represent the manganese sublattice. The subperiods as well as the resulting lattice parameter are indicated on the photograph.The result of high resolution electron microscopy are consistent with the genuine incommensurate nature of this structure.

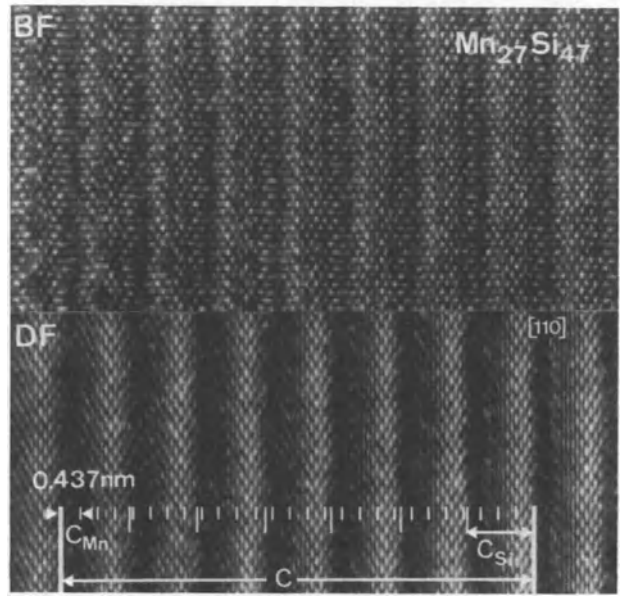

Fig.33. High resolution images of $Mn_{27}Si_{47}$ along the [110] zone; bright and dark field images of the same area are reproduced. The superperiods of the Si-sublattice and of the Mn sublattice are indicated separately.

The orientation anomaly in the diffraction pattern can be explained by assuming that neighbouring silicon helices are gradually shifted along their axis with respect to the manganese framework.

SHORT RANGE ORDER IN ALLOYS

Introduction

Many alloys, when rapidly quenched from above the ordering temperature, exhibit a state of short range order, characterized in reciprocal space by the occurrence of diffuse scattering in the diffraction pattern. The question as to the nature of the corresponding direct space atom configurations has been the subject of intense speculation. The observed diffuse scattering may be caused either by **concentration waves** or by **microdomains**. Recently high resolution electron microscopy has contributed to the interpretation of such diffuse scattering. We shall briefly present two recent examples.

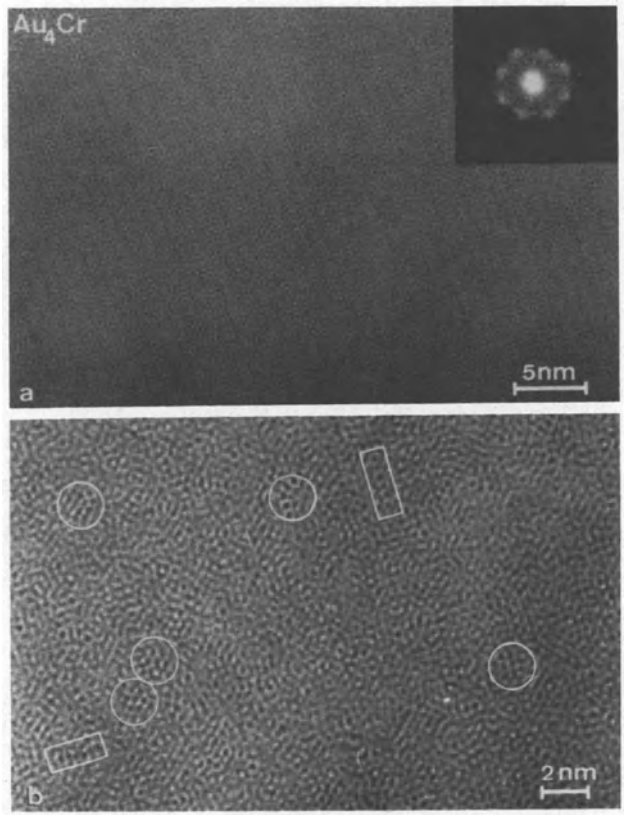

Fig. 34. High resolution images of quenched Au_4Cr presenting the 1½0 type SRO diffuse reflections.
(a) Small magnification; the inset is an optical diffraction pattern of the negative reproducing also the 1½0 diffraction spots
(b) High magnification: note the presence of microdomains.

1½0 Type Alloys (Van Tendeloo, Amelinckx and de Fontaine, 1984)

Quenched Au_4Cr presents the 1 ½ 0 type of diffuse spots which are characteristic of most short range order alloys of the Ni_4Mo-type. A high resolution image of such a specimen is reproduced in fig.34,a at small magnification and in fig.34,b at high magnification. The optical diffraction pattern of the high resolution micrograph produces the typical 1 ½ 0 spots (inset), proving that the direct space information is recorded in the

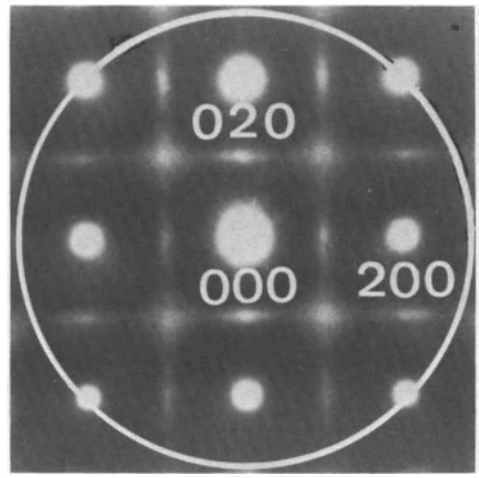

Fig. 35. Diffuse scattering in Pt_3V quenched from 1100°C; the intensity is located on lines in reciprocal space.

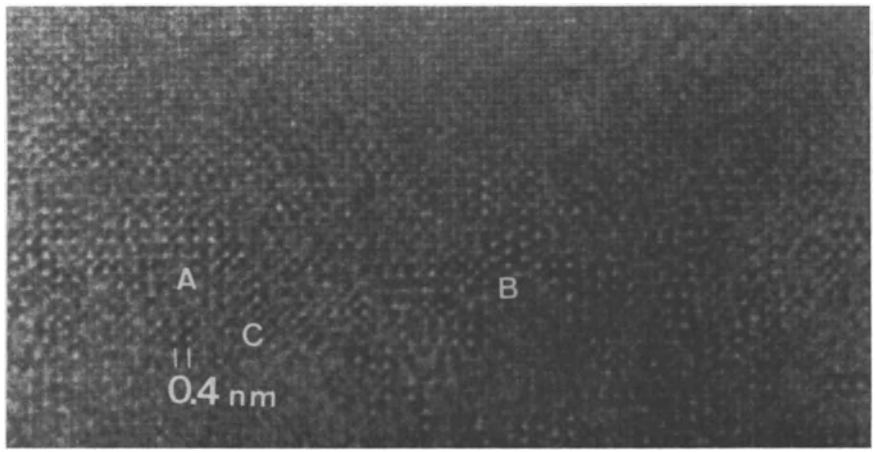

Fig. 36. High resolution image of short range ordered Pt_3V; note the presence of microdomains of both $L1_2$ and DO_{22} structure.

micrograph. Very small clusters of dots, having the configuration of the Mo-squares in the Ni_4Mo structure are visible in the image. They occur intimately mixed with small clusters of triangular configurations typical of the DO_{22} structure.

Optical masks consisting of dot patterns representing the adequate mixture of small islands of squares and triangles in all possible orientation variants produce optical diffraction patterns

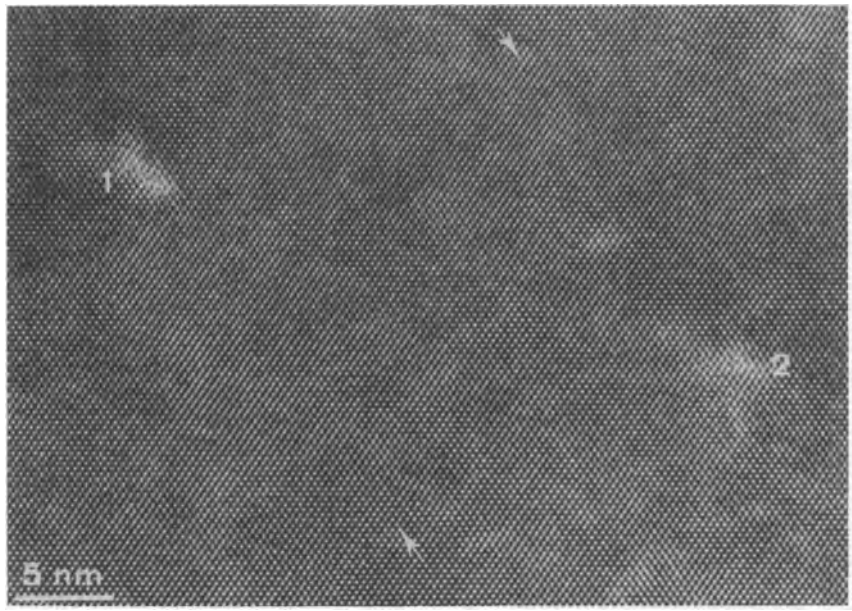

Fig. 37. Low magnification, high resolution image along the [110] zone of 60° dislocations in silicon. The dots represent pairs of atom columns.

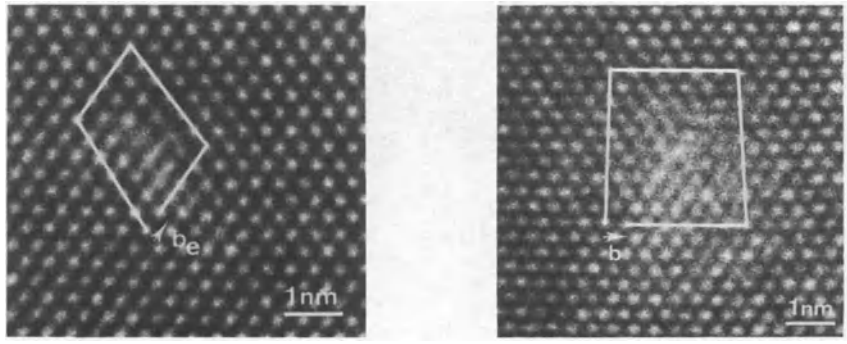

Fig. 38. High magnification high resolution image of the 60° dislocation 2 of fig.37

Fig. 39. High magnification high resolution image of a 90° dislocation in silicon.

simulating closely the electron diffraction pattern of Au_4Cr. These observations were considered to support the microdomain model for 1 ½ 0 type of short range order (Ruedl et al, 1968).

S.R.O in Pt_3V

In the diffraction pattern of Pt_3V quenched from above 1100°C, diffuse lines were found next to the FCC spots (fig.35). A high resolution image (fig.36) made from such a diffuse diffraction pattern, including the basic FCC reflections, reveals that the structure consists of a mixture of small islands containing atom clusters in the DO_{22} and $L1_2$ configurations, in all possible orientation and translation variants. Also in this case optical simulation has confirmed this model (Schryvers et al,1984).

DEFECT IMAGES

Dislocations

Informative images can be obtained for edge dislocations and for the edge part of mixed dislocations when viewed along a zone axis parallel with the dislocation line. Under these conditions the configuration consists of straight atom columns parallel with the zone axis. The strain field of an edge dislocation is two-dimensional since there is no strain parallel with the dislocation line. The configuration of atom columns in the vicinity of the dislocation core can then be considered as an image of this strain field. (Spence, 1977; Bourret et al, 1978).

Fig.37 shows two 60°-dislocations in a silicon specimen imaged along the [110] zone. When viewing the photograph under grazing incidence along the arrows one observes the supplementary half-planes of "atoms". A magnified image of dislocation 2 is shown in fig.38. The Burgers circuit drawn around the dislocation determines the projected Burgers vector as $\bar{b}_c$. Fig.39 shows a 90° dislocation in silicon also viewed along the [110] zone (Bender et al, 1985).

Planar Defects

Since atom positions can be imaged under suitable imaging conditions it is obvious that the geometry of planar interfaces such as stacking faults,crystallographic shear planes (Mc.Lagan et al, 1977) anti-phase boundaries and twin boundaries can be revealed as well.

Fig.11 shows the dark field superlattice image (mode 7) of a specimen of Au_4Mn; the bright dots represent manganese columns. The presence of domains belonging to two twin related orientation variants with a common c-axis is quite obvious. Each of these domains is further fragmented by anti-phase boundaries with a $(1/10)[3\bar{1}5]$ displacement vector. All anti-phase boundaries have the same type of displacement vector and are situated in $\{100\}$ type planes of the Au_4Mn structure; their energy is clearly anisotropic and depends on the displacement vector, strongly favouring one out of the theoretically possible vectors (i.e. all FCC lattice vectors)(Van Tendeloo and Amelinckx, 1978,b).

Fig.40 shows an isolated stacking fault in 2H-ZnS (Wurtzite); it is of the type ABABCACAC... i.e. involving two cubic triplets. This type of fault can be generated by the passage of a single Shockley type partial. Since at room temperature the stacking fault energy in 2H-ZnS is negative Schokley partials in a dissociated glide dislocation will separate infinitely far apart; they may generate in this way the stable cubic phase.(Secco d'Aragona et al, 1966; Blank et al, 1964).

A microtwin lamella in cubic ZnS (sphalerite) is imaged in fig.-41. The twin interfaces are coherent and form one triplet in the hexagonal stacking, the stacking symbol being ...ABCABCBACBA... (Bender et al, 1985).

Fine structure of antiphase boundaries

All geometrically conceivable antiphase boundaries need not actually be present because the interfacial energy may be too large for most of them. In the gold-manganese system, for alloys with a composition in the vicinity of Au_4Mn we noted a strong preferential orientation of the APB's in well annealed specimens; they tend to be situated in $\{100\}$ planes of the Au_4Mn structure. Moreover all observed single APB's have a displacement vector which encloses with the interface normal the largest angle which is compatible with the FCC lattice i.e. they are of the type represented in the left part of fig.42,b(horizontal part). Such APB's are as close as possible to conservative. As represented in the same figure a change in orientation over 90° causes the same APB to become strongly non-conservative (vertical part). A number of such angular configurations has been observed in Au_4Mn (fig. 42,a) in each case it was found that one leg of the angle was simple and the other one was dissociated

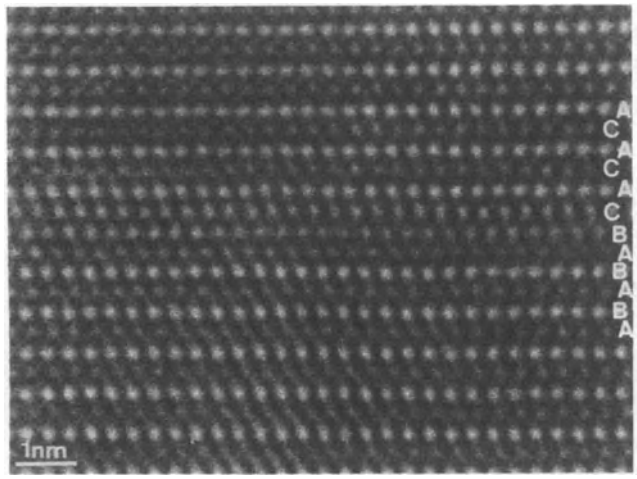

Fig. 40. Stacking faults in 2H-ZnS (wurtzite).

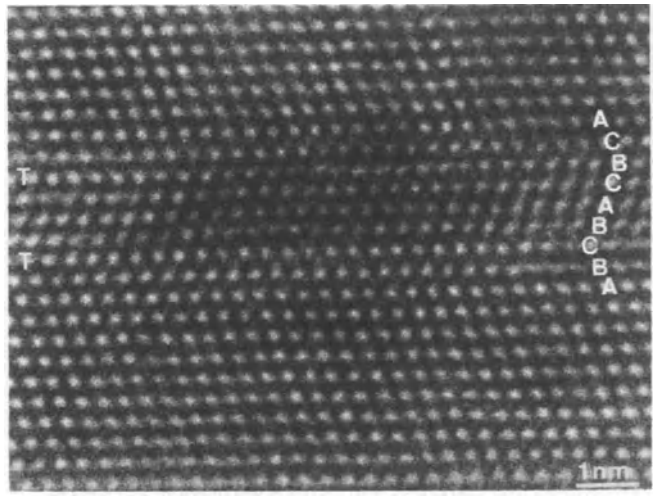

Fig.41. Coherent microtwin in cubic ZnS (sphalerite).

in two components being both of the same type as the simple leg (fig. 42,b). This is considered to be evidence for the instability of the strongly non-conservative APB's in an alloy of this composition (Van Tendeloo and Amelinckx, 1981).

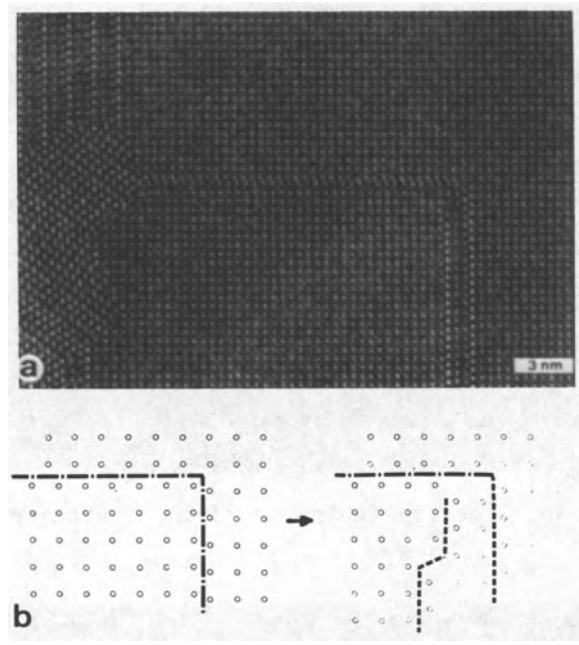

Fig.42. Dissociation of APB in Au_4Mn.
(a) Rectangular arrangement of APB's in Au_4Mn. One leg is simple; the other one is dissociated in two components separated by three manganese columns;
(b) Analysis of the observed configuration (a) in terms of manganese columns. Left the configuration before and right after dissociation.

In the Au_5Mn_2 structure the anti-phase boundaries have a displacement vector of the type $1/7[201]$, i.e. it is one seventh of a superlattice vector. On thermal treatment anti-phase boundaries can thus be eliminated from a monodomain area of the crystal by merging of seven of these anti-phase boundaries, leaving perfect structure. This phenomena can be observed in fig.43.

COINCIDENCE PATTERNS

The structure of Au_4Mn can be formed in six different a priori equally probable ways within the same FCC lattice. The unit cells of the six possible orientation variants are shown in fig.44 with respect to a cube representing the basic FCC lattice. The image of fig.11 exhibits different orientation variants derived from the same FCC structure.

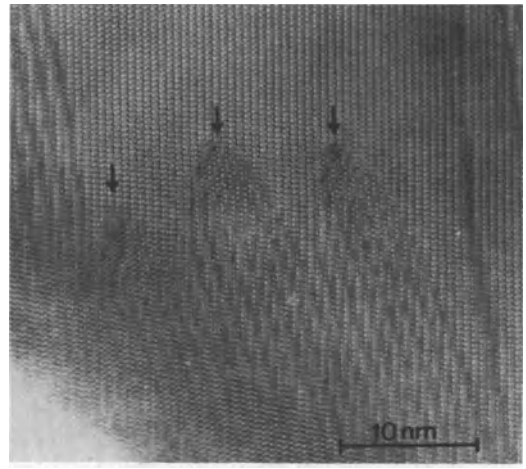

Fig. 43. Merging of seven APB's in the Au_5Mn_2 restoring perfect material.

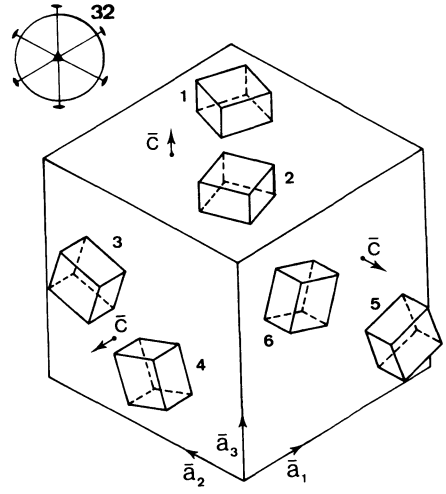

Fig.44. Schematic representation of the orientation variants of the Au_4Mn structure with respect to the host lattice represented by a cube.

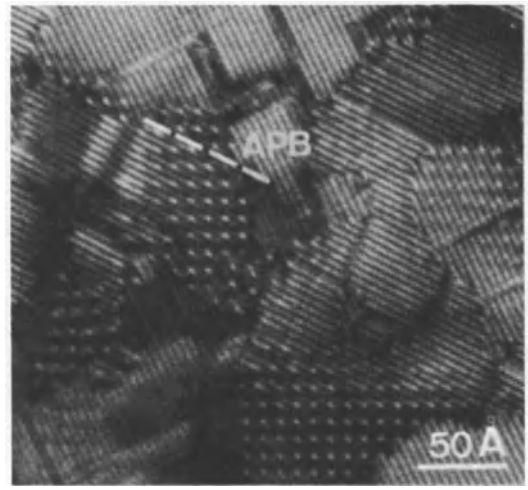

Fig.45. Poorly resolved domain structure in Au_4Mn; the prominently bright dots image the coincidence lattice between two overlapping coaxial orientation variants.

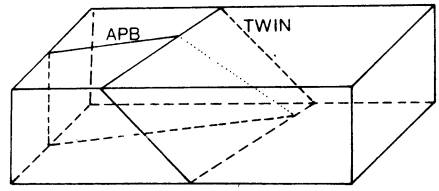

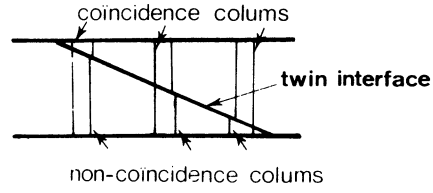

Fig.46. Cross section showing coincidence and non-coincidence columns intersecting an inclined twin interface between two coaxial variants in Au_4Mn.

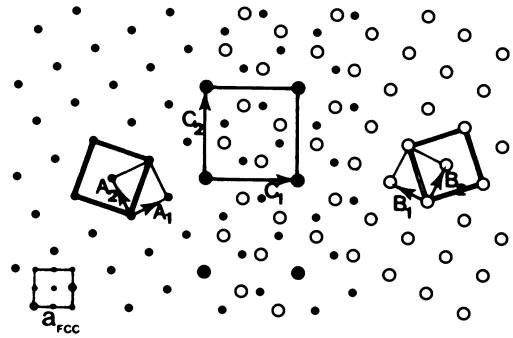

Fig. 47. Geometrical construction used to derive the lattice of coincidence columns observed in the overlap region between two coaxial variants in Au_4Mn (cfr. fig.45).

In fig.45 variants with a common c-axis (coaxial variants) overlap in part being separated by an inclined interface. This geometry is shown in cross section in fig.46. Where the two variants overlap a square grid of prominently bright dots is observed. The geometry of this grid is quite different from that of the bright dots imaging the Mn-columns in the normal Au_4Mn structure. It turns out that these bright dots mark the positions of Mn-columns which are continuous across the interface. This can be deduced from the simple geometrical construction of fig.47. The square grids of Mn columns in the two orientation variants are drawn with different symbols left and right of the overlap part; the overlap pattern in this central part has the same geometry as the prominently bright dots in fig.45 (Van Tendeloo and Amelinckx, 1978,a).

This observation is in fact a direct experimental proof that continuous manganese columns are imaged as bright dots also in the other manganese structures under the same imaging conditions.

Coincidence patterns occur frequently in ordered alloys because simple orientation relationships exist between different orientation variants.

ACKNOWLEDGEMENTS

I would like to thank my collegues and friends Prof.Dr.J.Van Landuyt, Dr.G.Van Tendeloo, Dr.D.Van Dyck, Dr.Bender, Dr.Yé, Prof. Dr.R.De Ridder and Drs.D.Schryvers for illuminating discussions and/or for the use of illustrations from joint papers.

REFERENCES*

Books and Review Papers

Amelinckx,S., 1964, The Direct Observation of Dislocations in Solid State Physics", F.Seitz and D.Turnbull, eds., Academic Press, New York.

Amelinckx,S.,1978 in "Diffraction and Imaging Techniques in Materials Science", S.Amelinckx, R.Gevers and J.Van Landuyt, eds. North Holland Publ.Cy, Amsterdam, 2nd Edition.

Amelinckx,S., 1978-79,Chemica Scripta, 14:197.

Amelinckx,S., 1981, in "Fifty of Electron Diffraction",P.Goodman, ed.,D.Reidel, New York.

Cowley, J.M.,1976,,High Resolution Electron Microscopy of Materials, in "Annual Review of Materials Science" 6:53.

Hashimoto,H., Endo, H.,Takai,Y.,Tomita,H.and Yokota,Y.,1978-79, Chemica Scripta, 14:23

Hawkes, P.W., 1972, "Electron Optics and Electron Microscopy"Taylor and Francis, London.

Hawkes, P.W., 1982,"Magnetic Electron Lenses",Springer Verlag,Berlin.

Hirsch,P.B., Howie,A., Nicholson, R.B.,Pashley,D.W.,Whelan,M.J.,1965 "Electron Microscopy of Thin Crystals",Butterworth, London.

Spence, J.C.H.,"Experimental High Resolution Electron Microscopy" Claredon Press, Oxford.

Thomas,G.,1962,"Transmission Electron Microscopy of Metals", Wiley,New York.

Thomas,G. and Goringe, M.J.,1979, "Transmission Electron Microscopy of Materials",J.Wiley, New York

Van Dyck,D.,1978, "Structure Imaging in Electron Microscopy" in "Diffraction and Imaging Techniques in Materials Science", S.Amelinckx, R.Gevers and J.Van Landuyt, eds.,North Holland Publ.Cy, Amsterdam.

Van Landuyt,J.,Van Tendeloo,G. and Amelinckx,S., 1984 "High Resolution Electron Microscopy of Polytypes" in "Progress in Crystal Growth and Characterization",Pergamonn Press, Oxford.

Van Tendeloo, G., Van Dyck, D., Van Landuyt, J. and Amelinckx,S., 1979, J.Solid State Chem., 27:55.

---

* Since this text is mainly intended for use as lecture notes, no attempt was made to give an exhaustive list of references which would be prohibitively long. We have whenever possible referred to survey papers or reference books, where the original sources can be found.

Research Papers

Allpress,J.G. and Sanders,J.V.,1973, Appl.Cryst.6:165
Anderson, J.C. and Hutchinson, J.L.,1975, Cont.Phys.16:443
Bender,H. et al,1984, to be published
Bernal, J.D.,1928, Nature,122:54
Blank, H., Delavignette,P.,Gevers,R., Amelinckx,S.,1964, Phys.Stat. Sol.,7:747
Bourret,A., Renault,A.and Austin, G.R., 1978, Chemica Scripta, 14:207
Braun, P.B.,1957, Philips Res.Report, 12: 491.
Carlsson, O and Hagg, G.,1932, Z.Krist.,83 : 308.
Coene, W., Van Dyck, D. and Van Landuyt,J.,1983, J.Micr.Spectr.,18: 17a.
Cowley, J.M. and Moodie, A.F.,1957, Acta Cryst. 10:609.
Cowley, J.M., 1959, Acta Cryst.,12 : 367.
Cowley, J.M., Iijima, S.,1972, Z.Naturf. A27 : 445.
De Ridder, R., Van Tendeloo, G. and Amelinckx, S., 1976,Phys.Stat. Sol.(a),33 : 383.
Dowell, W.C.T., 1963, Optik, 20 : 535.
Dubey, M., Singh, G. and Van Tendeloo, G.,1977,Acta Cryst.,A33:276.
Fejes, P.L., 1977, Acta Cryst., A33 : 109.
Glaser, W., 1952, "Grundlagen der Elektronoptik",Springer Verlag, Wien.
Goodman, P. and Moodie, A.F., 1974, Acta Cryst., A28 : 536.
Grinton, G.R. and Cowley, J.M., 1971, Optik, 34 : 221.
Hashimoto, H., Mannami, M. and Naiki, T.,1961, Phil.Trans.Royal Soc.253 : 459.
Hibi,T., 1962, in "Fifth Int.Congress on Electron Microscopy", Academic Press, New York, p.KK1.
Hutchinson, J.L., 1978-79, Chem.Scripta, 14 : 181
Jeitschko, W. and Parthé, E.,1967, Acta Cryst., 22 : 417.
Lynch, D.F., Moodie, A.F. and O'Keefe, M.A., 1975, Acta Cryst.,A29 : 537.
Lynch,D.F. and O'Keefe, M.A., 1972, Acta Cryst.,A28 : 536.
McLagan, D.S., Bursill, L.A. and Spargo, A.E.C.,1977, Phil.Mag.,35: 757.
Maldonado, A. and Schubert, K., 1964, Z.Metallk., 55:619.
Menter, J., 1956, Proc.Roy.Soc. A236 : 119.
O'Keefe, M.A., 1973, Acta Cryst., A29 : 389.
Ruedl,E., Delavignette, P. and Amelinckx, S.1968, Phys.Stat.Sol., 28:305.
Scherzer, O., 1949, J.Appl.Phys., 20 : 20.
Schryvers, D., Van Landuyt, J. and Amelinckx, S., 1983, Mat.Res. Bull., 18 : 1369.
Schryvers, D., Van Landuyt, J., Van Tendeloo, G. and Amelinckx,S., 1983, Phys.Stat.Sol., 75 : 607.
Schryvers, D., Van Tendeloo, G. and Amelinckx, S.,1984, Mat.Res. Bull.(to be published)

Schryvers, D., Van Tendeloo, G., Van Landuyt, J.and Amelinckx, S. 1983, Phys.Stat.Sol(a), 75 : 613.
Schubert, K., Kieffer, B., Wilkens, M. and Haufler, R.,1955, Z. Metallk.,46 : 692.
Secco d'Aragona, F. Delavignette, P. and Amelinckx, S.1966, Phys. Stat.Sol.,14 : K115.
Spence, J.H., 1977, Acta Cryst., A34 : 112.
Van Dyck, D., Van Tendeloo, G. and Amelinckx, S., 1982, Ultramicroscopy, 10 : 263.
Van Landuyt, J. and Amelinckx, S., 1971, Mat.Res.Bull., 6:613.
Van Landuyt, J., Amelinckx, S., Kohn, J. abd Eckart, D.W.,1974, J.Sol.State Chem., 9 :103.
Van Sande,M, De Ridder, R., Van Tendeloo, G., Van Landuyt, G. and Amelinckx, S., 1978, Phys.Stat .Sol. a48 : 383.
Van Tendeloo, G. Amelinckx, S. and deFontaine, D., 1984, Acta Met. (to be published).
Van Tendeloo,G. and Amelinckx,S.,1977, Phys.Stat.Sol.,(a).,43:553.
Van Tendeloo,G. and Amelinckx,S.,1978a, Phys.Stat.Sol.(a).,47:555.
Van Tendeloo,G. and Amelinckx,S.,1978b, Phys.Stat.Sol.(a).,49:337.
Van Tendeloo,G. and Amelinckx,S.,1978c, Phys.Stat.Sol.(a).,50:53.
Van Tendeloo,G. and Amelinckx,S.,1979, Phys.Stat.Sol.(a)., 51:141.
Van Tendeloo, G. and Amelinckx, S., 1981, Phys.Stat.Sol.(a) 65 : 73;ibid, 65 : 431.
Van Tendeloo, G. and Amelinckx, S., 1984, Phys. Stat.Sol.(a), to be published.
Van Tendeloo, G. , De Ridder, R. and Amelinckx, S., 1978, Phys. Stat;Sol.(a).,49 : 655.
Van Tendeloo, G. Van Landuyt, J. and Amelinckx, S., 1982, Phys.Stat Sol. (a), 70 : 145.
Yé, H.Q. and Amelinckx, S., 1983, Proc. NATO Advanced Study Institute, Crete, to be published.

ELECTRON MICROSCOPY IN REAL COLOURS

J. B. LePoole

Delft University of Technology

Delft, Holland

If we want to see the colors of an object, we have to illuminate with multicolored light, preferably "white light". Accept my apologies for not defining "white" more accurately, since it has little bearing on the fundamentals of my talk.

Unfortunately, we have no multicolor electrons and so "electron microscopy in real colors" would seem an impossible goal. We shall see however, that by their interaction with matter, it shold be possible to give electrons a color tag.

Some ten years ago it occurred to me that the fact that the cross-section for absorption of a photon of energy e_{ph} is proportional to the cross-section for an energy loss $\Delta E = E_{ph}$ for fast electrons, could be the basis of real colour electron microscopy. Already at that time, being no longer an active electron microscopist myself, I made the suggestion at the E.M.A.G. Conference in Bristol, 1976, hoping that somebody would try the idea. Apparently this didn't happen up till now. For this reason it is put up for discussion here, with far more emphasis than when I suggested it eight years ago.

Not only is it fascinating but the colour of matter could be determined in details well below the wavelength of the colour concerned. When I inquired whether medical research and diagnosis could benefit from increased resolution

in familiar colours, I received an enthusiastic response. Since many of the STEM's have an energy loss analyser with a sufficiently high resolution to have three separate channels in the 1.5 to 3.5 eV. region, the experiment should not take a tremendous effort.

Let's now turn our attention to the resolution that can be expected. According to Isaacson and Rose, we have to expect non-localization of the energy losses. A rough estimate of the magnitude of this effect can be made as follows.

The average scattering in inelastic collisions is $\alpha = \Delta E/2E$. Putting $\Delta E = 2eV$ and $E = 50$ kV we find $\alpha = (2)(\omega^{-5})$. This small angle would allsmall angle would allow a resolution of $1/2\alpha\lambda = 25000x0.055Å = 1400Å = 0.14\mu m$. There are indications however that this rough estimate is highly inaccurate; taking the *average* scattering angle as a basis seems a very simple assumption. Therefore a resolution of less than 0.1 micron may very well be obtained, which would indeed carry medical microscopy quite a bit further in terms of resolution.

How to Carry Out the Experiment

(1) Make three sequential negatives, with electrons having suffered energy losses of 1.5 to 2.3 eV, 2.1 to 2.9 eV. and 2.7 to 3.5 eV respectively. If these negatives are illuminated by light of 0.65, 0.5 and 0.4 micrometers wavelength, the superimposed projected images will form a picture in real colors.

(2) The three images could be made simultaneously to reduce radiation damage, if the spectrometer is adapted to have three simultaneous channels. This will require a greater effort, however.

Finally I'd like to mention the method for obtaining electron loss images in a CTEM as proposed by Watanabe at the Philadelphia conference in 1962. As most high resolution spectrometers allow a large field of image in the non-dispersive direction, but only a small field in the dispersive direction, Watanabe put the entrance slit in the final screen, and scanned the entire image over this slit, while moving the photographic emulsion at a speed corresponding to the scanning speed. Thus he obtained a large number of very exciting results. However, the radiation dosage to the specimen in this method is enormous. It can be very much reduced by illuminating only the part of the specimen which corresponds to the slit. In doing so, the slit itself is no longer

necessary. In this way a most troublesome phenomenon can be avoided, namely the stripes in the final image, produced by the edge roughness of the slit.

Thinking this through, one finds that the illuminated line width can be many times the resolution of the microscope, provided the photographic emulsion travels with the same speed as the image points of the illuminated area of the specimen. In other words, the image field in this dispersion direction can be put to use. Simultaneous registration of the three colours is difficult.

Other Difficulties

The cross-section for electrons is much smaller than for photons. It means that radiation damage may cause a problem or even make the whole thing useless. Since we are talking of very low resolution (70 to 100 micrometers) and serious radiation damage usually starts a 3 to 30 electrons per sq. Å or 300 to 3000 electrons per pixel, we still have some 1.5 to $30x20^6$ electrons available for each image element. That might just be enough and perhaps we can afford greater damage than at high resolution. Finally there may be surface phenomena that ruin the whole idea.

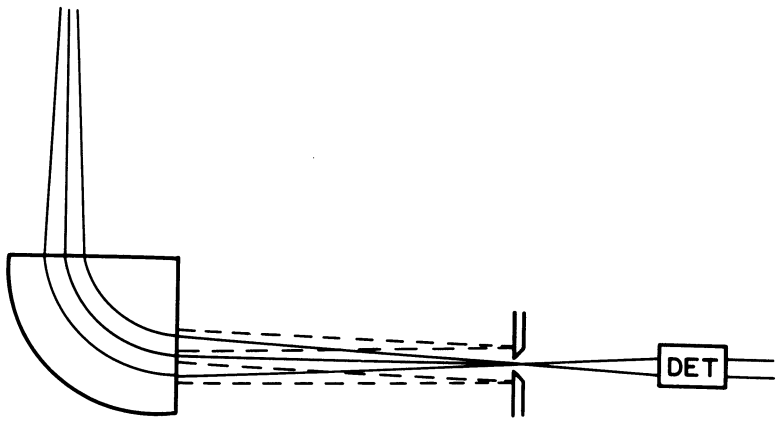

Fig. 1. Recording one color at the time.

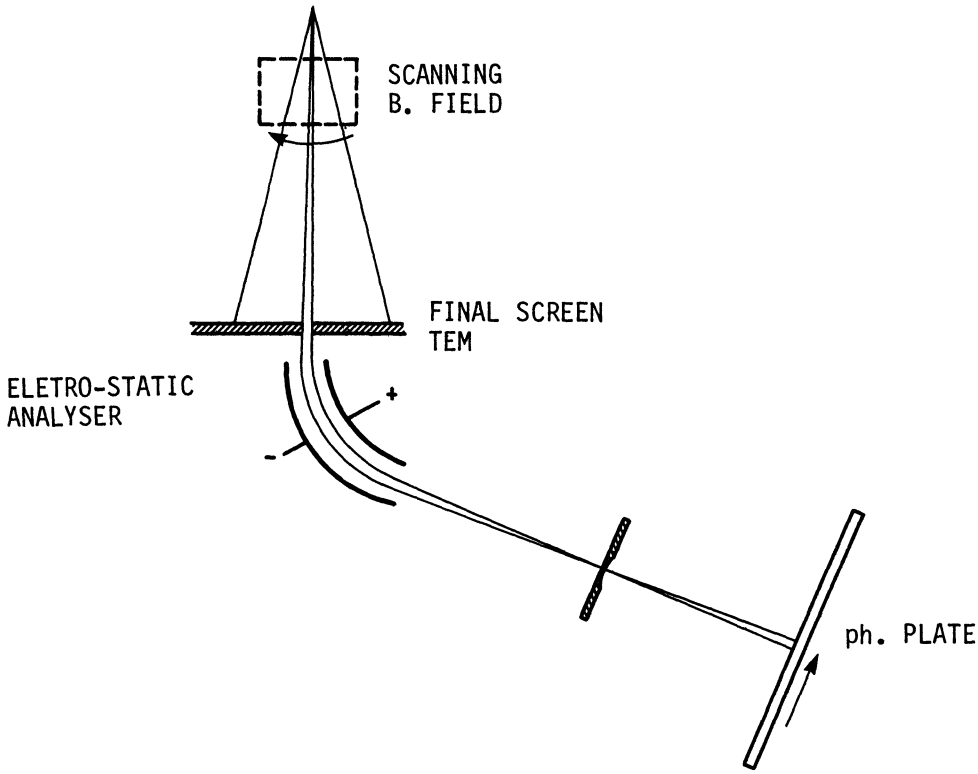

Fig. 2. Eletro-Static Analyser.

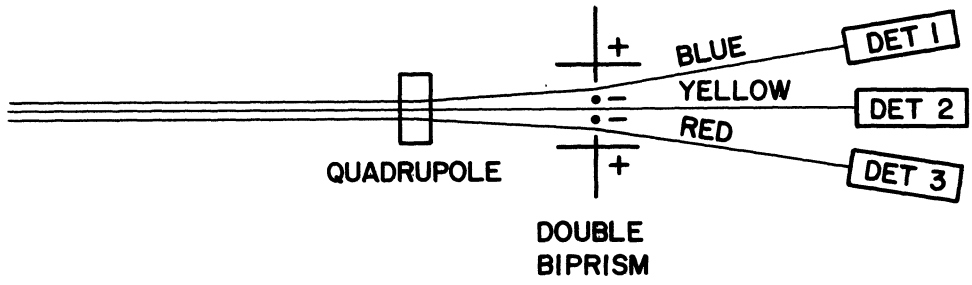

Fig. 3. Simultaneous recording of three colors.

SCATTERED ELECTRONS IN BIOLOGICAL STRUCTURE DETERMINATION

F. Peter Ottensmeyer

The Ontario Cancer Institute
500 Sherbourne Street
Toronto, Ontario, Canada
M4X 1K9

Of the various atomic particles or quanta of electromagnetic radiation available for probing the finestructure of biological objects, electrons have a particularly favourable place. The wavelength of the particle at an energy of 100 keV is about 0.0037 nm, offering the promise of high spatial resolution. Its cross-section of interaction with matter is sufficiently small to penetrate a specimen 100 nm thick with ease, but large enough to interact at least once in that thickness. In addition it can be focused by electrostatic and magnetic fields, permitting the construction of electron microscopes.

While ideal lenses that in resolution can approach the wavelength limit of the electron have not been produced, modern electron microscopes nevertheless have a resolving power between 0.2 and 0.3 nm. However, in images of biological specimens even this limit has not been achieved. The reasons for this lie in the interplay between the contrast necessary to see the object, the number of electrons necessary to detect the contrast in the presence of the natural fluctuations of counting statistics, and the fragility of the object under the stress of electron bombardment.

Under conventional, bright field imaging the primary concern has been the lack of contrast, caused by the fairly small absolute scattering cross-sections of the light atoms of biological matter. This has been overcome by the use of heavy metal contrast agents which permeate or coat the biological specimen, outlining or decorating its structure. This gain in contrast is accompanied by a stabilizing effect on the structure with the result that in general very little heed is paid to the necessity of minimizing

electron dose to spare the specimen. However, the price paid for stability and contrast is resolution. The biologically relevent detail observed is now no longer determined by the resolution of the microscope but by the size of the heavy metal contrast agent. Since metal ions used are at best slightly smaller than 1 nm the resolution of the image is limited to about 2 nm (1), almost a factor of ten worse than the microscope potential. Nevertheless, even this resolution, being over one hundred times better than that of light microscopy, has been primarily responsible for our present detailed knowledge of the fine structure of cells and subcellular organelles.

The quest for higher spatial resolution per force must obviate the use of heavy metals. This means a direct confrontation with the problem of contrast and of specimen fragility. Dark field electron microscopy has been developed by us and others to approach a solution to lack of contrast. This approach will be discussed below. Elsewhere, two techniques are under development to overcome the effect of radiation damage to the specimen. One uses the redundancy of information in crystalline specimens to reduce the electron dose to the specimen (2); the other attempts to immobilize radicals and fragments caused by electron bombardment by the use of specimen temperatures below 10°K (3,4). Both of these are compatible with the dark field approach.

One of the deleterious effects of the interaction of electrons and matter is the transfer of energy from the electron to the specimen, exciting molecules and atoms, producing radiation induced structural alterations, and resulting in blurring of the image due to chromatic aberrations. On the positive side, since this transfer of energy frequently is characteristic of the kind of atom or molecule in the specimen, the energy analysis of the strong signal of the transmitted electrons permits a chemical analysis of the specimen with sensitivities of detection of as few as 30 to 50 atoms and spatial resolutions in elemental mapping as good as 0.3 to 0.5 nm (5-7). This technique is one of the newest approaches to the analysis of the submicron world both in biology and materials science, and a very powerful approach indeed. The technique, dicussed later in this paper, is a natural outgrowth of the dark field approach.

Dark Field Electron Microscopy

Unstained biological specimens, composed of light atoms, scatter electrons relatively ineffectively. As a consequence bright field microscopy, which to a first approximation produces images by the elimination of electrons that are scattered by the specimen out of a limiting aperture, results in rather low contrast images. This contrast is enhanced somwhat by interference effects (phase contrast) between the few electrons that are still scattered

into the aperture and the unscattered beam. Since in either case the image information is contained in the scattered electrons, a technique that uses the scattered electrons only, dark field electron microscopy, can under the right conditions produce a vastly increased contrast in images of unstained specimens. However, successful imaging with scattered electrons is not easily achieved, requiring the simultaneous combination of several factors - specimen preparation, illumination, imaging conditions - each of which is substantially different from that in bright field electron microscopy.

Instrumental Conditions

Dark field conditions in electron microscopy can be produced in a number of ways, three of which are shown in Fig. 1. In every

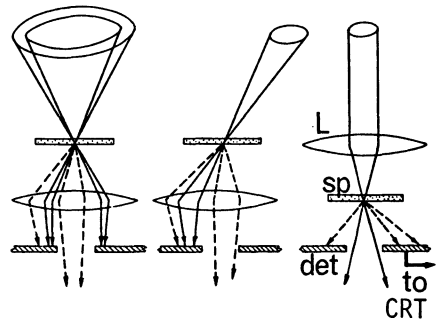

Fig. 1. Dark field operating conditions. (a) Hollow cone illumination. (b) Tilted beam illumination. (c) STEM operation. The region of the specimen "sp" is shown in relation to the objective lens "L", followed by the objective aperture. In STEM the aperture acts as an electron detector "det" from which the dignal is led to a cathode ray tube "CRT".

case the primary, undeflected electron beam is prevented from contributing to the image, producing a dark field image using only electrons that have been scattered by the specimen. Other methods, that produce dark field by moving the objective aperture off the optic axis or placing a beam stop in the aperture (8), in general deteriorate image resolution, since the region of the objective lens of the electron microscope is very sensitive to electrostratic and magnetic perturbations. Hollow cone illumination (Fig. la) and oblique illumination (Fig. lb, a one sided version of Fig. la) are more ideal and are still readily achieved in most modern fixed beam

electron microscopes. The method in Fig. 1c (9) deserves special attention, since it represents the most efficient collection and use of scattered electrons. Here the unscattered beam passes through an annular aperture, while the scattered electrons are captured on the aperture and processed electronically to produce an image on a cathode ray tube. This arrangement is possibly only in a scanning transmission electron microscope (STEM), in which a finely focused beam is swept in a raster pattern over the specimen.

Successful dark field imaging must also take into account that the dark field signal is only a small percentage of the total (bright field) beam signal. In the STEM this signal can be enhanced electronically. However, in the fixed beam microscope the signal must be increased in two ways: first, by increasing the illumination with the use of inordinately large condenser apertures concomitant with the reduction in the excitation of the first condenser lens; and second, by more efficient collection of the scattered electrons with as large an objective aperture as the resolution limit of the microscope permits (10). As an example for the Siemens Elmiskop 102 we use 600 μm and 60 μm apertures in the condenser and objective lenses repectively. For the Philips EM300 the values are 500 μm and 40 μm, while for the Jeol 200CX we have used 650 μm and 40 μm apertures for the two lenses. In each case the first condenser lens excitation was reduced to give a minimum spot size that just filled the viewing screen. The additional benefit is a reduction in coherence under these conditions, which otherwise would produce unwanted interference artefacts.

Finally, the exquisite fragility of the unstained biological specimen demands that every effort must be made to reduce the electron dose to a minimum. This includes the use of a suitable minimum exposure technique (11,12) in which the specimen is only illuminated while its image is recorded. It includes the efficient collection of electrons (large objective aperture; see above), a low magnification matched to the desired resolution, a fast recording film, and optimum development for speed and grain size.

Noise and Radiation Damage

Considering the modifications in modus operandi to achieve dark field images, is the effort warranted, particularly in light of statements which indicate that 30 to 80 times the radiation dose is needed compared to bright field imaging (13)? Since bright field and dark field imaging are complementary processes, should such a large factor in dose obtain?

Calculation indicates that it does not. Table I shows that under a typical set of conditions, greater contrast for equivalent or even better signal to noise conditions is achieved in dark field

using exactly the same dose. The starting point of the calculation is a carbon object 7.0 nm in height on a 3.0 nm carbon support, which in bright field produces a contrast of 5% (14) and in dark field a contrast of 70% (contrast = net signal/background + signal). The assumptions based on experimental measurement are:

1) that a signal-to-noise ratio of 5.0 was required (15)
2) that the STEM captures 50% of the scattered signal (16)
3) that tilted beam dark field in the fixed beam microscope is about 20% as efficient as the STEM in capturing scattered electrons, considering geometries and intensity distributions.

In the formula derived from Rose (17):

$$N = \frac{K^2(2+C)}{C^2}$$

where N is the number of electrons required to delineate a picture

Table 1

Signal Properties in Bright Field and Dark Field Conditions

	Background	Signal plus background	Net signal	Contrast	Combined noise	Signal to noise ratio
Bright field	19,500*	18,525	975	0.05	195	5.0
STEM dark field	209	696	488	0.70	30.1	16.2
Tilted beam dark field	41.8	139.4*	97.6	0.70	13.5	7.25

Background, signal and noise are given in numbers of electrons.
Preconditions: -- 7.0 nm carbon object on 3.0 nm carbon film producing a contrast of 0.05 in bright field.
-- Signal-to-ratio in bright field = 5.0.

* To record these electrons at an optical density of 1.0 on photographic film (1 e/μm^2) a pixel size of 140 μm is required in bright field, only 12 μm in dark field.

element with a contrast C and a signal-to-noise ratio K, the factor (2 + C) reflects the fluctuations both in the signal region and the background region. In the bright field case about 20,000 electrons are required to define an image element with 0.05 contrast almost independent of support thickness, at a signal-to-noise level of 5.0. Even though only 488 of these are scattered and detected by the dark field detector in the STEM, the resulting signal has a contrast of 0.70 (depending on support thickness) and a signal-to-noise ratio of 16.2. In the conventional TEM this signal-to-noise ratio drops to 7.25, comparable to the bright field case, but still at a contrast of 0.70. The telling difference is that the net signal at 97.6 electrons in tilted beam dark field is about 20 times smaller than the incoming beam at close to 20,000 electrons. On the surface this seems to indicate a twenty-fold difference in dose level. However, this is not the case, since the same exposure is required to detect the signal in both cases. To compensate for the difference during photographic recording of the signal, the magnification of the image must be changed by about a factor of ten between the techniques in order to capture the required number of electrons within the linear recording range of the film. Taking into account the minimum image element (pixel size) to record the maximum signal at an optical density of 1.0 (1 e/μm^2), the magnification for 0.5 nm pixels in dark field would be 24,000X, in bright field 280,000X.

Thus the magnification, matched to the image resolution requirement, is a crucial element in dose comparisons and minimization of radiation damage in dark field.

Energy Loss and Chromatic Aberration

The instrumental conditions mentioned above have so far only considered the gross quantitative aspects of electron scattering from a biological object. A further important aspect is the observation that for light atoms a large proportion of the electrons lose energy on being scattered. This transfer of energy to the specimen has three consequences. On the positive side it leaves an imprint of the chemical composition of the specimen in the energy spectrum of the electrons traversing the specimen. This will be used to advantage below. On the negative side, the energy transfer is the cause of specimen destruction and, due to chromatic aberrations of the lens, the electrons that have suffered an energy loss are no longer focused in the same plane, resulting in a superposition of blurred images on the sharp image produced by elastically scattered electrons. The thicker the specimen, the greater is the proportion of electrons scattered with an energy loss. With energy filtration, as described below, the sharp image can still be extracted even from a thick specimen; but with conventional microscopes the only recourse is to make the specimen exceedingly thin. An exception is the scanning transmission

Table 2

Proportion of Scattered Electrons for Different Thicknesses

Thickness *	Unscattered P(0)**	Singly scattered P(1)	Multiply scattered P(2+)	P(2+)/P(1)
3.00	0.050	0.149	0.801	5.362
2.00	0.135	0.271	0.594	2.195
1.26	0.284	0.357	0.359	1.004
1.00	0.368	0.368	0.264	0.718
0.50	0.607	0.303	0.090	0.297
0.30	0.741	0.222	0.037	0.166
0.10	0.905	0.090	0.005	0.052

* Thickness is measured in unit of mean free path.
** $P(n) = m^n e^{-m}/n!$, where "m" is the average thickness.

electron microscope which, because it has no lenses following the specimen, has no chromatic aberration.

Tissue Sections

For carbon atoms two out of every three scattered electrons suffer an energy loss (18). Since multiple scatter compounds this effect, it is imperative for dark field imaging to stay in a single scatter regime. Table 2 shows the proportion of electrons that are unscattered, singly scattered and scattered more than once for Poisson statistics depending on thickness "t" measured in units of mean free path. It is clear that for a thickness of one mean free path multiple scatter is as strong as single scatter. A relatively acceptable proportion is only reached for a thickness of 0.3, where multiple scatter is reduced to 17% of single scatter. The high proportion of unscattered electrons under these conditions is of no consequence, since it does not contribute information, nor produce radiation damage.

This is borne out in practice in unstained images of tissue sections (19). Images of thick sections are blurred and produce very little contrast. Only the thinnest sections, dark gray or transparent by interference colours and estimated to be about 30 nm thick, produce sharp images with excellent contrast. Since the

mean free path for carbon is about 90 nm at 100 kV, the best images are obtained experimentally for thicknesses of about 0.3 mean free paths or less.

Macromolecules

For macromolecules, which in general are naturally rather thin specimens, it is imperative that the support film on which they are held be very thin as well, to avoid not only a decrease in contrast related directly to the relative thickness of the specimen components, but also blurring from chromatic aberration that makes focusing and astigmatism adjustment of the microscope very difficult.

With such precautions in instrumental operation and specimen preparation it has been possible in several laboratories to obtain micrographs of individual atoms such as Br, I, Pd, Os, and U by dark field both in the STEM and in fixed beam transmission microscopes (20-23).

Biological macromolecules pose an additional degree of difficulty due to their fragility under electron bombardment during image recording. Nevertheless, reproducible detail, frequently as fine as 0.5 nm has been observed in numerous unstained molecules such as DNA (10,24), myokinase (25), protamine (25), valinomycin (26), vasopressin (27), parathormone (28), metallothionein (29), alphafetoprotein (30), glucagon, secretin, adrenocorticotrophic hormone (31) and many others. In the case of protamine and glucagon, the detail in the dark field image provided a sufficient geometric constraint, that, together with other physico-chemical data on these molecules, it was possible to construct three-dimensional models of their structure with atomic detail (32,33). For protamine this has been verified by the subsequent derivation of the structure by x-ray crystallography (34).

A further verification of the potential detail visible in dark field images was obtained on the basis of a challenge from Klug (35) that the 0.54 nm repeat should be visible in dark field images of protein alpha helices. Objective computer analysis of micrographs of the alpha helix of poly-L-lysine indicated that despite radiation damage and a very high structural noise level from the carbon support the 0.54 mm repeat was present in the Fourier transform, though visibly masked by other fine structural detail in the image itself (36). This additional detail was due to the rather large side chains of the lysine moieties. Moreover, this sidechain information was sufficiently preserved in the image to permit a computational tomographic reconstruction in which both the polypeptide backbone and the lysine side chain were visualized (37).

Energy Filtration

Scattering of electrons with a transfer of energy to the specimen has in general a deleterious effect on the specimen due to radiation damage, and on the image due to chromatic aberration. The chromatic effect can be eliminated by the use of a scanning transmission electron microscope with no post-specimen lenses, or by an imaging electron spectrometer incorporated in the fixed beam transmission electron microscope. The latter approach has been applied to dark field images of thicker specimens (38) using an imaging filter adapted from the work of Castaing and Henry (39), with very dramatic increases in contrast and in resolution. Moreover, even in bright field the effect of eliminating electrons that had suffered energy losses and that still contributed to the image, was a marked increase in contrast (38). Like systems have been built (40), while other devices have included a system of crossed electric and magnetic fields (41,42), as well as two all-magnetic imaging electron energy filters incorporating four and three sector magnets respectively (43,44). Scanning transmission electron microscopes are served similarly by the addition of a single magnetic sector spectrometer (45,46).

An imaging energy filter in a fixed beam electron microscope acts as a spectrometer in which the energy losses incurred by the electrons in exciting atoms and molecules at every point in the image are analysed in parallel. In general such an energy loss spectrum (Fig. 2) consists of a continuum of intensities which after a few low energy fluctuations decrease with increasing energy loss. Superposed on this decreasing intensity are stepwise increases that occur at characteristic ionization thresholds of electronic shells of the atoms constituting the specimen under the electron beam. Thus the atomic composition of a thin specimen can readily be determined, similar to the more common analyses of x-rays which are released by the excited atoms on relaxation.

Elemental maps can be produced by such a device with limits of detection as low as 30 to 50 atoms and spatial resolutions as good as 0.3 to 0.5 nm (5-7). Both of these attributes are about two orders of magnitude better than x-ray microanalysis, the next most sensitive technique.

A map of a specific atomic element is obtained by taking a minimum of two energy selected images, one at an energy above the chosen atomic ionization edge, which includes the characteristic signal superposed on a non-characteristic background, and another at an energy just below the ionization edge to obtain a measure of the background alone. The difference between the two images, suitably normalized to compensate for differences in exposure, is the quantitative spatial distribution of the chosen element.

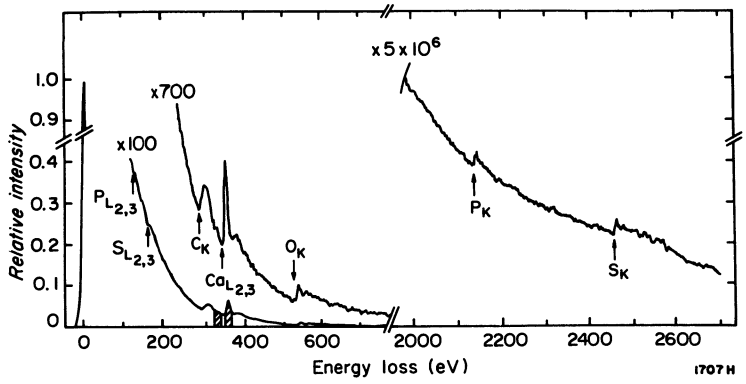

Fig. 2. Typical electron energy loss spectrum from a thin sample near a bone-forming cell. The hashed regions indicate two energy bands that would be used to obtain an elemental map of calcium.

The characteristics that can be expected from the technique are summarized in Table 3. However, a limitation is the requirement that for ease of interpretation of spectra, and even

Table 3

Specifications for Energy Loss Spectroscopy and Elemental Mapping

Spatial resolution	0.3 -0.5 nm	in image
Energy resolution	1 eV	1.5 mradian
	15 eV	15 mradian
Minimum detectible mass	1.5×10^{-21}g	in image
	(30 atoms P)	
Minimum mass fraction	0.5 -1.5 %	in spectrum
Detectible atoms	Z = 1 - 92	
Image points	1	spectrum
	512 x 512	digital evaluation
	5×10^7	photographic plate
Beam current	1 nA	STEM
	1000 nA	Fixed beam EM

more stringently for elemental mapping, only single scatter of the traversing electron must occur within the specimen. For multiple scattering the energy spectra of successive scatter events would fold over each other. Deconvolution of spectra is being attempted (47,48), but for elemental maps this process would have to be carried out at every image point, making quantification for thick specimens a virtual impossibility. Once again, referring to Table 2, this implies that the specimen thickness must be of the order of 0.3 mean free paths, or about 30 nm or less, just as in the dark field case.

Analysis and Structure

A particularly attractive feature for biological applications is the fact that even low Z atoms, e.g. B, C, N, O, F etc., have very strong signals. For ionization of a given inner electronic shell, such as the K-shell, this signal does decrease with increasing Z, but for atoms with larger atomic number the strong signal from higher shells (L-shell, M-shell, etc.) whose ionization occurs at lower energies of excitation, should be used instead, since their cross-sections are correspondingly larger.

The strong signal brings with it a high detection efficiency and high spatial resolution. Thus not only can the 300 P atoms in a single nucleosome, the substructure of the chromosome, be detected, but there is sufficient detail in the spatial distribution of this signal that it can be interpreted as the path of the DNA-phosphorus through the 10 nm particle (5,49). In fact knowledge of the path of the DNA by elemental mapping using this technique has led to the reconstruction of the complete protein-DNA complex that comprises the nucleosome (6). The spatial resolution of the technique therefore is so great that one need no longer stop merely at chemical analysis, but can incorporate and use the chemical information in high resolution structural analysis of macromolecular complexes.

A similar attempt is in the preliminary stages for the structure of the ribosome (50).

However, elemental mapping in tissue sections is also advanced orders of magnitude by the sensitivity and resolution of the technique. A case in point is the analysis of the earliest nucleation sites of mineralization in cartilage. Extrapolation from x-ray microanalysis of more advanced mineralization would argue that calcium even at the earliest stages is precipitated as a calcium phosphate. Elemental mapping by scattered electrons quite clearly indicated that this is not so, that calcium is initially intimately associated with a sulphur-containing macromolecule (51), and only later forms its well-known chemical liaison with phosphorus.

The applications of the technique, not having been fully explored, appear boundless. In addition to the work on the nucleosome, the ribosome and on cartilage mentioned above, elemental mapping by scattered electrons has been applied to bone (52), muscle (53), crustacean (54), plant (55), bacteria, marine microorganisms and numerous other specimens.

Certainly there are limitations. The dose that is required is of the order of a few Cb/cm^2. This is a low dose compared to doses used in x-ray microanalysis, but high with respect to damaging doses for structural integrity. In addition, in spite of the high energy resolution in the spectrum, some spectral overlap still occurs, such as the carbon K-edge and the potassium L-edge. Further interference is caused by the extended fine structure above one edge reaching into the region of a higher energy edge, such as occurs between the Si L-edge and the P L-edge. Two edges may be separable in the spectrum, but still cause difficulties in elemental mapping, because one may lie in the reference region of the other. This is the case with the uranium O-edge and the phosphorus L-edge.

Conclusion

The use of scattered electrons alone to produce dark field images in electron microscopy can bring with it increased contrast in micrographs of biological specimens with the concomitant potential of higher resolution. Higher dose levels compared to bright field microscopy are not necessary, if one considers and aims for equivalent signal-to-noise ratios. This is particularly true for the scanning transmission electron microscope.

Energy analysis of the scattered electrons extracts additional information from the beam, which permits chemical analysis. The signal extracted is still so strong that a spatial resolution of 0.3 to 0.5 nm has been obtained in elemental maps, and sensitivities of detection as good as 30 to 50 atoms have been measured. Both of these attributes are a factor of 100 better than x-ray microanalysis.

The major limitation for both dark field electron microscopy and for energy selected imaging is the requirement of a specimen so thin that only a single scatter event occurs on traverse of the specimen by electrons. Radiation damage is an inevitable consequence of the requirement of quantum statistics for high resolution imaging. It can be minimized at present by careful attention to technique and in future by imaging at very low specimen temperatures. Nevertheless, even with these limitations the use of scattered electrons offers one of the most powerful approaches to the structure of the submicron world.

Acknowledgements

I thank J. Robinson for her careful preparation of the manuscript. The work was supported by the Ontario Cancer Treatment and Research Foundation and grants from the National Cancer Institute of Canada and the Medical Research Council of Canada.

References

1. D.J. Misell, in Image Analysis, Enhancement and Interpretation, Vol. 7 of Practical Methods in Electron Microscopy. A.M. Glauert, Ed. (North Holland, Amsterdam, 1978), p. 91.
2. P.N.T. Unwin and R. Henderson. J. Mol. Biol. 94:425 (1975).
3. M.K. Lamvik, D.A. Kopf and J.D. Robertson, Nature 301:332 (1983).
4. J. Lepault, J. Dubochet, I. Dietrich, E. Knapek and E. Zeitler, J. Mol. Biol. 163:511 (1983).
5. D.P. Bazett-Jones and F.P. Ottensmeyer, Science 211:169 (1981).
6. G. Harauz and F.P. Ottensmeyer, Nucleosome reconstruction via phosphorus mapping. Science (in press).
7. K.M. Adamson-Sharpe and F.P. Ottensmeyer, J. Microsc.122:309 (1981).
8. G. Dupouy, F. Perrier and P. Verdier, J. de Microscopie 5:655 (1966).
9. A.V. Crewe, J. Wall, L.M. Welter, J. Appl. Phys. 39:5861 (1968).
10. F.P. Ottensmeyer, Annu. Rev. Biophys. Bioeng. 8:129 (1979).
11. R.C. Williams and H.W. Fischer, J. Mol. Biol. 52:121 (1970).
12. F.P. Ottensmeyer, R.F. Whiting, E.E. Schmidt, R.S. Clemens, J. Ultrastruct. Res. 52:193 (1975).
13. E. Carlemalm, Ch. Colliex and E. Kellenberger. Contrast formation in electron microscopy of biological material, in: "Advances in Electronics and Electrophysics", P.W. Hawkes, ed., Academic Press, New York, in press.
14. R.D. Heidenreich, "Fundamentals of Transmission Electron Microscopy, Interscience Publishers, New York, (1964), p.35.
15. A. Rose, "Vision: Human and Electronic", Plenum Press, New York (1973), p.14.
16. F.P. Ottensmeyer, D.P. Bazett-Jones, H.P. Rust, K. Weiss, F. Zemlin and A. Engel. Ultramicroscopy 3:191 (1978).
17. A. Rose, "Vision: Human and Electronic", Plenum Press, New York (1973), p.12.
18. R.F. Egerton. Phys. Stat. Sol. A37:663 (1976).
19. F.P. Ottensmeyer and M. Pear, J. Ultrastruct. Res. 51:253 (1975).

20. A.V. Crewe, J. Wall and J. Langmore. Science 168:1338 (1970).
21. R.M. Henkelman and F.P. Ottensmeyer. Proc. Natl. Acad. Sci. USA 68:3000 (1971).
22. H. Hashimoto, A. Kumao, K. Hino, H. Yatsumoto and A. Ono. Jpn. J. Appl. Phys. 10:1115 (1971).
23. D. Dorignac, M.E.C. Maclachlan and B. Jouffrey. Nature 264:533 (1976).
24. F.P. Ottensmeyer, Biophys. J. 9:1144 (1969).
25. F.P. Ottensmeyer, R.F. Whiting, E.E. Schmidt and R.S. Clements. J. Ultrastruct. Res. 52:193 (1975).
26. F.P. Ottensmeyer, D.P. Bazett-Jones, J. Hewitt, G.B. Price, Ultramicroscopy 3:303 (1978).
27. F.P. Ottensmeyer, J.W. Andrew, D.P. Bazett-Jones, A.S.K. Chan, J. Hewitt, J.Microsc.(Oxford) 109:259 (1977).
28. A.M. Fiskin, D.V. Cohn and G.S. Peterson. J. Biol. Chem. 252:8261 (1977).
29. A.M. Fiskin, G. Peterson and F.O. Brady. Ultramicroscopy 2:389 (1977).
30. A.J. Luft and F.L. Lorscheider, Biochemistry 2:5978 (1983).
31. A.P. Korn and F.P. Ottensmeyer, J.Ultrastruct.Res. 79:142 (1982).
32. F.P. Ottensmeyer, R.F. Whiting, A.P. Korn, Proc. Natl. Acad. Sci. USA 72:4953 (1975).
33. A.P. Korn and F.P. Ottensmeyer, J. Theoret. Biol. 105:403 (1983).
34. R.M. Warrant and S. Kim. Nature 271:130 (1978).
35. A. Klug. Direct Imaging of Atoms in Crystals and Molecules. Status and Prospects for Biological Sciences. Chemica Scripta 14:291 (1978-79).
36. D.W. Andrews and F.P. Ottensmeyer, Ultramicroscopy 9:337 (1982).
37. G. Harauz, D.W. Andrews and F.P. Ottensmeyer, Ultramicroscopy 12:59 (1983).
38. R.M. Henkelman and F.P. Ottensmeyer, J. Microscopy 102:79 (1974).
39. R. Castaing and L. Henry. C. R. Acad. Sci., Paris B255:76 (1962).
40. R.F. Egerton, J.G. Phillip, P.S. Turner and M.J. Whelan J. Phys. E 8:1033 (1975).
41. G.H. Curtis and J. Silcox. Rev. Sci. Inst. 42:630 (1971).
42. W.H.J. Andersen and J. Kramer. Proc. Fifth Europ. Cong. Electron Microsc., Institute of Physics, London (1977) p.146.
43. D. Krahl, K.H. Herrmann and W. Kunath. Electron optical experiments with a magnetic imaging filter, in: "Electron microscopy 1978" (Proc. 9th Intnl. Cong., J.M. Sturgess, ed., Microsc. Soc. Canada, Toronto) Vol 1, p.42.
44. G. Zanchi, J. Sevely and B. Jouffrey. J. Microsc. Spectrosc. Electron. 2:95 (1977).
45. A.V. Crewe, M. Isaacson and D. Johnson. Rev. Sci. Instrum 42:411 (1971).

46. R.F. Egerton. Ultramicroscopy 3:39 (1978).
47. R.D. Leapman and C.R. Swyt. A practical method for removing plural scattering from core edges in EELS. Proc. 39th Ann. Meet. Electron Microsc. Soc. America, G.W. Bailey, ed., Claitor's, Baton Rouge (1981), p. 196.
48. A.B. Roy, Proc. 39th Ann. Meet. Electron Microsc. Soc. America, G.W. Bailey, ed., Claitor's, Baton Rouge (1981), p.522.
49. D.P. Bazett-Jones and F.P. Ottensmeyer. DNA organization in nucleosomes. Can. J. Biochem. 60:364 (1982).
50. A.P. Korn, P. Spitnik-Elson, D. Elson and F.P. Ottensmeyer. Specific visualization of ribosomal RNA in the intact ribosome Eur. J. Biochem. 31:334 (1983).
51. A.L. Arsenault and F.P. Ottensmeyer. Proc. Natl. Acad. Sci. USA 80:1322 (1983).
52. A.L. Arsenault and F.P. Ottensmeyer. J. Cell Biol. 98:911 (1984).
53. H. Shuman, A.V. Somlyo and A.P. Somlyo. Electron energy-loss analysis in biology: application to muscle, and a parallel collection system. In: "Microprobe Analysis of Biological Systems", T.E. Hutchison and A.P. Somlyo, eds., Academic Press, New York (1981), p.273.
54. A.L. Arsenault, J.D. Castell and F.P. Ottensmeyer. Tissue and Cell 16:93 (1984).
55. F.P. Ottensmeyer. Science 215:416 (1982).

AN IMPROVED METHOD FOR HIGH CONTRAST PHASE ELECTRON MICROSCOPY

J. B. LePoole

Delft University of Technology

Delft, Holland

Ever since Scherzer published his theorem that rotationally symmetric lenses forming a real image without space charge or space currents show positive spherical aberration, efforts have been made to circumvent the limitations by leaving rotational symmetry or introducing space charges.

Neither of these have produced a better resolution than the conventional rotationally symmetric magnetic lens. In many conversations I had with Ernst Ruska, who agrees that his choice in 1931 had been a lucky one, he postulated the principle, that he expected no improvement of resolution by first messing up the image quality in any organized way by whatever means, and then try to produce an isotropic image of improved quality.

History has proved him right so far. There is, however, one means of improving resolution that I think deserves a try-out because it violates Ruska's principle only in the slightest possible way.

It has been known ever since the excellent book by Zworykin, Hillier, Vance, and Ramberg on electron optics appeared that electron mirrors have some qualities no other electron optical element possesses:

a) the spherical aberration can be of chosen sign;

MIRROR PHASE CONTRAST OBJECTIVE

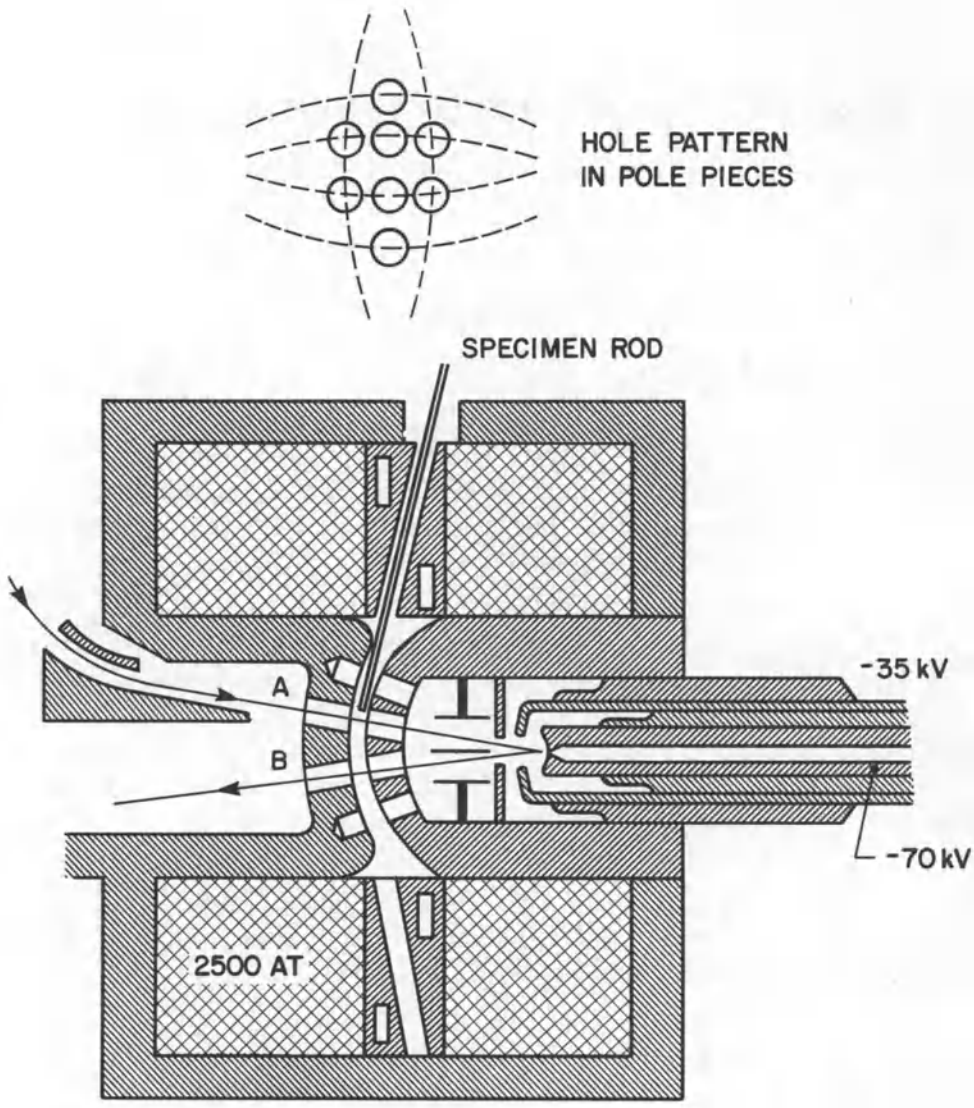

Figure 1

b) the chromatic aberration is negative in most cases.

We should be more attentive to what our light optical colleagues are doing. It has been known that optical mirrors have no chromatic aberration. Furthermore, since mirrors can be described as lenses with n = -1 (Bouwers) the factor n-1, describing many of the properties of optical lenses has a greater absolute value than any known optical glass (exception TiO_2 n = 2.6 and diamond n = 2.5). Thus aberrations are smaller. Hence the success of Bouwers' concentric optical mirror system.

Second rule of optical design: In a symmetrical system with M = -1 coma equals zero. Now coma is a difficult error to correct. It usually results from not correcting spherical aberration where it is first generated.

Conclusion

1. By choosing the proper shape of the reflecting surface, spherical aberration can be corrected.

2. By choosing an approximately M = -1 coma is corrected.

3. By using the smallest angle between incident and emerging principal ray, the astigmatism, being proportional to β^2 can be reduced to a minimum. We all know that astigmatism can be corrected by a simple quadrupole.

Summing up, we arrive at the following solution, which has not been tried yet; and only violates Ruska's principle in the slightest possible way. (See fig. 1). A specimen in the middle of magnetic lens (A) would be virtually imaged with a magnification of roughly 2x. The central ray (principal ray) would be reflected by the mirror on the axis of a second lens (B) energized by the same coil as lens (A). The lateral distance between (A) and (B) would have to be slightly larger than a microscope grid, say 4 mm. Assuming the principal plane of the mirror to be 30 mm away, this would lead to a half angle between axis and principal rays of .067 rad. and axial astigmatism could be estimated at $\frac{1}{2} \times (.067)^2 f 60 \mu m$. The magnification of 2 x would require correction of axial astigmatism by $\frac{60}{4} = 15 \mu m$ which is about an order of magnitude more than in conventional microscopes. Meanwhile, by proper de-

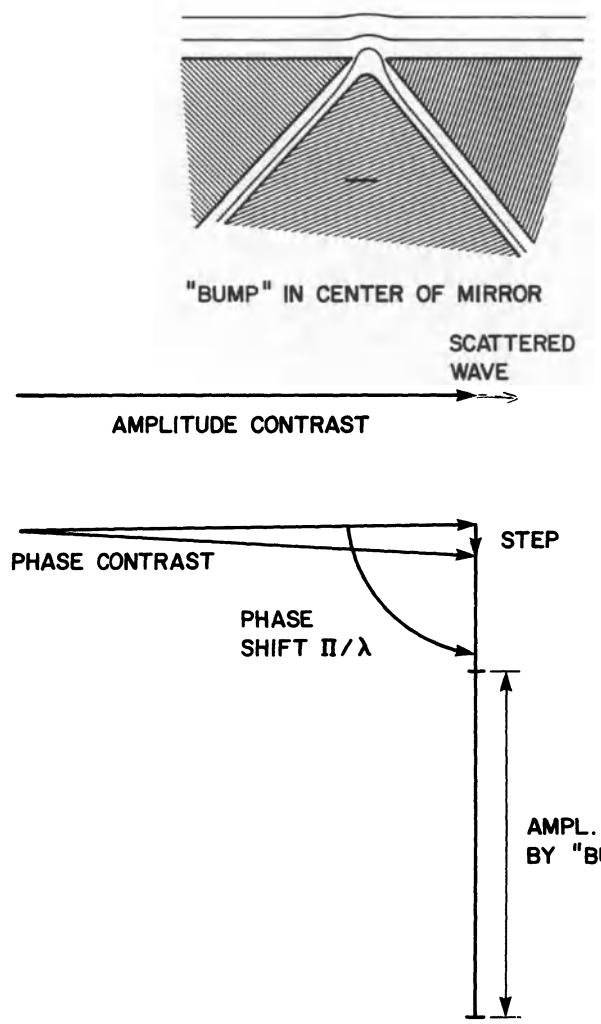

Figure 2

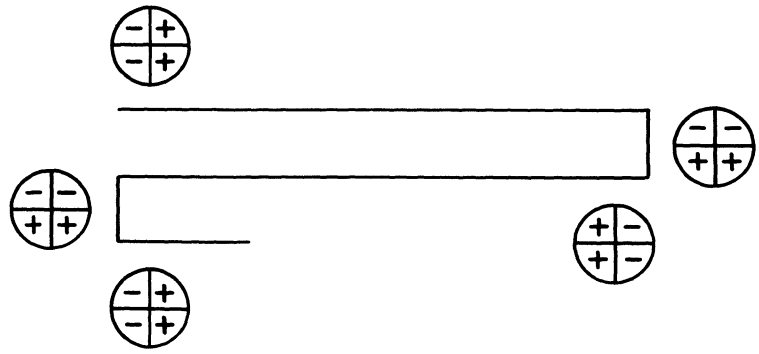

Figure 3

sign of the mirror C_S and C_C could be made < 0 to correct the entire system.

Now, what have we gained? Assuming all this can be carried out with sufficient accuracy of alignment, we would focus all electrons emerging from one point in the object into one point of the image! Result: a perfect image but no contrast! This surely is not what we're after! Now, let's turn our attention again to what our optical colleagues can teach us, especially Zernike.

He noticed that we are dealing with a phase object, and comparing that with an amplitude object there is one striking difference: A weak sinusoidal amplitude object, represented by a flat wave of sinusoidal varying amplitude would create a sharply focused diffraction pattern in the back focal plane of the objective. A weak sinusoisdal phase object would do the same, with the important difference, that the -1 and +1 order would be 90° phase shifted, compared to the amplitude object. If therefore we could arrange for a phase shift of 90° in the non-scattered zero-order wave, the image would be like that of an amplitude object. Furthermore, if the amplitude of the non-scattered wave could be reduced, the relative contrast would be greatly enhanced; in other words, the setup would be very sensitive to small phase differences.

Zernike reduced the non-scattered wave amplitude by absorption. In electron optics this would destroy coherence. Hence we have to use coherent scattering to reduce the amplitude of the non-scattered wave. By using the electron mirror, we can use a sharp point in the center to deform the reflecting V =0 plane (fig. 2). We would get a sharply curved equipotential plane, coherently scattering the wave, hence, reducing the local amplitude and arrive at Zernike's ideal condition that the non-scattered and a scattered wave have an amplitude of comparable magnitude. The great success of Zernike's phase contrast microscope was created not only by the 90° phase shift, but by carefully reducing the zero order wave to fulfill this condition. Since the same system can be varied to give amplitude contrast, a similar increase in contrast could be obtained.

Now let's turn our attention to the STEM. As we know that phase contrast needs a reference phase and only one element is irradiated at the time, it would seem that phase-contrast in a STEM cannot exist. We do, however, have the phase gradient contrast as proposed by

Dekkers and de Lang. It is produced by having a detector consisting of two semicircles, and registering the difference in signal of both detector-halves. Now could this phase-gradient signal be integrated? This seems less complicated than it really is. If we were to integrate along a normal scanning line we would lose the phase information going from the end of one line to the beginning of the next line.

However, since more and more scanning microscopes are provided with digital scanning, there is nothing to keep us from using the following scanning mode. Arriving at the end of a line, the scan should move to the next line, and return in the opposite direction. However, as the integration should always be in the direction of the movement, it would be necessary to turn the detector over 90° at the moment the spot moves to the next line, and again over 90° as the next line is scanned in opposite direction. This can easily be accomplished by having the circular detector consist of 4 segments to to be switched to change sign at the proper moment as follows in figure 3. The reference phase could then, in principle, be determined by the entire frame, by adjusting the integrator until the next scan starts at the same level. Contrast would be controlled as in any STEM. A comparison of amplitude and phase contrast shows that a factor of 40 can be gained by using the method described above.

ENERGY DEPOSITION BY X-RAYS AND ELECTRONS

Janos Kirz

Physics Department,
SUNY at Stony Brook,
Stony Brook, NY 11794

INTRODUCTION

The majority of the methods that form the subject of this Institute involve the use of electrons or soft X rays. It appears useful, therefore, to review the nature of the interaction of these particles with matter. Our discussion will not break new ground; in fact, it will remain rather elementary. A general bibliograpy for further study will be provided, however[1-10].

We will approach the subject from the point of view of the microscopist interested in the study of radiation sensitive biological specimens. It has been realized for some time .[11] that radiation damage limits the resolution attainable in the electon microscopy of such specimens. A detailed understanding of the damage mechanism still does not exist, but a great deal of work has been done to characterize it and to find ways to do microscopy with minimum damage. It is generally agreed that the damage under a given form of irradiation increases with radiation dose, defined as the amount of energy per unit mass absorbed by the specimen. This then focuses our attention to the nature of the energy deposition process.

We shall also comment on other aspects of the interaction which are relevant to the selection of specimen thickness and environment, and which determine the contrast.

ENERGY DEPOSITION BY SOFT X-RAYS

The dominant interaction of soft X rays with matter is the *photoelectric effect*. In this process the incident photon is absorbed by the target atom, and its entire energy is spent on liberating a bound electron. Part of the energy then is left in the form of a vacancy in the resulting ion, while the rest of it shows up as the kinetic energy of the liberated photoelectron.

The vacancy left in the atom is subsequently filled from a less strongly bound shell in the atom. At higher energies, this is frequently a radiative process, generating characteristic X-ray fluorescence. In the energy region of interest to us (100-1000 eV), however, fluorescence is rare, and the Auger process dominates. Here the same outer shell that provides the electron to fill the inner shell vacancy will also lose a second electron that carries off the excess energy. This Auger electron will therefore have a characteristic energy that only depends on the atom and on the two energy levels involved.

If the atom is very close to the surface of the specimen, the photoelectron and the Auger electron both have a chance to escape. Microscopes have been built that make use of these secondary particles for surface-sensitive imaging, (although the majority of instruments now in use involve probes other than soft X rays[12]). If the atom is not near the surface, however, the secondary electrons inevitably lose their energies in collisions with other atoms, so the entire initial photon energy ends up being deposited in the specimen. The range of these low energy secondaries is typically less than 30 nm, so the energy is localized in a small volume.

Based on the work of Durup and Platzman[13], it was widely believed that the most damaging aspect of the interaction is the "Coulomb explosion" of the molecule that contained the atom which was photoionized. The argument to support this view is a very simple and appealing one: after the Auger process, the atom is left doubly ionized. The two vacancies then repel each other, migrating apart, grabbing electrons from adjacent atoms in the molecule. Eventually the molecule breaks up into two singly charged radicals, which in turn repell each other and will never recombine. In fact, work on molecules in the gas phase, and at higher energies shows dramatic evidence of molecules exploding following inner shell vacancy formation[14]. It was widely expected that this evidence could be extrapolated to the use of X rays too soft to cause inner shell vacancies, leading one to conclude that these soft X rays would cause less radiation damage. In fact it was a considerable surprise when Goodhead and his group[15] showed that, on an equal dose basis, these very soft X rays are

more damaging than the harder ones, (which are capable of generating the Auger process).

The mean free path of soft X rays in matter depends strongly on the photon energy and on the elements present in the target. The elemental sensitivity depends on the sharp discontinuities where the photon energy crosses the ionization threshold of a given shell in the atom. At these so-called absorption edges the cross section changes by about an order of magnitude (see Figure 1). Between edges the mean free path varies roughly as the cube of the photon energy. Given a specimen of a certain thickness, it is then possible to choose the X-ray energy that will match the mean free path to the thickness. This will often lead to optimal conditions for imaging.

Given the number of X-ray photons incident on the specimen, N_o, the number absorbed, N, is given by

$$N = N_0(1 - \exp(-\mu\rho t))$$

where μ is the mass absorption coefficient, ρ is the density, and t is the specimen thickness. The mass absorption coefficient is $\mu = n\sigma/\rho$, where σ is the photoelectric cross section, and n is the number of atoms per unit volume.

We should point out that if the specimen is thin enough to transmit most of the radiation incident upon it, then the energy deposition is roughly uniform throughout (more highly absorbing clusters receiving larger doses, transparent regions less). If the specimen is thick or absorbing enough to attenuate the beam significantly, then the side of the specimen facing the incident beam receives a higher dose than the exit side. The extreme situation is that of the bulk specimen that absorbs all.

Most forms of soft X-ray microscopy use variations in the absorptivity of the specimen for generating contrast in the image. These variations may be due to differences in density, elemental composition, or thickness. To keep the radiation dose to the specimen as small as possible, one needs to maximize the information in the image generated by recording the fraction of the incident photons transmitted as a function of position[9]. The optimal situation is found when the wavelength and specimen thickness are matched in such a way that on the average about half the incident photons are transmitted.

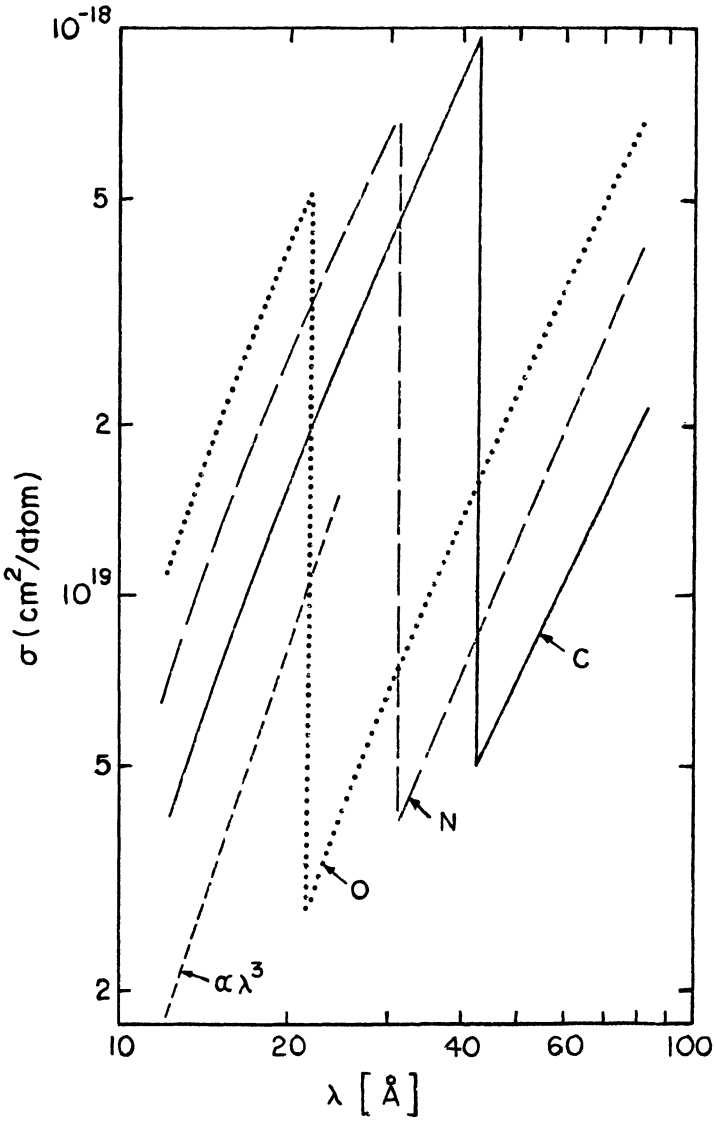

Figure 1. Absorption cross section for carbon, nitrogen and oxygen in the soft X-ray region, based on Ref. 3. The dashed curve indicates the slope corresponding to a cubic wavelength dependence.

ENERGY DEPOSITION BY ELECTRONS

Most electron microscopes and related instruments use electrons with energies in the 20 - 200 keV range to form the image. The interaction of these electrons with the specimen is a great deal more complex than that of soft X-rays. The X-ray photon carries a modest amount of energy which it either deposits in the specimen in its entirety or not at all. The electron, by contrast, enters the specimen with a great deal of energy, of which it leaves behind a varying, but generally small fraction.

A large fraction of the interactions of the incident electron with the atoms in the specimen are elastic collisions, in which very little energy is transferred, and which is most often used for image formation. Another, comparable fraction of the interactions is inelastic, involving significant energy loss by the incident electron. (We ignore bremsstrahlung, since it is responsible for only a small fraction of the energy deposited in the specimen.) The energy loss spectrum contains a great deal of information about the specimen, and electron energy loss spectroscopy (EELS) has been used effectively for mapping light elements in thin specimens, and for a variety of other studies. Elemental sensitivity depends on the fact that a significant fraction of the inelastic collisions lead to inner shell ionization of atoms in the specimen, with cross sections which peak at energy loss values just above the ionization threshold (Fig.2). In less frequent occasions the electron will lose a large fraction of its energy to an electron in the specimen which then acquires enough energy to undergo collisions also, and eventually even leave the specimen.

It is convenient to characterize the interactions of the electrons in terms of a mean free path, a quantity that is inversely proportional to the cross section. The inelastic mean free path characterizes the probable spacing between inelastic collisions. Fig. 3 shows the typical energy dependence of this quantity. We see that as the energy increases to a few hundred keV, the inelastic mean free path grows to a maximum value of about 2000 Å in a specimen of unit density. Further increase in beam energy has little effect on this quantity. The energy dependence of the elastic mean free path follows much the same pattern.

Electron microscopy and EELS are best performed when the specimen thickness is less than or comparable to the mean free path. Under these circumstances if an incident electron has undergone an interaction in the specimen at all, it has most likely undergone only one interaction, and if the interaction was inelastic, the energy deposited in the specimen is on the average about 30-40 eV. If the specimen is thicker, the odds are that the electron will

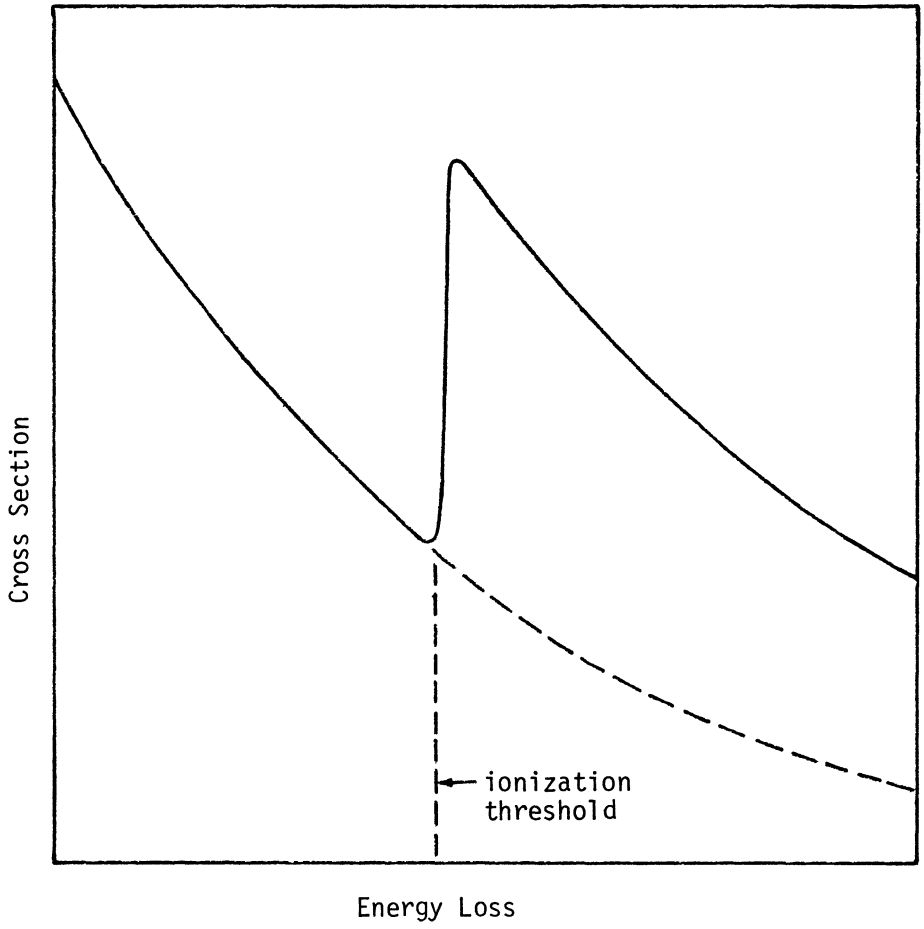

Figure 2. Typical electron energy loss spectrum near an inner ionization threshold.

undergo multiple interactions. The energy deposited in the specimen increases roughly in proportion to the number of interactions, while the information gained does not. In fact, multiple interactions typically *reduce* the amount of useful information the emerging electron carries. Contrast is most often generated by variations in the elastic scattering cross section. Since this quantity increases rapidly with increasing atomic number, heavy metal stains are commonly used to enhance contrast in the image.

Since the inelastic mean free path is at most 2000 Å, specimens for electron microscopy should be no thicker than this value for keeping the information to radiation dose ratio favorable. Radiation resistant specimens can be thicker, especially if a high voltage instrument is used. Nevertheless, thick specimens cause a variety of difficulties associated with loss of resolution and contrast due to multiple scattering.

If the specimen is very thick, the electron eventually loses all its energy and stops. The stopping distance, or range, is also shown as a fuction of energy in Fig. 3.

THE RADIATION DOSE

Radiation dose is defined as the energy deposited per unit specimen mass. In the case of soft X-rays the dose is given by

$$D = N_0E(1 - \exp(-\mu\rho t))/(\rho At)$$

where E is the energy of the X-ray photon, and A is the specimen area upon which N photons are incident. In practical units,

$$D(\text{rads}) < 1.610^{-14}\Phi E(\text{eV})\mu(\text{cm}^2/\text{g})$$

where Φ is the flux N_0/A in photons/cm^2, and we neglected the exponential attenuation factor.

In case of electron irradiation the incident flux is generally specified in terms of the current density, J. In that case the radiation dose to the specimen is

$$D = \frac{J\tau}{e}\,\frac{1}{\rho}\,\frac{dE}{dx}$$

where τ is the exposure time, and $\frac{1}{\rho}\frac{dE}{dx}$ is the stopping power. In practical units, where $J\tau$ is in Coulombs/cm^2, and $\frac{1}{\rho}\frac{dE}{dx}$ is in eV cm^2/g,

$$D(\text{rads}) = 10^6(J\tau)\frac{1}{\rho}\frac{dE}{dx}$$

While one generally tries to minimize the dose delivered to radiation sensitive specimens, there exist situations when in fact one wishes to *maximize* the dose. This is the case in particular in lithography and in contact microscopy. Typically a polymer needs to be damaged in the exposed areas to a point where it is easily dissolved in an appropriate solvent. Typical doses necessary are in the range of 1000 joules/gram, or 10^6 rads.

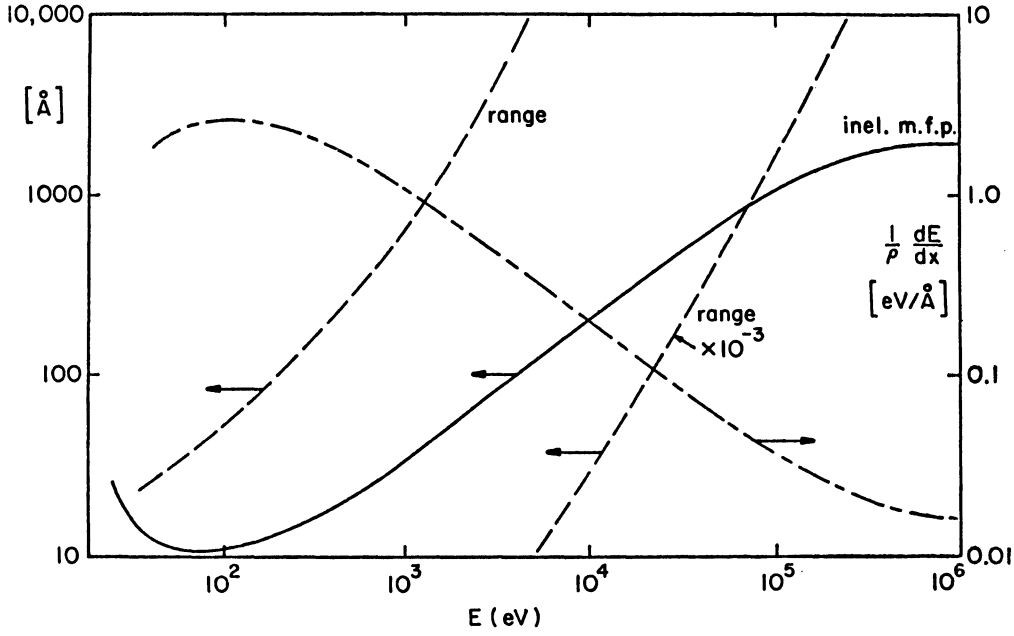

Figure 3. Inelastic mean free path (solid), range (dashed), and stopping power (dot dashed) for electrons, based on Refs. 6 and 7.

REFERENCES

Interactions of X rays with matter

1. H. A. Compton and S. K. Allison, X Rays in Theory and Experiment, Van Nostrand, New York, (1935).

2. N. A. Dyson, X Rays in Atomic and Nuclear Physics (Longman, London, (1973).

3. B. L. Henke, P. Lee, T. J. Tanaka, R. L. Shimabukuro, and B. K. Fujikawa, *Atomic Data and Nuclear Data Tables* 27, 1 (1982).

Interaction of electrons with matter

4. N. F. Mott and H. S. W. Massey, The Theory of Atomic Collisions (Clarendon, Oxford, 1965).

5. M. S. Isaacson, Specimen Damage in the Electron Microscope, in Principles and Techniques of Electron Microscopy, Vol. 7 (M. A. Hayat, ed.), (Van Nostrand Reinhold, New York, 1976). p. 1

6. A. Cole, *Radiation Res.* 38, 7, (1969).

7. J. C. Ashley, IEEE Trans. Nucl. Sci. NS-27, 1454 (1980), *Radiation Res.* 90, 433 (1982).

Comparisons of X-ray and electron beams

8. M. Isaacson and M. Utlaut, *Optik* 50, 213 (1978).

9. D. Sayre, J. Kirz, R. Feder, D. M. Kim, and E. Spiller, *Ultramicroscopy* 2, 337 (1977).

10. J. Kirz, Scanning Electron Microscopy 1980, Vol. 2, p. 239

11. For detailed reviews see Ref. 5 and V. E. Cosslett, *J. Microsc.* 113, 113 (1978).

12. See for example the lectures by R. Caudano at this Institute.

13. J. Durup and P. L. Platzman, *Int. J. Radiat. Phys. and Chem.* 7, 121 (1975).

14. T. A. Carlson and R. M. White, *J. Chem. Phys.* 48, 5191 (1968).

15. D. T. Goodhead, *Radiation Res.* 91, 45 (1982).

SYNCHROTRON RADIATION AND THE SUBMICRON WORLD: SELECTED ACTIVITIES AT THE DARESBURY LABORATORY, UK

P.J. Duke

SERC Daresbury Laboratory
Daresbury
Warrington, WA4 4AD, UK

1. INTRODUCTION

The last few years has seen a massive development of synchrotron radiation (SR) sources for the study of the sub-micron world with the consequence that the use of SR has become an accepted technique for the study of macromolcules such as proteins, partially ordered materials such as muscles and polymers, and other materials in both crystalline and amorphous forms. This review outlines the principles of SR production and indicates how SR is being applied to a variety of x-ray imaging problems. This theme is illustrated by references to the SR source (SRS) at the Daresbury Laboratory.

2. THE SYNCHROTRON RADIATION SOURCE

2.1 Production of Synchrotron Radiation

Electromagnetic radiation is produced whenever electrons are accelerated. In particular electrons moving in a curved trajectory under the influence of a magnetic field emit radiation by virtue of their acceleration in a direction which, for circular motion, is normal to the velocity vector of the electron. This is illustrated in Fig.1 which shows how the almost isotropic radiation emission from slowly moving electrons is converted into a forward going cone of opening angle $\sim 1/\gamma$ radians when the electron is travelling at a speed close to that of light. Here γ is the relativistic factor given by

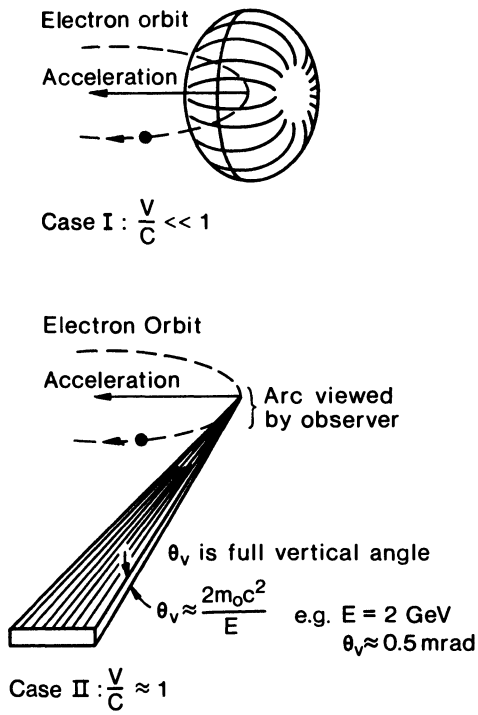

Fig.1. Radiation emission pattern by electrons in circular motion. Case I v/c << 1. Case II v/c ≃ 1.

$$\gamma = \frac{E}{m_o c^2} = \frac{1}{\sqrt{1-\beta^2}} \qquad (1)$$

where E is the total energy, $m_o c^2$ is the rest energy of the electron (0.511 MeV) and β is the ratio of the velocity of the electron to the velocity of light. The spectrum of the emitted radiation for an electron trajectory of radius R can be characteristed by a quantity λ_c given by

$$\lambda_c = \frac{4}{3} \pi \frac{R}{\gamma^3} \qquad (2)$$

The characteristics of the SRS are given in Table 1, and the intensity of the radiation as a function of wavelength is given in Fig.2.

Table 1: SRS Main Parameters

Beam Energy	2.0 GeV	
Electron Current	100 - 300 mA	
Beam Lifetime	8 - 10 hrs or greater	
Beam Dimensions	Present Lattice	High Brightness Lattice
from	4.8 × 1.2 mm^2	1.8 × 0.3 mm^2
to	12.9 × 0.6 mm^2	2.8 × 0.4 mm^2
Characteristic Wavelength	3.9 Å from bending magnets (1.2 T)	
	0.9 Å from wiggler magnet (5.0 T)	

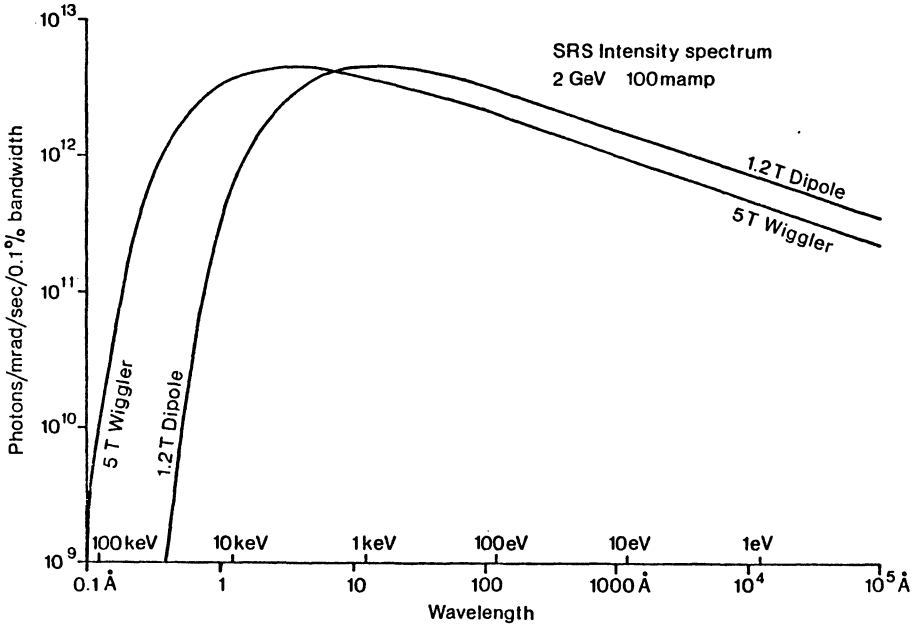

Fig.2. Synchrotron radiation spectrum from the SRS when operating at an electron energy of 2 GeV with 100 mA of stored electron current. Spectra are shown from the standard dipole magnets with 1.2 T magnetic field and from the 5 T superconducting wiggler magnet.

The radiation emitted by the electrons is polarized in the plane containing the electron orbit. This polarization is very pronounced at wavelengths $\lesssim \lambda_c$ and is an important feature of the radiation which contrasts sharply with the unpolarised nature of the radiation from all other sources particularly in the x-ray region. As would be expected the vertically polarised component is zero in the forward direction so that a sim-

ple Gaussian approximation to the angular distribution of the radiation is valid only for the horizontally polarised component. This approximation is given by

$$\sigma = \frac{0.57}{\gamma} \left(\frac{\lambda}{\lambda_c}\right)^{0.43} \text{ radians} \qquad (3)$$

where σ is the standard deviation of the Gaussian distribution. A comprehensive treatment of the production and properties of SR is given by Krinsky (1983).

2.2 Brightness of SR Sources

The properties of SR considered so far depend only on the gross features of the electron storage ring which is used as the radiation source. The photon intensity emitted into a horizontal angular interval as defined for example by a horizontal collimator and integrated over the total vertical angular interval (which is in general very small - typically a fraction of a milliradian) is defined entirely by λ_c which determines the position of the peak of the emission spectrum and by the number of stored electrons. The latter is related to the stored electron current by equation (4).

$$2\pi R_{av} i = N e \beta c \qquad (4)$$

where R_{av} is the mean orbit radius (total circumference/2π), N is the number of circulating electrons and e the electronic charge.

It follows from this that the photon intensity does not change much from one storage ring to another and only at the high energy end of the spectrum ($\lambda < \lambda_c$) is there a marked difference between sources. This is illustrated in Fig.1 which compares the intensity from the dipole magnets of the SRS with the intensity derived from a 5 Tesla superconducting wiggler magnet. The spectra are almost the same except for wavelengths less than λ_c for the dipole magnets. The wiggler source emits $\sim$ 10 $\times$ more photons in the region of 1 Å and the difference is even more marked at wavelengths shorter than this.

This approximate equivalence of sources is no longer the case when the spectral brilliance (sometimes called brightness and defined as photon/(mm^2.mrad^2.sec) into unit fractional band pass) is considered. For many experiments this is the parameter which defines the usefulness of the source and which can be strongly source dependent since it depends on the electron beam size and divergence at the SR production point. It is this quantity which is preserved in any optical system and even for

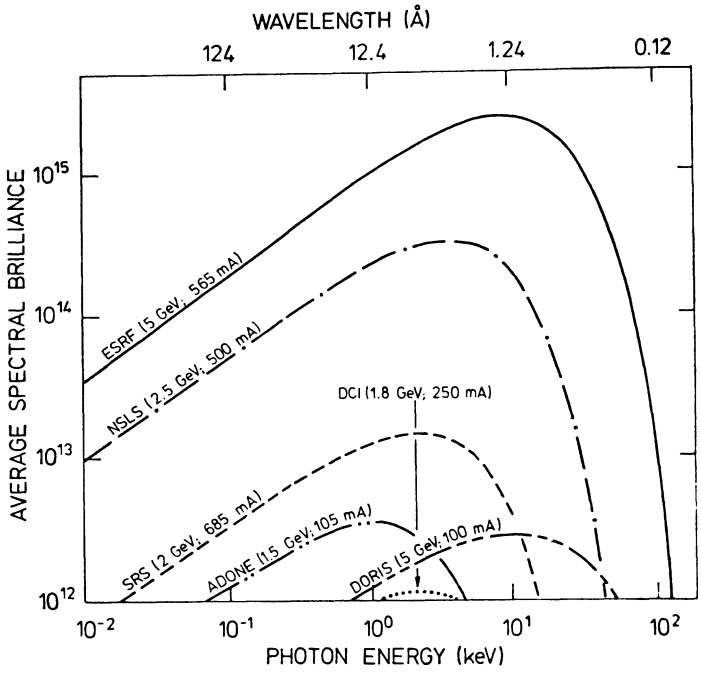

Fig.3. Average spectral brilliance (photons/mrad^2.mm^2.sec)) into 0.1% band pass for various synchrotron radiation sources. This figure is illustrative only and does not necessarily reflect present-day performance or projected performance figures.

direct illumination without any intervening active optical elements the number of photons reaching a sample in unit time will be greater the brighter the source provided that the sample is smaller than the extent of the photon beam at that point. In Fig.3 a comparison is made between the spectral brilliance curves for a number of electron storage rings, both proposed and in existence (Farge and Duke, 1979). It must be noted that the brilliance, by definition, takes into account the electron beam dimensions in both the horizontal and vertical direction (σ_y,σ_z) and the vertical beam divergence ($\sigma_{z'}$). The latter is combined with the photon divergence σ_γ from equation (3) to give an effective divergence

$$\sigma_{z'} = \sqrt{\sigma_{z'} + \sigma_\gamma} \qquad (5)$$

which is in general dominated by σ_γ at long wavelengths and by $\sigma_{z'}$ only for $\lambda << \lambda_c$. The new generation of electron storage

rings have been designed to maximize the photon brightness as far as possible.

2.3 The Source from the User Point of View

The average user of SR is not so much concerned about the complex equipment behind the concrete wall which separates the experimental area from the storage ring itself. What the user is aware of is that the source of radiation can easily become a master rather than a servant and the enthusiastic experimenter can be confronted by frustrating periods of down time just at the moment when the measurements are on the verge of success. Even if the source is operating normally the user is nevertheless aware of the need for regular refills of the storage ring, which interrupt the progress of the experiment, and the regular exponential decline of the photon flux as a function of time during the data collection period. Long beam lifetimes of eight hours or more are almost essential to reduce the number of refills, to avoid too great a variation in heat load on beam line optical elements and eliminate rapid changes in data rates at detectors. Nevertheless, judging by the increasing number of users of SR and the quality of the work they are producing, the scientific advantages outweigh the irritations and difficulties. In the next section some of the work carried out at the Daresbury SRS, relevant to the theme of this school will be described.

3. X-RAY IMAGING

3.1 Introduction

The term x-ray imaging can be interpreted in a variety of ways. At its simplest level it can be thought of as providing a direct visual image of the layout of the constituents of a material (atoms, molecules, molecular aggregates) at the submicron level. However the idea of imaging can be extended to indirect imaging in which a series of quite complex operations need to be performed on the raw data before a recognizable image is formed. An example of the first is x-ray microscopy or microradiography and of the second is crystallography. The latter does indeed provide an image of the internal layout of the material but the image is formed in an abstract reciprocal space which must be transformed into real space to obtain a useful image.

In principle all of the x-rays transmitted by or reflected from an amorphous or crystalline structure contain imaging information, i.e. contrast imposed on the outgoing beam by fluctuations in the sample. For example, density fluctuations in

the sample will modify the intensity distribution of the transmitted photon beam. Departures from perfection in the crystal lattice structure will modify the intensity distribution in the Bragg and Laue diffracted beam. Changes in the chemical constituents of the material will modulate both the inelastic and transmitted photon beams. Unfortunately these processes will also modulate the phase of the outgoing radiation. Such changes are hard to detect experimentally.

Resolution and contrast are two essential parameters for any system of imaging. Spatial resolution is limited by the optical system (in the broadest sense), by the detector and ultimately by the wavelength of the radiation. Contrast is limited by the signal/background ratio induced by the feature under examination.

The high intrinsic brightness of the SR source offers many advantages over other sources for x-ray imaging. Such advantages include the illumination of small samples and/or small surface or volume elements, improvement of the signal/background ratio to achieve contrast for features close to the resolution limit and enabling trade-off between intensity, short time slices and/or narrow wavelength band-pass. The latter is important for investigations needing difference imaging across absorption edges. The high frequency repetitive time structure has been used to provide x-ray strobe pulses to reveal the presence of time-dependent contrast and to "freeze" crystal phenomena on a microscopical scale.

3.2 Topography

Fig.4 shows the Laue diffraction pattern from a single crystal of beryl (Herres and Lang, 1983) taken using the"white" radiation topography camera (Bowen, Davies et al., 1981, 1982b). Each set of planes in the crystal lattice projects an image of the crystal onto the detector which in this case was Ilford L4 Nuclear Emulsion. Each individual image is formed at an angle $\theta_{hk\ell}$ to the incident beam direction given by the Bragg condition $2d_{hk\ell}\sin\theta_{hk\ell} = n\lambda$, where λ is the x-ray wavelength which satisfies the condition for an image generating combination of θ and d. The relative intensity of the image depends on the structure factor for that particular reflection and on the x-ray intensity at that particular wavelength.

Careful examination shows that in general each image contains structure which is directly related to the small mis-orientations and defects in the regular array of lattice planes. This method of studying the micro-structure of crystalline materials has been available for many years. The advantage of SR in this instance is not merely that the high intensity leads

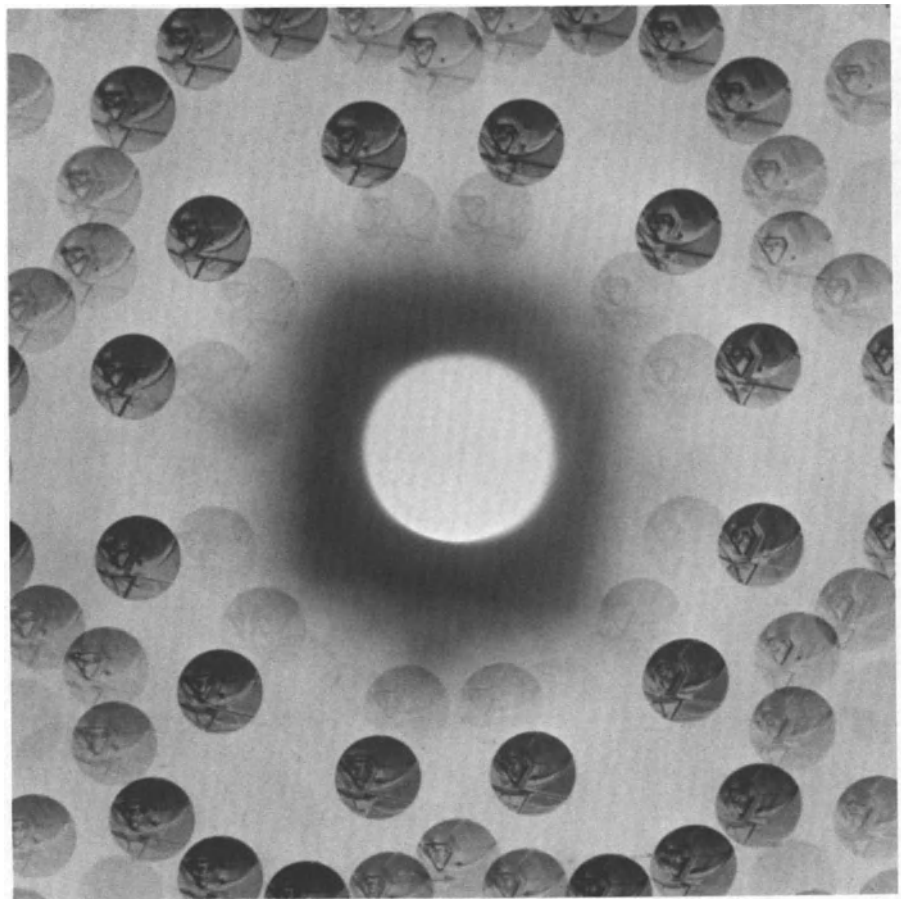

Fig.4. Synchrotron radiation Laue topographs of a beryl crystal. (Herres and Lang, 1983). Reproduced by courtesy of the H.H. Wills Physics Laboratory, Bristol, UK.

to shorter exposure times (minutes or seconds instead of hours) but also that the availability of broad band radiation means that the setting-up time is greatly reduced. In addition the high natural collimation of the radiation means that the sample-detector distance can be quite large without significant degradation of resolution, thus making it possible to study samples in non-standard environments (high pressure, high or low temperature, magnetic field, hostile chemical environments, etc.) without the need to operate the detector in the immediate neighbourhood of the crystal.

A whole range of examples of diffraction imaging of crystal lattice structure has been reviewed in the Proceedings of a recent Daresbury Study Weekend (Bowen 1982a). One particularly interesting example is the imaging of surface accoustic waves (SAW) travelling across a lithium niobate crystal (Whatmore, Goddard et al., 1982). In this measurement the SAW device, illuminated by the pulsed x-radiation from the SRS, was excited in time with the arrival of the x-ray pulses. The x-ray topograph shown in Fig.5 shows not only the layout of the surface waves but also hitherto unknown interactions of the surface waves with the crystal lattice structure in the first few Ångströms of the crystal surface.

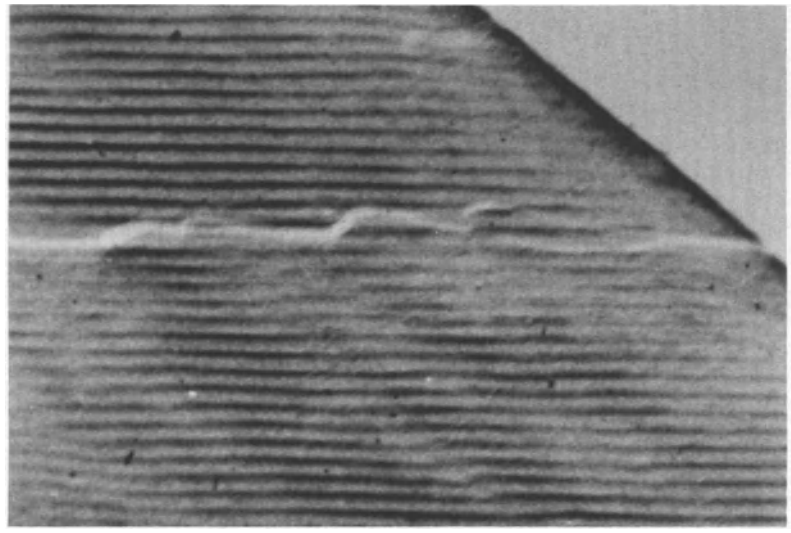

Fig.5. Stroboscopic x-ray topograph of travelling Rayleigh waves taken with the driving signal phase locked to the pulsed synchrotron radiation emission.

Similar work but studying the propagation of both bulk and SAW waves has been carried out at the Hasylab SR centre at Hamburg, W. Germany (Gluer, Graeff et al., 1982; Cerra and Graeff, 1983). The x-ray stroboscopic topograph promises to provide a tool for the study of the dynamic behaviour of crystals with implications not only for materials science but also for crystalline materials of biological interest.

3.2 Protein Crystallography

The use of SR for the crystallographic study of proteins and other biologically interesting materials is increasing at a very rapid rate. In the UK all the protein crystallography

groups now have major programmes at the SRS. Radiation damage, which might have been thought to be a serious problem, has turned out quite differently to what might have been expected. Crystallographic data obtained with SR is of much higher quality than that obtained from conventional sources and extends to higher resolution. Because of the higher brightness of the radiation at the sample (several hundred times that from a rotating anode source) data can be collected before the effects of damage induced by the radiation become apparent. The high intensity of the radiation means that reflections out to larger angles can be recorded, thus improving the spatial resolution of the analysed data. A particular difficulty in protein crystallographic work is the growth of crystals. The rate of data collection depends on the volume of crystal available. Reference to Fig.1 shows that very intense fluxes of x-radiation at around 1 Å or less are available from the SRS wiggler magnet. The crystallography station using a beam line from this magnet can be expected to reach fluxes 1000 × those available from rotating anode x-ray generators. A study aiming to develop the crystallography of minute crystals has begun at this station (Helliwell, 1984; see also Eisenberger, Newman, 1984). A start is being made with crystals of medium molecular weight compounds such as di and trisaccharides, zeolites etc which are simple to handle since they are stable in air and can be mounted on glass fibres. The next stage will be to work towards higher molecular weight compounds such as oligo-nucleotides, oligo-saccharides and related complexes. Recent work has yielded 15 packs of oscillation camera data from a disaccharide (MacKie and North, 1984), with crystal dimensions of $25 \times 5 \times 150\ \mu m^3$. The first impression of the photographs is that they are blank but closer inspection reveals minute spots. From this set of photographs the previously unknown unit cell has been determined. The exposure time was equivalent to 20 hours for a full data set of 180° (at an SRS energy of 1.8 GeV and an electron beam current of 170 mA).

Another approach to the investigation of very small crystals is to use the Laue method (Hails et al., 1984; Moffat, Szebenyi, 1984) to obtain many reflections by exposing the crystal to broad band radiation. The intensity in the broad band "white" radiation beam transmitted through about 0.1 mm of beryllium foil is enormous. The wavelength band-pass extends from ~ 0.2 Å to ~ 4 Å so that many orders of reflection can be recorded for one orientation of the crystal. For example a Laue photograph of a $25 \times 10^3\ \mu m^3$ (average linear dimensions ~ 30 μm) crystal of IRCOP (an indium, copper, phosphor complex) was obtained in less than a 0.5 minute exposure when the SRS was operating with a single stored bunch of electrons (SRS energy 1.8 GeV, stored current 20 mA). This approach to crystallographic work makes it possible to investigate the crystal-

linity of minute quantities of material from a mother liquor. If the sample turns out to be crystalline the symmetry properties of the unit cell can be explored. In principle the Laue data can be used to make a first structure determination although the problem of overlapping orders needs to be solved. This has been done by Wood, Thompson, et al (1983) who have carried out a preliminary refinement of $\alpha A\ell PO_4$ (berlinite) from Laue photographs taken at the SRS. The positional parameters obtained agreed very well with recent high accuracy conventional single-crystal structure refinement. Their method involved the rejection of Laue spots containing multiple diffraction (almost 20% of the data). The addition of energy determination such as by using a film pack interleaved with Cu or Aℓ foil to collect the diffraction data could be used to resolve the overlapping orders so that more complex structures could be investigated.

3.3 Absorption Spectroscopy

The use of the EXAFS (extended x-ray absorption fine structure) method for determining molecular structure is an important contribution of SR to the study of the submicron world. Experimentally it consists in the measurement of the x-ray absorption coefficient as a function of x-ray energy on the high energy side of an absorption edge. The fine structure observed is related to the immediate chemical environment (out to a range of a few Å) from the absorbing atom. The theory of the process is closely related to LEED (low energy electron diffraction) and the experimental method could be described as using the photo-emitted electrons from the absorbing atom to probe the layout of the neighbouring atoms by means of electron diffraction. A useful analogy is with a radar station which sends out a signal from the transmitter and detects the signal bounced back from the surrounding objects (houses, trees etc). The outgoing photoelectron waves behave at distance r from the absorbing atom like

$$\frac{e^{ik.r}}{r} \; Y_{L\pm1,m} \qquad (6)$$

where $k = \sqrt{2(E - E_o)}$, E and E_o are the energies of the incident x-ray beam and the energy at the absorption edge respectively and $Y_{L\pm1,m}$ is the spherical harmonic for an out-going wave with quantum numbers $(L\pm1,m)$. (For absorption from the K-shell of an atom L=0 so that only the P state spherical harmonic contributes). The absorption cross section can be written (Pendry 1981) as

$$\sigma_a(1 + \chi\ (k)) \qquad (7)$$

where σ_a is the absorption cross section for a free atom and $\chi(k)$ contains the interference effects between the outgoing and back scattered photoelectron waves. In the EXAFS regime of the absorption spectrum it is assumed that there is only single scattering of the photoelectron wave so that $\chi(k)$ can be approximated (for K-edge absorption) by

$$\chi(k) = \sum_j (k R_j^2)^{-1} \sin(2kR_j + 2\delta_1 + \psi_j) \left| f_j(\pi) \right| \qquad (8)$$

where R_j is the distance of the j^{th} atom from the absorbing atom, δ_1 is the phase shift of the outgoing and backscattered photoelectron waves induced by the central atom, ψ_j is the phase shift between the outgoing and the backscattered waves introduced by the j^{th} atom and $f_j(\pi)$ is the amplitude of the backscattering factor (whose phase is ψ_j). This equation illustrates the basic principle of the method and indicates that the absorption spectrum observed is the interference between sine waves generated by the backscattering atoms. Detailed discussions will be found in the literature (e.g. Garner and Hasnain, 1981).

The EXAFS technique is being applied to a wide variety of organic and inorganic materials in both an amorphous and crys talline state. A particularly interesting application is to the stereochemistry of haemoglobin. This is particularly im portant because Perutz (1970) proposed a mechanism for the biologically essential function of oxygen transport which in volves the movement of the Fe atom relative to its nearest neighbours. In the complex shown in Fig.6 the Fe atom is displaced by (0.56 ± 0.03) Å from the plane defined by the four N atoms, whereas in liganded haemoglobin they lie either in or close to that plane. EXAFS has been applied to the study of this effect by a number of authors (Eisenberger, Shulman, 1978; Perutz, Hasnain et al., 1982). Fig.7 taken from the latter publication shows how the EXAFS spectrum can be built up from the contributions from the shells of near-neighbour atoms and how the Fourier transform of the distribution becomes a closer and closer approximation to the transform of the experimental data. In practice an interative procedure is followed in which phase shifts for the absorbing and backscattering atoms are calculated using the methods developed by Lee and Pendry

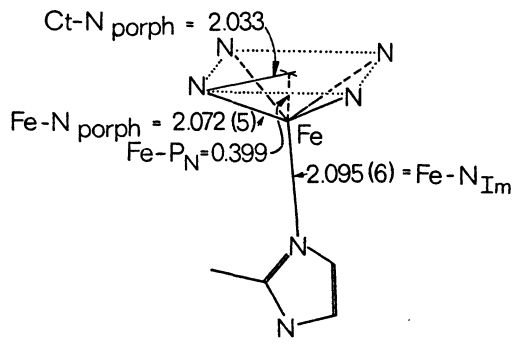

Fig.6. Sterochemistry of iron coordination in the oxygen free picket fence haem complex. Distances shown are in Ångström units with the standard errors in units of 0.001 Å shown in parenthesis. (Jameson et al., 1980).

(1975). Experimental data were collected for both de-oxyhaemoglobin and also for the so-called picket-fence porphyrin complex for which accurate crystallographic information is available (Jameson, et al., 1980). The distance of the Fe-atom from the N atoms in the porphyrin ring was found to be (2.06 ± 0.01)Å as was also found by Eisenberger, Shulman et al., (1978). These latter authors concluded from this that the Fe lay in the plane of the N atoms but this conclusion relied on combining the Fe-N EXAFS data from deoxyhaemoglobin with the length of the half-diagonal of the porphyrin ring (2.045 Å) corresponding to a particular model compound. There is no particular reason for making this choice and a survey of iron porphyrins shows that the halfwidth of the porphyrin ring varies from just under 2 Å to 2.043 Å depending on the compound selected. The EXAFS results certainly show that the Fe-N distance is the same in both the picket-fence and deoxyhaemoglobins but it is also clear that the distance from the Fe to the haem plane cannot be obtained from the EXAFS data alone. A new high resolution crystallographic study using SR at Orsay, France by Fermi et al (1984) confirms the value of 2.06 Å for the Fe-N

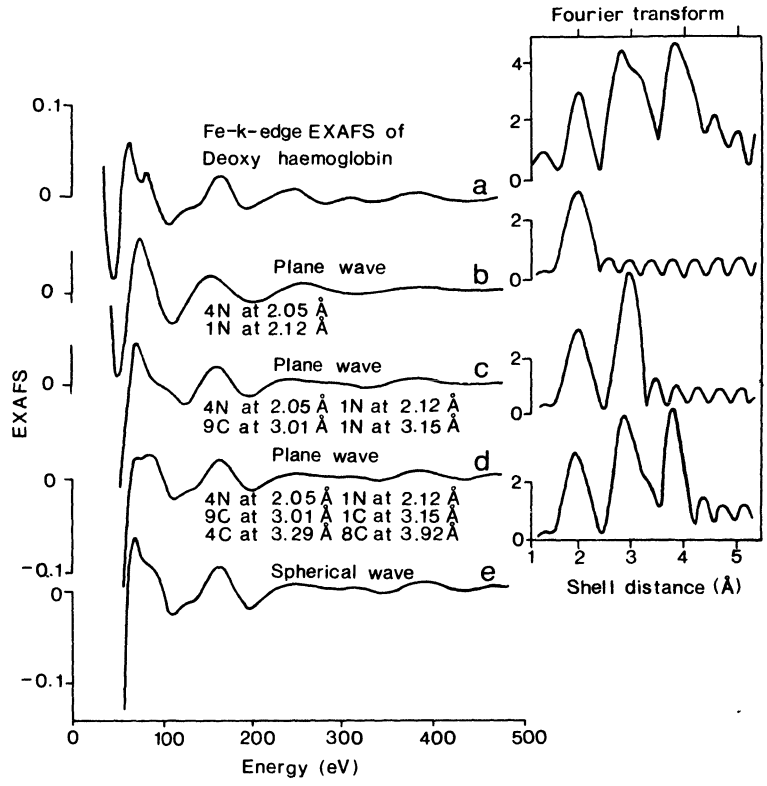

Fig.7. EXAFS and Fourier transforms of human deoxyhaemoglobin
(a) Experimental curve and the transform derived from it
(b) Calculated curves taking into account scattering from nearest neighbours only (first shell)
(c) Same for first and second shell
(d) Same for first three shells.
Note that (a)-(d) were calculated using the plane wave approximation
(e) EXAFS curve calculated using the spherical wave method.
The Fourier transforms have been multiplied by R^2 to show the radial distributions of the atoms surrounding the iron (Perutz, Hasnain, Duke, et al., 1982).

distance - in excellent agreement with the EXAFS work. It also demonstrates that the mean distance of the Fe atom from the centre of the haem plane is 0.38 Å in deoxyhamoglobin.

Table 2. Parameters used to simulate the EXAFS associated with the Fe K-edge of deoxyhaemoglobin and deoxy picket fence complex.

Atom	Deoxyhaemoglobin σ^2 (Å^2)	Deoxyhaemoglobin R (Å)	Deoxy 'picket fence' σ^2 (Å^2)	Deoxy 'picket fence' R (Å)	Single crystal X-ray analysis
4N	0.004	2.05	0.006	2.06	2.07
1N	0.006	2.12	0.006	2.11	2.10
9C	0.003	3.01	0.011	3.01	3.09
1C	0.003	3.15	0.003	3.15	3.14
4C*	0.003	3.29	0.008	3.34	3.45
8C*	0.003	3.92	0.006	3.89	4.30

R denotes the distance of the atom from the Fe atom. σ^2 is a Debye Waller factor and is equivalent to ΔR^2. $E_0 = 15$ eV. The difference in Debye Waller factors of the 9 carbon atoms is significant and derives from a difference of EXAFS at ~300 eV and of the amplitudes of the Fourier terms at ~3 Å.

EXAFS measurements have recently been carried out on a single crystal of carboxy-myoglobin. Since the incident x-rays from the SR source are strongly polarized with the electric vector in the horizontal plane the crystal can be oriented to exploit the angular dependence of the outgoing electron wave function. This means that the wave can be used as a directional probe (e.g. at right angles to or in the plane of the porphyrin ring). Fig.8 shows some results from a first measurement (Hasnain, Bianconi et al., 1984). Curve (d) in the figure shows data in which the electric vector lies close to the plane of the porphyrin ring. In curve (a) the crystal has been rotated so that the electric vector is almost at right angles to that plane. The change in the EXAFS spectrum particularly at an energy of ~ 150 eV above the edge can be clearly seen. An analysis of the EXAFS data shows that for CO-myoglobin the Fe-N distance is (2.00 ± 0.01)Å.

There are also important changes in the near-edge (XANES) structure as a function of crystal orientation. In particular the prominent peak at ~ 25 eV above the edge, which is present when the electric vector is oriented close to the Fe-Co direction is not present when the electric vector is oriented close to the porphyrin plane. In the XANES region of the spectrum the analysis is much more complicated than in the EXAFS region (Pendry, 1981; Bianconi, 1981) because of the low energy of the photoelectrons, multiple scattering and local crystal symmetry are much more important than for EXAFS. In principle bond-angle information can be extracted from the XANES spectrum and such an analysis is being attempted for the data presented here.

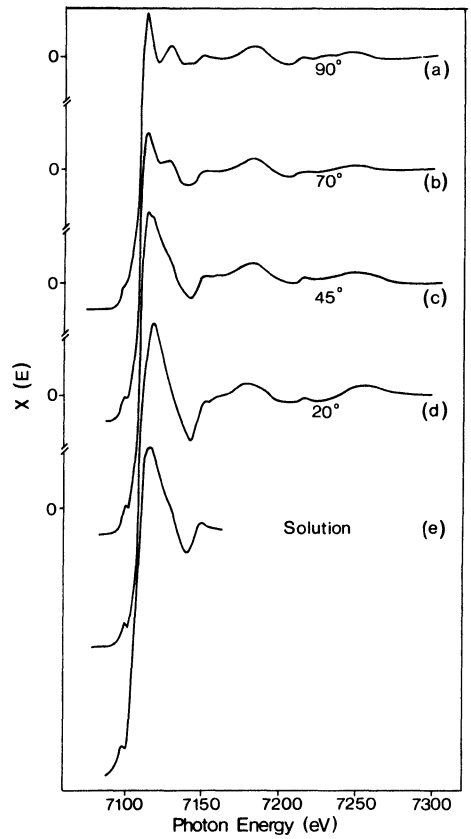

Fig.8. Preliminary EXAFS and XANES spectra from a single crystal of CO-myoglobin. Curves (a)-(d) show the effect of progressively rotating the crystal so that the electric vector of the incident radiation moves from near normal to the haem plane (a) to approximately in the haem plane (d). Curve (e) shows the near edge structure of CO-myoglobin in solution. (Hasnain, Bianconi, et al., 1984).

3.4 Recent Developments

A very fruitful area of research for SR is the development of surface studies. Some of the earliest work in this field (and a continuing intense area of investigations) is the employment of SR as a source for photoemission spectroscopy of electrons from solid surfaces. The short range of the electrons in any solid material, combined with their angle and energy selection makes photoemision a very valuable probe for the

study of surfaces at the submicron level. In particular the known direction of the electric vector of the radiation, relative to the surface orientation, as well as the ability to tune to any wavelength in the VUV or XUV region are both essential features of SR surface studies. The techniques of EXAFS and diffraction can also be applied to surface studies using SR. A novel approach which use the x-ray standing wave pattern, developed by Bragg diffraction at a crystal surface, combined with the known polarization state of the radiation has been used at the Hasylab (Hamburg, FRG) to probe the distribution of adsorbed atomic layers on a crystal surface (Bedzyk, 1984; Materlik, 1984).

The use of SR for dynamic x-ray imaging is an exciting new development. Initial developments employed the use of linear detectors to sample the x-ray diffraction pattern from biological fibres undergoing transitions induced by environmental changes (Huxley, 1983). More recently a 2D-detector has been employed to sample time dependent x-ray diffraction patterns over a much larger area of reciprocal space. For example a multiwire detector has been used to begin a study of time-dependent conformational changes in DNA (Greenall, Nave 1984).

4. FUTURE DEVELOPMENT OF SR SOURCES

4.1 The SRS High Brightness Lattice Project

In accordance with the principles annunciated in section 2 of this review the main thrust of SR source development is towards higher spectral brilliance. SR sources now being designed, built or commissioned attempt to optimise electron beam dimensions and divergence and also include provision for multipole insertion devices (wigglers, undulators, wavelength shifters) right from the start of the project. The Daresbury SRS was designed in the early 1970's and is in fact the world's first purpose-built x-ray source dedicated to SR experiments. Improvement of spectral brilliance of an already existing source is a daunting prospect since it involves the re-design of the magnetic lattice and may not in fact be possible. Studies carried out at Daresbury have shown that there are several options for reducing the electron beam dimensions in the SRS (Suller, 1980) and one of these, which involves inserting a second quadrupole focusing magnet into each straight section around the storage ring (Saxon, 1983) is being adopted. This should reduce the beam emittance from its present value of 1.5×10^{-6} m.rad to 1.1×10^{-7} m.rad. The present vertical dimensions of the beam would be reduced from $\sim$ 1 mm to $\sim$ 0.4 mm and the the present rather large horizontal dimensions (4.7 - 12.7 mm fwhm) would be reduced to the range 1.75 - 2.5 mm de-

pending on the position around the storage ring. The engineering design work for this modification is now complete and the work will start in October 1986. Special small size quadrupole insertions are being prepared so that no major changes to the SR beam line locations will be required. An important side effect of the modification is that the magnetic lattice will have radically different properties in respect of the phase stability of the circulating electrons. For a given SR energy loss an electron will move out of phase by a much smaller amount compared with the present lattice so that the r.f. voltage required to provide for phase stability will be considerably reduced. The net result will be that the existing r.f. system should be able to support an extra 200 mA of stored electron beam. The present maximum current is 300 - 350 mA so that much larger currents than at present should be possible up to a limit, fixed by beam instabilities, which is yet to be determined.

4.2 The European SR Project (ESRP)

The development of high brightness SR sources took an important step forward in 1982 with the formation of the ESRP by a broad consortium of European countries. The principal aim of the ESRP is the production of a design for a European SR Facility of maximum spectral brilliance in the x-ray region. The optimisation of such an SR source has been described by Thompson (1982) and the scientific background to the project by Farge and Duke (1979). Table 3 gives a list of the main parameters of this source and Fig.9 shows the spectral brilliances which will be obtainable from the different types of radiation port. The source has been designed particularly with the x-ray user in mind but the ESRF could of course provide longer wavelength radiation such as might be required

Table 3. ESRF Main Parameters

Taken from ESRP Internal Report ESRP/IRM/7/83. M. Preger (1983)

Energy		5 GeV	
Circumference		772 m	
Characteristic wavelength		0.9 Å from bending magnets	
		0.5 Å minimum from multipole wigglers	
		0.2 Å minimum from wavelength shifters	
		0.9 Å from undulator fundamental	
Beam dimensions in straight sections (fwhm)			
	from	0.15 × 0.02 mm^2	0.26 × 0.03 $mrad^2$
	to	1.02 × 0.09 mm^2	0.04 × 0.01 $mrad^2$
Electron current		100 mA in multibunch	
Number of long (~ 5 m) straight sections			32

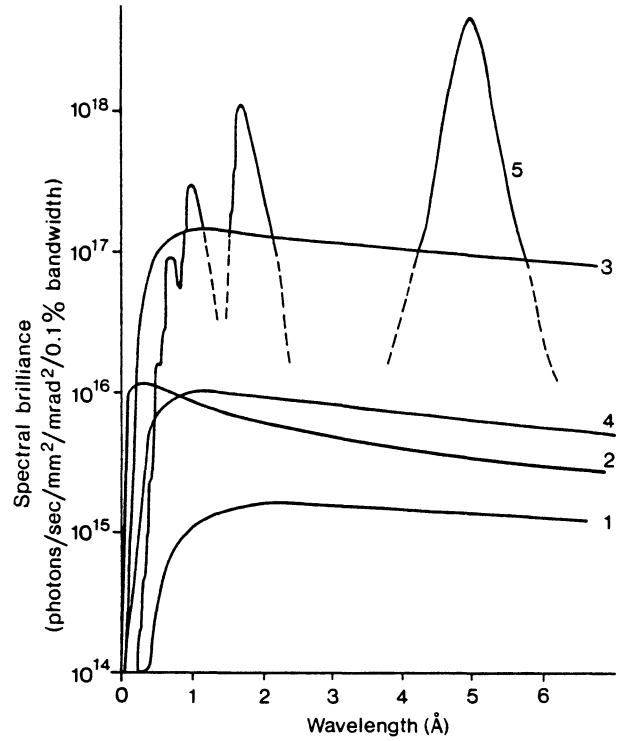

Fig.9. Spectral brilliance for different ports on one varient of the proposed European Synchrotron Radiation Source. 1, Dipole magnet; 2, Wavelength shifter, 3,4, Multipole wigglers at two different locations; 5, Undulator. Energy 5 GeV, beam current 343 mA

for x-ray microscopy of biological materials if no other sufficiently intense source is available.

5. CONCLUSION

Proposals similar to the ESRF have been made for intense synchrotron sources in the USA and sources intermediate in brilliance between the SRS and the ESRF are already operating at Brookhaven National Laboratory, USA and at Tsukuba, Japan. It seems clear that synchrotron radiation is now well established on a world-wide scale as a radiation source for research into the submicron region of the natural world.

6. ACKNOWLEDGEMENTS

I am indebted to my colleagues at the Daresbury Laboratory and elsewhere for their constant advice, help and encouragement. The sources of information are included in the references to the original publications and I am most grateful to these authors for their ready agreement to include their material in this review.

REFERENCES

Bedzyk, M.J., Materlik, G., Kovalchuk, M.V. 1984, X-ray standing wave modulation electron emission near absorption edges in centro and non-centro-symmetric crystals. DESY SR/84-06.

Bianconi, A., 1981, X-ray absorption near edge structures (XANES) and their applications to local structure determination. In Garner and Hasnain (1981) pp13-22.

Bowen, D.K., 1982a, The application of synchrotron radiation to problems in materials science. Daresbury Study Weekend Proceedings DL/SCI/R19.

Bowen, D.K., Davies, S.T., Clark, G.F., Nicholson, J.R.S., Tanner, B.K., Roberts, K.J., and Sherwood, J.N., 1981, The x-ray topography station at Daresbury Laboratory. SERC Daresbury Laboratory Report, DL/SCI/P304E.

Bowen, D.K., Davies, S.T., Clark, G.F., Nicholson, J.R.S., Tanner, B.K., Roberts, R.J. and Sherwood, J.N., 1982b, The x-ray topography station at Daresbury Laboratory. Nucl. Instrum. & Meth., 195:277.

Cerva, N. and Graeff, W., 1983, Contrast investigations of surface accoustic waves by stroboscopic topography. 1. Orientation Contrast. DESY SR/83-15.

Eisenberger, P., Newsam, J.M., Leonowicz, M.E., and Vaughan, D.E.W., 1984, Synchrotron x-ray diffraction from a 800 μm^3 zeolite microcrystal. Nature, 309:45.

Eisenberger, P., Shulman, R.G., Kincaid,B.M., Brown, G.S., and Ogawa, S., 1978, Extended x-ray absorption fine structure determination of iron nitrogen distances in haemoglobin. Nature, 274:30.

Farge, Y., and Duke, P.J., (Eds), 1979, European Synchrotron Radiation Facility, Supplement 1, The Scientific Case, European Science Foundation, Strasbourg, France.

Fermi, G., Perutz, M.F., Shaanan, B., and Fourme, R., 1984, The crystal structure of human deoxyhaemoglobin at 1.74 Å resolution. J.Mol. Biol. 175:159.

Garner, C.D., and Hasnain, S.S., (Eds), 1981, EXAFS for inorganic systems. Proceedings of the Daresbury Study Weekend, DL/SCI/R17.

Gluer, C.C., Graeff, W., Möller, H., 1982, Stroboscopic topography of quartz resonators with synchrotron radiation. DESY SR 82/01.

Greenall, R., Nave, C., Fuller, R.W., 1984, Time resolved x-ray diffraction using the Daresbury Area Detector. To be published.

Hails, J., Harding, M., and Helliwell, J.R., 1984. To be published.

Hasnain, S.S., Bianconi, A., Perutz, M.F., and Phillips, S., 1984, Direct structural information around Fe in carboxymyoglobin using EXAFS. To be published.

Herres, N., and Lang, A.R., 1983, X-ray topography of natural beryl using synchrotron and conventional sources. J. Appl. Cryst., 14:47.

Huxley, H.E., Simmons, R.M., Faruqi, A.R., Kress, M., Bordas, J., and Koch, M.H.J., 1983, Changes in x-ray reflections from contracting muscle. J. Mol. Biol., 169:469.

Jameson, G.B., Molinaro, F.S., Ibers, J.A., Collman, J.P., Brauman, J.I., Rose, E., and Suslick, K.S., 1980, J. Am. Chem. Soc. 102:3224.

Krinsky, S., Perlman, M.L., and Watson, R.E., 1983, Characteristics of synchrotron radiation and of its sources., In Koch, E.E.(Ed) Handbook on Synchrotron Radiation Vol.1a, North Holland Publishing Co., Amsterdam, Holland.

Lee, P.A., and Pendry, J.B., 1975, Theory of the extended x-ray absorption fine structure. Phys. Rev., 11B:2795.

Materlik, G. and Zegenhagen, J., 1984, X-ray standing wave analysis with synchrotron radiation applied to surface and bulk systems. DESY SR/84-05.

Moffat, K., Szebenyi, D., and Bilderback, D.M., 1984, X-ray Laue diffraction from protein crystals. Science, 223:1423

Pendry, J.B., 1981, The theoretical basis of EXAFS and edge structure. In Garner and Hasnain (1981) pp5-12.

Perutz, M.F., 1970, Nature, 228:726.

Perutz, M.F., Hasnain, S.S., Duke, P.J., Sessler, J.L., and Hahn, J.E., 1982, Sterochemistry of iron in deoxyhaemoglobin. Nature, 295:535.

Preger, M., 1983, A flexible lattice for ESRP - Status report. ESRP Internal Report ESRP-IRM-7/83.

Saxon, G., 1983, A proposed lattice modification to the Daresbury SRS. Presented at the 1983 Particle Accelerator Conference, Santa Fe, New Mexico, USA. To be published in IEEE Trans. Nucl. Sci.

Suller, V.P., 1980, A survey of possible lattice modifications for the SRS. Daresbury Laboratory Internal Report, DL/SCI/TM23A

Thompson, D.J., 1982, Optimization of a synchrotron radiation source. Daresbury Laboratory Preprint, DL/SCI/P336A, and Nucl. Instrum. & Meth. Phys. Res., 208:1.

Whatmore, R.W., Goddard, P.A., Tanner, B.K., and Clark, G.F., 1982, Direct imaging of travelling Rayleigh waves by stroboscopic x-ray topographs. Nature, 299:44.

Wood, I.G., Thompson, P., Matthewman, J.L., 1983, A crystal structure refinement from Laue photographs taken with synchrotron radiation. Acta Cryst. B39:543.

PROPERTIES OF POLYMER RESISTS

D. M. Shinozaki[1], J. Wm. McGowan[2], P. C. Cheng[3] and K. H. Tan[4]

[(1)]Faculty of Engineering, University of Western Ontario, London, Ontario, Canada

[(2)]Director , National Museum of Science and Technology, Ottawa, Ontario, Canada

[(3)]Department of Anatomy, University of Illinois at Chicago, Chicago, IL, 60612 USA

[(4)]Canadian Synchrotron Radiation Facility, Physical Science Laboratory, University of Wisconsin, Stoughton, WI, USA

INTRODUCTION

X-ray contact microscopy consists of exposing a recording medium through the specimen of interest. It is an old technique, called in the earlier literature, contact microradiography[1]. Advances in the microelectronics industry and efforts to increase the number of elements in integrated circuits have led to improvements in lithographic techniques recently. For contact microscopy using x-rays important products of these advances has been the availability of ultra-high resolution polymer films such as poly(methyl methacrylate) to record the image, and the development of suitable high intensity soft x-ray sources.

Both electron beam writing and soft x-ray lithography have been developed in attempting to reproduce the extremely fine patterns in micro-circuit fabrication and both have used polymer resists as the image re-

cording medium. Considerable work has been published on the electron beam/resist interaction[2], but relatively little on the x-ray/resist interaction. One of the more detailed studies in the latter area has been the work of Spiller and Feder[3]. The physical problem can be separated into two parts; the processes related to (i) the exposure and (ii) the development of the polymer resist.

In order to improve the resolution and sensitivity of polymer resists the following must be considered:

(1) The interaction between the x-ray photon and the polymer molecule,
(2) The role of irradiation parameters such as photon energy, photon flux, bandwidth, and polarization,
(3) The influence of resist parameters such as purity, molecular weight, resist thickness, molecular structure,
(4) The effect of the substrate

When the radiation dosage is insufficient to crosslink the polymer, the molecules are broken up and the development of a resist such as PMMA is a dissolution process. The irradiated polymer has a lower molecular weight and therefore dissolves in a solvent more easily. (A negative resist is one which crosslinks upon irradiation while a positive resist is one in which the molecules break up). The quality of the final image on the surface of the resist depends on the process of development. The dissolution parameters which must be controlled are:

(1) Temperature
(2) Fluid velocity at the resist surface
(3) Immersion time
(4) Solvent concentration

The properties of the resist itself affect all of these exposure and development parameters. On of the first steps in understanding the relationship is to understand the basic polymer molecule.

POLYMER MOLECULES

Synthetic polymers consist of large molecules with molecular weights typically in the range $10^4 < MW < 10^7$. Commercial carbon based polymers such as poly(methylmethacrylate) (PMMA) are large molecules in the form of long chains. Typical dimensions of a fully extended polethylene molecule

would be of the order of 25,000Å x 5Å (50,000 atoms of C and H with 16,000 C atoms along its backbone). The C-C bond is about 1.5Å and the C-H bond about 1.1Å.

These extremely long molecules generally dissolve very slowly in typical solvents like methanol, if they do at all. In the solid state, polymers which are used as resists are ideally structureless or amorphous, with the long molecules randomly tangled. To dissolve such a solid requires the movement of long molecules from the surface layer into solution. Rapid dissolution of the resist requires the reduction of the average molecular weight which is accomplished by irradiating the resist with electron beams or x-rays. The dissolution rate obviously depends on the molecular weight and the usual parameters such as the flow rate at the surface, the diffusion coefficient of the solvent in the polymer, the temperature, the thermodynamic driving force for dissolution, and the mobility of the polymer molecule. The mobility of the molecule depends on the molecular structure.

The structure of the polymer molecule may be regular (iso- or syndiotactic) or irregular (atactic). The electronics industry requires resist systems with resolutions well under 1 micron, with developed profiles controlled to a much smaller size. Soft x-ray microscopy needs the highest possible resolution, the limit of which is suggested as 50Å[3]. The size of the molecule and the molecular arrangements at this scale preferably should be random, so that the substructure of the polymer resist does not interfere with the developed image.

It should be noted that direct observation in the transmission electron microscope of thin films of polymers such as polystyrene has revealed a nodular structure on the scale of 100Å or less. Polystyrene is nominally amorphous, as is PMMA and other useful resists, but when examined at the limit of its useful resolution in this way, shows that its own substructure can interfere with recorded images. On this scale of observation, the molecular size itself is significant, and any local ordering as may happen with poly(vinyl chloride) (syndiotactic PVC crystallizes), can result in resist artefacts which are not expected from the pure chemical formula.

Crystalline materials with highly perfect structures over large areas (corresponding to the image area) might also be used, provided the defect structure does not interfere with the image. Crystalline polymers inevitably have a crystallite size of around 100Å which precludes their use as an image recording medium. An example of such a morphology, which at the same time

illustrates the use of soft x-ray contact microscopy in revealing such structure is found in the work of Leung *et al.*[4].

The flexibility of the molecule depends on the molecular structure, as do the dissolution rate, and the radiation damage effects. The basic structural variables which affect the properties of the resist are:

(1) Branching, in which the main chain has shorter lengths of the main chain attached, usually randomly along the main chain. The branch points are regions with different arrangements of chemical bonds, and may be relatively easy to break upon irradiation. The relationship between the stability of a particular bond and the susceptibility to scission under irradiation has been thoroughly studied in the UV region.

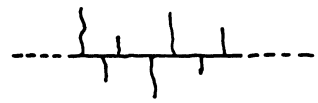

Figure 1

(2) Side-groups; Chemical groups attached to the main chain. In amorphous polymers such as resists (PMMA), these are attached on random sides of the main chain (atactic), although in other polymers such as polypropylene the CH_3 group is always attached to the same side (isotactic).

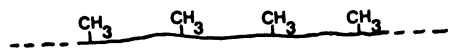

Figure 2

(3) Crosslinking; In which the main chains, sidegroups or branches from different molecules are covalently bonded. The effect of crosslinking is to reduce the mobility of the molecules and therefore reduce the rate of dissolution. At high crosslink densities, the whole resist layer becomes one giant molecule, forming a network which cannot be dissolved but can undergo swelling if the solvent diffuses into the layer.

Figure 3

(4) Copolymerization; The repeat unit of a homopolymer such as PMMA is chemically identical to every other repeat unit. When copolymerized, two or more chemically distinct repeat units are arranged in various ways to form random, block or alternating copolymers. It is possible to add more than two kinds of repeat units (A, B, C, *etc.*) to form terpolymers and so on. This is one way of introducing in a controlled way different chemical groups into the molecule. The different chemical groups can have different stability and different photon absorbing properties. The resultant copolymer is, in effect, engineered on a molecular scale to produce a resist with the precise physical and chemical properties.

TYPICAL KINDS OF CHEMICAL BONDS

The chemical bonds in the molecule are broken in the process of irradiation of the resist, and if they remain broken, will result in a lower molecular weight solid which dissolves more readily (positive resist). Alternatively the broken bonds can reform to join different molecules and to form crosslinks. In the latter case the irradiated solid becomes insoluble at high crosslink densities and the resist is a negative one. The sensitivity of the resist depends on the susceptibility of the chemical bond to breakage and the placement of the bond in the molecule. Typical synthetic polymer repeat units are shown below in Figure (5) and typical bond dissociation energies are shown in Table (1).

Table 1

	kcal/mol
CH_3 - H	102
C_2H_5 - H	99
C_6H_5 - H	103
CH_3 - Cl	84
C - Cl	78
CF - F	118

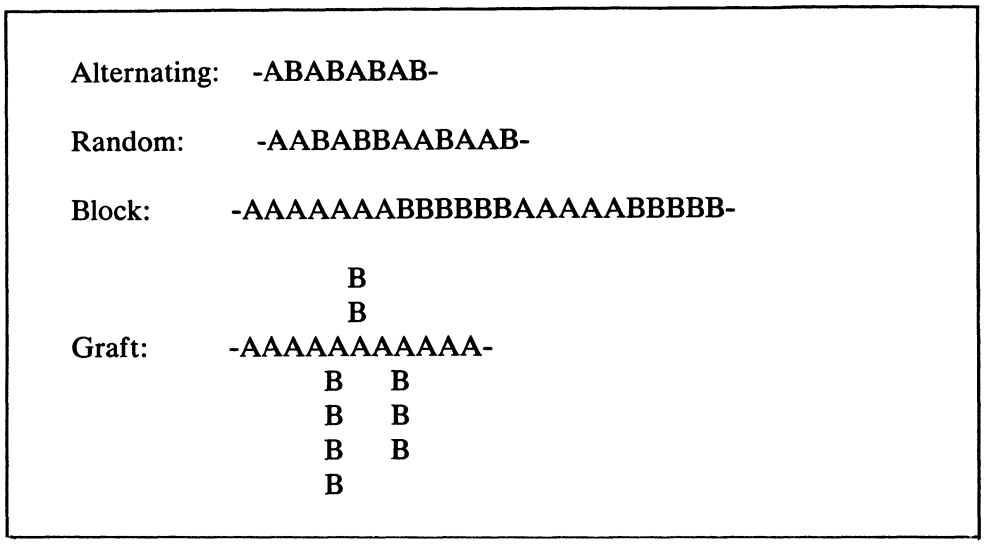

Figure 4

Polyethylene

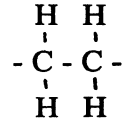

Poly(vinyl chloride)

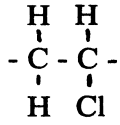

Polystyrene

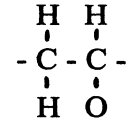

Poly(methyl methacrylate)

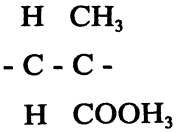

Figure 5

INTERACTION BETWEEN PHOTONS AND POLYMER MOLECULES

All materials are affected by radiation in some way, but the exact physical and chemical changes depend on the kind and energy of the radiation. Higher energy photons (harder x-rays), and even electron beams used in lithography generally cause similar kinds of damage to the polymer molecule, while lower energy photons such as UV radiation affect the molecule somewhat differently. Table (2) shows the approximate ranges for the different portions of the electromagnetic spectrum. There is a considerable literature on the effects of UV radiation on polymers[5,6,7], and on the effects of ionizing radiation such as gamma rays[8]. The soft x-ray photon energies are between these two ranges, and very little discussion has been published on the molecular effects in this range. The one end of the soft x-ray range overlaps the UV and the other end overlaps the hard x-ray range. The exact energy or energy band which is used to irradiate the polymer will obviously dictate the kind of damage that results. Photons which are resonantly tuned to particular K shell ionization processes will affect the polymer molecule in a way different from those which lead to non-specific damage in the molecule.

Table 2

	eV	(Å)		eV	(Å)
Vacuum Ultraviolet	10	(1240)	to	100	(124)
Soft x-rays	100	(124)	to	1000	(12.4)
Hard x-rays	1000 and greater				

ULTRAVIOLET RADIATION EFFECTS ON POLYMERS

In the near UV, the absorption of low energy photons can be highly localized at particular bond sites within the molecule (for example at chromophoric groups). The resultant photochemical reactions depend on the allowed electronic transitions within the molecule. This depends entirely on the chemical structure within each molecule[5]. The absorption of the photon can result in the production of radicals, in chain scission or in the emission of photons as a result of a return to the ground or excited state. The photon energy obviously determines the mechanism(s) of absorption and/or damage. For example, in the UV range, the primary effect is the production

of excited states within the molecule. This process is temperature independent. The excited molecule can undergo secondary reactions (involving the molecules, ions or radicals) which include: (1) dissociation of the molecule, and (2) electronic energy transfer, in which the energy absorbed in the primary process is transferred to another part of the molecule or another molecule. A subsequent interaction with a second molecule can involve a molecule of the same species or of a different kind (in which case it may be called a quencher molecule). The energy transfer may also occur to electronic, vibrational or rotational states by the absorption and emission of photons ($h\nu$).

The exact molecular structure therefore has a significant influence on degradation reactions in polymers and their subsequent development following irradiation. The original polymerization process used to manufacture the polymer can result in small numbers of defects in any polymer molecule and even these can increase the degradation reaction rates. An example is found in saturated polyolefins, which should not absorb UV radiation. The significant degradation rates observed even at wavelengths of $\lambda > 3000$Å has been ascribed to the presence of carbonyl groups ($\rangle C=O$) and ($C=C$) bonds formed within the molecule during synthesis. In general, commercially produced polymers will vary slightly in structure and molecular weight distribution, depending on the manufacturer, although they may be of identical nominal composition. The exact damage kinetics may therefore be affected by the source of the polymer.

In another process related to photochemical degradation mechanisms, the presence of small molecules, atoms or impurities in the polymer can result in preferred absorption by the small molecule and subsequent transfer of energy to the polymer molecule. This results in an excited state within the polymer molecule which can then produce chain scission. It should be noted that the reverse process of primary excitation of the polymer and subsequent energy transfer to the impurity molecule can enhance the stability of the polymer by draining the damaging energy into non-polymeric molecules[5].

Within a pure polymer system with no defects in the chain, the energy deposited in one part of the long chain molecule can be transferred along the length of the molecule through the side groups or along the backbone. There is also a possibility of transferral of energy between molecules. Guillet[8] has suggested the the backbone mechanism may occur at the higher photon energies towards the x-ray region, which is of obvious interest to the soft x-ray microscopist.

In discussing the ultimate resolution of contact soft x-ray microscopy, which is of the order of 50Å[3], the diffusion of energy away from the region of primary absorption may be quite important. Of course, for UV the resolution would be limited by the wavelength of the radiation and not by this energy spread. However as the photon energy is increased into the soft x-ray region, these kinds of mechanisms will be increasingly significant. For the UV range, the experimental measurement of the absorption spectrum is useful in identifying the presence of significant fractions of chemical bonds which absorb strongly. The UV end of the soft x-ray absorption spectrum will reveal significant chemical bond effects.

At the other end of the soft x-ray spectrum, the hard x-rays overlap, and the predominant mechanism of radiation damage is much less dependent on the exact chemical bonding state.

X-RAY IRRADIATION DAMAGE IN POLYMERS

The photoelectric effect is the predominant result of irradiation with hard x-rays or gamma rays. Incident photons have energies which can cause ejection of an inner shell electron when absorbed. The energy of the photoelectron is equal to the difference between the photon energy ($h\nu$) and the binding energy of the electron (ofthe order of a few hundred eV for C,N, and O atoms). These photoelectrons are subsequently absorbed by the polymer molecules and damage ensues. The resolution of a resist in this case is primarily determined by the average path length of the photoelectron in the polymer. This is similar to the spreading of the damaged region over a volume greater than that irradiated by the electron beam in an scanning electron microscope or in an electron beam writing machine used for e-beam lithography.

Since the path length of the photoelectron depends on its kinetic energy, the higher energy x-rays have larger damaged volumes and the resolution becomes poorer. However as the photon enrgy decreases, the wavelength increases and diffraction effects become significant. Spiller and Feder suggest that an incident wavelength of about 50Å will give the highest resolution images in PMMA[3]. This corresponds to a photon energy around 277 eV. , slightly lower in energy than the carbon absorption edge, in the middle of the soft x-ray range.

The results of x-ray irradiation on the polymer molecule are:

(1) the breakage of chemical bonds within the main chain (chain scission) at the side-groups of the molecule or at the chain ends. Depending on the polymerization reactions, the chemical bonds will be different in these regions of the molecule.

(2) the formation and disappearance of unsaturated groups (radicals). The bond may break forming unpaired electrons, and may remain broken, reacting in some other way, or may recombine to reform the molecule.

(3) The crosslinking of the resist if the bonds form between the molecules.

In general terms, the difference between the UV and the higher energy photons is that the UV photon interacts specifically with particular chemical bonds while the higher energy hard x-rays produce photoelectrons whose effect is much less dependent on the exact chemical environment. Hence hard radiation often results in random chain scission, and small fractions of different chemical species are not as significant as in the UV range. Once the molecule has been broken in some way, the subsequent process can follow some different paths.

CHAIN SCISSION AND CROSSLINKING

The absorption of the photon energy by the resist depends on the wavelength of the radiation. In terms of the positive resist, the desired result is chain scission and a reduction in the molecular weight. However the breaking of the main chain to form radicals also results in a finite probability of recombination of the radicals to heal the scission. Alternatively, different molecules can bond to form crosslinks. The molecular mobility will affect the recombination rate, but exact mechanisms are not clearly understood. The rate of accumulation of radiation damage can be simply related to the absorbed dose in the following way. The extension of this approach to account for simultaneous crosslinking and chain scission is described in Jellinek[6].

Number Average Molecular Weight: $M_n = \frac{\Sigma N_i M_i}{\Sigma N_i}$

Number of Molecules per gram before Irradiation: $\frac{N_A}{M_{n,o}}$

Number of Molecules per gram after Irradiation: $\frac{N_A}{M_{n,D}}$

Number of Damaged Molecules: $\frac{G(s)D}{100}$

where:

G(s) = Number of Main Chain Scissions per 100 eV absorbed

D = Absorbed Dose (eV / gm.)

N_A = Avogadro's Number

N_i = number of molecules of ith species

$M_{n,o}$ = M_n (at zero dose)

$M_{n,D}$ = M_n (at dose = D)

Total number of molecules after damage = number of molecules initially and number of damaged molecules.

$$\frac{N_A}{M_{n,D}} = \frac{N_A}{M_{n,o}} + G(s)D/100$$

$$M_{n,D} = \frac{M_{n,o}}{\frac{1 + G(s)DM_{n,o}}{100N_A}}$$

Thus to obtain G(s), measure $M_{n,D}$ as a function of D.

For a most probable molecular weight distribution, determined from the polymerization conditions, $M_w / M_n = 2$

$$\frac{1}{M_{w,D}} = \frac{1}{M_{w,o}} + \frac{G(s)D}{200N_A} = \frac{\sum N_i M_i^2}{\sum N_i M_i}$$

(where M_w is the weight average)

It is then possible to estimate G(s) by measuring the shift in molecular weight distribution. The number average molecular weight is used here, but it should be noted that there are a number of different measures of molecular weight such as weight averages and viscosity averages which appear in the literature.

An example of the approach used to quantify exposure/development parameters in the study of electron beam resists is reviewed by Hawryluk[10]. The various methods of relating the dissolution parameters to the irradiation dosage, or "dissipated energy" are discussed. The dissolution rate varies with depth into the resist because the absorption of the energy varies with depth for the typical electron energies used. Given the energy absorption as a function of depth:

$$D(z) = \frac{NE(z)}{e}$$

where: N coulombs/ cm^2
E(z) energy dissipated per e^- at depth "z"
e eV/ cm^3

and assuming an empirical relationship between molecular weight after irradiation M_f, (which is the number average molecular weight) and the dissolution rate R (nm/second):

$$R = R_o + \frac{\beta}{M_f^{\alpha}}$$

where R_o, β, α are assumed empirical constants and M_f is given by the expression:

$$M_f = \frac{M_{n,o}}{1 + \frac{G(s)DM_{n,o}}{100N_A}}$$

There is a need for similar experimental measurements for the soft x-ray region. The earlier discussion on the mechanisms in the UV and in the hard x-ray regions suggest the electron beam results such as those reviewed by Hawryluk[10] and Bowden[2] should be similar to those which will be found in the high energy part of the soft x-ray spectrum. However the mechanisms operating in the lower energy range, towards the UV end, suggest a much stronger dependence on the photon energy through its effect on the different chemical bonds.

An important first step in examining the radiation damage/development dependences on photon energy is to measure the absorption coefficient over this range.

MEASUREMENT OF ABSORPTION COEFFICIENTS IN THE SOFT X-RAY RANGE

For any solid, if the absorption mechanism is one of generation of photoelectrons, the proportion of radiation absorbed in a layer of thickness "dx" is (dI/I_o)whereI_o is the intensity incident on the layer "dx", and μ is the mass absorption coefficient, a property of the material. Through a thin film of overall thickness "x" the intensity transmitted is given by the Lambert-Beer expression:

$$I_T = I_o \exp(-\mu x)$$

For a given material, as the wavelength of the radiation increases (the photon energy decreases) the material appears more opaque to the radiation and the absorption coefficient increases smoothly. As the incident radiation wavelength increases across a K edge the photon energy just on the low energy side of the edge is insufficient to knock out a K electron from the atom. The intensity transmitted at this wavelength is suddenly much higher than the intensity on the high energy side of the edge. The absorption coefficient shows a sudden drop as the wavelength increases across a K edge. Similar absorption edges are observed for L edges (corresponding to L electrons). The wavelength of the various absorption edges depends on the amount of en-

ergy necessary to knock the respective electron out of its atom, and this depends on the electron structure. The lighter elements have K edges at correspondingly longer wavelengths. In the soft x-ray range, some of the interesting edges are given in Table 3.

Table 3

Element	Edge K	L_I	L_{II}	L_{III}
C	43.648			
N	30.990			
O	23.301			
Na	11.478			
Mg	9.5117			
P	5.7866	81.02	96.843	
S	5.0182	64.228	76.049	76.519
Cl	4.3969	52.084	61.366	61.672
K	3.43645	36.352	42.020	42.452
Ca	3.07016	31.068	35.417	35.827

Polymers used commonly for resists are mainly carbon based molecules with hydrogen, oxygen, nitrogen and chlorine being often included in the molecule. The composite absorption coefficient can be calculated simply by adding the weighted absorption coefficient of each element, provided the photon energy is high enough (at short wavelength). As the photon energy decreases, however, the interaction of the photon and the molecule reflects the kinds of chemical bonds in the molecule, and the simple calculation of the absorption coefficient from elemental data may be inaccurate. The absorption spectrum must therefore be measured by experiment over the relevant soft x-ray range to determine absorption behaviour. Recent published work includes that of Bohn, Taylor and Guckel[11].

Specimen Preparation

To calculate the absorption coefficient (μ) as a function of x-ray wavelength, the incident intensity (I_o) transmitted intensity (I_T) and specimen thickness (x) must be measured. Since soft x-rays are attenuated strongly in materials, even in carbon based polymers, a relatively thin film is required, of

the order of one micron or less. The specimen should be homogeneous, uniform in thickness, and free of pinholes. Materials such as biological specimens which are usually inhomogeneous in structure and in chemical composition will give absorption coefficients which are some weighted average of the various phases present. In such cases, it may be useful to homogenize the material to prepare a uniform specimen.

In the case of synthetic materials such as polymer resists, which are spun onto silicon or glass substrates in solution, the spinning process should produce a uniform thickness over the area of interest. The preparation of a flat, even surface is also important for high resolution x-ray imaging. The normal spin coating process involves depositing a specified amount of polymer solution (for example 6% w/v PMMA in chlorobenzene) onto a silicon wafer. The wafer is held to a plate by a vacuum and is accelerated to a predetermined rotational speed. The solution spreads outward on the wafer and as it spreads, the solvent evaporates, changing the flow characteristics of the solution. The initial concentration of the resist solution and the rotational speed strongly affect the final resist thickness. For purposes of x-ray microscopy, the final quality (uniformity and thickness) of the resist are best determined experimentally for a given resist. Hovever there have been some attempts to numerically model the spin coating process[12].

Once a polymer film has been spun, a number of standard techniques can be used to measure the thickness of the film, including direct observation of the spun layer in a fractured edge in the scanning electron microscope.

There are other methods of preparing uniform films of polymers besides spinning. A glass microscope slide can be dipped into a fairly dilute solution of the polymer (often less than 10% w/v). Upon smoothly withdrawing the glass slide, and allowing the solvent to evaporate, a thin polymer film is left on the slide. Careful scraping of the edge of the slide breaks the adhesion of the edge of the film which can then be floated off on the surface of water. Occasionally, the edge of the glass slide can be touched with a dilute hydroflouric solution to initiate the decohesion before floating off on water.

Using similar dilute solutions, a variety of other methods can be used to produce a thin specimen, for example, solvent casting on hot liquid surfaces or direct casting on non-adherent surfaces such as mica.

After making the film, the residual solvent is removed by baking and/or baking in a vacuum. The failure to remove the solvent can result in its absorption spectrum being superimposed on that of the polymer film. For example, chlorine peaks resulting from the residual chlorobenzene have been observed in PMMA spectra. With irradiation in the soft x-ray beam, the chlorine peaks disappear as the chlorobenzene was driven off.

The free standing polymer film can then be mounted on a specimen holder. If the film is brittle or very thin (less than 1000Å, for example), it may be necessary to support the film on a transmission electron microscope grid. After checking the film for holes or defects in the optical microscope, the specimen and holder are mounted in the x-ray source chamber. The chamber is prepumped, then opened to the monochromator and the synchrotron beamline.

X-ray Source

To measure absorption coefficient spectra, a monochromatic tunable x-ray source is needed. The high intensities needed can be obtained most easily on a synchrotron radiation source. Various monochromators have been used, and the Canadian Synchrotron Radiation Facility (CSRF) at the University of Wisconsin has a so-called "grasshopper monochromator", a grazing incidence instrument. This has good energy resolution (of the order of 0.1 eV at low energies) but relatively low intensities. The energy range studied was limited by the source itself (Tantalus has a usable output over the range from 10 eV to ~280 eV) but future experiments will use Aladdin which has a usable range from 10 eV to 1000eV.

It was found that the characteristics of the monochromator output could produce anomolous absorption spectra. For example in the wavelength region near the carbon edge (~43 Å), the output from Tantalus drops off sharply, and the monochromator output shows contamination from the zero order radiation. The radiation incident on the specimen is therefore not monochromatic and the absorption spectra is anomolously high in this region. At longer wavelengths, the monochromator output is contaminated with second order (higher energy) radiation, again resulting in an absorption spectrum artefact. In short, quantitative measurements of absorption behaviour of polymer films depend on the spectral output from the monochromator, and proper corrections are essential.

Typical measured absorption spectra in the region of interest are shown in Figures 6, 7, 8, and 9. The carbon edge is clearly seen, along with the relevant edges associated with the different chemical elements. The energy resolution obtainable using the CSRF monochromator is much higher than is evident from these curves.

Dissolution of Irradiated Resists

After x-ray exposure and before development in a solvent, the latent image in the resist consists of regions of different average molecular weight. The developed image results from differential dissolution rates in the various regions of the resist. The process of dissolving the resist occurs near the solvent-resist boundary, and consists of (a) diffusion of the solvent into the resist ,(b) swelling of the polymer film as the solvent diffuses in to form a gel layer (c) movement of the polymer molecules into the solvent, the rate of which is determined by the thermodynamic driving force and the constraints imposed by the molecular mobility. The resolution and sensitivity of soft x-ray contact microscopy therfore depends on the dissolution process itself. For example the formation of a thick boundary layer of gel and the consequent swelling of the resist can distort the image considerably, particularly if the swelling process results in plastic deformation of the resist. The resist can contract to its original dimensions after the solvent is removed by drying. However in an etching process, topographic structures of close to 100Å are being formed and it is possible that the image may be permanently distorted on this scale. An example may be found in studies of polyglycidyl methacrylate-co-ethyl acrylate. Fine structures are obliterated by the extreme swelling during wet development[13,14,15].

The rate of dissolution also is affected by the fluid flow conditions at the resist-solvent boundary. The rate at which polymer molecules move from the gel state in the interfacial layer can be increased by increasing the solvent velocity at the boundary. While microstructures as small as 100 A are being formed in the resist surface by differental dissolution,the local fluid flow conditions are continuously changing. The quantitative relationship between the subsequent SEM or TEM image of the etched resist, and the original specimen is not easily determined. In fine line electron beam lithography, Hatzakis has shown that the developed resist surface contour is related to the radiation iso-dose contours. The exact shape of the developed line exposed through a high contrast mask changes with development[16,17]. Other related work is discussed in Wittels' review[15].

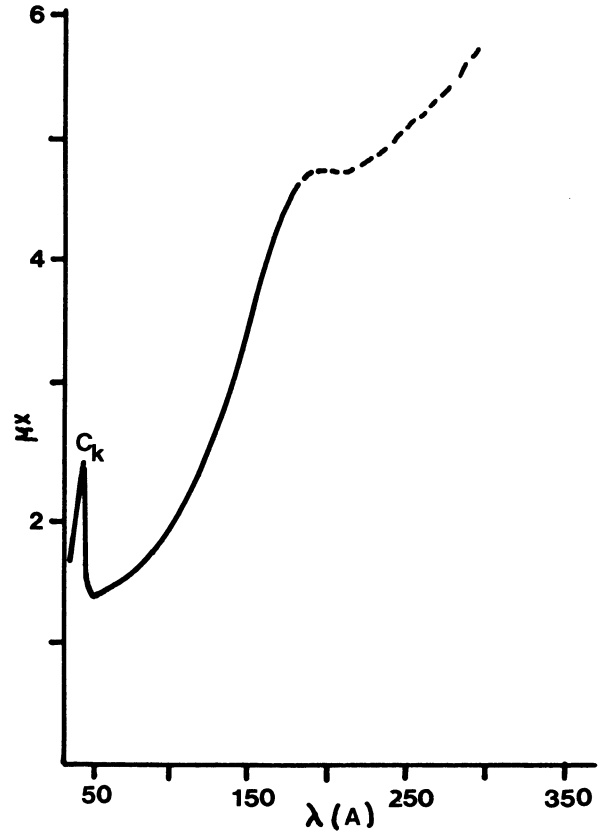

Figure 6. Absorption coefficient as a function of x-ray wavelength for pure carbon film.

For these reasons, it is essential that the development conditions (termperature, flow rate, concentration) be specified and controlled in producing high resolution x-ray images. In addition, the standard development curves (change in resist thickness during development as a function of irradiation dose) measured over broad areas may not be appropriate when the structures being examined approach 100Å, which approaches molecular dimensions in these long chain materials. The molecule may extend over the boundaries of the microstructure and the dissolution rate is limited by the entanglement in the gel.

High Resolution Examination of Soft X-ray Images

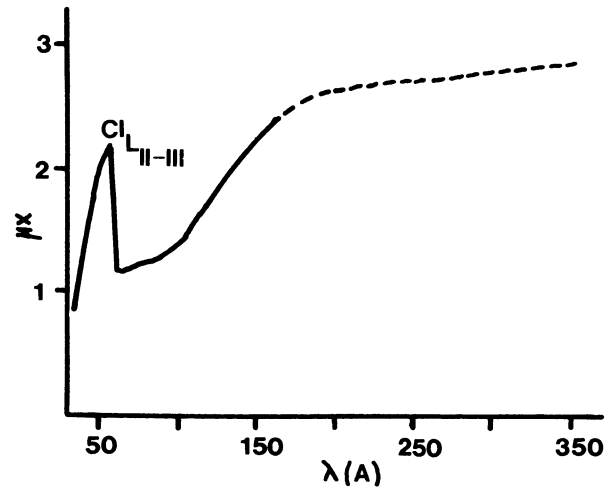

Figure 7. Absorption coefficient spectrum for poly(vinylchloride) film showing the chlorine edge which obscures the carbon edge.

At the scale of 50 to 100Å it has been shown that a number of factors related to the resist properties have an important influence on the quality of

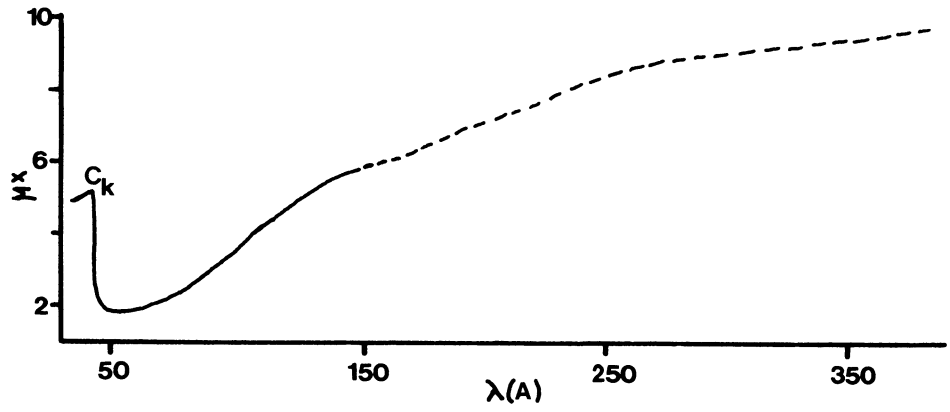

Figure 8. Absorption coefficient spectrum for PMMA.

the image. After obtaining the developed image on the surface of the resist, what is observed is affected by (1) the substructure in the resist itself and (2) any substructure which is produced by the observation technique.

Direct observation of polymers in the electron microscope is known to produce irradiation artefacts. In polyethylene for example, crystalline microstructures are distorted upon examination in the scanning electron microscope[18,19]. Soft x-ray resists are sensitive to electron beam damage and it is inevitable that high resolution images would be changed if the resist is examined directly in the electron microscope.

To circumvent this problem, a replication process of the developed image has been used. First a high resolution soft x- ray image is developed in PMMA. Light development was used to produce a light relief image in the

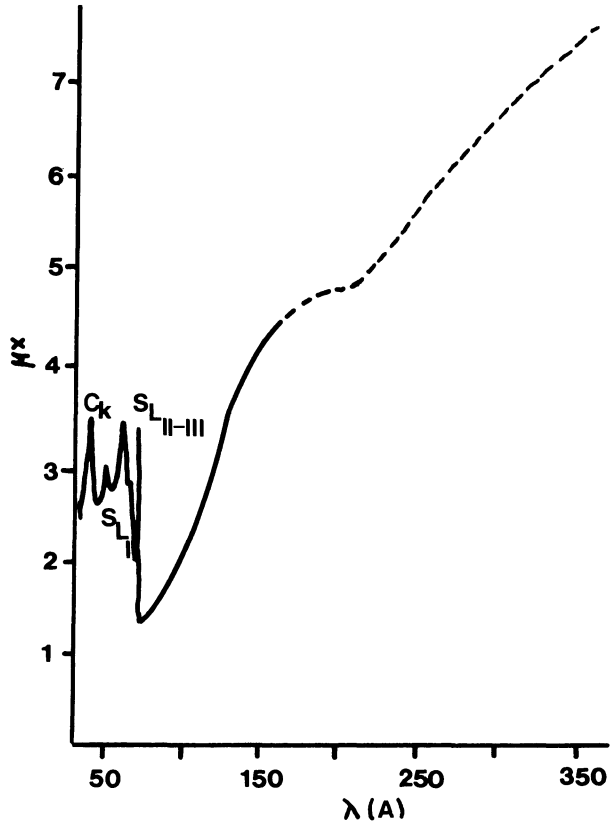

Figure 9. Absorption coefficient spectrum for PBS (resist) revealing the sulphur edges and the carbon edge.

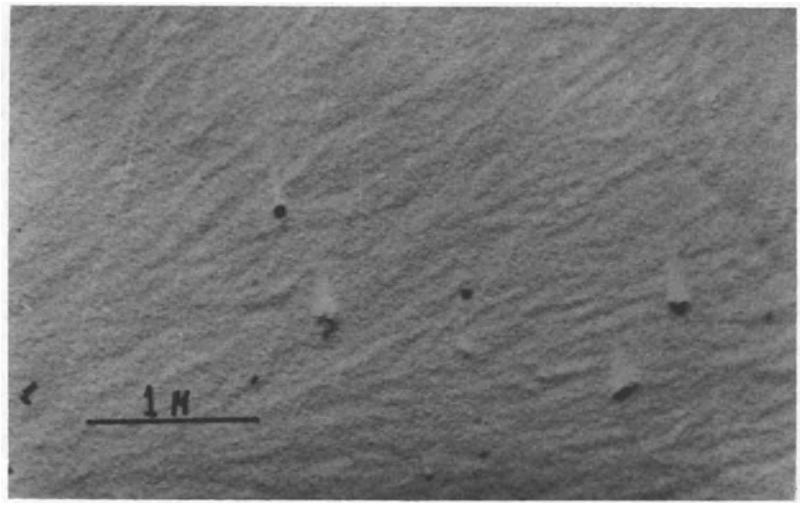

Figure 10. Spherulitic microstructure of cast polyethylene (laboratory soft x-ray source operating at 1.8 keV exposed for 60 hours at low beam current).

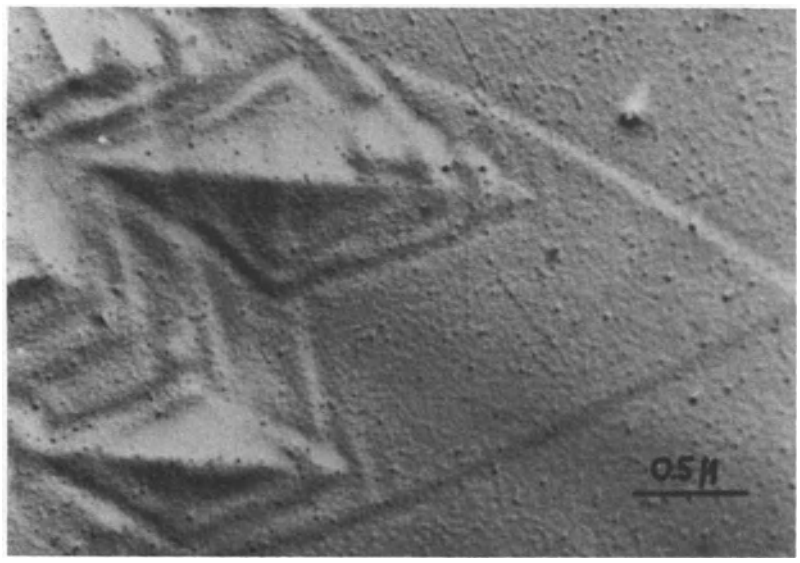

Figure 11. Layered single crystals of polyethylene (each layer 97Å thick)(Laboratory soft x-ray source at 1.8 keV for 30 hours).

surface of the PMMA. This topographic image was then coated with Pt at a shallow angle of about 5° to the PMMA surface using vacuum evaporation. A 120Å thick film of carbon was evaporated onto the Pt. The sandwich on the PMMA was scored into squares about 2 mm on a side. The glass substrate was dissolved by floating the slide on the surface of a 2% solution of HF in water with the carbon film on top. The HF was washed off in distilled water, and the 2mm squares of PMMA supported carbon films were picked up on transmission electron microscope grids. The PMMA was dissolved in acetone, leaving the carbon replicas on the grid. These were examined in the transmission electron microscope. Examples of the images are shown in Figures 10 and 11.

These carbon replicas have potential resolutions better than that proposed for the soft x-ray imaging, so the limitation is simply in the x-ray imaging step. In addition, Pt shadowed carbon replicas are sensitive to small step heights on the surface of the PMMA. The differential heights on the exposed and developed PMMA are a manifestation of the differential absorption in the original specimen, hence good resolution in this sense depends on distinguishing small step heights. The technique therefore produces a stable, electron beam insensitve image with high resolutions in the plane of the image and in the direction normal to the image (useful for microchemical analysis).

ACKNOWLEDGEMENTS

Support from NSERC (Natural Sciences and Engineering Research Council of Canada; Conseil de recherches en sciences naturelles et en genie du Canada) and the Centre for Chemical Physics at the University of Western Ontario is gratefully acknowledged. Related work was supported by the Medical Research Council of Canada. All the absorption measurements were carried out at the Canadian Synchrotron Radiation Facility (CSRF) beamline. Various people, including R. Howe, W. Leung, A. Knaut and P. Perquin have helped in the experiments.

REFERENCES

1. V. E. Cosslett, X-ray optics and x-ray microanalysis, H. H. Pattee, V. E. Cosslett, A. Engström (eds.), Academic Press, 1963.

2. M. J. Bowden, CRC Critical Reviews in Sol. St. Mater. Sci, 8, 223, 1979.

3. E. Spiller, R. Feder, X-ray Optics Applications to Solids, H. J. Queisser (ed.), Topics in Applied Physics, 22, 35, 1977.

4. W. Leung, D. M. Shinozaki, J. Wm. McGowan, accepted for publication in J. Mater. Sc., (1984).

5. B. Ranby, J. F. Rabek, Photodegradation, photo-oxidation and photo-stabilization of polymers, Wiley, 1975.

6. H. H. G. Jellinek, Aspects of Degradation and Stabilization of Polymers, Elsevier, 1978.

7. T. Kelen, Polymer Degradation, Van Nostrand, 1983.

8. A. Charlesby, Atomic Radiation and Polymers, Pergamon, 1960.

9. J. Guillet, Degradation and stabilization of polymers, G. Geuskens (ed.), Applied Science Publishers, 181, 1975.

10. R. J. Hawryluk, *J. Vac. Sci. Techn.*, 19, 1, 1981.

11. P. W. Bohn, J. W. Taylor, H. Guckel, *J. Vac. Technol.*, 12, 1276, 1975.

12. W. W. Flack, D. S. Soong, A. T. Bell, D. W. Hess, *J. App. Phys.*, 56, 1199, 1984.

13. E. D. Feit, M. E. Wurtz, G. W. Kammlott, *J. Vac. Sci. Techn.*, 15, 944, 1978.

14. W. D. Buckley, J. A. Dalle Ave, Proc. 8th Int. Conf. on Electron and Ion Beam Technology, Seattle, 458, 1978.

15. N. D. Wittels in Fine Line Lithography, R. Newman (ed.), North-Holland, 1, 1980.

16. M. Hatzakis, *App. Phys. Lett.*, 18, 7, 1971.

17. M. Hatzakis, *J. Vac. Sci. Tech.*, 12, 1276, 1975.

18. G. Ungar, A. Keller, *Polymer*, 21, 1273, 1980.

19. D. T. Grubb, *J. Mater. Sci.*, 9, 1715, 1974.

FABRICATION OF VERY SMALL STRUCTURES

C.D.W. Wilkinson

Department of Electronics
and Electrical Engineering
The University, Glasgow G12 8QQ U.K.

INTRODUCTION

In the past five years, new technologies have emerged which make possible the fabrication of structures on a nano-metre scale. The driving force behind these developments is the microelectronics industry - as it is economically advantageous to put more electronic devices onto a given area of silicon there is a constant need to reduce the linewidths used in devices. However, there are applications of very small structures in many fields other than electronic device fabrication. The physics required to describe the transport of charges and of phonons changes when the carriers are confined in a small structure - the very smallness of the structure affecting the dynamics of the carriers. In biology microelectronic techniques have been used to make microelectrodes.

The aim of this paper is to discuss the two basic processes involved in the fabrication of very small structures : lithography which is used to alienate the pattern and etching which is used to produce a relief structure in the material. The first step is a formulation of the topography of the pattern to be made ; this may consist of a large scale drawing of the pattern or it may be coordinate data of the pattern stored in a computer. A radiation sensitive layer - the resist is then coated upon the substrate to be patterned, and the resist is selectively exposed. The latent image stored in the resist is transformed into a relief pattern at the development stage. The resist is said to have positive tone if the effect of the radiation is to degrade the resist so that degraded material is removed by the developer (see fig. 1(a)).

On the other hand, if the effect of the radiation is to harden the resist so that upon development the unexposed material is removed the resist is said to have negative tone (see fig. 1(b)). The relief pattern in the resist can then be used in one of two ways.

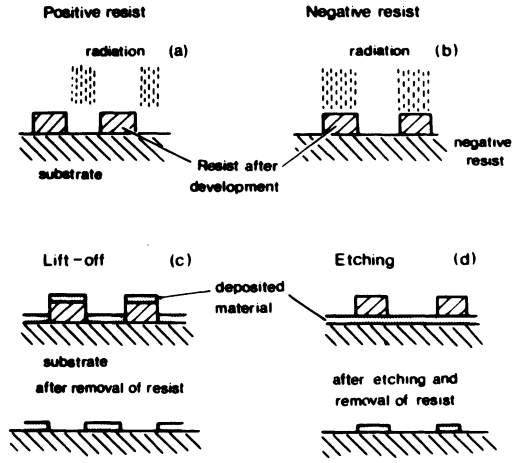

Fig. 1 : (a) positive resist (b) negative resist (c) additive processing (d) subtractive processing

In additive processing a coating of the desired material is deposited upon both the resist and onto the unlying substrate. The resist layer (with its overcoat) is then removed in a suitable solvent leaving the desired pattern of material on the substrate. This process is known as lift-off; it is particularly suitable for high resolution lithography as the need for a high resolution etching process is removed [1,2]. For the process to work well, it is necessary that none of the deposited materials lies on the walls of the resist pattern but only on the top of it. Thus it is desireable to produce an undercut profile in the resist. An alternative method of additive processing is to deposit material by plating from the substrate. If subtractive processing is used, the relief pattern of the resist acts to impede an etch. Thus the underlying substrate is cut away except where it is protected by the resist (see fig. 1(d)).

Photolithography

Photolithographic techniques are employed widely in the microelectronics industry to produce lines down to about one micron in width. The fundamental limit to the available resolution is set by the wavelength of light employed; using UV illumination it is possible to print 0.5 μm gaps and 0.5 μm lines. In the context of high resolution lithography, photolithography is important as it provides a means of delineating a large area but low resolution area which surrounds a high resolution area written by other means. An example is given in fig. (2), which shows a micrograph of a 5 micron wide stripe of polymeric material defined by photolithography with a small middle section defined by electron beam lithography in which the line narrows to 0.3 μm. The resist employed in this case was PMMA (poly(methylmethacrylate)) which can be exposed by both UV light and an electron beam.

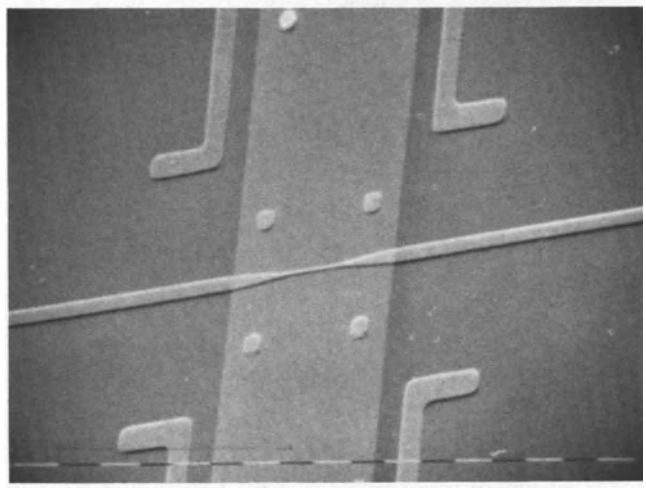

Fig. 2: Overall stripe defined by photolithography with narrow centre section defined by electron beam lithography aligned using the four marks.

Electron Beam Lithography

In essence, electron beam lithography employs a modified scanning electron microscope to provide a focused beam which is used to expose a layer of electron sensitive resist [3]. The beam is scanned over the substrate using a pair of deflection coils and the beam is turned off and on (blank) to define the pattern. The deflection and blanking of the beam are normally under the control of a computer.

The area over which the beam can be deflected is limited; so the specimen is moved between exposures on the stage - often under laser interferometric control.

The major use of such machines at present is to make masks which will be printed using photolithography. For such applications as the minimum linewidth required is say 0.5 micron the electron beam spot size will typically be 0.1 micron. However, for very high resolution lithography a much smaller spot is needed in the range of 2 to 10nm; so converted scanning transmission electron microscopes are used.

Interaction of electron beam with resist

An electron beam on hitting a solid substrate suffers elastic scattering in which the electrons change their direction and in eleastic scattering in which energy is lost to the material and secondary electrons are formed. A Monte Carlo simulation of the trajectories of 100 electrons incident with 50kV energy upon a 0.3 micron resist film on a Silicon substrate is shown in fig. 3. It will be noticed that some electrons penetrate as far as 10 microns and that some electrons are backscattered and return to the resist layer. For the 10kV beam incident upon the same structure, the initial spreading of the beam in the resist is larger and the total penetration much less (see fig. 4).

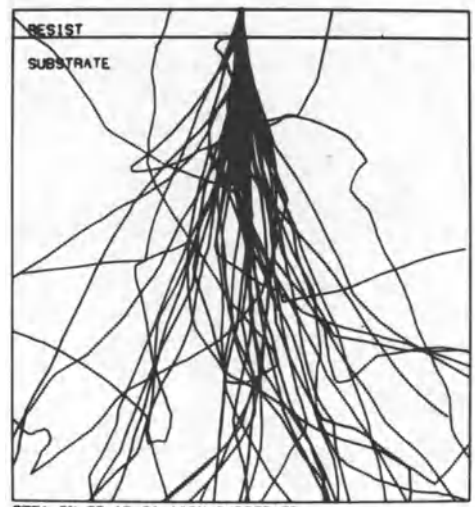

Fig. 3 : Monte Carlo simulation of a 50kV point beam.

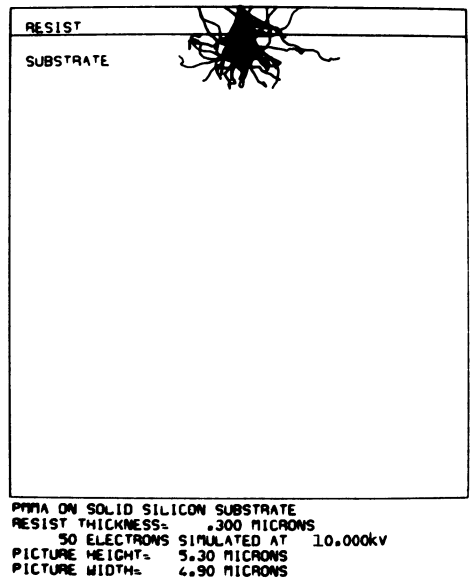

Fig. 4 : Monte Carlo simulation of a 10kV point beam.

It is clear that as the spreading of the primary beam is less at higher voltages, it is advantageous for high resolution lithography to use as high a voltage as possible. The backscattered electrons expose the resist at considerable distances from the point of entry thus adding a general diffuse exposure, and there by reducing the contrast of the written line.

Electron Beam Resists

Many materials can be used as electron beam resists; organic polymers are widely employed as it has proved possible to tailor the polymer chemistry to produce material that has good sensitivity to electron exposure, reasonable resistance to wet and dry (plasma) etching and can easily be applied as a thin film by spinning. In a positive polymeric resist the action of the electron is to reduce the molecular weight of the irradiated polymer thus rendering it soluble in a solvent - nonsolvent developer solution. A widely used positive high resolution resist is PMMA - poly (methylmethacrylate).

Certain inorganic films exhibit positive resist behaviour under high exposure. 1.5nm wide lines have been etched in a film of NaCl using a dosage of 5-50 C/cm^2 (4) Holes 2nm in diameter have been formed in metal beta-aluminas (5) at extreme dosage levels.

In negative polymeric resist the action of the electron beam irradiation is to further polymerise the material rendering it insoluble in a solvent for the unexposed resist. There is normally a trade off between sensitivity and resolution in negative resists. Very high resolution can be obtained in negative polymeric resists of relatively low starting molecular weight - an example is shown in figure 5.

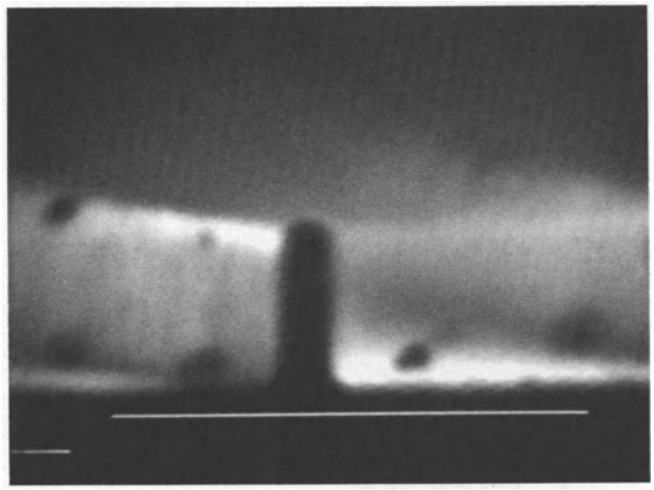

Fig. 5 : 0.1 μm wide 0.4 μm high negative resist pattern in Phillips HRN resist 1 micron marker.

An extreme case of this is the use of hydrocarbon polymerised by the electron beam as a negative resist by Broers (6) which made 8nm wide lines by etching of a Tungsten-Rhenium film.

The use of membrane substrates

The effects of back-scattering can be eliminated by using a very thin substrate. Beaumont et al [1] exposed a positive electron beam resist PMMA 50nm thick on a thin (50nm) carbon substrate and after development, overcoated the specimen with 10nm of Gold-Paladium and then used lift-off to leave 16nm lines on centre to centre spacings down to 55nm. The specimen could be examined in a TEM (one of the advantages of using a thin substrate). Broers[7] using a 3nm probe exposed PMMA on a Silicon nitride membrane and argon beam etched 12nm wide lines.

Comparison between thick and thin substrates

A direct comparison has been made of electron beam lithography on thick and thin substrates (8). A membrane of Si_3N_4 was formed by selective etching of Silicon and overcoated with resist. The electron beam was scanned from the solid substrate onto the membrane. For lines spaced 1 micron apart there was no change in linewidth between the thick and thin substrate regions (see fig. 6)

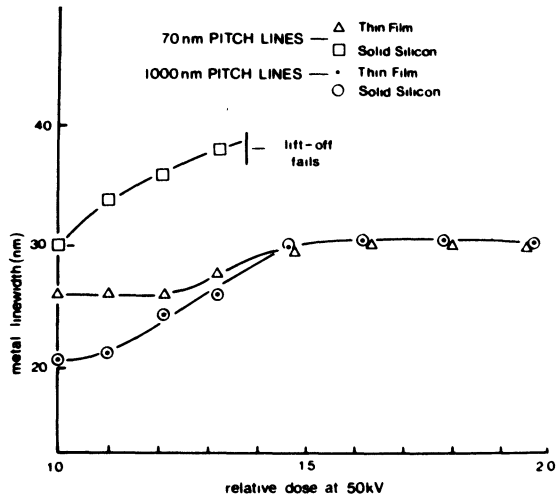

Fig. 6 : Linewidth versus exposure on thin and thick substrates.

However, for lines spaced 70nm apart the lines on the thick substrate were wider and as the exposure was increased from the minimum level necessary for exposure, it was found the exposure latitude before lift-off failed was small.

The use of thin substrates is not limited to dielectric films Mackie et al (9) formed membranes of GaAs 50nm thick and showed that 20nm lines could be written on these membranes.

A vital aspect of lithography is an ability to align a second exposure to the pattern created after the first exposure. For this purpose, an image of the first pattern must be formed in the microscope and in general scanning transmission images have higher contrast than scanning reflection images. Realignment to 30nm has been demonstrated on thin membranes (10).

Factors limiting the resolution of electron beam lithography

When a primary electron beam strikes a layer of resist, low energy secondary electrons are formed. The range of these low energy secondary electrons ultimately limits the resolution of electron beam lithography.

The range of these low energy electrons [11] has been measured directly by exposing PMMA to a low voltage beam through a grid and after development of the PMMA, finding the deptn of exposed regions. The results are shown in fig. 7.

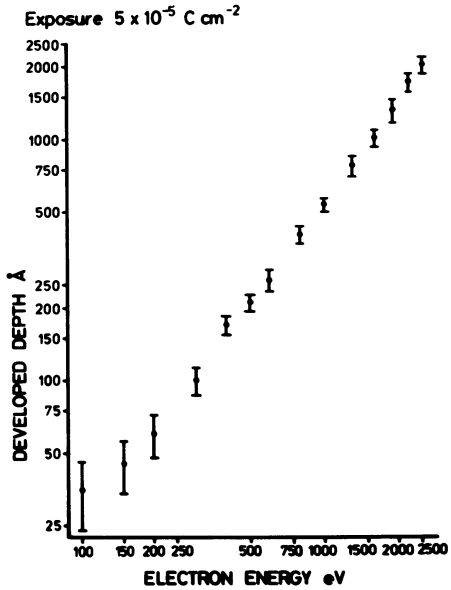

Fig. 7 : Depth of exposure regions after development as a function of incident voltage in PMMA.

In order to calculate the minimum linewidth that can be obtained, it is necessary to know the distribution of energy of secondary electrons. This can be obtained by measuring the energy of a high voltage electron beam after passage through a thin film of PMMA. The resulting predicted minimum linewidth is 3nm or so for an infinitely narrow beam, while the experimental results obtained for minimum linewidth in PMMA is 11nm with a 8nm beam [12] (see fig. 8) giving reasonable agreement. On the other hand the minimum centre to centre spacing that can be obtained is of the order of 40nm, which suggests that some other factor is playing a role.

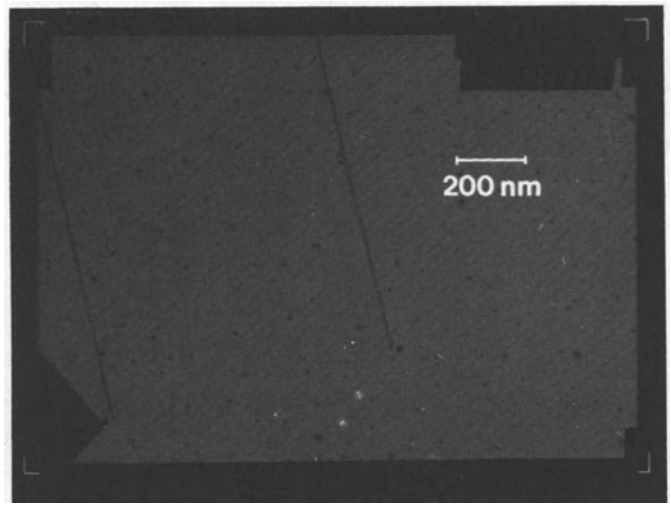

Fig. 8 : 11nm wide metal lines formed by lift-off.

A possible explanation lies in the size of the PMMA polymer. It is believed that when PMMA is spin-coated onto a substrate, the polymer chains are not left randomly intertwined but rather tend to be coiled so that in a small volume there are only a limited number of coils. When the exposure of a small volume has reduced the molecular weight of the polymers sufficiently, all the affected polymers will develop.

One potential limit to resolution must be considered in all lithographic processes - statistical fluctuations in the number of particles (electrons, ions or protons) which are necessary to expose a small area. For example in PMMA a dosage of $3 \times 10^{-3} C/cm^2$ is used in high resolution pattern writing. Thus a 10 x 10nm area receives some 2000 electrons on average with a fluctuation in this number of the order of $\sqrt{2000}$. This 2% fluctuation is acceptable; but clearly this resist would not be suitable for the exposure of a 1 x 1nm area even if all other constraints were removed.

X-ray lithography

X-rays have been used for printing high resolution patterns written by some other means. The basic process is similar to the printing using UV light employed in photolithography. The desired pattern composed of regions opaque to X-rays is made on a substrate transparent to X-rays and this mask is placed close to a substrate coated with an X-ray resist and exposed to X-rays [13,14]. The X-rays illumination give rise to secondary electrons which expose the X-ray resist.

The choice of X-ray wavelength for maximum resolution is a compromise. For a given feature size the choice of energetic X-rays having a short wavelength reduces the effects of diffraction but increases the range of the secondary electrons. For sub 0.1μm features, Carbon radiation of 4.4nm wavelength is normally employed while for 0.5μm feature size printing Rb(0.46nm) and Si(0.83nm) targets have been used.

Using a mask fabricated by shadowing techniques Flanders [15] demonstrated that 17.5nm lines and spaces can be printed by X-ray lithography. The mask consisted of sets of two tungsten lines, 17.5nm wide and approximately 100nm high, spaced by 20nm of carbon. The mask by successive shadow evaporation of tungsten and carbon onto a square wave relief pattern of period 180nm formed in a thin polyimide membrane. The resulting mask showed a high transmission (contrast) ratio for the Carbon K radiation of 90% (Carbon) to 18% (Tungsten). This high contrast ratio arises from the high X-ray attenuation of tungsten and the extreme aspect ratio of metal lines which are available using shadowing techniques.

In replication of arbitrary patterns written by electron beam lithography, metal lines in the original mask 114 down to 68nm in width were replicated into gaps between the metal on the reproduced metal pattern 90 to 50nm wide [16]. The metal mask lines were gold palladium 55nm thick which had a transmission of 0.6 at Carbon K wavelength, which gave a relatively low contrast image.

Achievement of narrow lines of an arbitrary pattern replicated by X-rays on a solid substrate requires very high aspect ratio lines on the mask. It seems unlikely that X-ray replication of e-beam written masks will be an easily used technique for linewidths less than 30nm in the near future.

Etching

In general a wet chemical etch removes material isotropically. Thus when etching takes place through a window in an etch resistant layer on top of the layer to be etched, undercutting of the window occurs. (see fig. 9.) If the aspect ratio (that is the ratio of the height to the width) of the desired final feature is small then often the undercutting can be tolerated. When one is concerned with very high resolution patterns of sub-micron sizes, it is often necessary to make high aspect ratio features (for example sub - 0.1

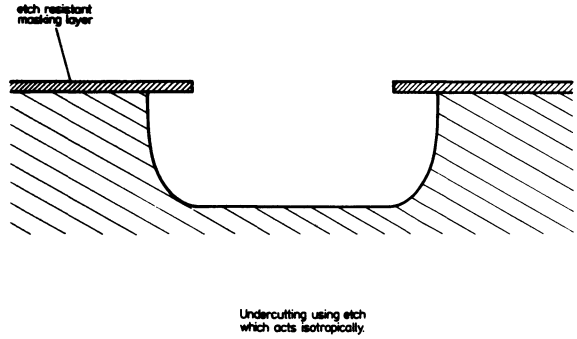

Fig. 9 : Effect of isotropic etch.

micron wide gates on Silicon MOSFET need to be as high as possible, to reduce the electrical resistance). Such high aspect ratios requires that the etching be anisotropic.

This can be achieved in two ways - either by using a chemical etches which attack different crystallographic faces of a material at different rates (this can be understood in a crude way by noting that the density of atoms in different planes differs) or by using ions directed at the surface to erode it preferntially.

Anisotropic chemical etching

In both the two examples of the anisotropic etching by wet chemicals to be discussed, the material are important in the electronic industry and probably the effects would not have been studied in such detail otherwise. (see fig. 10).

Refluxed boiling sodium hydroxide attacks the (100) plane of Silicon but hardly erodes a (111) plane. Thus if a square window is cut in a layer of silicon oxide on top of a (100) face of Silicon, after etching a rectangular pyramid is formed [17]. Again if a (110) substrate is used and a series of grooves parallel to the (111) direction are opened in the oxide then a series of fins are formed in the Silicon - fins 300 microns deep and a few microns wide have been demonstrated.

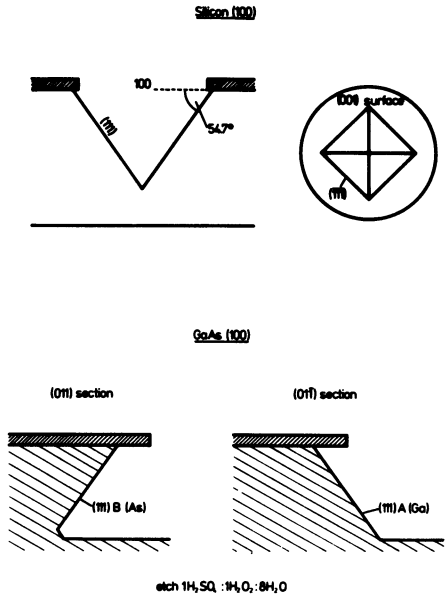

Fig. 10: Typical etching pattern using anisotropic etches in Si and GaAs

In Gallium Arsenide the position is more complicated. GaAs is not centro-symmetric. The (111) plane has the minimum etch rate as in Silicon - but it is necessary to distinguish between (111)A or Ga rich surface and the (111)B or AS rich surface. Thus (011) section on an etched groove on a (100) surface gives a dovetailed section while a (011) section shows a V-groove [18].

Such selective etching in Silicon has been used to form a variety of structures, from nozzles for ink jet printers [19] to V-grooves for better power devices. With the correct etches the (111) surface on which the etch stops can be atomically smooth - this has been employed as a means of measuring the size of focused electron beams down to 4nm.[20].

Ion Etching

When an ion in vacuum is directed at a surface, the resulting collision and/or chemical reaction can cause erosion of the surface. A patterned layer of different etch rate deposited on the surface is used to transfer the desired pattern into the surface. If the ions used are chemically inert (for example the noble gases), the erosion of the surface is determined by purely physical phenomena

and the phenomena is described as physical sputtering. On the other hand if a chemically active specie is used, both physical and chemical processes can take place.

The ions can be formed in a variety of ways. In ion beam etching, a gas is ionsied by a hot filament and the ions are extracted as a beam through a series of charged grids. Alternatively, an r.f. discharge can be used to ionise the gas. It is helpful to divide etching using an r.f. charge into two regimes. In plasma etching, a relatively high pressure gas is ionised often by electrodes outside the vacuum chamber and the ions suffering many collisions acquire relatively low energy. The substrate is immersed in the plasma and the etching action is mainly chemical in nature, and is usually isotropic. On the other hand, in reactive ion etching, a relatively low pressure gas is ionised by a r.f. field between two electrodes, the substrate to be etched is placed on the driven electrode while the other is earthed and a considerable d.c. voltage is built up between the electrodes. This d.c. voltage causes the ions to have considerable energies on impact with substrate, the etching action is both chemical and physical and the etching is often an isotropic. The distinction between the two regimes is not sharp but is convenient.

There is very great interest in this field at the moment, so no attempt can be made to cover the whole area. Rather an example will be considered to illustrate the techniques involved.

Polyimide Transfer Layer

In high resolution lithography, it is often difficult to combine qualities of high resolution and good etch resistance in a single material. Multiple level lithographic techniques have been developed in which the uppermost level is used to create the pattern, which is transferred into an underlying etch-resistant layer, which itself is used as the mask for the desired etching of the substrate. A common choice for the intermediate etch-resistant layer is polyimide, an organic polymeric coating widely used in the electronics industry which withstands high temperatures (350°C) and attack by many common chemicals. Polyimide has the property (which it shares with other organic polymers) that under reactive ion etching in oxygen vertical walls are formed and ridges of high aspect ratio can be formed.

Singh et al [21] formed ridges of polyimide by reactive ion etching in oxygen which were 30nm wide and 120nm high. The polyimide was masked by a silver doped arsenic trisulphide resist layer - a negative electron resist. The etch rate of As_2S_3 in O_2 is very small. The polyimide was etched in a 13.56 MHz r.f. discharge of pure O_2 at a pressure of 20 m Torr and a glass flow rate of 20 scc/minute.

Acknowledgements

My thanks go to my colleagues at Glasgow University ; in the Department of Electrical Engineering, Dr. Steve Beaumont, Professor John Lamb, Dr. Bhanwar Singh (now at Pennsylvannia State University, Philadelphia), Mr. Colin Binnie, Dr. Stuart Mackie, Dr. Steve Rishton (now at IBM Research Centre, Yorktown Heights), Mr. Will Patrick, Mr. Calum MacGregor and Mr. Clive Reeves, and in the Department of Natural Philosophy, Professor Bob Ferrier and Dr. John Chapman. The technical assistance of Mr. John Crichton, Mr. D. Gorlay, Mr. A. Stark was vital to this work. I would like to thank Professor Hank Smith of MIT, Dr. Rich Howard of BTL, Holmdel, Professor Dick Pethrick of Strathclyde University and Professor Dan Prober of Yale for useful conversations.

The work at Glasgow University is supported by the Science and Engineering Research Council (U.K.).

References

1. S.P. Beaumont, P.G. Bower, T. Tamamura and C.D.W. Wilkinson, 'Sub 20nm wide metal lines by electron beam exposure of thin PMMA films and lift off', Appl. Phys. Lett. 38, 436, 1981.
2. H.G. Craighead, R.E. Howard, L.D. Jackel, and P.M. Mankiewich, '10nm linewidtn electron beam lithography on GaAs', Appl. Phys. Lett. 42, 38-40 1983.
3. G.R. Brewer, 'Electron beam technology in microelectronic fabrication', Academic Press, New York, 1980.
4. M. Isaacson and A. Murray, 'In-situ vapourisation of very low molecular weight resists using 1/2nm diameter electron beams' J. Vac. Sci. Technol., 19, 1117-20, 1981.
5. M.E. Mochel, C.J. Humphreys, J.A. Eades, J.M. Mochel and A.M. Petford, 'Electron beam writing on a 20A scale in metal aluminas', Appl. Phys. Lett. 42, 392-394 1983.
6. A.N. Broers, W.W. Molzen, J.J. Cuomo and N.D. Wittels, 'Electron beam fabrication of 80 metal structures', Appl. Phys. Lett., 29, 596-598 1976.
7. A. Broers, 'Resolution limits of PMMA resist for exposure with 50kV electrons', J. Electrochem. Soc. 128, 166-1970, 1981.
8. S.P. Beaumont, B. Singh, C.D.W. Wilkinson, 'Very high resolution electron beam lithography - thin films on solid substrates?', Porc. 10th Electron and Ion Beam Sci. Technol. Conf., Montreal, Canada, 1982.
9. W.S. Mackie, S.P. Beaumont, C.D.W. Wilkinson and J.S. Roberts, 'High resolution lithography on thin active semiconductor membranes', Proc. 10th Electron and Ion Beam Sci. Technol. Conf., Montreal, Canada, 1982.

10. W.S. Mackie, S.P. Beaumont, P.G. Bower and C.D.W. Wilkinson, 'Very high resolution alignment of e-beam written patterns' Microcircuit Engineering 82, Grenoble, France.
11. S.A. Rishton, S.P. Beaumont and C.D.W. Wilkinson, 'Measurement of the effect of secondary electrons on the resolution limit of PMMA', Proc. Microcircuit Engineering 82, Grenoble, 1982.
12. W.S. Mackie, Ph.D. Thesis, Glasgow University, June 1984, (unpublished).
13. H.I. Smith, P.L. Spears and S.E. Bernackie, 'X-ray lithography: A complementary technique to electron beam lithography', J. Vac. Sci. Tech., 10, 913-917, 1973.
14. D. Maydan, G.A. Coquin, J.R. Maldonado, S. Somekh, D.Y. Lou and G.N. Taylor, 'High speed replication of sub-micron features on large areas by X-ray lithography', IEEE Trans. El. Devices, ED-22, 429-433, 1975.
15. D.C. Flanders, 'Replication of 175 lines and spaces in polymethylmethcrylate using X-ray lithography', Appl. Phys. Lett. 36, 93-96, 1980
16. S.P. Beaumont, P.G. Bower, T. Tamamura and C.D.W. Wilkinson, 'Replication of very nigh resolution e-beam written masks by carbon K X-ray contact printing', Proc. Microcircuit Eng. 81, Lausanne, 1981.
17. D. B. Lee, 'Anisotropic etching of silicon', Journal of Applied Physics 46, 4569-4574, 1969.
18. D.W. Shaw, 'Localised GaAs etching with acidic hydrogen peroxide solutions', J. Electrochem Soc. Am. 128, 874-880, 1981.
19. E. Bassons and E.F. Baran, 'The fabrication of high precision nozzles by the anisotropic etching of (100) silicon', J. Electrochem. Soc. Am., 125, 1321-1327, 1978.
20. S. Rishton, S.P. Beaumton and C.D.W. Wilkinson, 'Measurement of the profile of finely focused electron beams in a scanning electron microscope', J. Phys. E. Sci. Instrum. 17, 296-303, 1984.
21. B. Singh, S.P. Beaumont, A. Webb, P.G. Bower and C.D.W. Wilkinson, 'High resolution patterning with Ag_2S/As_2S_3 inorganic electron beam resist and reactive ion etching', J. Vac. Sci. Technol. B 1, 1174-76, 1983.

LENSES FOR SOFT X-RAYS AND X-RAY MICROSCOPY EXPERIMENTS

G. Schmahl, D. Rudolph, B. Niemann,
P. Guttmann, and J. Thieme

Universität Göttingen,
Forschungsgruppe Röntgenmikroskopie
Geismarlandstr. 11, D-3400 Göttingen
Fed. Rep. of Germany

INTRODUCTION

X-ray microscopy can be used for investigations in the fields of biology, medicine, physics, especially materials science and probably other fields, as e.g. polymer science. In biology, it is possible to investigate specimens with a thickness of up to several microns, especially living cells and cell organelles in a natural state. For such investigations, the wavelength region between 2.3 nm and 4.4 nm is best suited because there is about an order of magnitude difference between the absorption coefficients for water and protein. This difference provides a natural contrast mechanism for the investigation of wet biological materials.

Microscopy with soft x-rays requires intense x-ray sources as well as high resolution x-ray lenses.

In this paper, the development of zone plates as x-ray lenses by use of a uv-holographic lithography technique is discussed. Condenser zone plates as well as high resolution micro zone plates for an imaging and a scanning x-ray microscope are described. In addition, results of x-ray microscopy experiments are presented, which have been performed with an imaging x-ray microscope installed at the BESSY electron storage ring in Berlin.

ZONE PLATES

Zone plates are circular gratings with radially increasing line density. The imaging with zone plates of zone numbers n > 100 obeys the same laws as imaging with thin refractive lenses. With r_1 = radius of the innermost zone, r_n = radius of the n-th zone, n = zone number and m = number of diffracted order, the focal length of a zone plate is approximately given by $f_m = r_1^2 \cdot \lambda^{-1} \cdot m^{-1}$. Because $f_m \propto 1/\lambda$, a zone plate has to be used with quasimonochromatic radiation with a bandwidth $\Delta\lambda$ given by $\lambda/\Delta\lambda \simeq n \cdot m$. The width of the outermost zone is $dr_n = r_n/(2n)$. The smallest distance of two point sources which can be resolved with a zone plate is given by $\delta \approx dr_n/m$. The maximum diffraction efficiency, i.e., the diffracted flux in a certain order divided by the incoming flux, is in the case of amplitude zone plates approximately 10% in the first, 2.6% in the second, and 1.2% in the third diffracted order. Up to now amplitude zone plates with efficiencies between 2% and 6% have been used. Higher diffraction efficiencies can be obtained by use of phase zone plates.

For x-ray microscopy experiments one needs two types of zone plates. First, the object has to be illuminated by a condenser. The condenser has to collect as much radiation as possible from the x-ray source. Second, to image the object, a high resolution zone plate is necessary, i.e. a zone plate with an outermost zone width dr_n as small as possible. This zone plate should have only one hundred to some hundred zones in order not to restrict the usable x-ray bandwidth too much. In consequence, high resolution zone plates have very small diameters in the region of about twenty microns to some hundred microns. We therefore call them micro zone plates.

As mentioned above and described in more detail[1,2,3] micro zone plates as well as condenser zone plates can be made using a holographic lithography tecnnique. Using this technique zone plate patterns are exposed by superimposing two coherent uv or visible laser beams of wavelength λ_v on a photoresist-coated substrate. The main problem in this case is to avoid

aberrations caused by the fact that the zone plate structure is generated with uv or visible light and is used in the microscope with a wavelength which is about a factor of a hundred shorter. These aberrations can be taken into account by use of aspheric wavefronts as discussed in more detail elsewhere[1,2,3].

The procedure to construct zone plates can be divided into the following five steps.

1. A zone plate interference fringe system $r_n = f(\lambda_x, f_x, n, V)$ is calculated. λ_x is the wavelength used in the x-ray microscope, f_x is the focal length, n is the number of zones and V is the x-ray magnification.
2. Aspherical wavefronts of wavelength λ_v are calculated, the superposition of which results in the wanted zone plate interference fringe system.
3. An optical system is calculated and built which generates in good approximation the required two aspherical wavefronts.
4. A photoresist layer is exposed with the zone plate interference structure generated by the superposition of the two wavefronts.
5. The photoresist zone plate structure is transferred into a zone plate consisting of metal rings on a thin foil sufficient transparent to soft x-rays.

Micro Zone Plates

Figure 1 shows one example of an optical arrangement to generate the interference fringe system of a micro zone plate, namely MZP3. A spherical wavefront of 257 nm radiation is devided by a four - element partly transparent beamsplitter made from fused silica into two convergent spherical beams. The uv wavelength is obtained by second harmonic generation of the 514.5 nm Ar^+ laser line.

To get the desired outer zone width of about 50 nm the last lens of the aplanatic lens system has to be built as an immersion lens. Then the effective construction wavelength will be $\lambda_v/n = 171.08$ nm and the smallest reachable outer zone width will be $dr_n = \lambda_v/4n = 43$ nm.

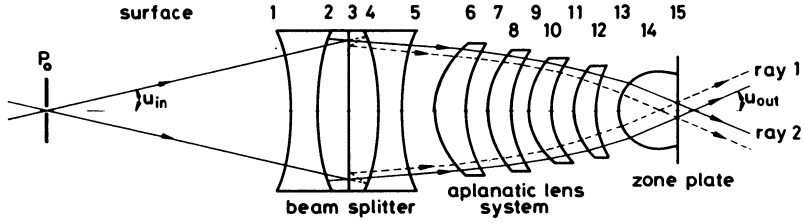

Fig. 1. Optical arrangement for the generation of the interference structure of a micro zone plate (MZP3).

The optimization of the parameters of the construction optics for the micro zone plate as well as the evaluation of its properties was performed by ray tracings. One can use ray tracing methods for the evaluation of the properties of an optical system when the approximation condition for geometrical optics (wavelength neglibly small, $\lambda \rightarrow 0$ or dimensions of the optical system large compared to λ) is satisfied[4]. This condition is satisfied for ultrasoft x-rays and for the uv-light used for the construction of the zone plate. The methods of ray tracings are described elsewhere[2].

To make a statement about the aberration-limited resolution d_{min} of the examined micro zone plate the diameter δ_{min} of the minimal confusion circle has to be determined: $d_{min} = \delta_{min}/V$. The micro zone plate will be a good one, if the aberration-limited resolution is substantially smaller than the diffraction-limited resolution: $d_{min} << dr_n$.

With the optimum solution for the optical system a micro zone plate with the following parameters has been constructed:
$r_1 = 1.756\ \mu m$, $f_x = 1.307$ mm for $\lambda_x = 2.36$ nm
$r_n = 27.8\ \mu m$, $dr_n = 55$ nm, $n = 251$.

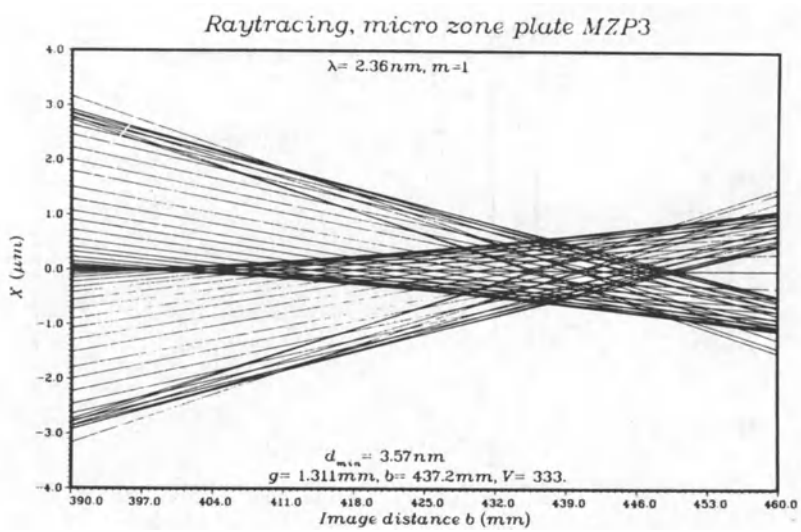

Fig. 2. Ray tracing through the micro zone plate in the optimum case.

Figure 2 shows a ray tracing for the micro zone plate. With an object distance of g = 1.311 mm an image distance of b = 437 mm is obtained for the minimal confusion circle, corresponding to a magnification of V = 333. The aberration-limited resolution is d_{min} = 3.6 nm and substantially smaller than the diffraction-limited one.

Using ray tracing methods the following rough relations were found:

1. The variation of the lens radii for the construction of a good zone plate cannot be done continuously, because the manufacturer of the lenses can only produce discrete sphere radii. Figure 3 shows the aberration-limited resolution as a function of the deviation of the lens radii from their optimum values. As expected the radius of the lens surface 14 (see Fig. 1) is the most critical one.
2. The displacement of the intrinsic aplanatic surfaces 12 and 14 (see Fig. 1) is allowed in only a small region. The position of this surfaces can therefore be used as precision correction, whereby the position of surface 14 is considerably more critical than that of surface 12.

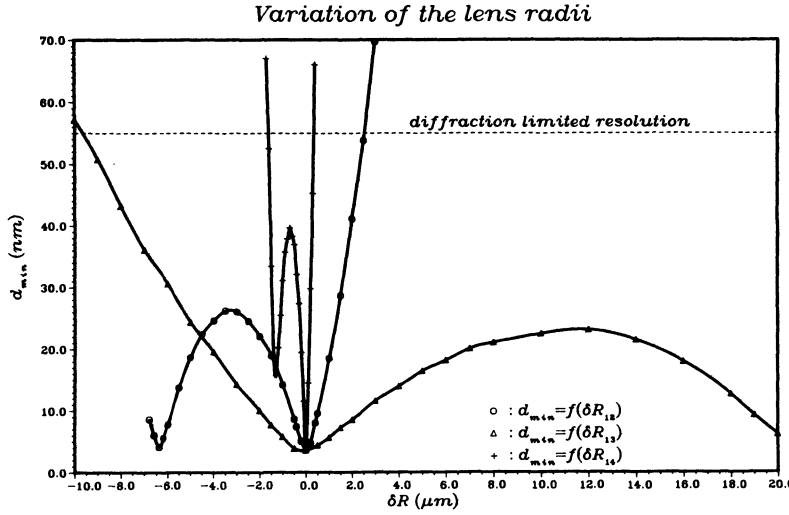

Fig. 3. Dependence of aberration-limited resolution on deviation of the lens radii from the optimum values.

3. The displacement of surface 13 is allowed in a greater region. Its position can be used for the rough determination of the solution for the zone plate construction optic.

The optimum solution was found especially by variation of the position of surface 13 and variation of the point P_o. The calculations were performed with the UNIVAC 1100 at the Gesellschaft für wissenschaftliche Datenverarbeitung (GWD) Göttingen[5].

The starting point for the calculations is the optimum solution for the optical system. If not otherwise stated, all curves for the aberration-limited resolution of the zone plate are valid for the x-ray wavelength λ_x = 2.36 nm and the magnification V = 300.

Calculations for the variation of the immersion lens thickness are essential because it is not known where exactly the micro zone plate will be built. The thickness of the immersion liquid and eventual dust particles will influence the position of the zone plate. It is the same whether the immersion liquid between the lens surface and the resist layer or a different

thickness of the immersion lens will give an other position for the zone plate than in the optimum case, because the immersion lens material and the immersion liquid have approximately the same refractive index. Figure 4 shows the result: for a constant P_0-value the usable range for the position ZZP of the zone plate is 2.4 µm (curve 1). For optimizing the P_0-value simultaneously this range will be expanded to 6.7 µm (curve 2).

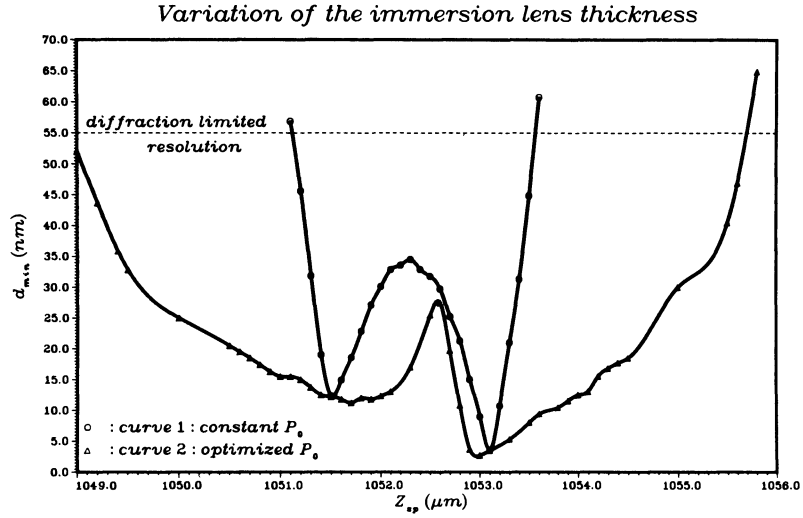

Fig. 4. Dependence of aberration-limited resolution on the immersion lens thickness.

In practical work, the size of the two wavefronts at the zone plate position will be a good indicator for the adjustment of the construction optic.

In the following the imaging properties of the micro zone plate, built with the optimum optical system, are evaluated. The interesting properties are the depth of field, the object field which can be imaged with full resolution, and the usable wavelength range.

The depth of field is very interesting for thick specimens. Figure 5 shows the aberration-limited resolution d_{min} for constant image distance as a function of the deviation δg from the desired object distance g. The usable range is $\delta g = \pm 1.3$ µm.

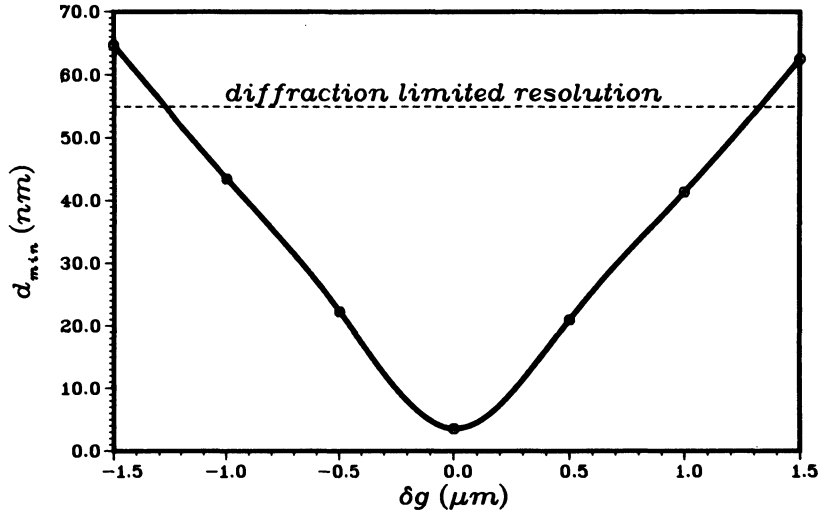

Fig. 5. Depth of field of the micro zone plate MZP3.

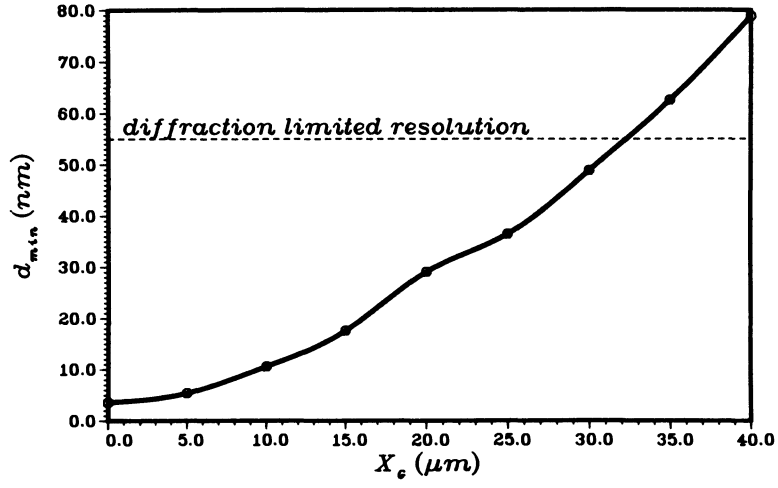

Fig. 6. Usable object field of the micro zone plate MZP3.

The aberration-limited resolution as a function of the displacement of the object point from the optical axis is shown in Fig. 6. The object field which is imaged with full diffraction-limited resolution is a circle around the optical axis of the zone plate with a radius of 32.5 μm. This means that 1047 x 1047 image points with full resolution of 55 nm can be imaged.

Calculations show that the use of the micro zone plate for a certain wavelength range around the wavelength for which the calculations have been performed is possible. In the range from λ_x = 0.3 nm up to λ_x = 10.3 nm the aberration-limited resolution is smaller than the diffraction-limited one (see Fig. 7).

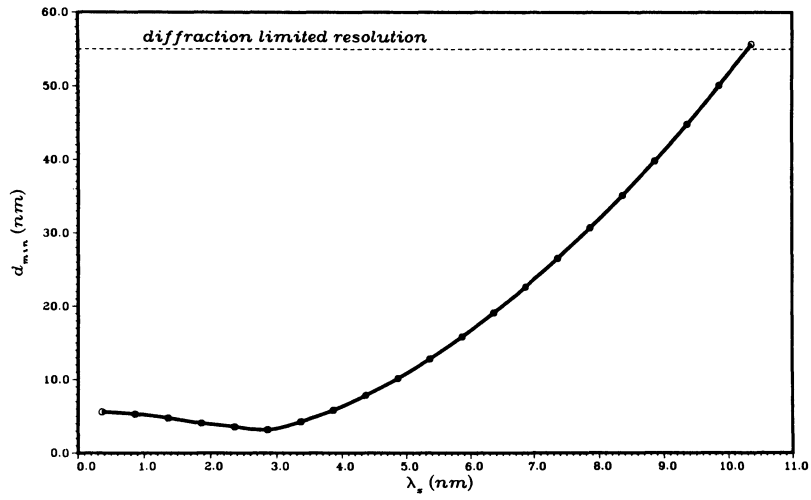

Fig. 7. Dependence of aberration-limited resolution on wavelength for MZP3.

Condenser Zone Plates

Figure 8 shows an optical arrangement for the generation of the zone plate interference structure of a condenser zone plate (KZP6) which has been built for our imaging x-ray microscope. For the superposition of two spherical wavefronts a photoresist phase hologram H (compare Fig. 8b) is illuminated with 257 nm radiation. The zero-order radiation of the slightly divergent wave which transmits the hologram is reflected by a spherical mirror of 40 mm diameter and a semitransparent plane mirror, resulting in one aspherical wavefront. The second aspherical wavefront is the diffracted first-order radiation of the hologram H. The interference fringe system of this hologram has been designed so that the resulting first-order wavefront, when superimposed with the zero-order wavefront - reflected by the spherical and semitransparent mirrors - results in the required interference fringe system. Because of the large zone number $n = 3.8 \cdot 10^4$ and the rather small width of the outermost zone $dr_n = 0.06\mu m$, the aberration correction requires a special optical system for the construction of the hologram H. This system is shown in Fig. 8a. The hologram is generated with $\lambda_v = 457.9$ nm and is recorded on a spherical surface. To match the fringe system of the hologram to the calculated fringe system the following parameters were varied during the calculations: curvature of the mirror in the left part of Fig. 8a, the angles of the superimposed wavefronts in respect to the normal of the hologram surface and the curvature of the hologram. The calculations in the course of which the parameters of the optical system are varied to optimize the imaging properties of the condenser zone plate were performed using ray tracing methods. As a result a point source in a distance of 15 m is imaged to a aberration-limited diameter of about 4.5 μm using an x-ray wavelength of 2.36 nm. This value is smaller than the object field illuminated by the condenser in the imaging x-ray microscope.

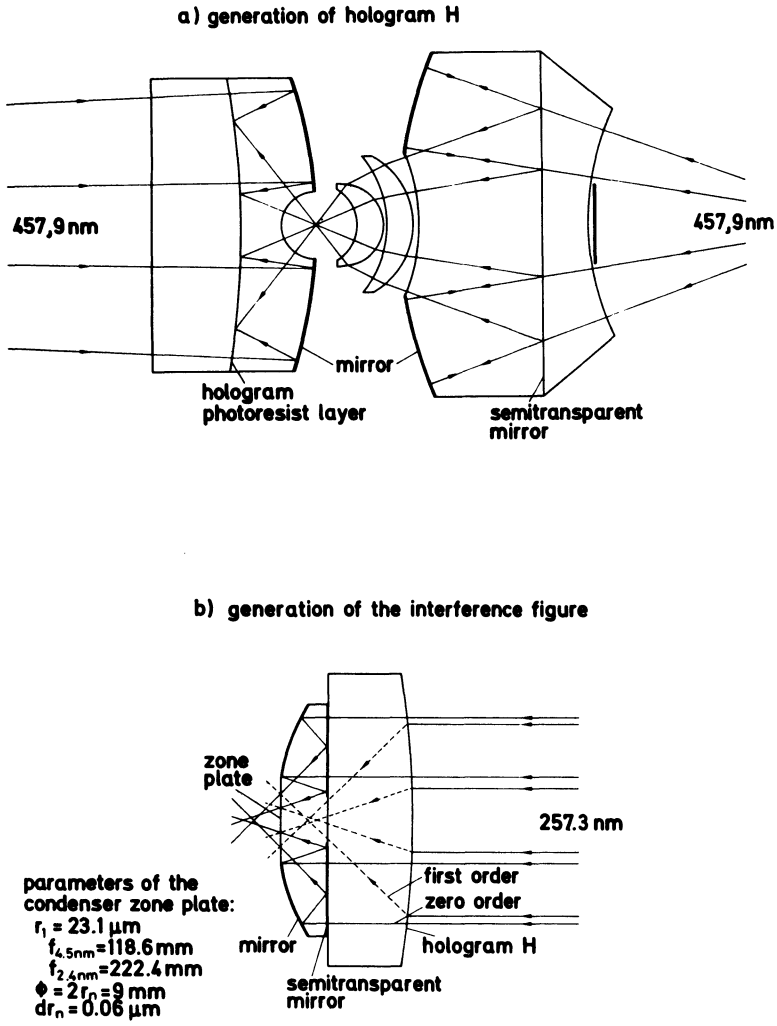

Fig. 8. Optical arrangement for the generation of the interference structure of condenser zone plate KZP6 for the imaging x-ray microscope.

Figure 9 shows the optical arrangement for the generation of a condenser zone plate KZP5 with r_1 = 36.15 µm, r_n = 1.25 mm, dr_n = 0.5 µm and n = 1196. In this case the lens L1LS is used as an immersion lens. The optical system can be used without the lens L1LS to construct the condenser KZP4 with r_1 = 49.8 µm, r_n = 1.25 mm, dr_n = 1 µm and n = 630. The two condenser zone plates are being constructed for the use in the scanning x-ray microscope.

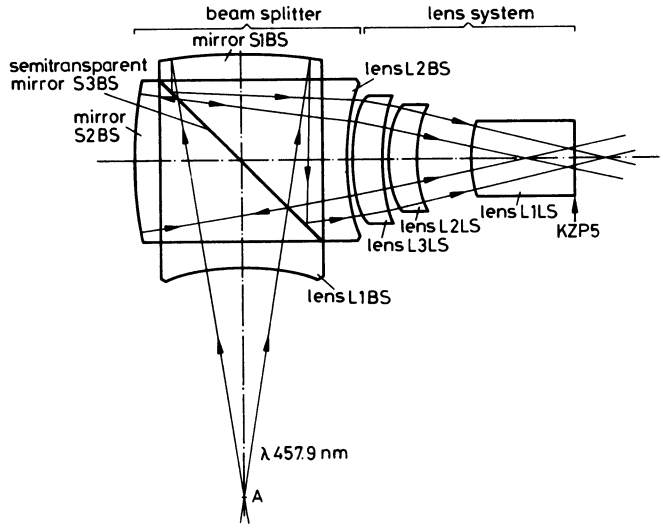

Fig. 9. Optical arrangement for the generation of the interference structure of condenser zone plates KZP5 and KZP4 for the scanning x-ray microscope.

The best solution of the optical system of Fig. 9 was found by use of ray tracing methods. In Fig. 10 a ray tracing through KZP5 is shown built with the best solution of the optical system. As can be seen in Fig. 10, the smallest circle of confusion, caused by aberrations, has a diameter of 27 nm which is very small compared to the diffraction-limited value.

In practice optical systems can only be built with certain tolerances. The radii of the spherical surfaces can be manufactured in very good agreement with the theoretical values. The thickness of the optical elements, however can vary. In Fig. 11 the influence of thickness variation of single elements of the optical arrangement of Fig. 9 on the aberration-limited resolution of the condenser zone plate KZP5 is

demonstrated. The quality of the condenser zone plates can in addition be influenced by a misalignment of the semitransparent mirror S3BS, which can in practice be as high as ±2'. This can be compensated by readjusting lens L1BS and mirror S1BS[6].

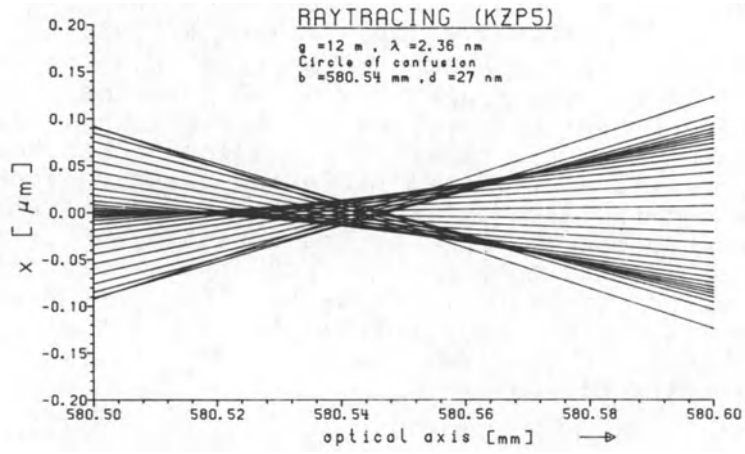

Fig. 10. Ray tracing through the condenser zone plate KZP5.

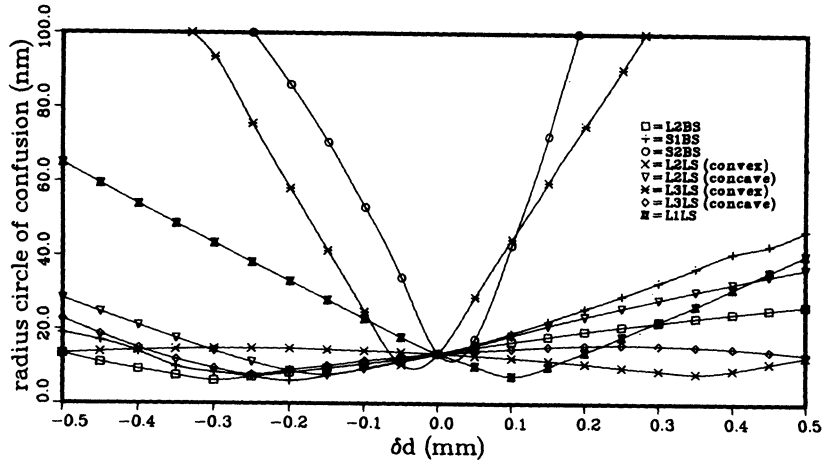

Fig. 11. Influence of the thickness of the optical elements on the aberration-limited resolution of KZP5.

A zone plate acts as a dispersion element when used with polychromatic radiation because f is proportional to $1/\lambda$. Together with a diaphragm a condenser can therefore be used as a linear monochromator with a spectral resolution of about $\lambda/\Delta\lambda = r_n/2\sigma$, with r_n = radius of the condenser zone plate and σ = radius of the diaphragm . The spectral distribution of the radiation transmitting the diaphragm in case of a linear monochromator of our scanning x-ray microscope is demonstrated in Fig. 12. A polychromatic synchrotron source of 100 µm diameter is imaged by use of KZP5, which has a distance of 12 m from the source. The distance KZP5 - diaphragm is 580.5 mm. The intensity distribution in the plane of the diaphragm has been calculated using the diffraction theory of Kirchhoff[8,6]. The calculations have been performed using polychromatic point sources. Because the synchrotron radiation is incoherent one can summarize the intensity distributions of these point sources to get the total intensity distribution of light penetrating the diaphragm. The full half width of the spectral distribution of Fig. 12 leads to a spectral resolution of this linear monochromator of $\lambda/\Delta\lambda = 183$.

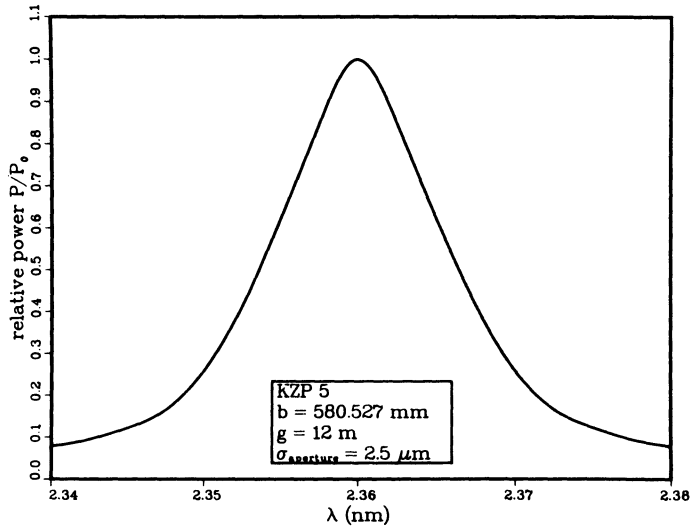

Fig. 12. The spectral distribution of the radiation transmitting the diaphragm in case of a linear monochromator of the Göttingen scanning x-ray microscope.

If radiation with this spectral distribution illuminates the micro zone plate MZP3, the scan spot in the image plane of MZP3 has an intensity distribution shown in Fig. 13. The diameter of the scan spot is 60 nm.

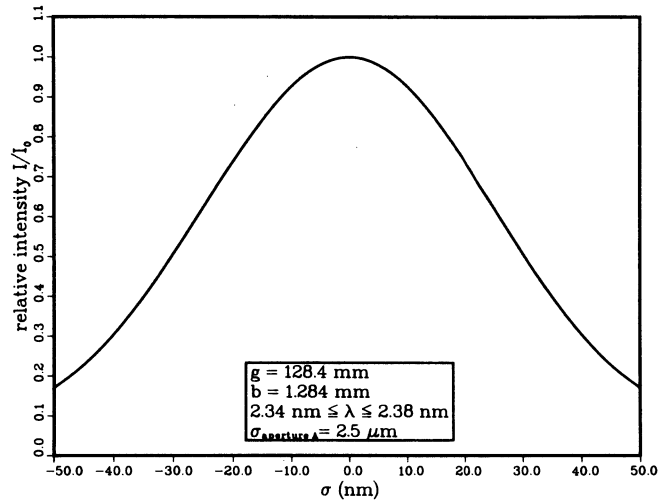

Fig. 13. Intensity distribution of the scan spot in the image plane of MZP3 in the Göttingen scanning x-ray microscope.

THE GÖTTINGEN X-RAY MICROSCOPE

The x-ray optical arrangement of an imaging microscope, installed at the BESSY electron storage ring in Berlin[9], is shown in Fig. 14. The polychromatic synchrotron radiation meets the condenser zone plate at a distance of 15 m of the source. The condenser zone plate, e.g. KZP3 with a diameter of 9 mm and a focal length $f_{4.5\ nm}$ = 304 mm or KZP6 with a diameter of 9 mm and a focal length $f_{2.36\ nm}$ = 226 mm generates a reduced image of the source. Together with the free diameter of the object chamber the condenser acts as a linear

monochromator. A stop in the central region of the condenser zone plate prevents zero-order radiation from reaching the object field and prevents first-order radiation of the condenser reaching the image field via zero-order of the micro zone plate. The zone plate objective (micro zone plate) generates a magnified image in the image field. The enlarged image can be viewed using a channel plate which converts the x-ray image into a visible image or it can be photographed directly. The x-ray magnification depends on the resolution which has to be matched to the resolution of the recording medium. Using fine grain photographic layers and zone plates with a resolution of about 50 nm, x-ray magnifications of up to 500x are used in this state of development. An additional optical magnification of the x-ray micrographs results in pictures with total

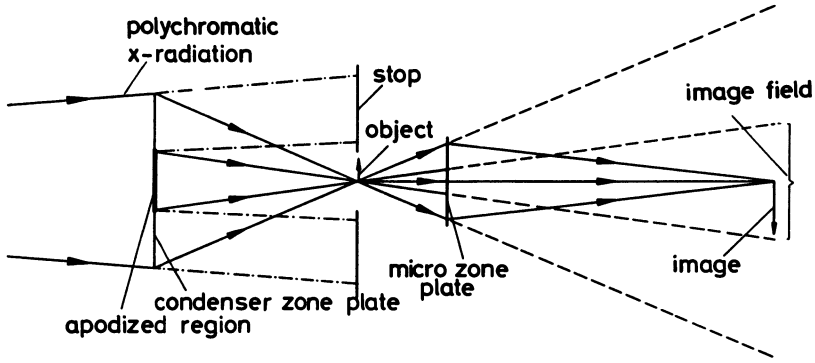

Fig. 14. X-ray optical arrangement of the imaging microscope.

magnifications in the region of about 10000x. Typical x-ray exposure times are 2 seconds to 30 seconds depending on the magnification, the object transparency, the spectral brilliance of the synchrotron source and the diffraction efficiencies of the two zone plates.

Figure 15 shows a photograph of the x-ray microscope in the BESSY laboratory and Fig. 16 shows some micrographs, made with this microscope. In Fig. 16a diatoms are imaged with 4.5 nm radiation. Figure 16b and c show images of 4 µm thick sections of liver cells, photographed with 4.5 nm radiation and exposure times of 10 seconds.

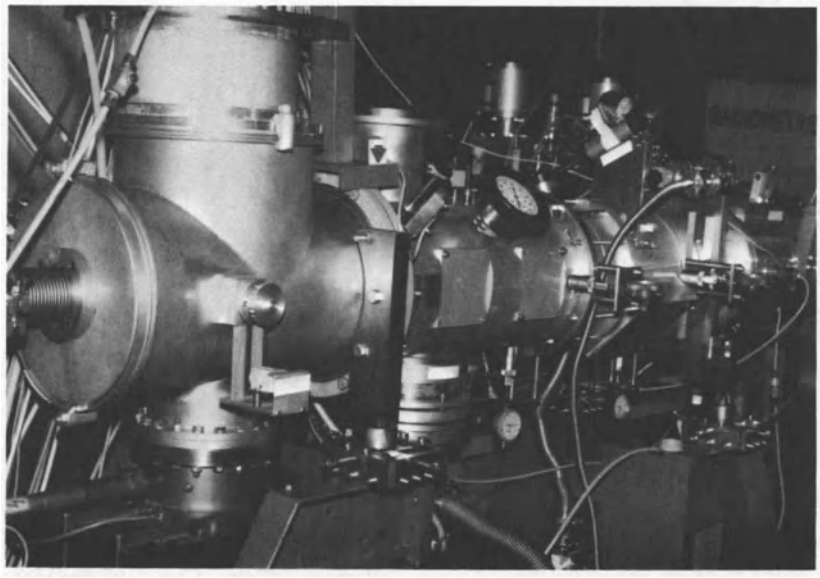

Fig. 15. The imaging x-ray microscope, installed in the basic research laboratory of the BESSY electron storage ring.

The following improvements of the imaging microscope are set in motion:

1. The construction of zone plates with better resolution and higher diffraction efficiencies.
2. Rapid change of the x-ray wavelength in the region $2.4\ \text{nm} < \lambda < 4.5\ \text{nm}$.
3. Preadjustment and prefocusing with visible light. Up to now, the adjustment and prefocusing of the specimen is done by channel plate control. The fine focusing is done by photographing a set of images. By this procedure the specimens are loaded with a radiation dose of a factor of about 100 more than necessary for the final exposure.
4. Use of detectors with a higher detective quantum efficiency.

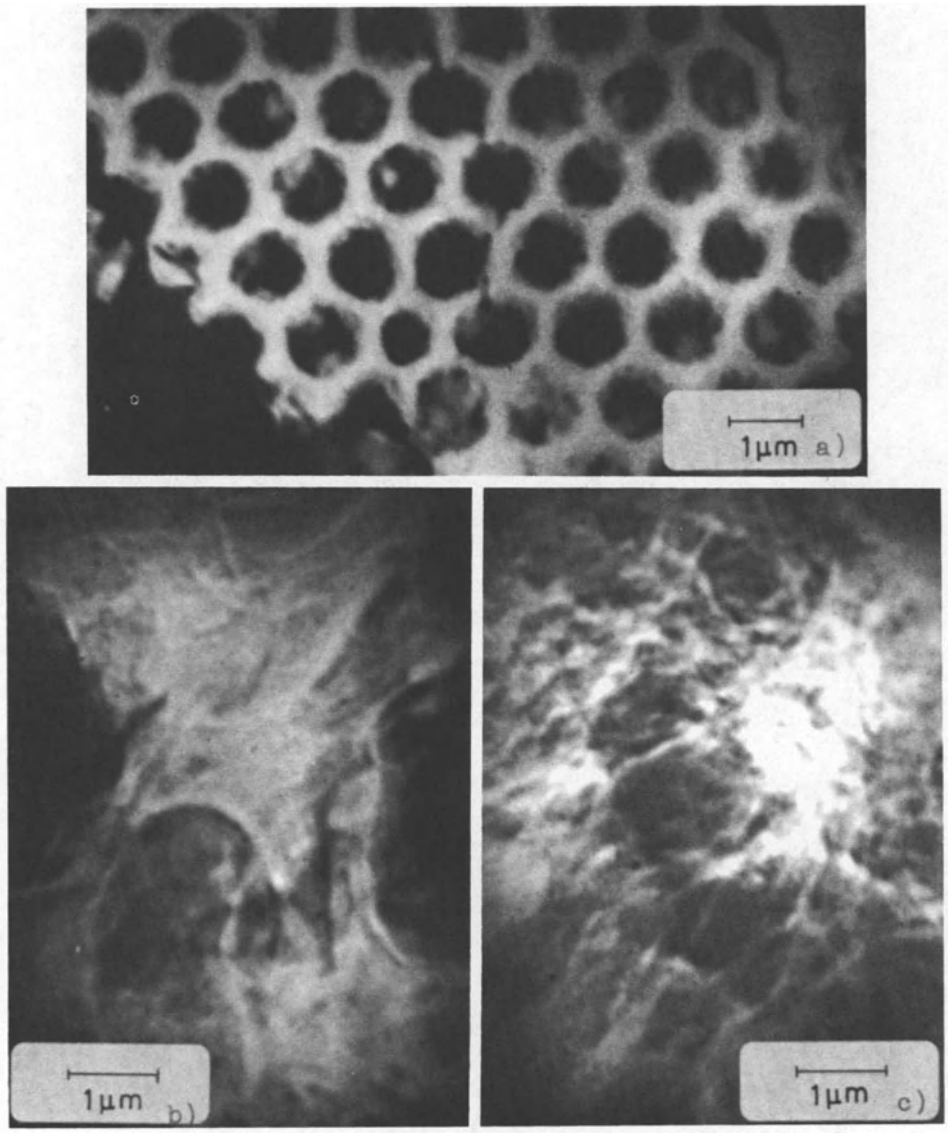

Fig. 16. (a) Image of diatoms, exposure time: 3 seconds.
(b) and (c) Images of 4 µm thick sections of liver cells, exposure time: 10 seconds. The images 16 (a) - (c) have been made with the wavelength of 4.5 nm with the x-ray microscope at the BESSY storage ring.

THE GÖTTINGEN SCANNING X-RAY MICROSCOPE

A further reduction of the radiation dose transferred to the specimen can be reached by use of a scanning x-ray microscope[10]. Another advantage of such a system is, that the specimens can be examined in real time work. In addition one can use the potentiality of electronic signal processing to record and analyse the resulting micrographs. In comparison, it will not be possible with a scanning system to get the short exposure times which have already been reached in this state of development with the imaging microscope. Both systems will therefore be complementary in future work.

The small x-ray image spot in the scanning x-ray microscope is achieved with two zone plates, which demagnify the synchrotron source in two steps. The first zone plate has a diameter of 2.5 mm and, by adjusting a diaphragm of 5 µm in diameter to an image point of a selected wavelength, it acts together with the diaphragm as a linear monochromator.

The diaphragm is then demagnified with a micro zone plate, illuminated with quasimonochromatic radiation, to the ultimate scan spot, through which the specimen is scanned. The scanning stage consists of two independent mechanical motions in perpendicular directions. The micro zone plate scans one line at a rapid speed. At the end of each line the direction of movement reverses. In this moment the object is moved in one step perpendicular, so that the micro zone plate scans the next line. For a picture of 200 x 200 elements the minimum scan time is 40 seconds corresponding to a pixel scan time of one millisecond and a scan time of 0.2 s for one line. The time scale for the mechanical motions and the data processing is therefore matched to one millisecond.

With the now existing zone plates and the synchrotron radiation of the BESSY storage ring we expect to get 10^5-10^6 photons/s in a 50-60 nm spot size diameter. To get higher photon densities for future work, it will either be necessary to use zone plates with improved diffraction efficiencies and/or synchrotron sources with a higher spectral brilliance, as e.g. undulators.

ACKNOWLEDGMENTS

The developments of the zone plates and the x-ray microscopes have been supported by the Stiftung Volkswagenwerk. The experiments at the BESSY storage ring are being supported by the Bundesministerium für Forschung und Technologie. We are grateful to the BESSY staff for the good experimental conditions. We thank Dr. F. Pfannkuch, Berlin, for the specimens of Figs. 16b and c.

REFERENCES

1. G. Schmahl, D. Rudolph, P.Guttmann and O. Christ, Zone Plates for X-Ray Microscopy, in: "X-Ray Microscopy", G. Schmahl, D. Rudolph, eds., Springer Series in Optical Sciences, Vol. 43, Springer-Verlag, Heidelberg (1984), p.63-74
2. P. Guttmann, Construction of a Micro Zone Plate and Evaluation of Imaging Properties, ibid., p.75-90
3. J. Thieme, Construction of Condenser Zone Plates for a Scanning X-Ray Microscope, ibid., p.91-96
4. M. Born, E. Wolf, "Principles of Optics", Sixth Edition, Pergamon Press, Oxford (1980)
5. P. Guttmann, "Theoretische Untersuchungen über hochauflösende Zonenplatten als abbildende Systeme für weiche Röntgenstrahlung", Diplomarbeit, Universität Göttingen (1982)
6. J. Thieme, "Theoretische Untersuchungen über Kondensorzonenplatten als abbildende Systeme für weiche Röntgenstrahlung", Diplomarbeit, Universität Göttingen (1984)
7. B. Niemann, D. Rudolph, G. Schmahl, Opt. Commun. 12 (1974), 160-163
8. G. Joos, "Lehrbuch der Theoretischen Physik", 11. Auflage, Akademischer Verlag, Frankfurt (1959)
9. D. Rudolph, B. Niemann, G. Schmahl and O. Christ, The Göttingen X-Ray Microscopy Experiments at the BESSY storage ring, in: "X-Ray Microscopy", G. Schmahl, D. Rudolph, eds., Springer Series in Optical Sciences, Vol. 43, Springer Verlag, Heidelberg (1984), p.192-202
10. B. Niemann, The Göttingen Scanning X-Ray Microscope, ibid., p.217-225

SCANNING SOFT X-RAY MICROSCOPY AT THE BROOKHAVEN LIGHTSOURCE

Janos Kirz

Physics Department,
SUNY at Stony Brook,
Stony Brook, NY 11794

INTRODUCTION

The project I am about to describe is the work of several people. My collaborators in the construction and operation of the instrument include Harvey Rarback and John Kenney from Stony Brook, Malcolm Howells from Brookhaven, Ralph Feder and David Sayre from IBM. The critical optical element, the Fresnel zoneplate, was fabricated for us at IBM under the direction of Dieter Kern and Philip Chang. We received invaluable help at various times from Roy Rosser, Michael Iarocci, Chris Jacobsen, Waiman Ng, Wen Bing Yun, and Bing Xin Yang. Several scientists came to join us with specimens of biological interest. I wish to mention particularly Francoise Cinotti, Jonathan Costa, James Hamos, Ed Lattman, and Jerry Pine, and express to them our gratitude for their interest, encouragement, and patience. This project would not have gotten off the ground without the generous support and encouragement from the management and the staff of the National Synchrotron Light Source.

I will first discuss the reasons why we chose to construct a scanning microscope, then provide a reasonably detailed description of the apparatus. The rest of the lecture will examine our experience with imaging and microanalysis to date, and our plans for future improvements.

WHY SCAN?

In any scanning instrument the optics that determine the resolution are placed ahead of the specimen. The image is formed by moving the specimen and the beam relative to each other in a raster fashion, and the signal observed in the detector is recorded as a function of position. The detector need not have any spatial resolution of its own.

The scanning scheme has several advantages that make it particularly well suited for X-ray microscopy. First of all, scanning instruments can make very efficient use of the radiation used to form the image, thus minimizing the radiation damage done to the specimen. This is achieved in two ways: since the detector need not have any spatial resolution, it can be made highly efficient. Furthermore, there is no need for optical elements between the specimen and the detector, thus another source of potential losses is eliminated. In addition, a scanning microscope allows both the sample and the detector to sit in an atmospheric environment, because they can be put in close proximity to each other.

The scheme also lends itself naturally to digital techniques. The detector counts individual photons, and the image is stored in a small computer in the form of counts collected as a function of position for display and statistical analysis. This information can then be manipulated to perform elemental mapping or contrast enhancement, as we shall see below. The image can also be observed in "real time" - as it is being made - so focusing and selecting areas of particular interest can be performed rapidly.

In our microscope the focused X-ray spot remains stationary, while the specimen is mechanically scanned. In this arrangement there are no off-axis aberrations to worry about, there is no problem with non-uniform illumination of the specimen, and at least in principle one has no limitation on the transverse dimensions of the object to be imaged. Effective magnification can be set by selecting the appropriate step size for the scan: finer steps result in increased magnification.

We should hasten to add that with all these attractive features come certain limitations too. To image moving objects, the "stop action" of a flash is very useful. We see no way, however, to combine flash with scanning. Scanning also puts special requirements on the X-ray source. To generate the highest resolution consistent with the diffraction limit, the focusing element must be coherently illuminated.

DESCRIPTION OF THE MICROSCOPE

The apparatus consists of three major logical components: the synchrotron light source, the probe-forming optics, and the computer controlled image acquisition system. We shall treat these in turn.

The Synchrotron Light Source

Our microscope operates at beamline U15 at the National Synchrotron Light Source, at Brookhaven National Laboratory. The beamline is supplied by a bending magnet of the ultraviolet ring which operates at 750 MeV. Because of the coherence requirements of the microscope we make use of only a small fraction of a milliradian of the source emittance. A toroidal grating monochromator operating at grazing incidence selects the desired wavelength in the range between 16Å and 45Å. The resolution of the monochromator is about 0.1Å at 30Å; in other words the resolving power is about 300. The monochromator deflects the beam in the vertical plane by 5.7 degrees. A plane mirror made of fused quartz renders the beam horizontal once again. This second reflection also helps reduce the higher order contamination in the monochromator output.

Our desire to avoid placing the specimen into the vacuum poses a significant complication: while the soft X- rays can not penetrate solid material more than a few microns thick, we must get the beam to pass from the ultrahigh vacuum into the atmospheric environment without endangering the integrity of the storage ring. We have chosen a scheme involving two thin windows to accomplish this task. (Fig. 1) The first window is a 1500Å thick aluminum foil. Though this object can only withstand a pressure difference of a torr or less, it is leak tight, and separates the ultrahigh vacuum region (the storage ring and the monochromator) from a high vacuum volume. The window that separates the high vacuum from atmospheric pressure is a 1200Å thick layer of silicon nitride, kindly provided to us by Dr. Ralph Feder. It supports atmospheric pressure over an area of nearly 0.2mmx0.2mm.

The high vacuum region between the two windows contains an ion pump, a vacuum gauge, and a pneumatically operated gate valve. The idea is that in case the silicon nitride window were to break (an event that we are fortunate enough to have not yet experienced), the gauge would sense the increase in pressure and isolate the upstream end of the high vacuum region with the gate

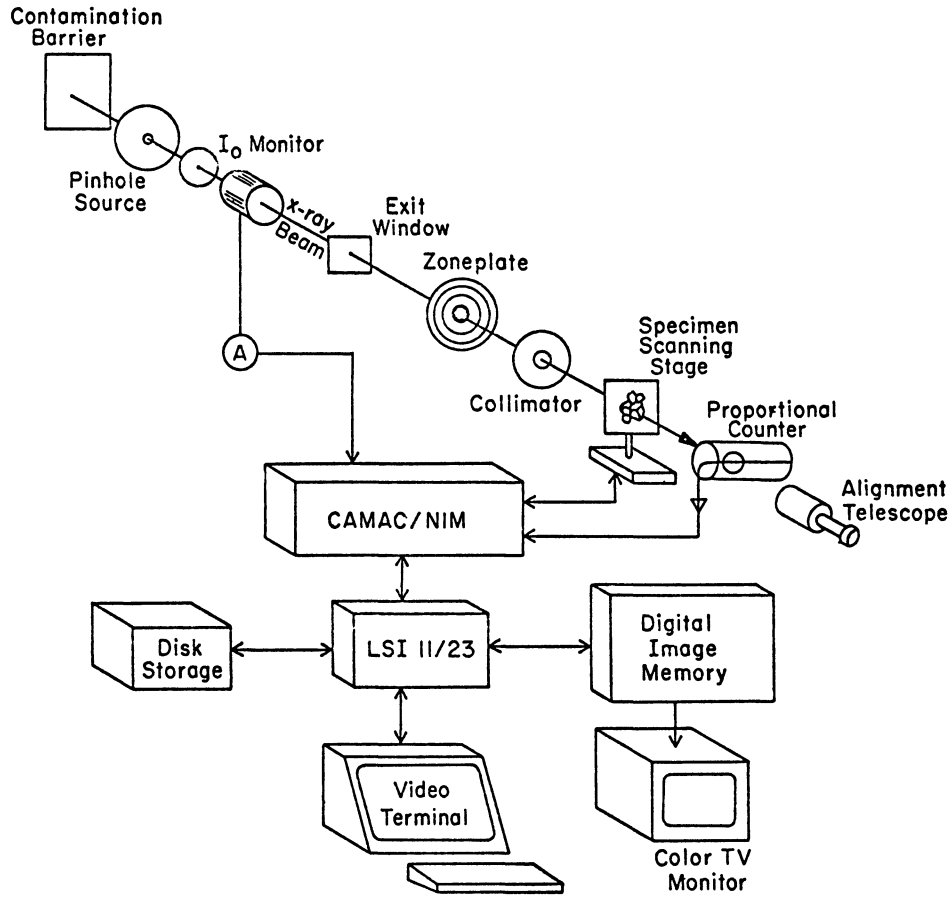

Figure 1. Schematic diagram of the microscope.

valve *before* the aluminum window were ruptured. This would also prevent us from compromising the vacuum of the synchrotron storage ring.

The Probe Forming Optics

The resolution of the microscope is determined by the size of the focal spot that we use to scan the specimen with. It is the purpose of the optics to

minimize the size of this probe, yet keep the intensity as high as possible to minimize the time it takes to take a picture.

We use a Fresnel zoneplate to form the probe. The zone plate is used, much as if it were a thin lens, to demagnify a well defined source. This source is a pinhole, 30 microns in diameter, placed 60 centimeters from the zoneplate. The probe (the focused beam spot) is about 5 millimeters from the zoneplate, so the geometrical demagnification factor is about 120. The real probe size is a convolution of this geometrically determined spot with the contribution due to diffraction. The size of the source pinhole was chosen to match the diffraction limited probe size. Further reduction would reduce the intensity in the probe without a significant improvement in resolution.

The zoneplate is an electron-beam fabricated gold structure on a silicon nitride membrane. It was made for us at IBM. The finest rings and spaces are 1500Å wide, the overall diameter is 88 microns. The central 44 micron diameter region is entirely opaque, so we are dealing with an annular region of zones. A collimator is mounted between the zoneplate and the specimen to remove the unfocused x-rays (Fig.2). The focus is in the shadow of the central opaque region.

Scanning and Computer Control

We chose to scan the specimen mechanically, while the soft X-ray probe remains stationary. The raster scan is under the control of a Digital Equipment Corporation LSI 11/23 microcomputer, which interacts with the microscope through CAMAC electronics. The actual scan is performed using a pair of piezoelectric actuators with a range of 100 microns. The position of the stage is monitored by a pair of linear variable differential transformers (LVDT-s). The scan position is controlled by a feedback loop implemented in software.

The stage itself is mounted on a standard optical mount with x,y,z translational adjustments for focusing and rough positioning. These motions are provided by dc motors. To facilitate focusing, the computer is capable of going through and storing a series of scans at predetermined stage positions along the beam direction. The operator need only evaluate the results to determine the proper setting.

X rays transmitted by the specimen are detected by a small flow proportional counter. This counter operates with P10 gas (90% argon, 10%

methane) at atmospheric pressure. The entrance window is a 1000Å thick carbon foil. The pulse height information provided by this counter is sufficient to discriminate against higher orders passed by the monochromator, which show up with double or triple pulse heights. To reduce the losses due to absorption in air, the region between the vacuum window and the proportion counter is normally flooded with helium. The entire instrument, from the thin aluminum window on, and including the zoneplate, the specimen stage and the counter, is rigidly attached to an optical bench. This bench in turn rests on a vibration isolation table.

The microscope operator tells the computer the number of lines and columns the scan is to consist of, the separation distance between pixels, and the dwell time at each pixel. The computer then takes over, accumulating the coordinates and the number of transmitted X-ray counts for each pixel. In the recent past, typical images contained from 100x100 to 140x140 picture elements, with the latter number being a temporary limit due to the computer memeory on hand.

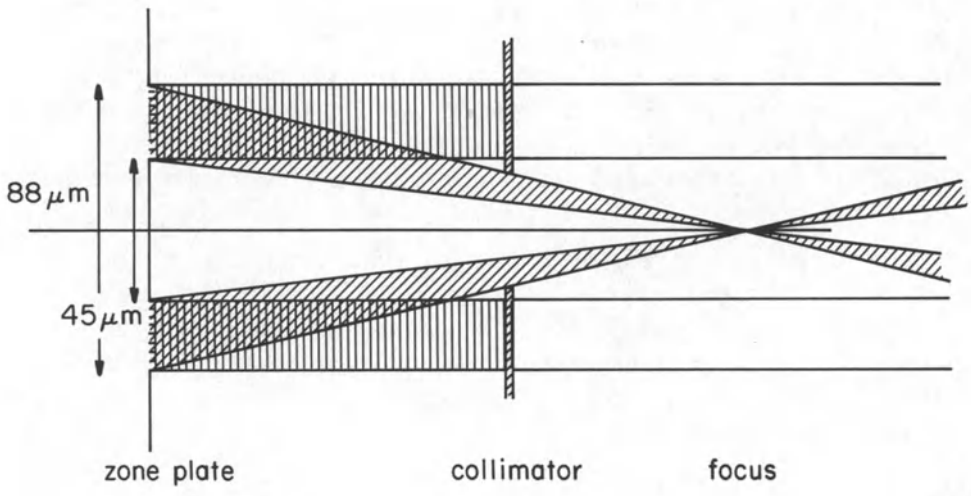

Figure 2. Arrangement of the zoneplate and collimator used in the microscope. (Not to scale) The focal length is 5mm at 30Å.

To be able to normalize the picture thus produced (that is to compensate for the variations in incident intensity primarily due to the slow decay in storage ring current), two methods are currently in use. The first one is to make use of a signal provided by the Light Source control room, in which the supplied voltage varies in proportion to the ring current. The second method makes use of a cesium iodide transmission photodiode located just before the zoneplate. While this thin foil absorbs about 30% of the X rays, it generates a photocurrent which is more directly proportional to the actual flux incident on the zoneplate.

The information accumulated by the computer is displayed in real time three ways. One display is based on an image memory tube that continuously refreshes a black and white television display. Since the tube is an analogue device, it is capable of reproducing the actual pixel locations regardless of whether they are on a perfect raster grid or not. As a result it is particularly well suited for monitoring the performance of the scanning stage. The second display is based on digital image memory. This memory has a capacity of 512x512 pixels with 8 bits of color gradation available at each pixel. The computer translates the transmitted beam intensity onto a false color scale, and the pixels are then displayed via the digital image memory on a color television tube. The pictures presented in Figures 4 through 6 were generated by photographing this color display. Finally, the third display appears on the computer's graphics terminal. It provides quantitative information pixel by pixel, displaying the counts recorded, or the actual stage position. An example of this display is provided in Figure 3.

In addition, when the image is complete, the operator has the option of storing it on disk or diskette in digital form. The image can also be processed then or at a later date. In particular one has the option of enhancing the contrast by setting appropriate levels for color boundaries, or of doing the elemental analysis described below. One can also recreate off line all three real time displays described above.

PERFORMANCE

The microscope has been in operation for about a year. It shares the beamline with a variety of other activities, but it has received about 50% of the available beam time. The wavelength for much of the work has been 31Å, where air, water, and silicon nitride are relatively transparent,

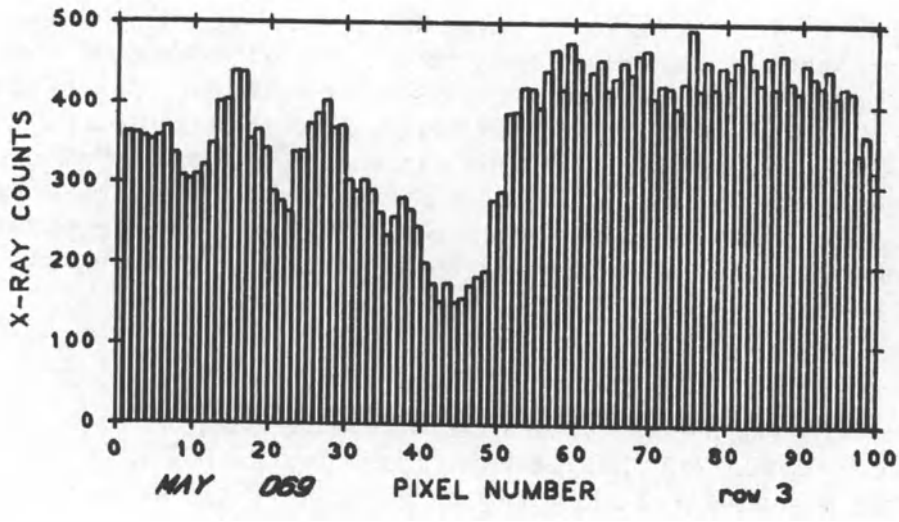

Figure 3. X-ray counts recorded along one line of a scan.

and where wet organic specimens show good contrast. The resolution has reached 0.2 microns, consistent with our expectations based on the diffraction limit of our current zone plate. Examples of images obtained are shown in Figs. 4-6.

Figure 4 is the image of a diatom. It illustrates the ability of the microscope to image wet specimens. Internal features of the organism are clearly visible.

Figure 5 illustrates the ability of the instrument to "zoom" by changing the step size in the scan. The object here is a pair of chromosomes, shown at three levels of magnification. The area enlarged is indicated by the square on the lower magnification images.

We have begun to develop the capability to map the distribution of selected elements. This involves the subtraction of two images of the same specimen area taken at slightly different wavelenths, but where the absorption coefficient of the element to be mapped changes rapidly. This rapid change

occurs near absorption edges. In this work the chromatic aberrations of zoneplates need to be considered, because as one changes wavelenths the focal length changes, and the specimen needs to be repositioned

without losing registration. At moderate resolution, however, we may choose to set the best focus for the average of the two wavelengths and take the two images without any repositioning.

The first specimen we examined this way is a section of rat bone, where we set out to locate calcium. In Figure 6 two images of the same specimen are shown. The area is 50 by 50 micrometers, the wavelengths are 35.4Å and 35.7 Å. (The L3 edge of calcium is at about 35.6Å.) The regions in the lower left of the images look identical. This is bone marrow, and contains no calcium. The rest looks drastically different, indicating a large calcium concentration, except in small areas where there are holes in the specimen. Further work, (including numerical evaluation of the images) is in progress.

FUTURE PLANS

At the present time it takes between 20 and 90 minutes to record an image of the kind shown. This time is much too long for an instrument in routine use. The limitation is strictly the incident intensity, and as the storage ring brightness improves the time drops apace. A much more drastic improvement is expected after the completion of the soft X-ray undulator, now under construction at the NSLS. This new source will provide several orders of magnitude more coherent flux than what we have at the U15 beamline.

We also anticipate a significant improvement in resolution, as the technology for zoneplate fabrication develops.

Most importantly we plan to make the instrument available to investigators who may want to use it to attack problems in biology.

* Supported in part by the National Science Foundation under Grant #PCM-8109358

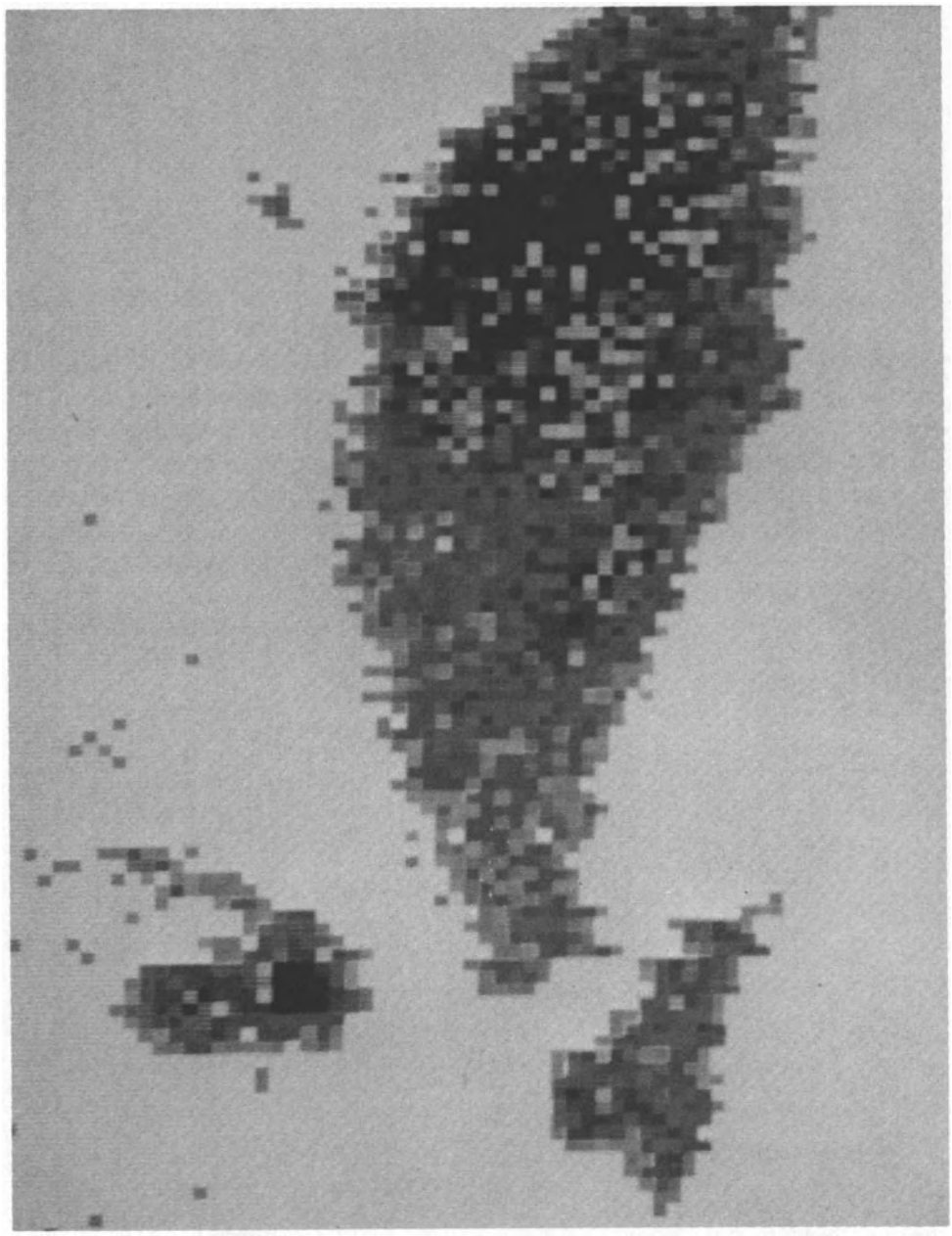

Figure 4. Image of the diatom Phaeodactylum Tricornutum. This diatom was in its natural wet state while in the microscope. The image covers an area 15 by 20 micrometers.

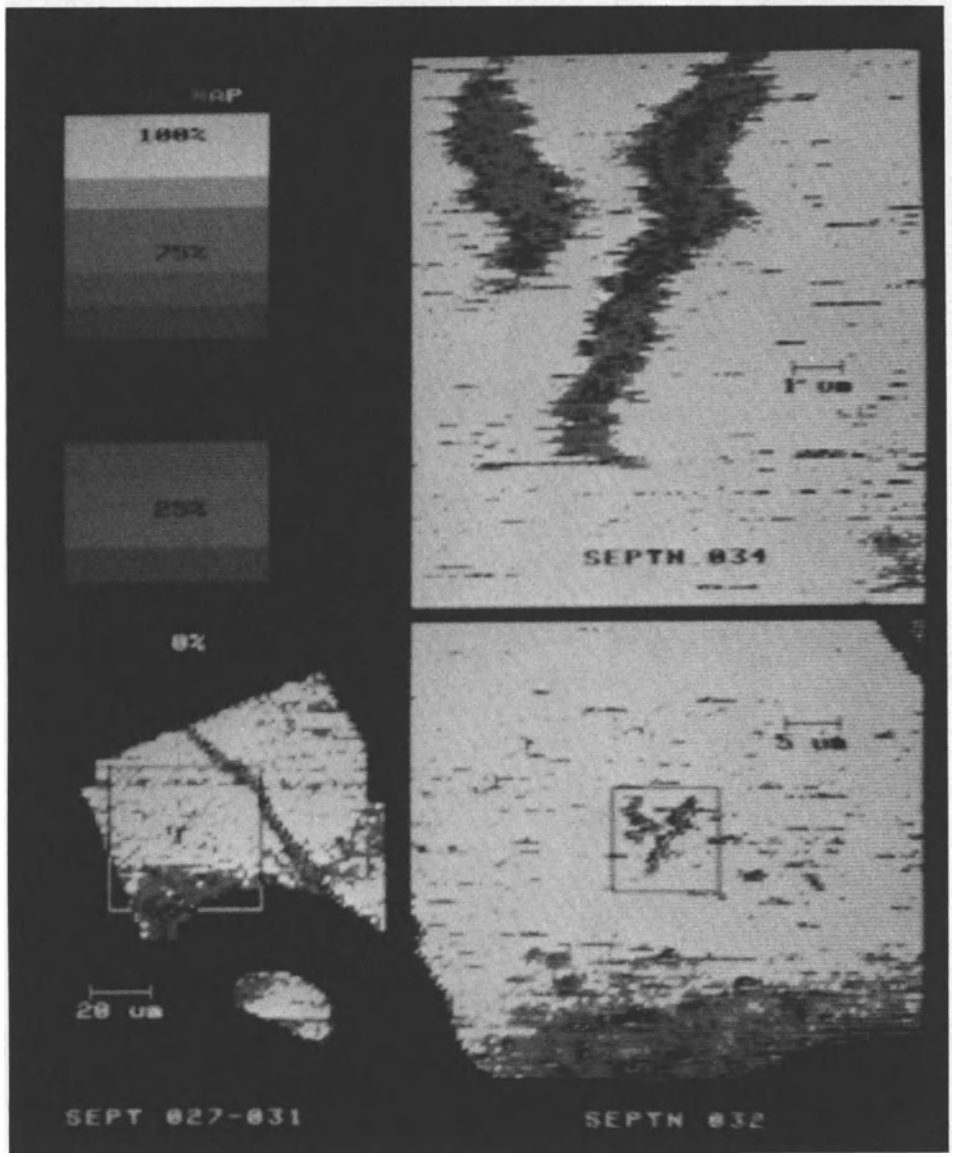

Figure 5. Images of HeLa chromosomes at three levels of magnification. Specimen courtesy of Dr. E. Lattman, Johns Hopkins University.

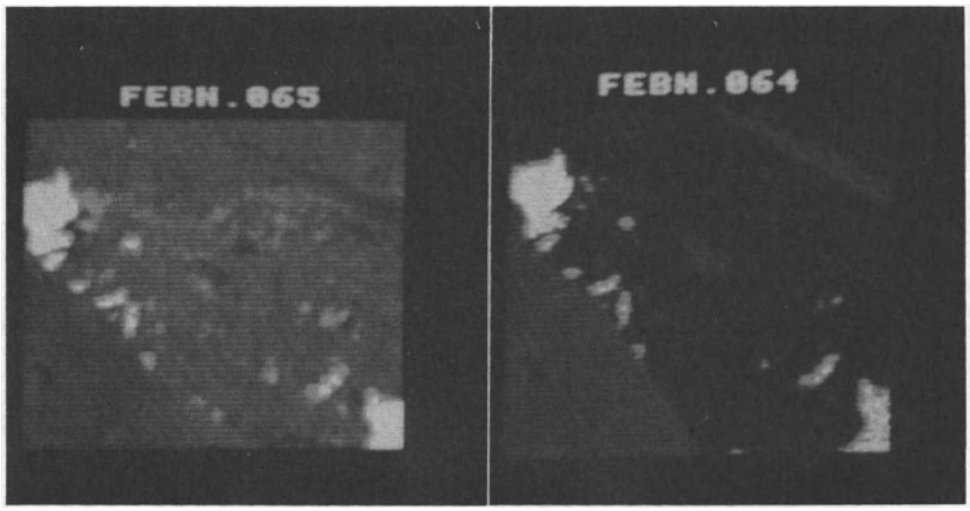

Figure 6. Two images of a section of rat bone. The area shown is 50 by 50 micrometers.The wavelengths used were: 35.4Å for the image on the left, 35.7Å for the image on the right. Specimen courtesy of Dr. F. Cinotti, Brookhaven National Laboratory.

BIBLIOGRAPHY

This bibliography is designed to serve several purposes, and is accordingly divided into several sections.

First, we should indicate the origins of the field, and acknowledge our indebtedness to the pioneers. Second, we should provide the reader with leads to the present state of the art. The third section is for those who wish more detail concerning our work.

The Beginnings

1. V. E. Cosslett and W. C. Nixon, X-ray microscopy (Cambridge Univ. Press, Cambridge,1960). This is a thorough review of the history and status of X-ray microscopy as it stood twenty-five years ago. A rich source of references to earlier work.

2. A. V. Baez, *J. Opt. Soc. Am.* 42, 756 (1952), and 51, 405 (1961). The first suggestion, and the first use of a zoneplate suitable for X-ray imaging.

3. G. Schmahl and D. Rudolph, *Optik* 29, 577 (1969). The first viable scheme for making high resolution zoneplates, and the introduction of the apodization idea.

4. P. Horowitz and J. A. Howell, *Science* 178, 608 (1972). The first use of synchrotron radiation for X- ray microscopy, and the first implementation of a scanning instrument in the field.

5. D. Sayre, *Proposal for the Utilization of Electron Beam Technology in the Fabrication of an Image Forming Device for the Soft X-Ray Region*, IBM Research Report RC-3974, Yorktown Hgts, N. Y. (1972). The first suggestion for the method used to make our zoneplate.

6. B. Niemann, D. Rudolph, and G. Schmahl, *Appl. Opt.* 8, 1883 (1976). The first soft X-ray microscope to use zoneplate focusing and a synchrotron radiation source.

Present Status

7. G. Schmahl and D. Rudolph, editors, X-Ray Microscopy, Springer Series in Optical Sciences Vol 43, 1984. This is the proceedings of a symposium held in Göttingen, in September 1983. All major projects in soft X-ray microscopy are discussed. In particular the article in this volume by Niemann and the one by Spiller describe the other scanning microscopes nearing completion.

8. E. Spiller, in Handbook on Synchrotron Radiation, Vol.1, edited by E. E. Koch (North Holland, Amsterdam, 1983). An excellent review, with particularly valuable sections on X-ray optics, and the relevant material properties.

9. J. Kirz and H. Rarback, Soft X-Ray Microscopes, *Rev. Sci. Instr.* 56, 1 (1985). Review article with extensive references.

10. R. Feder, J. Wm. McGowan and D. Shinozaki, editors, this volume. (Plenum, 1985). It will surely contain the latest information.

11. H. Rarback, The Development of a Scanning Soft X-Ray Microscope, Ph, D. Dissertation, SUNY at Stony Brook, N. Y. 1983 (unpublished). Detailed description of the instrument.

12. D. Kern, P. Coane, R. Acosta, T.H.P. Chang, R. Feder, P. Houzego, W. Molzen, J. Powers, A. Speth, R. Viswanathan, J. Kirz, H. Rarback and J. Kenney, in Science with Soft X-rays, edited by F. J. Himpsel and R. Klaffky, SPIE Conference Proceedings Vol. 447 (SPIE, Bellingham, Wa. 1984). Details concerning the fabrication and performance of the zoneplate used in our microscope.

13. H. Rarback, J. M. Kenney, J. Kirz, M. Howells, P. Chang, P. J. Coane, R. Feder, P. J. Houzego, D. Kern and D. Sayre, in Ref. 8. Further details on the resolution of the instrument.

DEVELOPMENT OF A SCANNING X-RAY MICROSCOPE AT THE DARESBURY LABORATORY

R.E. Burge, A.G. Michette, P. Charalambous,
M.T. Browne, M.J. Simpson and C.J. Buckley
Queen Elizabeth College*, London

P.J. Duke
Daresbury Laboratory

1. INTRODUCTION

The application of x-radiation to microscopy has been known for many years (Cosslett and Nixon, 1960). However early attempts to exploit and develop the potential of x-radiation in this field foundered on the low brightness of the sources then available and the lack of suitable methods of x-ray focusing. The advent of synchrotron radiation (SR) as a source of soft x-rays, the development of high quality x-ray reflectors and the fabrication of custom-built high resolution x-ray diffractive elements have transformed the situation. Now several laboratories are actively pursuing the development of focusing x-ray microscopes and at the same time attacking classical x-ray microscopy (contact and projection micro-radiography) with renewed vigour. All of these applications and developments have been reviewed by Schmahl and Rudolph (1984) which provides an excellent up-to-date survey of this field.

This article will concentrate on one particular line of development which is being followed jointly at Queen Elizabeth College*, London and at the Daresbury Laboratory of the Science and Engineering Research Council in the UK. Section 2 will describe the source of soft x-radiation. In section 3 the development of high resolution focusing elements (Fresnel zone plates) will be described and the results of some initial

---

*From 1/8/84 King's College, Strand, London WC2 2LS

tests will be given. In section 4 the parameters of the microscope will be defined and the future programme outlined. Lastly we will focus on certain areas where significant improvements can be expected over the next few years.

2. SOFT X-RAY SOURCE

2.1 The Daresbury SRS

The SR source (SRS) at the Daresbury Laboratory has been operating as a research instrument with a broad based experimental programme for several years. The parameters of the SRS are shown in Table 1. In particular the SRS provides a substantial flux of soft x-ray photons from 20 Å - 50 Å which is being used for a developing programme in contact microscopy and lithography. For an x-ray optical system the important parameter

Table 1: SRS Parameters

Beam Energy	2.0 GeV
Electron Current (maximum)	100 - 300 mA
Beam Lifetime	8 - 10 hrs or greater
Beam Dimensions (FWHM) from	4.8 × 1.2 mm^2
to	12.9 × 0.6 mm^2
Characteristic Wavelength	
Dipole Magnet (1.2 T)	0.388 nm (3.88 Å, 3.2 keV)
Wiggler Magnet (5 T)	0.093 nm (0.93 Å, 13.3 keV)
Photon Flux at 4.4 nm	4 × 10^{12} photons/(mrad.sec) into 0.1% BW at 100 mA

Table 2: Figure of Merit for Soft X-ray Microscopy at 4.4 nm

Storage Ring	Location	Approximate Date	Energy	FOM
SRS Dipole	Daresbury UK	Now	2 GeV	7 x 10^{11}
SRS Undulator	Daresbury UK	1985	2 GeV	6 x 10^{12}
SRS HBL Dipole	Daresbury UK	1987	2 GeV	6 x 10^{12}
SRS HBL Undulator	Daresbury UK	1987	2 GeV	2 x 10^{14}
BESSY Dipole	Berlin FRG	Now	800 MeV	2 x 10^{13}
NSLS Dipole	Brookhaven USA	Now	700 MeV	6 x 10^{12}
NSLS Undulator	Brookhaven USA	In preparation	2.5 GeV	6 x 10^{15}
ESRF Undulator		Proposed	800 MeV	4 x 10^{17}
ALS Undulator	Berkeley USA	Proposed	1.3 GeV	5 x 10^{17}
ESRF Undulator		Proposed	5 GeV	1 x 10^{18}

Figure of merit (FOM) is in units of photons/(sec.mm^2.$mrad^2$) into 0.1% band width for a stored electron current of 100 mA and a photon wavelength of 4.4 nm.

is not so much the intensity as the brightness (flux/unit area/unit solid angle) which defines a kind of figure of merit (FOM) for soft x-ray microscopy with a synchrotron source. Table 2 shows a comparison of values of FOM for several sources. It is clear from this table that the SRS dipole magnet source compares unfavourably in this respect and that an x-ray microscope based on the dipole magnet source, while being useful as a preliminary test bed, would not provide the basis for a user instrument.

2.2 Undulator

An undulator (Poole, Munro et al) consists of a series of magnets which generate a spatially alternating magnetic field of period λ_o. This imparts a high frequency oscillation of frequency ν_o and wavelength λ_o to electrons of velocity βc ($\nu_o\lambda_o=\beta c$) in the frame of reference of the moving electron and the electron will emit radiation at this same frequency in its own reference frame. This radiation is transformed to the laboratory frame and at the same time Doppler shifted so that the observed wavelength $\lambda\simeq\lambda_o/2\gamma^2$. For a long undulator with many periods the radiation is amplified by a factor between N and N^2. In the ideal case the radiation from successive periods adds constructively at the detector because the time taken for the relativistic electrons to traverse one period is almost equal to the time taken for the radiation to cover that same distance. The expression for the output wavelength must be corrected slightly, both to allow for the slight mismatch between electron and radiation path difference and also to allow for an off-axis observer. In fact

$$\lambda_i = \frac{1}{i}\,\frac{\lambda_o}{2\gamma^2}\left[1 + \frac{K^2}{2} + \gamma^2\theta^2\right] \qquad (1)$$

where
- i = harmonic number
- λ_o = magnet period
- γ = relativistic factor = electron energy/electron rest energy (0.511 MeV)
- θ = angle of emission relative to the electron trajectory
- K = deflection parameter = $93.4\lambda_o B_o$
- B_o = On axis magnetic field

The bandwidth of the radiation from the i^{th} harmonic is given by

$$\frac{\Delta\lambda}{\lambda_i} = \frac{1}{iN} \qquad (2)$$

where N is the number of periods. The intensity of the radiation is discussed in detail by Krinsky (1983).

For a weak field undulator, where K is small and the transverse motion of the electrons is non-relativistic ($\beta_{transverse} << 1$) then the predominant wavelength is that given by equation (1) with the harmonic number i=1. For strong field undulators with large K, and $\beta_{transverse} \lesssim 1$ many harmonics are apparent and the output spectrum as a function of viewing angle becomes more complex. A further complication, which in practice can be definitive in determining the performmance of the undulator, is the divergence of the electron beam. It is clear from (1) that this will introduce a spread in the values of output wavelength and lead to a bandwidth which is much larger than that given by equation (2). If the beam divergence has a standard deviation of σ then

$$\frac{\Delta\lambda}{\lambda} = \frac{(\gamma\sigma^2)}{1 + K^2/2} \qquad (3)$$

The Daresbury SRS undulator at present under construction consists of 10 periods, each period comprising 2×4 units of $SmCo_5$ permanent magnetic material with a remanent field of 0.9 T. The arrangement of the blocks in one period is shown diagramatically in Fig.1 and the magnet parameters in Table 3. The magnet will be inserted into a specially prepared drift space between dipole magnets 4 and 5 in the SRS.

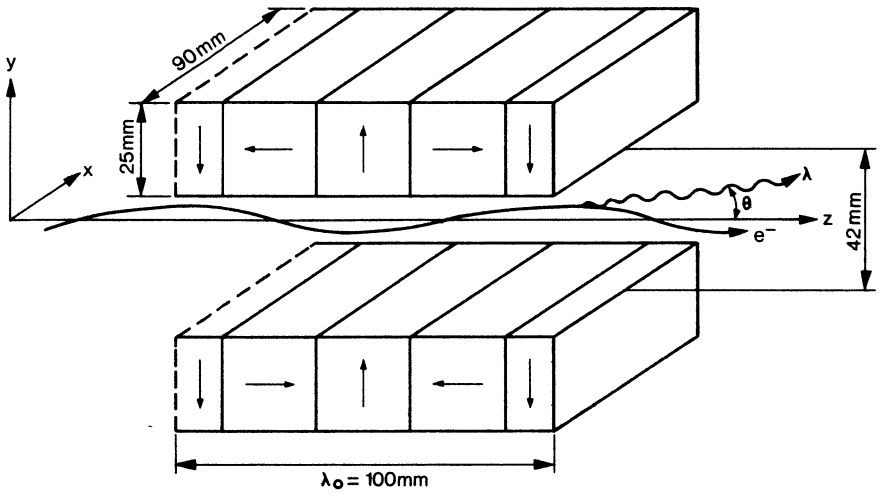

Fig.1. Basic SRS undulator geometry.

Table 3. SRS undulator magnet parameters

Period, λ_0	100 mm
Number of periods, N	10
Total length	1 m
No. of blocks per period, M	4
Block height, h	25 mm
Block width	90 mm
Gap, g	42-120 mm
K	3.25 - 0.25
Remanent field, B_r	0.94 T
Electron beam parameters (fwhm):	
Dimensions	12.2 × 1.9 mm^2
Divergence	2.4 × 0.6 $mrad^2$

The undulator gap can be manually adjusted to provide a range of magnetic fields. At low field on axis and with 450 MeV electrons stored in the synchrotron the undulator should emit

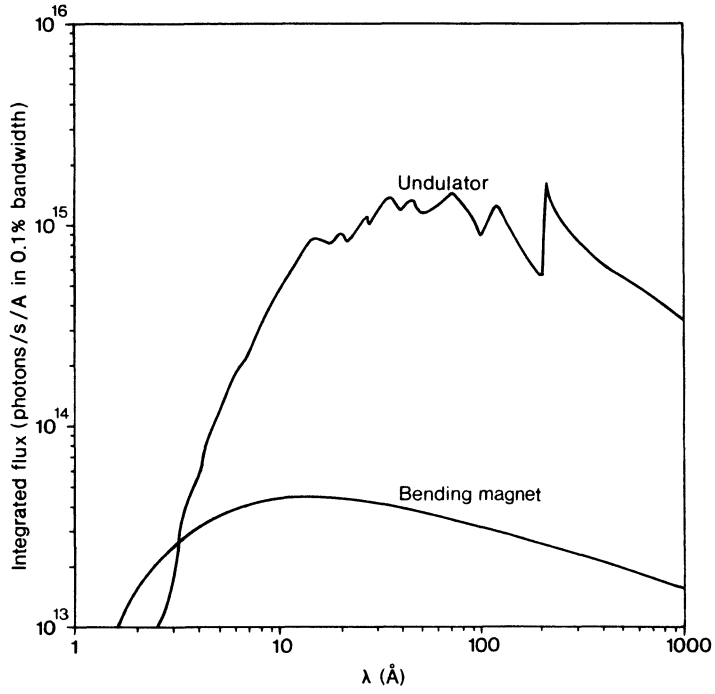

Fig.2. Total flux from the undulator integrated over all angles (2 GeV, K = 3.245) and the vertically integrated SRS dipole magnet spectrum (per mrad horizontally).

radiation predominantly in the visible region of the e.m. radiation spectrum. This visible radiation will be useful for diagnostic purposes such as the study of electron beam behaviour, comparison of predicted and actual output etc. The soft x-ray spectrum expected from the undulator is shown in Fig.2 where the spectrum is compared with that observed from the 1.2 T dipole magnets of the SRS. Compared with the dipole magnets there is an enhancement factor of 70-80 in radiation flux. The interference effects from the undulator poles which enhance the spectrum at the fundamental wavelength of 190 Å and its higher harmonies can be clearly seen in the spectral structure.

Reference to Table 2 shows the value of the undulator as source for x-ray microscopy. The predicted FOM is increased by almost an order of magnitude compared with that from a standard dipole magnet.

3. X-RAY FOCUSING ZONE PLATES

3.1 Focusing by x-ray reflection

It is well known that the refractive index of all materials for x-radiation is slightly less than unity so that at grazing incidence angles x-rays can be reflected by total external reflection. This method is being used to fabricate an x-ray microscope optical system (Franks and Gale, 1984) with a resolution in the region of $\gtrsim$ 1μm.

The development of high reflectivity multilayer devices (Barbee, 1984; Dhez, 1984; and Warburton, Rek et al., 1984) which are essentially Bragg reflectors with a 2d spacing appropriate to the soft-x-ray region are also being developed as optical elements for x-ray microscopy. A prototype XUV microscope using this technique has been constructed by Haelbich (1980) and a more advanced instrument is being commissioned by Spiller (1984).

3.2 Focusing by x-ray diffraction

The microscope to be installed at the SRS will use circular transmission diffraction gratings whose line spacing follows the Fresnel zone plate law given by equation (4).

$$r_n^2 = n \lambda f \qquad (4)$$

where n is the zone number with radius r_n, λ is the wavelength and f the focal length of the zone plate. The ultimate resolution of these devices is defined by the size of the Airy disc

generated in the image plane by a point source in the object plane

$$\delta = 1.22\ dr_n = 1.22\ \frac{r_n}{2N} \qquad (5)$$

where dr_n is the width of the n^{th} zone. The dimensions of a zone plate for microscopy in the submicron region can easily be computed. If, e.g. δ is to be 0.1 μm then r_n/N = 0.164 μm and for eg N = 100 zones r_n = 16.4 μm. The focal length of this hypothetical zone plate will be ~ 0.6 mm at the carbon K edge (4.4 nm) for first order diffraction in the zone plate.

3.3 Fabrication of zone plates using a STEM

Zone plates of these approximate dimensions are being prepared by a lithographic technique using contamination writing in a Scanning Transmission Electron Microscope (Vacuum Generators HB5). The writing process involves the breakdown of residual hydrocarbon molecules in the STEM vacuum by the electron beam. It is believed that the hydrocarbons form a thin layer on the specimen surface and that these are dissociated by the impact of the electron beam. The carbon atoms then form a narrow cone of polymerised carbon around the point of impact. The rate of formation of this contamination cone depends on the electron current in the STEM and the level of contamination in the STEM vacuum. This carbon deposition process can be used to write extremely fine lines with a format determined by the x,y scanning of the beam. The minimum line width is ~ 10 nm and the height of the cone can be up to ~ 0.15 μm. The cone can be even higher but large height to width ratio leads to instability and cone collapse.

In order to draw accurate patterns the electron beam scan must be limited to a few μm^2 (primary field) and the stage must be mechanically scanned (or rotated) to patch together a series of primary fields using appropriate registration marks. These problems and the methods which were used to solve them are described in Michette, Browne et al (1984) and Michette and Burge (1984).

3.4 Tests of zone plates

Two batches of zone plates have been produced so far. Direct tests on the first batch of zone plates using the scanning x-ray microscope (Rarback, Kenney et al., 1984) in the U15 beam line at the Brookhaven NSLS have been used to indicate directions in which improvement was deemed to be necessary. These

tests are described in more detail by Michette and Burge (1984). They yielded an efficiency of 0.3% for first order diffraction. The theoretical efficiency is given by (Simpson, 1984)

$$\varepsilon = \frac{\text{Focused Intensity}}{\text{Incident Intensity}} = \frac{(T_t - T_a)^2}{\pi^2} \qquad (6)$$

where T_t and T_a are the amplitude transmissions through the transmitting and absorbing zones respectively and:

$$T_{t,a} = \exp(-\frac{1}{2} \mu_{t,a} \, dz_{t,a}) \qquad (7)$$

where $\mu_{t,a}$ is the appropriate absorption coefficient and $dz_{t,a}$ is the thickness of the respective zone. The low efficiency exhibited by these zone plates indicated the need for improvements in the manufacturing method.

Indirect tests on the zone plates were also carried out. In particular a simple test using moiré fringes was used. Two identical perfect zone plates give straight line fringes when the centres are slightly displaced and zone plate pattern fringes for larger separations (see eg Chau, 1969). This test, made by superimposing two identical micrograph copies of the same zone plate has been used to indicate (by departures from linearity or circularity of the moiré fringes) regions of malformation of the original zone plate.

3.5 Impovements in the manufacturing procedure

One particular problem which has been identified is the ratchet effect which is caused by inequality of the x and y scans so that arcs drawn at the same radial position but in adjacent sectors do not join up. This problem has been tackled by drawing an initial skeleton of registration marks and parts of selected arcs in each primary field. The amount of ratchet at the edge of each sector can then be computed and since the completed arcs must join at the edges of the first and last sectors, the average ratchet error can be calculated and used to correct the positions of the arcs drawn in each field. The arcs themselves can still be incorrectly positioned radially because of small variations in the vertical position of the rotating stage between sectors which lead to changes in the magnification of the scanning system. Once the skeleton has been drawn and the ratchet correction applied any deviation of an arc of the zone plate from its calculated position can also be corrected for. Examination of the moiré pattern for zone plates created by this improved method shows that no significant errors are present. Of course the correction procedures

described here only apply when the sectors are almost identical to start with. Any large changes that may take place from time to time cannot be corrected for and if such a change happens during zone plate writing the only answer is to abandon it and start again.

4. PARAMETERS OF THE X-RAY MICROSCOPE

The initial aim of this development programme is to install a high resolution scanning x-ray microscope on the undulator beam line with a view to the initial commissioning of the instrument early in 1986. The broad band photon beam from the undulator will be focused by a mirror/grating monochromator onto a pinhole which will act as the radiation source for the microscope. The microscope will have a horizontal scanning stage and the soft x-ray beam will be oriented vertically by a multilayer reflector giving ~ 90° reflection (angle of incidence close to 45°). This reflection at the Brewster angle ($n \simeq 1$) means that the x-ray beam will be 100% plane polarised with the electric vector in the horizontal plane. The acceptance of the zone plate optical system for diffraction limited optics is given by

$$(1.22\ \lambda)^2 \times 10^{-6}\ \text{mrad}^2.\text{mm}^2. \qquad (8)$$

which is equivalent to the coherence condition as defined eg by Howells (1982). The number of photons expected in the scanning spot is then the product of the FOM from Table 1 and the acceptance after folding in efficiency factors for the other optical elements and the fractional bandwidth of the monochromator. Assuming 1% overall efficiency and a 5% zone plate efficiency then the order of magnitude of the photon flux at the scanning spot will be between 10^5 and 10^6 photons/second into a diffraction limited scanning spot of 0.1 μm^2 (defined by the minimum zone width of the zone plates described above). According to the theoretical calculations of Sayre, Kirz et al (1977) this should allow a typical biological specimen of thickness 1-2 μm^3 to be scanned in a time period of order 10 seconds with good contrast.

5. FUTURE DEVELOPMENTS

5.1 Improved zone plates

The development of the zone plates described in sections 3.3 and 3.4 is continuing and the next stage, which has already started, is to fabricate gold zone plates which can be either free-standing gold structures linked together with spokes or

gold/carbon sub strates in which the gold provides the opaque region and the carbon becomes the transparent region of the zone plate as described by Michette and Burge (1984). Carbon polymer zone plates have their maximum efficiency very close to the carbon K-edge at 4.4 nm and are less effective at other wavelengths. For example at 3 nm (close to the N_K and Ca_L edges) an Au/C zone plate would be 3 × the efficiency of a C zone plate of the same dimensions. Attempts are being made to deposit gold atoms in the open areas between the carbon polymer rings. These would then be used directly as focusing elements or as self-supporting units (with incomplete arcs to provide spokes).

5.2 Improved source characteristics

In October 1986 it is planned to shut down the SRS for a period of 5-6 months to install additional quadrupole focusing magnets which will reduce the emittance of the electron beam by a factor ~ 10. The improvement to the FOM for microscopy work in the undulator beam line is indicated in Table 2 which shows a factor of 30 improvement over the FOM prior to the lattice improvement programme. In terms of the parameters of section 4 this will reduce the data collection time to a time less than 1 second for the same resolution and contrast level.

5.3 The European dimension

The ultimate development for soft x-ray microscopy is represented in Table 2 by the European Synchrotron Radiation Facility (ESRF) which is being proposed by a consortium of European countries (Farge, 1979). A soft x-ray undulator installed on the proposed high brightness 5 GeV electron stroage ring would have a FOM for x-ray microscopy many orders of magnitude higher than anything available on present-day synchrotron sources.

6. CONCLUSION

The Daresbury SRS is now committed to x-ray microscope development. The programme envisages the development of a scanning x-ray microscope to be commissioned in 1986 prior to the SRS improvement programme.

7. ACKNOWLEDGEMENTS

We are indebted to our colleagues at the Daresbury Laboratory, particularly M.W. Poole and R.P. Walker for discussions

on undulator theory and performance and to A. MacDowell, I.H. Munro and J.B. West for the development of the undulator beam line. Dr. R. Rosser (Imperial College, London, UK) assisted in the tests of zone plates at Brookhaven National Laboratory.

REFERENCES

Barbee, T.W., 1984, Multilayers for x-ray optical applications. In Schmahl and Rudolph (1984) pp144-162.

Chau, H.H.M., 1969, Moiré patterns resulting from superposition of two zone plates. Appl. Opt. 8:1707

Cosslett, V.E. and Nixon, W.C., 1960, X-ray microscopy. Cambridge University Press, Cambridge, UK.

Dhez, P., 1984, Use of multilayers for XUV optics. In Schmahl and Rudolph (1984) pp139-143.

Farge, Y., 1979, European Synchrotron Radiation Facility. The feasibility study. European Science Foundation, Strasbourg, France.

Franks, A. and Gale, B., 1984, Grazing incidence optics for x-ray microscopy. In Schmahl and Rudolph (1984) pp129-138.

Haelbich, R.P., 1980, A scanning ultra soft x-ray microscope with multilayer coated reflection optics. Scanned Image Microscope pp413-433, Academic Press, London, UK.

Howells, M., Kirz, J., and Krinsky, S., 1982, A beam line for experiments with coherent soft x-rays, BNL Report 32109.

Krinsky, S., Perlman, M.L., and Watson, R.E., 1983, Characteristics of synchrotron radiation and of its sources. In Handbook on Synchrotron Radiation. Vol.1a, E.E. Koch (Ed.) North Holland Publishing Co., Amsterdam, Holland.

Michette, A.G., Browne, M.T., Charalambous, P., Burge, R.E., Duke, P.J. and Simpson, M.J., 1984, Fabrication of small line width diffraction optics for use with soft x-rays. In Schmahl and Rudolph (1984) pp109-118.

Michette, A.G. and Burge, R.E., 1984, Manufacture and test of objective zone plates for use in a scanning transmission x-ray microscope, submitted to the Proceedings of the Royal Microscopical Society, London, UK.

Poole, M.W., Munro, I.H., Taylor, D.G., Walker, R.P. and Marr, G.V., 1983, Development of an undulator for the SRS, Nucl. Instrum. & Meth. 208:143

Rarback, H., Kenney, J.M., Kirz, F., Howells, M.R., Chang, P., Crane, P., Feder, R., Houzego, P.J., Kern, D.P., and Sayre, D., 1984, Recent results from the Stony Brook Scanning Microscope. In Schmahl and Rudolph (1984) pp203-216.

Sayre, D., Kirz, J., Feder, R., Kim, D.M., and Spiller, E., 1977, Ultramicroscopy, 2:337.

Schmahl, O. and Rudolph, D., (eds), 1984, X-Ray Microscopy, Springer Series in Optical Sciences No.43, Springer Verlag, Berlin, W. Germany.

Simpson, M.J., 1984, PhD Thesis, Queen Elizabeth College, London, UK.

Spiller, E., 1984, A scanning soft x-ray microscope using normal incidence mirrors. In Schmahl and Rudolf (1984) pp226-231.

Warburton, W.K., Rek, Z.U., and Barbee, T.W., Jr., 1984, Performance tests on layered synthetic microstructures. In Schmahl and Rudolf, pp163-170.

X-RAY CONTACT MICROSCOPY

Ralph Feder and Veronica Mayne-Banton

IBM T. J. Watson Research Center, P.O. Box 218, Yorktown Heights, New York 10598

INTRODUCTION

Present day optics, both photon and electron, have been used to produce instruments to image and resolve large objects that are visible with a simple magnifying glass and objects as small as several atomic distances. The optical microscope played a most important role in the early part of this century in the biological field and still does. However, with the development of the electron microscope (EM) in the fifties a new world was opened up in the field of solid state physics and biology. The major limitation of the electron microscope over that of the optical system was that the specimen required special processing. For example samples had to be thinner than 100 nm. Furthermore, the contrast mechanism of the electron with the material were such that biological specimens had to be stained as well. This allowed the electrons to be able to distinguish between two low atomic numbers. Great strides were made in developing specific stains such that when applied to biological specimens they attach themselves to specific sites. This procedure is used to this day with great success. Images of thin sections of almost every known cell have been obtained with the electron microscope. One of the major controversies is over the techniques that are used to prepare the living cell for the EM. Various techniques used today are whole mounts, freeze fracture and critical point drying. We will not go into the details of these techniques but leave this to the reader to obtain a more complete description by M. A. Hayat (1970). After this preparation, which is intended to preserve the organelles in their natural

state and position when they were alive, the specimen if too thick must be sectioned. This may or may not require embedding the specimen in a plastic medium before sectioning.

Goby (1913) reported on the use of x-rays to obtain an image of a specimen on photographic emulsion. By viewing the developed film in an optical microscope he was able to magnify the image to the point where the grain size of the emulsion became apparent. Since then x-ray imaging has been used extensively in metallurgy and also medicine where we are all too familiar with the use of x-rays to image parts of the human anatomy. Since the early years attempts have been made to increase the magnification by projection techniques using point sources by Ardenore (1939), Cosslett and Nixon (1952), Cosslett (1965) and Engström (1966), or with Fresnel zone plates by Baez (1961), Pfeifer *et al.,* (1973), Mollenstedt *et. al.,* (1966) and Schmahl *et al.,* (1980), grazing incidence mirrors by Kirkpatrick and Baez (1948) and Silk (1977), reflection optics by Haelbech *et al.,* (1979) and Spiller (1981),and scanning systems by Schmahl *et al.,* (1980), Pattee (1953), Horowitz and Howell (1972), Kirz *et al.,* (1980), Haelbech *et al.,* (1980) and Schmahl *et al.,* (1978). Until a few years ago the resolutions obtainable using x-rays as the probe have been no better than that of an optical microscope. A good review of this field during the initial years is given by Cosslett and Nixon (1960), Kirkpatrick and Pattee (1957) and Cosslett (1965). The significance of using x-rays to image biological specimens is given by Hall *et al.,* (1972) and Engstr öm (1962). In the past decade there has been an explosion of activity in the use of x-rays to image biological specimens. Examples of some of this activity have been reported by, L. Manuelidis *et al.,* (1980), J. Wm. McGowan *et al.,* (1979), R. Feder *et al.,* (1976), B. J. Panessa-Warren and J. B. Warren (1980), and E. Spiller *et al.,* (1976).

Advantages in using x-rays for imaging

We can ask ourselves the question, "why is x-ray imaging important?" It becomes extremely valuable if we can not only see the ultrastructure of a cell but also determine its function. So any new information would add another piece to the "jig-saw puzzle".

There are many benefits in using x-rays for imaging. First, with the use of photons in the region 1-10 nm wavelength, a region where the soft x-rays present a favorable condition for the microscopy of biological material.

In this region the x-rays provide good contrast for practically all elements and especially good contrast for low atomic number elements which is the dominant species in biological material (Sayre *et al.,* 1977a; 1977b; and Sayre *et al.*, 1978). This of course means that, unlike the electron microscope, staining is not required. However, it is appropriate to mention here that at this point in time it is fruitful to stain specimens so that a direct comparison can be made with the EM. As you will see the images obtained with x-rays are not always recognizable and therefore require this comparison to be made. Second, the ability to choose and produce monochromatic x-rays of specific wavelength and the fact that the x-ray absorption of every element is a function of the incident x-ray energy gives us the ability to vary the x-ray contrast of any object. Fig.1 is a plot of the linear absorption coefficient per micron of material as a function of wavelength for various elements.

Third, the high penetrating power of the x-rays allow thicker specimens to be imaged than that allowed in the electron microscope; this is discussed by Kirz and Sayre (1980). This means that a great many biological samples could be imaged in their fixed state without sectioning. Fourth, with the high penetration and the sensitivity to wavelength it is possible to obtain three dimensional information. Stereographic images can eventually lead to a "micro-CAT" scanner. Fifth, with the ability to choose the wavelength and the knowledge of the absorption of protein and water it is then possible to image a living cell by x-rays. The imaging in this case is very dependent on the x-ray source which must be delivered in a very short time in order to obtain a "stop motion" image.

X-RAY IMAGING

The two major methods that use x-rays for imaging involve the contact technique and scanning techniques. The former is a relatively simple, high resolution method that can be used in almost every laboratory environment where a simple x-ray source is used. This method produces a 1:1 image and requires an electron microscope to give the high magnification. The latter method involves a more complicated set-up which requires a high intensity x-ray source. This system gives an image in real time and is now being worked on by several groups. A more detailed discussion will be given by others at this conference. This paper will be devoted solely to the contact technique, and specifically to the details of the technique, others will discuss some of the results obtained by this method.

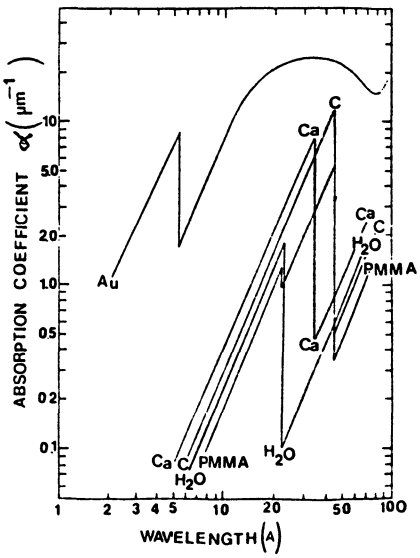

Fig 1. Absorption coefficient plotted as a function of wavelength for a variety of elements. All wavelengths are in the soft x-ray region.

CONTACT MICROSCOPY: THE TECHNIQUE

After the early attempts to use x-rays to image objects on photographic emulsion the greatest advances were made in the past several years. The impetus came through the developments that were rapidly taking place in the fabrication of integrated circuits. Circuit fabrication involves the use of lithography, which is the technique used to transfer an image from a photographic plate (mask) to a substrate such as silicon. The substrate is composed of a silicon wafer with a thin film of plastic known as resist spun on top of the wafer. The image of the mask is transferred to the resist by first exposing the mask substrate composite to a parallel beam of light and then developing the resist. In order to miniaturize circuits other techniques had to be developed one of which was the capability to write patterns with an electron beam. This naturally led to the development of a resist that was sensitive to electrons (Haller *et al.*, 1968). More recently x-rays were introduced to act as the light source. Developmental programs are still underway throughout the world to perfect this technology. It was from this latest development that the "door was opened" to perfect high resolution contact microscopy (Spiller *et al.*, 1976). The resist that was developed for the electron beam pattern generator was found to be sufficiently sensitive to x-rays to serve as the recording medium. The initial x-ray source used was a commercial variety and was used successfully to image simple structures (Feder, 1970; Spears and Smith, 1972). Later

more sensitive resists were developed with similar high resolution capabilities, (Haller *et al.*, 1979), and more sophisticated x-ray sources were used for more interesting and challenging x-ray microscopic imaging. Figure 2 is a schematic of the contact imaging process.

In this case the specimen is brought in intimate contact with the resist surface. It can either be mounted directly on the resist or it can be mounted on an x-ray microscope grid. After development the resist will exhibit a three dimensional relief structure which is actually a photon density map of the specimen, i.e., the height of the resist is a function of the x-ray absorption in the specimen. The resist is then coated with a thin metal layer (about 10nm) as a conductor to prevent charging. This is then examined in the scanning electron microscope (SEM) or the transmission electron microscope (TEM). These two instruments are used to magnify and view the resist profiles. Fig. 3 shows the complete specimen preparation and x-ray procedure schematically.

Scanning Electron Microscopy

The simplest and most aesthetic magnified pictures obtained of the protuberances on the resist are obtained by the scanning electron microscope. The picture gives a three dimensional image of the resist which is more pleasing to the eye but is more difficult to interpret. It is difficult to compare the surface of the original specimen with the surface profiles as shown by the image in the resist. Since the x-ray image is due to the internal structure as well as the surface irregularities. Furthermore, surface profiles do not lend itself too easily to any image processing. However, this method of examination will be shown to have more value when the resist thickness is too thick to allow small variations of thickness to be recorded. The use of the SEM does not require any special substrate on which the resists is spun, a flat solid substrate is all that is needed.

Transmission Electron Microscopy

The technique used by practically all biologists to examine their specimens is with a transmission electron microscope. The contrast of the specimen shows up as a simple grey level scale on the photographic plate. To make this technology more amenable to the biological community, since it is their most common method for viewing objects, a substrate was developed in which the developed resist could be viewed through the TEM. Using the known silicon technology a substrate only 100 nm thick of Si_3N_4 was fabricated over a frame of Si. The dimensions of the Si frame were such that it fit into a

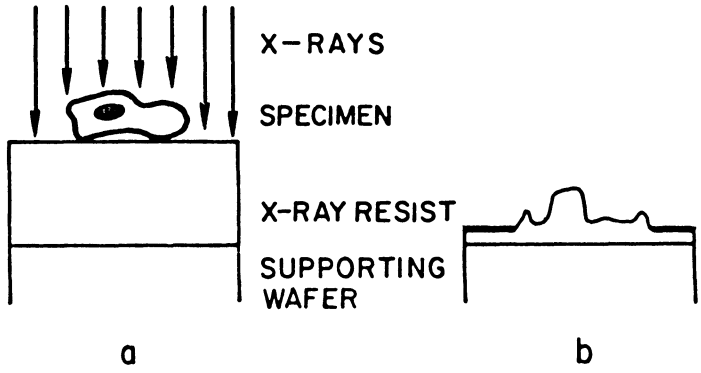

Fig. 2 Schematic of contact imaging. (a) Contact imaging of specimen into resist where incident x-ray beam is modified by the absorption of the specimen. (b) The resist after development and metallization. The resist profile is then magnified and read out by electron microscopy.

3 mm EM grid holder (Feder and Sayre, 1980). Fig. 4 is a schematic showing the steps required to produce the TEM substrate.

The photographs obtained with the TEM of the developed resists give an exact comparison with the TEM image obtained from an examination of the original specimen. The attenuation of the electron beam is a function of the thickness or electron opacity of both the resist and specimen. The comparison can only be made with the understanding that the photograph of the x-ray image was made by the photon absorbance of the specimen plus the electron absorbance of the resist, whereas the specimen electron image is made purely by the electron absorbance of the specimen.

RESOLUTION OF THE RESIST

To record an x-ray transmission pattern the most common detectors used in x-ray imaging are photographic plates or film. As explained earlier the technique of contact x-ray microscopy was previously limited by the resolution

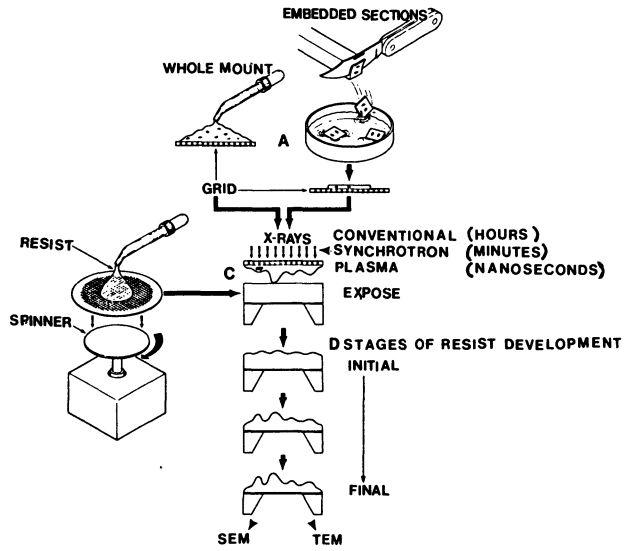

Fig. 3 Specimen preparation and x-ray imaging of biological specimen. Initial procedure as shown with specimen mounted on grid, either by microtoming embedded specimen or placing a drop of the dilute specimen solution on a grid. Next step shows resist being spun on a substrate. The resist is now exposed to x-rays such that the transmitted x-rays are absorbed by the resist. After development and metallization the x-ray resist is examined in the SEM or TEM.

of this detector. It wasn't until the industrial development of a detector (resist) in the fabrication of integrated circuits, that one could image submicron structures. Also, when fully developed, the resist produced a three dimensional structure which acted as a barrier over certain areas to allow further processing of the substrate. Depending upon the resist which was made of an organic polymer it was not only sensitive to electron but was sensitive to photons ranging in wavelengths from the visible region down into the x-ray region. The development of the resist produced a three dimensional pattern because the incident radiation modified the resist such that the developer was able to remove the exposed region and leave the unexposed areas intact.

If we consider a high resolution resist such as polymethylmethacrylate (PMMA) it is first prepared by dissolving the polymer in chlorobenzene. The concentration will depend upon the thickness of the film desired. A few drops of the solution is spun onto a substrate. Again,the speed at which the specimen is spun also depends upon the thickness of the film de-

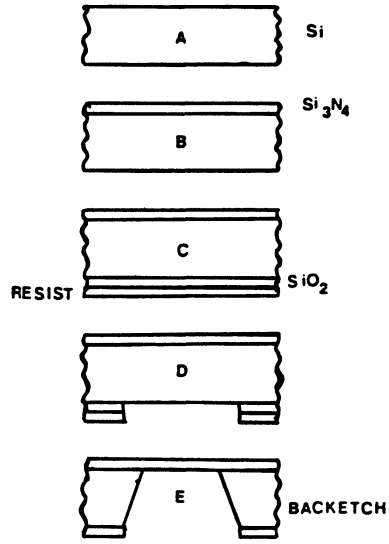

Fig. 4 Above figure shows the step by step process to fabricate TEM x-ray substrates. This procedure results in a free standing 1000 Å Si_3N_4 membrane on a Si frame.

sired. The spinning operation will produce consistent thicknesses to within 2 nm. The film is then dried and cured at 160 ° C. for 1 hour. Depending upon its final use the thickness used will vary from 50 nm to 1000nm. In exposing the resist to a modified x-ray beam, i.e., an x-ray beam that is transmitted through a biological cell, a fraction of the transmitted beam will be absorbed. These absorbed photons will produce secondary electrons which, depending upon their energy, will proceed to break the chains of the polymer resulting in chain scission. The affected molecules will in effect have a lower molecular weight leading to a higher solubility of the resist. It is the mean free path of these secondary electrons that will determine the resolution of the resist. This was found experimentally to range from 5 nm to 20 nm for incident x-ray wavelengths from 2 nm to 4 nm. The normal developer for PMMA is methylisobutyl ketone (MIBK) used in concentrated form or diluted with isopropyl alcohol. Therefore, the higher the exposure the higher the dissolution rate of the polymer (Ranby and Rabak, 1975). A plot of the these parameters is shown in Figure 5.

The figure also gives the details of another resist which is more sensitive thereby faster than PMMA and yet retains its high resolution capabilities.

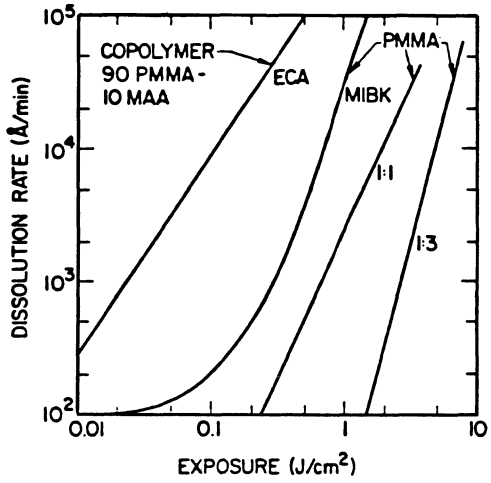

Fig. 5 Dissolution rate vs. exposure for PMMA and PMMA-MAA copolymer resist. The three curves for PMMA represent the dissolution rate using different concentration of developer. The slope of the curves which specify the contrast of the resist shows its dependence on the exposure and type of development.

This resist is a copolymer of polymethyl-methacrylate and methacrylic acid (PMMA-MAA). This resist has been used extensively by the author and coworkers in obtaining a large number of high resolution images under various conditions. The slopes of the curves indicate that above a minimum exposure the γ (contrast of the resist) is greater than 1. That is small ratios between different exposures can result in larger ratios in the dissolution rate. So for small differences in contrast in a specimen and with the proper exposure small differences in photon absorbance in the specimen will be made visible in the x-ray image.

RESOLUTION LIMITATIONS OF THE TECHNIQUE

The inherent resolution limit of the technique is determined by some of the physical parameters of the experimental conditions. This effect results in penumbral blurring. This is shown in Figure 6. The blurring or resolution is defined by the equation $S_p=s(d/D)$. This tells us that the specimen thickness

will contribute to a loss in resolution. However, for specimens as large as 1 μm, source size 1 mm, and a source to specimen distance of 20 cm the resolution is equivalent to the highest resolution attainable in the resist due to the scattered electrons.

A more important effect may be due to diffraction. We examine the case of near field diffraction (Fresnel diffraction) and consider the simplest case where the uppermost point of the specimen is causing the diffraction. In reality diffraction occurs throughout the depth of the specimen. From standard texts the first intensity maximum in Fresnel diffraction exists at $d = (a/\lambda)$ where a is the specimen thickness. Using the same parameters that were used to determine the effect of penumbral blurring we get a $d = 20$ nm. With these values the diffraction blurring contributes most to the loss in resolution.

X-RAY SOURCE

In order to solve the varied problems in x-ray microscopy, it is necessary to have a variety of x-ray sources. These range from the standard laboratory x-ray source to a source that is tuneable to any desired wavelength and another source that produces x-rays in a very short pulse. X-ray beam uniformity and source size are important due to their contributions to the resolution and contrast in the resist.

Conventional x-ray source

The standard laboratory x-ray source produces x-rays by electron bombardment against a solid target. The x-ray emission from this source is a strong characteristic radiation whose wavelength depends upon the target material. Superimposed on the characteristic radiation is a broad band of white radiation whose magnitude and energy depends upon the accelerating voltage of the incident electron beam. A number of discrete wavelengths can be obtained in this way. The advantage of this system is that it is relatively inexpensive and can be part of any laboratory facility. The disadvantage is that the x-ray flux is low and requires several hours to expose and form an image in the resist. Furthermore the number of discrete wavelengths obtainable is very limited. This type of source is shown schematically in Figure 6.

Synchrotron radiation source

Synchrotron radiation is at the present time the most intense continuous source available for soft x-rays. It has an effective small source size and

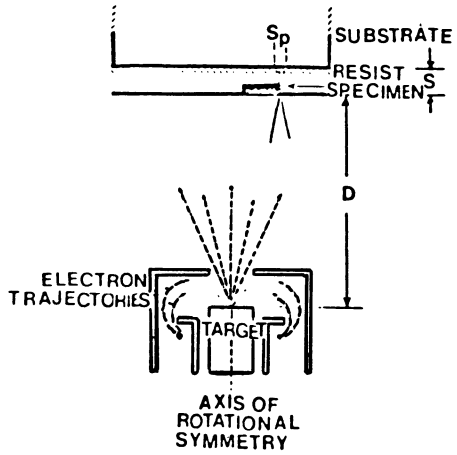

Fig. 6 Schematic of a conventional x-ray exposure system. The penumbral blurring S_p is due to the source size d, distance of source to specimen D and spacing of specimen to resist s.

for all practical purposes is considered to be a parallel beam. Since there are several speakers discussing the scanning x-ray system a more complete description of this x-ray source will be left to them. As far as contact x-ray microscopy is concerned, the synchrotron as an x-ray source has several important advantages. First, exposure times are now measured in minutes. Second, the range of x-rays produced by the synchrotron is a continuous band depending upon the energy of the electron beam being accelerated in the ring. The use of a grating or other techniques of monochromating the beam makes the x-ray beam "tuneable". The advantage of tuneability allows the user to obtain images of a variety of specimens above and below the absorption edge. The two images when subtracted will give the concentration and location of the particular element in question. The negative aspect of the synchrotron is the high cost of building and operating such a system. Consequently synchrotron centers have been established to service the needs of many users. However, it is unlikely that the casual user can have ready access to one these machines. The cost of these machines is in the millions and the technology is still in a state of flux.

Pulsed X-ray Sources

There are two types of x-ray sources that fall into this category. They are the laser induced plasma source and the z-pinch flash x-ray source. The

x-ray emission of these sources last anywhere from 1 nsec to 100 nsec. Any one of these sources can play a very important role in imaging living biological cells.

Laser Induced Plasma X-ray Source

This system is actually the replacement of an electron impact source which is present in a conventional x-ray system with a powerful, focused laser beam (Nagel *et al.*, 1978). This beam when focused on a solid target produces a hot plasma which in turn emits x-rays. The short pulse of the laser (1-10 nsec.) will produce a burst of x-rays with sufficient intensity to expose a high resolution resist detector. Attempts have been made using a laser to generate enough x-rays (single burst mode) to expose resist but without success. However, there is much activity in the laser field to create a system that will be satisfactory in the field of x-ray lithography. It is hoped that x-ray microscopy will benefit from a spin off of this technology. Figure 7 is a schematic of such a system.

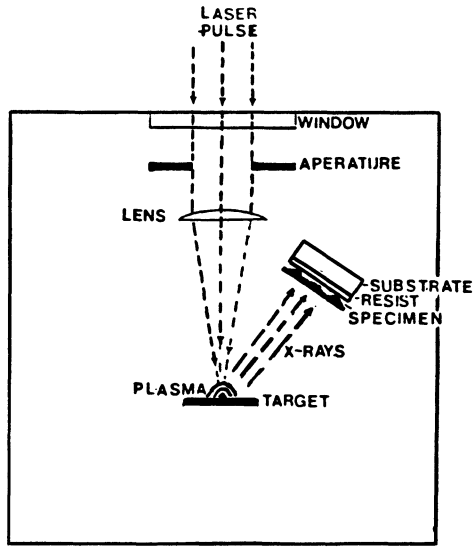

Fig. 7 Schematic of an plasma generated by a laser pulse. Drawing shows a possible configuration of the source and specimen.

Z-pinch X-ray Source

This flash or "puff" source produces a hot plasma by creating a very high magnetic field around a coaxially produced puff of gas (Pearlman and Riordan, 1981; Bailey *et al.*, 1982). The field will "pinch" the gas along its axis until it reaches a very high temperature creating the plasma. The plasma in turn emits a wide band of x-rays. The flash takes place within 100 nsec. Figure 8 is a schematic of such a source.

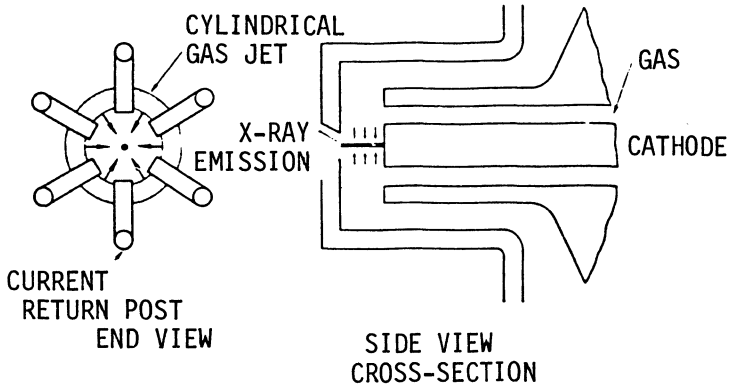

Fig. 8 To form a tightly pinched plasma x-ray source, electrical current is pulsed through an annular gas cylinder. The cylinder is imploded by magnetic forces onto the gas jet axis, resulting in a high temperature plasma.

This system has been used successfully to obtain the first high resolution x-ray images of a living cell This x-ray source has recently been introduced as a product (Maxwell Laboratories Inc.). A more detailed discussion of these experiments will be given in a subsequent talk by M. Baldini. A machine of this type and possibly future laser sources for x-ray production are about 100,000-200,000 dollars. The cost is low enough that it could be made available in many laboratories.

IMAGING OF LIVING CELLS

In order to image wet biological materials, it is necessary first to provide an environment around the biological material such that the biological cell would remain alive and healthy during the time it takes to prepare and expose the specimen to the x-ray beam. In addition the chamber holding the specimen

must, in the case of contact x-ray microscopy, be able to withstand a vacuum environment. This wet chamber that was successfully used is shown in Figure 9.

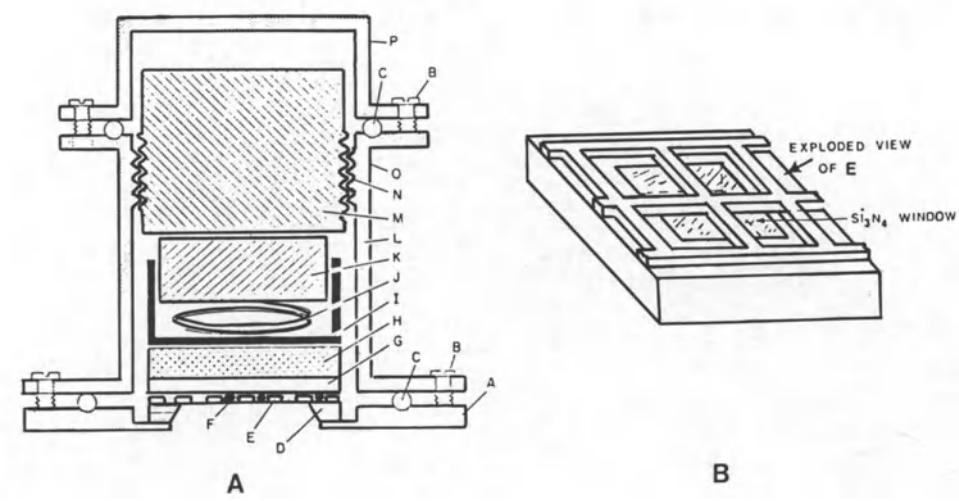

Fig. 9 Detailed drawing of the wet chamber used to image a living cell. The baseplate (A) is used to hold the Si_3N_4 vacuum window (D). (E) is a lithographically produced grid to act as sub-chambers for the living cells (F). The resist (G) is spun on a flat substrate (H). (I) through (P) represent the body of the chamber which denotes a spring and spring compressor enclosed within the chamber. The diagram in Fig. 9B is an exploded view of (E), the grid-like sub-chambers constructed on the surface of the Si_3N_4 window.

Second the x-ray source in use must be of the proper wavelength such that it can distinguish between water and protein, i.e., the absorption of each should be sufficiently different to register on the resist. The z-pinch plasma x-ray unit does have such a favorable emission plus the short burst of x-rays to guarantee the "stop motion" picture of the living cell. Figure 10 is a plot of the absorption curves of water and protein.

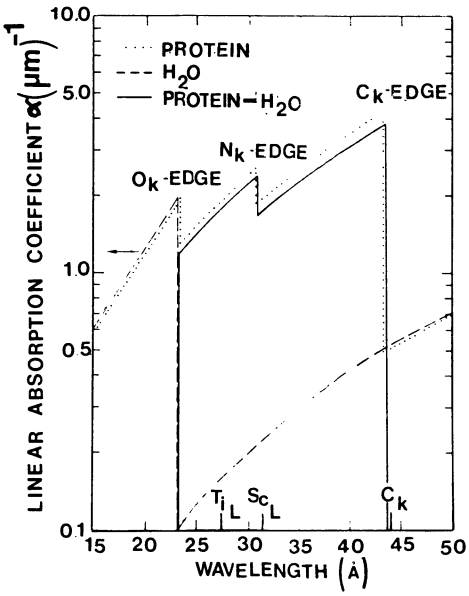

Fig. 10 The linear absorption coefficient per micron of material plotted as a function of wavelength. The graph as shown by the solid line represents the difference between the absorption of protein (dotted line) and water (dashed line). Note the x-ray "window" between 24 Å and 44 Å.

Several examples of the type of images one can obtain using this technique are shown in the next series of figures. Other more detailed pictures using the contact technique will be shown and discussed by other speakers, M. Baldini and P.C. Cheng.

The entire discussion on the use of x-ray contact microscopy involved the imaging of biological subjects. This should not be taken literally. Other subject material which may be of great importance is in the imaging of three dimensional integrated circuit patterns or thin films in general. An x-ray image was actually made of a thin film of Cu-Al which was annealed to form precipitates. It was assumed that the precipitates would be homogeneous and the contrast between Cu and Al would be great enough to obtain an image of the precipitates. This is shown in Figure 11a, and Figure 11b.

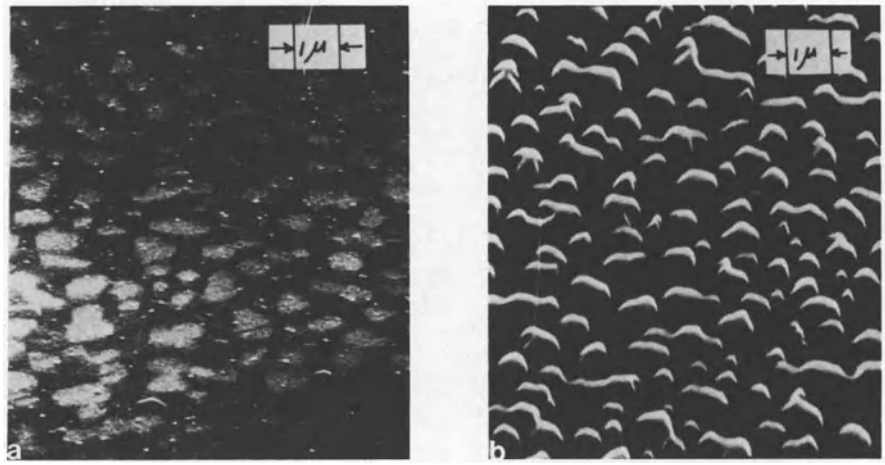

Fig 11. SEM photographs of a Cu-Al thin film annealed to create precipitates. Fig. 11a represents the then film showing the difference in electron contrast between the Cu-Al precipitates and the surrounding medium. Figure 11b is the x-ray image of the thin Cu-Al film. Note the inhomogeneity of the precipitates showing up as irregular shapes and heights. Homogeneous precipitates would show up as right circular cylinders.

Both of the above figures are SEM photographs of the original thin film (Fig. 11) and the x-ray resist of the same thin film. The light colored areas in the left picture represent the precipitates and are more absorbing than the surrounding film of Al. This is shown very clearly in Figure 11a where the bumpy resist areas are the precipitates but they do not show up as a homogeneous absorber. A number of the resist protuberances show a variation in height within each precipitate. This could only mean that there is more than one compound within the precipitate.

One of the simplest biological systems was used to evaluate the contact technique. Images were obtained of some bacteria including *E. coli* and *Spirillum*.

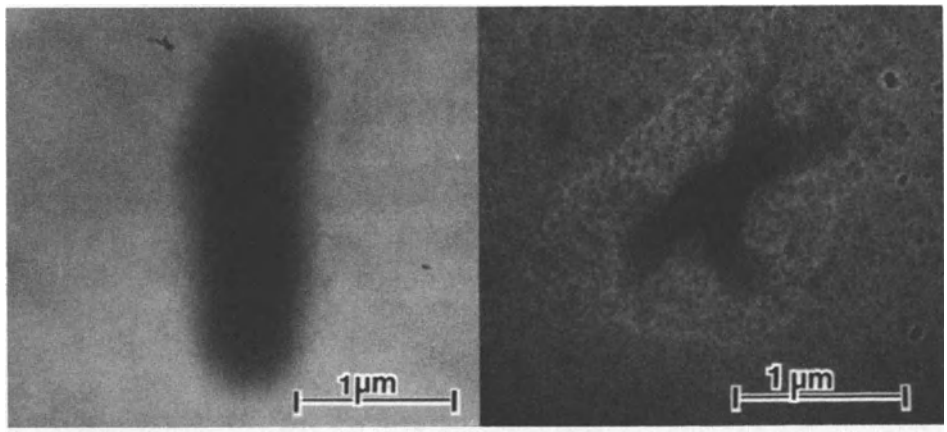

Fig. 12 TEM pictures of *E. coli.* The left picture shows the unstained whole-mount *E. coli.* The x-ray image of the same bacterium is shown on the right which exhibits an x-ray dense, backbone-like structure.

The above figures are TEM photographs of the unstained *E. coli* bacterium on the left. The image shows no visible structure. However, the picture on the right which is the x-ray image of the same *E. coli* shows the bacterium to contain a sub-structure. At higher magnification the skeletal structure shows a more detailed fine structure which is not shown here.

The above figures are of an unstained *Spirillum* bacteria. This bacterium has a spiral-like configuration. The TEM picture on the left shows the twisted features of the bacterium. The picture on the right is the x-ray image of the same bacterium. The x-ray image shows a spiral like structure with some similarities to the one on the left and a number of differences.

In conclusion the x-ray contact technique has progressed far enough that the results are of interest to the biologist. However, the major thrust today is to explain the x-ray images of the specimens which in most cases look different than that seen in the TEM. It is obvious that the photon absorption in the specimen is very different than the electron absorption. This is true in most

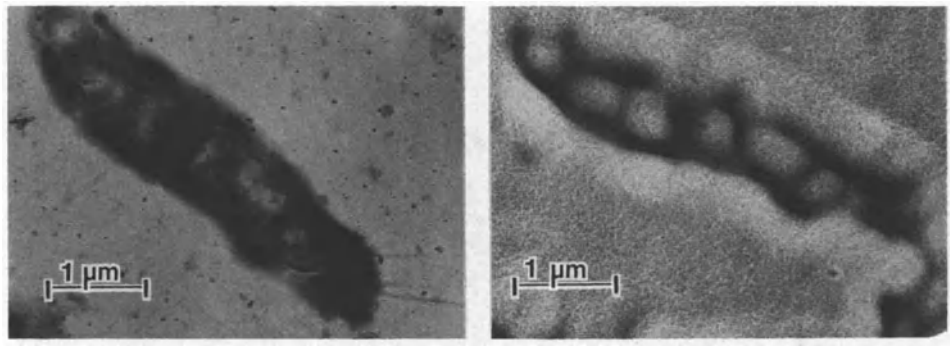

Fig 13. TEM pictures of a *Spirillum* bacterium. The left picture shows some internal structure. The x-ray image on the right emphasizes the internal spiral-like structure.

of the specimens that have been examined. This then makes the field of x-ray microscopy that much more interesting.

ACKNOWLEDGEMENT

The authors would like to thank Mary Beth Perna and Lynn Kettell for their technical assistance.

REFERENCES

M. von Ardenore, 1939, Zur Leistungsfahigkeit des elektronen-schattenmikroskopes und uber ein röntgenstrahlen-schattenmikroskop, Naturwissenschaften 28:485.

S. V. Baez, 1961, Fresnel zone plates for optical image formation using extreme ultraviolet and soft x-radiation, *J. Opt. Soc. Amer.,* 51:405.

J. Bailet, A. Ettinger, A. Fisher and R. Feder, 1982, Evaluation of the gas puff z pinch as an x-ray lithography and microscopy source, *Appl. Phys. Lett.*, 40:33.

V. E. Cosslett and W. C. Nixon, 1952, An experimental x-ray shadow microscope. *Proc. Roy. Soc. (London) B,* 140:422.

V. E. Cosslett, 1965, X-ray Microscopy, *Rep. Prog. Phys.,* 28:381.

V. E. Cosslett and W.C. Nixon, 1960, X-ray Microscopy, Cambridge Univ. Press, Cambridge, England.

A. Engström, 1966, Physical techniques in biological research. ed. A.W. Pollister vol 111 Part a, Academic Press 87.

A. Engström, 1962, X-ray microanalysis in biology and medicine, Elsevier, Amsterdam.

R. Feder, D. Sayre, E. Spiller, J. Topalian, and J. Kirz, 1976, Specimen replication for electron microscopy using x-rays and x-ray resist. *J. App. Phys.*, 47: 1192.

R. Feder, 1970, X-ray projection printing of electrical circuit patterns, *IBM Tech. Rep.,* TR 22.1065:1.

R. Feder and D. Sayre, 1980, Recent developments in x-ray contact microscopy. *Ann. N.Y. Acad. Sci.,* 342: 213.

R. Feder, J. L. Costa, P. Chaudhari and D. Sayre. 1981, Improved detail in Biological Soft X-ray Microscopy: Study of blood platelets. *Science*, 212:1398.

P. Goby, 1913, X-rays in microradiography, *C.R. Acad. Sci. Paris*, 156:686

R. P. Haelbech, A. Segmuller and E. Spiller, 1979, *Appl. Phys. Lett.,* 34:184.

R. P. Haelbech, W. Staehr and C. Kunz, 1980, *Ann. N.Y. Acad. Sci.,* 342:148.

T. A. Hall, H. D. E. Rockert and R. F. L. de C. Saunders, 1972, X-ray microscopy in clinical and experimental medicine, Charles C. Thomas, Springfield, Illinois.

I. Haller, M. Hatzakis, and R. Srinivasan, 1968, High resolution positive resists for E.B. exposure. *Res. Dev.,* 12:251.

I. Haller, R. Feder, M. Hatzakis, and E. Spiller, 1979, Copolymers of Methyl Methacrylate and methacrylic acid and their metal salts as radiation sensitive resists. *J. Elec. Chem. Soc.,* 126:154.

M. A. Hayat, (1970) Principles and techniques of electron microscopy, Van Nostrand Reinhold Company.

P. Horowitz and J. S. Howell, 1972, A scanning x-ray microscope using synchrotron radiation, *Science,* 178:608.

P. Kirkpatrick and A. V. Baez, 1948, Formation of optical images by x-rays, *J. Opt. Soc. Amer.,* 38: 766.

P. Kirkpatrick and H. H. Pattee Jr., 1957, Handbuch der Physik, ed. S. Flugge.

J. Kirz, R. Burg and H. Rarbach, 1980, Plans for a scanning transmission x-ray microscope *Ann. N. Y. Acad. Sci.,* 342:135.

J. Kirz and D. Sayre, 1980, Soft x-ray microscopy of biological specimens. Synchrotron Radiation Research , ed. Winick and S. Doniach, Plenum Publishing: 277.

L. Manuelidis, J. Sedat and R. Feder, 1980, Soft x-ray studies of interphase chromosomes. *Ann. N. Y. Acad. Sci.,* 342:304.

J. W. McGowan, B. Borwein, J. A. Medeiros, T. Beveridge J. D. Brown, E. Spiller, R. Feder, J. Topalian and W. Gudat, 1979, High resolution microchemical analysis using soft x-ray lithographic techniques. *J. Cell Biology,* 80:1979.

G. Mollenstedt, H. J. Einighommer, K. H. Grote and U. Mayer, 1966, S-ray Optics and Microanalysis, eds. R. Castaing, P. Deschamps and J. Philibert (Hermann, Paris) :15.

D. J. Nagel, J. M. McMahon, R. R. Whitlock, J. R. Grieg, R. E. Pechacek and M. C. Peckerar, 1978, Lithography and high resolution radiography with pulsed x-rays, *Jap. J. of App. Phys.,* 17:472.

B. Panessa-Warren and J. B. Warren, 1980, Determining biological fine structure by differential absorption of soft x-rays, *Ann. NY Acad. Sci.*, 342:350.

H. H. Pattee, 1953, The scanning x-ray microscope , *J. Opt. Soc. Am.*, 43:61.

J. Pearlman and J. C. Riordan, 1981, X-ray lithography using a pulsed plasma source. *J. Vac. Sci. tech.*, 19:1190.

C. D. Pfeifer, L. D. Ferris and W. M. Yen, 1973, Optical image formation with a fresnel zone plate using vacuum-ultraviolet radiation, *J. Opt. Soc. Am.*, 63:91

B. Ranby and J. F. Rabak, 1975, Photodegradation, photooxidation and photostabilization of polymers, Wiley and Sons, N.Y.

D. Sayre, J. Kirz, R. Feder, D. M. Kim and E.Spiller 1978, Assessment of the potential of ultrasoft x-ray microscopy. *Ann. N. Y. Acad. Sci.*, 306:286.

D. Sayre, J. Kirz, R. Feder, D. M. Kim and E. Spiller, 1977, Potential operating region for ultrasoft x-ray microscopy of biological materials. *Science*, 196:1339.

D. Sayre, J. Kirz, R. Feder, D. M. Kim and E. Spiller, 1977, Transmission microscopy of unmodified biological materials: comparative radiation dosages with electrons and ultrasoft x-ray photons, *Ultramicroscopy,* 2:337.

G. Schmahl, D. Rudolph and B. Niemann, 1978, X-ray microscopy of biological specimens, *J. Phys Colloq.*, 39:202.

G. Schmahl, D. Rudolph, B. Niemann and O. Christ, 1980, X-ray microscopy of biological specimens with a zone plate microscope. *Ann. N. Y. Acad. Sci.*, 342:368.

K. Silk, 1977, X-ray imaging. *Proc. SPIE*, 106:113.

D. L. Spears and H. I. Smith, 1972, *Electronic Letters*, 8:102.

E. Spiller, 1981, High resolution soft x-ray optics, *Proc. SPIE.* :316.

E. Spiller, R. Feder, J. Topalian, D. Eastman, Wl. Gudat and D. Sayre, 1976, X-ray microscopy of biological objects with carbon *K* and with synchrotron radiation, *Science 191:1172.*

ULTRA SOFT X-RAY CONTACT MICROSCOPY:

A NEW TOOL FOR PLANT AND ANIMAL CYTOLOGY

P. C. Cheng (鄭炳令)[1], J. Wm. McGowan[2], K. H. Tan (陳金華)[3], R. Feder[4], and D. M. Shinozaki[5]

[1]Department of Anatomy, University of Illinois at Chicago, Chicago, Illinois, 60612, USA

[2]National Museum of Science and Technology, Ottawa, Ontario, K1A 0M8, Canada

[3]Canadian Synchrotron Radiation Facility, Physical Science Laboratory, University of Wisconsin, Stoughton, Wisconsin, 53589 USA

[4]IBM T. J. Watson Research Center, Yorktown Heights, New York, 10598, USA

[5]Faculty of Engineering Sciences, University of Western Ontario, London, Ontario, N6A 5B9 Canada

INTRODUCTION

The invention of the light microscope in the 17th century marked the beginning of modern biology. Since then, biologists have been capable of studying tissue structures beyond the resolution of the naked eye. In the 1940's, the development and subsequent rapid advancement of the electron microscope posted a new milestone in biological research. Because of its high resolution,

the electron microscope has contributed significantly to the understanding of cellular structures. However, fundamental physical problems, such as difficulty in handling hydrated specimens, has limited the progress of electron microscopy. The use of soft x-rays for microscopy of biological specimens has many important advantages. Not only does the short wavelength of x-rays promise spatial resolution in the order of 10 nm, but also the large penetration depth offered by x-rays provides a potential tool for the study of thick specimens. In contrast to electrons, photons may be absorbed but are virtually not scattered. Therefore, the thickness of the specimen, and the air or water constituents of living cells, may reduce the image intensity but will not blur it. Furthermore, the image contrast of x-ray microscopy is energy-dependent. Therefore, it is possible to image unstained samples or perform microchemical analysis by carefully selecting the x-ray energies over a certain absorption edge.

Despite the advancement in medical and industrial hard x-ray technology, focusing and collimating of x-rays remain difficult tasks. At present, four imaging techniques are available: true microscopy (Rudolph *et al.*, 1984; Duke, 1984; Rosser, 1984; Silk, 1981; Spiller, 1984), scanning x-ray microscopy (Horowitz and Howell, 1972; Rarback *et al.*, 1984; Niemann, 1984), photoelectron x-ray microscopy (Polack and Lowenthal, 1984) and contact microscopy. Contact microscopy is the oldest and simplest technique among them, and it is the technique which we intend to focus on in this article. X-ray contact microscopy was pioneered by Goby (1913), who has studied structures of plant tissue, insect and foraminiferes. Later, Dauvillier (1927, 1930) and Lamarque (1936) have continued such work with other biological specimens. More recently, Engström and his associates (Engström, 1946, 1962, 1966, 1980; Cosslett, 1960) have performed many fundamental studies using this technique. The first generation of contact radiographs used silver halide as the detector. Naturally, the resolution of the image is limited by the size of silver grain. With the introduction of a high resolution x-ray resist (Spiller *et al.*, 1976; Feder *et al.*, 1977), the second generation contact radiographs have become a potential tool for the study of cellular ultrastructures. To date, high resolution x-ray contact microscopy has been used to image many different types of biological specimens (McGowan *et al.*, 1979, 1980; Panessa *et al.*, 1980a, 1980b, 1980c, 1984; Feder, 1981; Cheng and Peng, 1981; Cheng *et al.*, 1982, 1984; Feder *et al.*, 1984; Spiller and Feder, 1978; Tan *et al.*, 1984). Structures which cannot be seen in electron microscopy have been reported (Feder *et al.*, 1981). Discussions on the theory and technology of x-ray microscopy have been published (Spiller and Feder, 1977; Sayre, 1980; Sayre and Feder, 1980; Kirz and Sayre, 1980; Kirz, 1980).

There are few biological specimens which are thin enough (or small enough) for transmission electron microscopy (TEM) without sectioning. Even with soft x-rays, most of the specimens are still too thick to be observed directly. At present, tissue sections are prepared by a few methods: sections are obtained either by embedding the tissue in paraffin or plastic, or by freezing of the tissue, and subsequently sectioning the embedded tissue using a microtome. For light microscopy studies, paraffin sections are routinely used. After sectioning, the paraffin is removed, and the sections stained and mounted between two glass plates. Unlike the plastic method, the paraffin embedding method does not provide adequate preservation of cellular structures at high resolution. The plastic embedded sections are desirable for electron microscopy not only for excellent ultrastructural preservation, but also the embedding material tends to stabilize the cellular structures against electron beam damage (Luft, 1973). Therefore, plastic sectioning has become the standard method for transmission electron microscopy. However, it is important to note that the epoxy embedding medium has nearly the same x-ray absorption properties as many biological materials. Therefore, the x-ray images of unstained plastic-embedded tissue suffers from lack of contrast. Even though most of the literature suggests that x-ray microscopy is a potential tool for unstained biological materials, one should consider the use of "stains" to increase image contrast (Kirz and Sayre, 1984), especially in plastic embedded tissue sections. Cytochemical and immunocytochemical methods which specifically label certain structures in the cell (such as the use of colloidal gold conjugated monoclonal antibodies) are also worth considering. Furthermore, the use of the polyethylene glycol (PEG) sectioning technique (Wolosewick, 1980) provides an alternative method, where the embedding matrix can be removed after the section is cut. Studying living tissue by means of x-ray microscopy is a considerable challenge for the biologist, since there are no available techniques which would allow us to prepare thin samples without the killing of the tissue.

In this article, we will examine the basic methods of x-ray contact microscopy with emphasis on the methods for biological specimen preparation and image interpretation. Examples and interpretation on both plant and animal tissues are given. The basic imaging technique of x-ray contact microscopy is discussed in another article of this volume (Feder and Mayne-Banton). X-ray absorption spectra of various biological compounds, supporting matrix and resists are presented. Knowing the x-ray absorption spectra of major biological compounds is essential for the precise determination of the absorption edges. This, in turn, is needed for the microchemical analysis.

IMAGES OF PLANT TISSUE

Plant tissues generally pose many challenges to the plant cytologist. The extracellular matrix, mainly the cell wall, poses a major barrier for direct observation of whole-mount specimens by transmission electron microscopes. Furthermore, many plant tissues are dense, such as pollen grains, spores etc., which always presents a greater difficulty with regards to an ultrastructural study. X-ray microscopy, using properly selected wavelengths, could provide a useful tool for studying such systems. Tan *et al.* (1984) showed an x-ray image of floral tissue of *Zea mays*. This image demonstrated the potential usage of x-ray contact microscopy on the study of thick botanical specimen. Many of the potential uses of x- ray microscopy have been proposed and discussed by Sarafis (1984).

In the past five years, we have imaged various botanical specimens to establish basic techniques of specimen handling and interpretation. Some of the results have been reported in paper form (Tan *et al.*, 1984), in short communication form (Cheng and Peng, 1981) and in abstract form (Cheng *et al.*, 1980, 1981). In this article, we intend to use some of our findings as examples to discuss the methods and interpretations of x-ray contact microscopy of botanical samples. The specimen which will be discussed is the anther tissue of *Caltha palustris*. The ultrastructure of *Caltha*'s anther tissue has been studied extensively (Cheng and Lin, 1980) which provides a basis for detailed interpretation of x-ray images.

Anther Tissue of *Caltha palustris* L.

The anther tissue of *Caltha palustris* used in this study was fixed in Cheng's fixative (Cheng *et al*, 1979), postfixed in osmium, and embedded in Spurr's medium. One micron sections were mounted on a 1x1 mm Si_3N_4 window by the aid of a specially made transfer grid (Cheng and Lin, 1981). X-ray

Figure 1. An interference microscope magnified x-ray contact image of the anther tissue of *Caltha palustris*. Contact microscopy offers a very wide field which is very useful for the study of tissue structure. Note the microsporangia consist of four layers of cells: the epidermis (E), endothecium (En), middle layer (M) and tapetum (T). The anther connective consists of two air sacs (AS) and vasculature (V). Within the microsporangium, developing pollen grains (P) are evident.

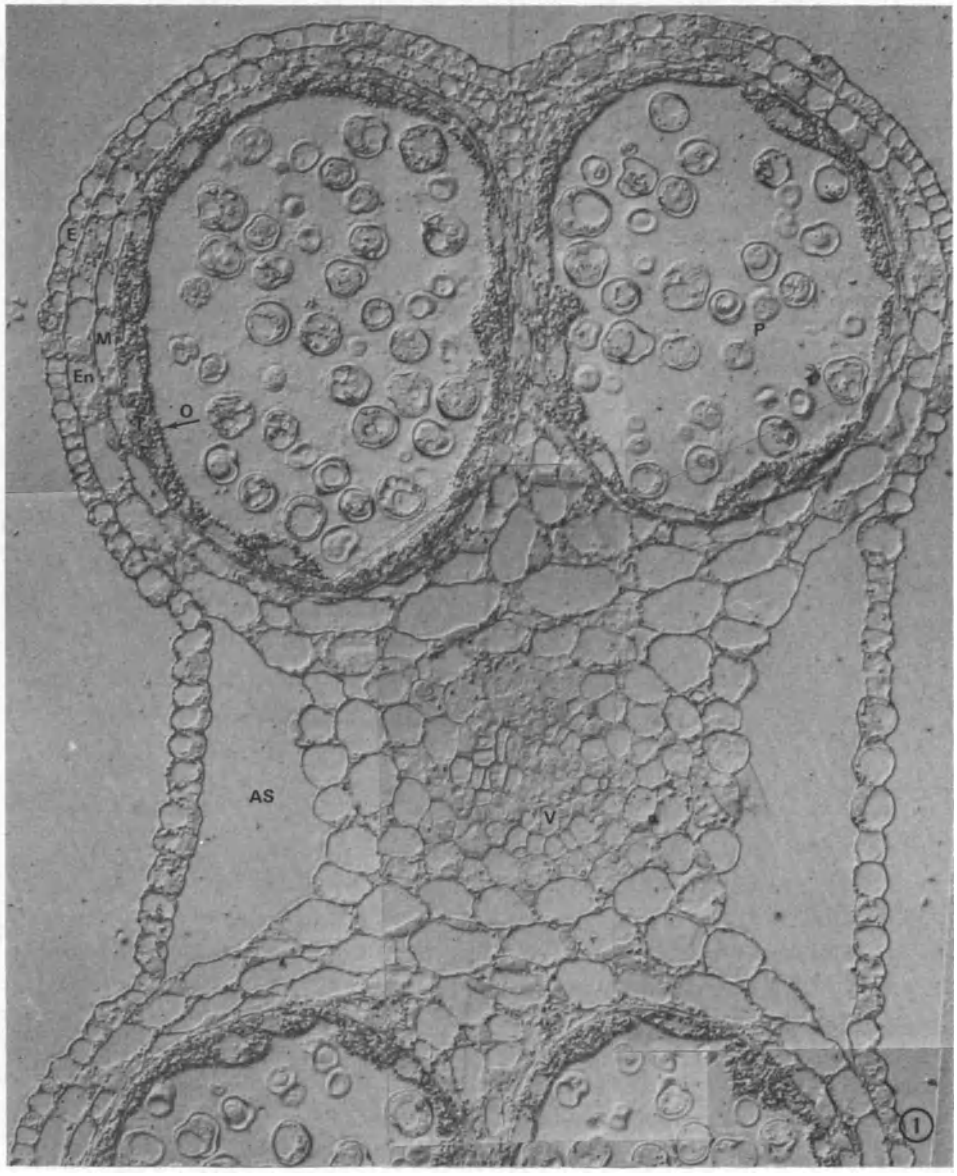
E
M
En
O
P
AS
V
1

exposures were made on a Si wafer-supported PMMA resist by 2.7 nm and 4.4 nm soft x-rays (Ti *L* and C *K* radiation).

The microsporangia of *Caltha palustris*'s anther consist of four layers of cells with developing pollen grains in the center locule. The four layers are the cuticle-bearing epidermis (E), vacuolated endothecium (En), middle layer (M) and dense tapetum (T) (Fig. 1 and 2). Figure 1 is an x-ray contact image magnified by an interference microscope. This image demonstrates the advantage of using contact microscopy for large field study; it is clear that the ability of looking at a large area of the specimen is very useful for the study of tissue structures. If high resolution image is required for detailed study, the same contact image can be magnified by a scanning electron microscope as shown in Fig. 2. Cytological features such as nucleus, nucleolus, vacuolus, cell wall and x-ray dense granules can be observed in the x-ray replica (Fig. 1, 2, 7, 10, 11, 12, 13, and 14). Large, prominent nucleoli are evident in the epidermal, endothecial, middle layer, tapetal cells and young pollen grains at both Ti *L* (Fig. 1, 2, 7, 10, and 13) and C *K* (Fig. 11) energies. Figure 2 is a composit picture of SEM-magnified contact images of a microsporangia. The images were taken with Ti *L* radiation (2.7 nm).

The innermost tapetal cells have a dense cytoplasm which contains many x-ray absorbing granules at both C *K* and Ti *L* energies (Fig. 1, 2, 7, 10, 11, 13 and 14). By comparing the soft x-ray replicas with light microscopic images of adjacent sections, it appears that the majority of these structures represent lipid granules. Since the granules can be stained readily by OsO_4 (Fig. 4) and Oil Red O (Fig. 3) but not PAS (Fig. 5) or Coomassie Brilliant Blue R-250 (Fig. 6), they do not contain significant amounts of PAS-positive carbohydrates or proteins. The TEM image also suggests that the x-ray absorbing structures are osmiophilic lipid granules and possibly some may be plastids and mitochondria (Fig. 8). On the locular surface of the tapetal cell, numerous orbicules can be found (Fig. 8, O). As reported by Cheng and Lin (1980), the orbicules of *Caltha palustris* L. consist of a sporopollenin matrix and a

Figure 2. Low magnification x-ray contact image (magnified by a SEM) of the anther tissue of *Caltha palustris*. The image was taken at Ti *L* (2.7 nm) x-ray from an aldehyde-osmium fixed, plastic embedded thin section (2 μm). Note the anther connective (Co), pollen grain (P) and four layers of cells which made up the microsporangia walls. Epidermis (E); endothecium (En); middle layer (M); tapetum (T); nucleus (N); nucleolus (No); starch granule (S); orbicule (O); exine (Ex); vacuole (v); electron beam damage on the resist (ED).

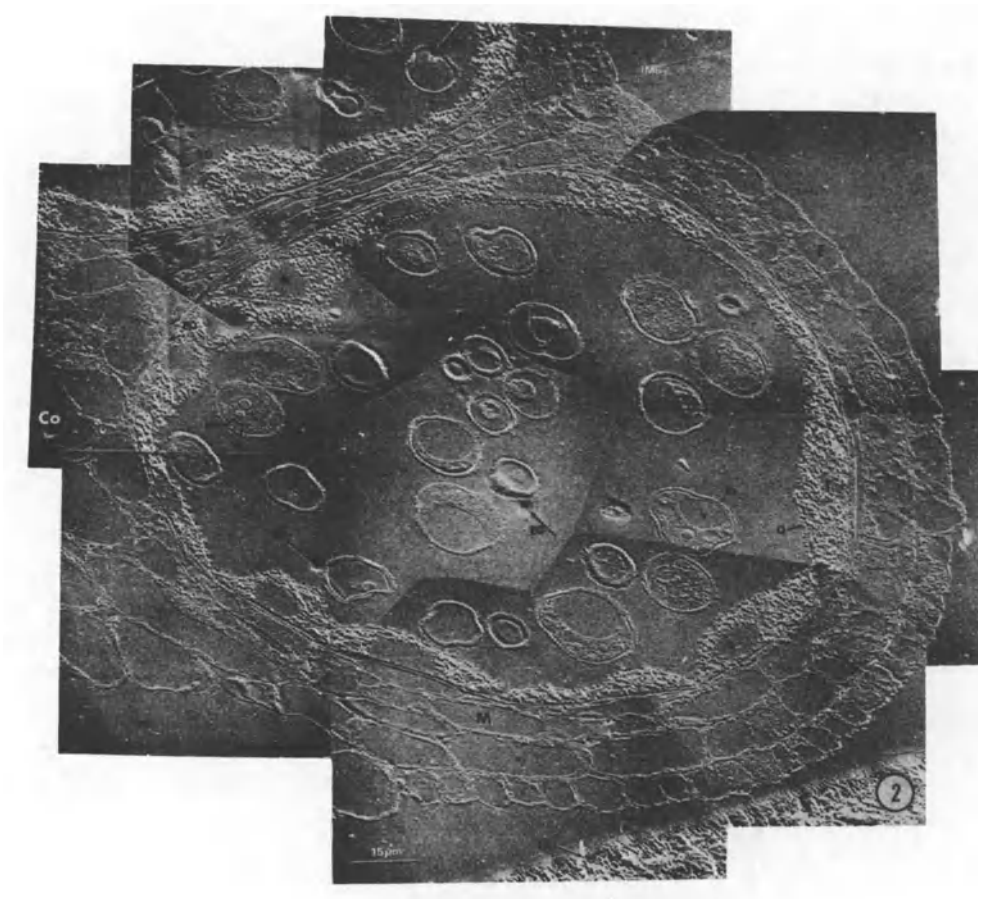
Co
M
15 µm
2

100-200 nm core. The core can be seen clearly in the TEM image in Fig. 8 and 9. A 7 nm thick electron translucent "plate" in the lipid core (Fig. 9, arrow heads) and tubular-like structures (Fig. 9, arrows) in the matrix have been reported (Cheng and Lin, 1980), but we could not identify any corresponding images of such structures on the x-ray replica at either energy. This may be due to the similarity of the x-ray absorption properties of the "plate" and core. The core can be observed in x-ray images taken both by C *K* and Ti *L* radiation. It is the smallest structure in the anther tissue which we can clearly identify in our x-ray lithographs. However, this figure by no means represents the resolution of the resist itself, merely the level of interpretation which can presently be achieved.

Pollen exine consists of a outer tectum and an inner nexine (Fig. 12 and 14) with interconnecting bacula which are readily distinguishable in the x-ray replica (Fig. 12). The low absorption layer (both C *K* and Ti *L*) beneath the

Figure 3. Cross-section of anther tissue embedded in polyvinyl alcohol, tissue stained with Oil Red O *en bloc* before embedding. Note the Oil Red O stained cytoplasmic lipid granules (arrow) in the tapetal cell (T). p: pollen grain, Co: anther connective.

Figure 4. Two micron thick section of anther tissue. The anther was fixed in Cheng's fixative, and then treated with 1% OsO_4. The cytoplasm of tapetal cells (T) contains numerous osmiophilic lipid granules. E: epidermis, En: endothecium, M: middle layer, P: pollen, O: orbicule, N: nucleus.

Figure 5. Half micron section of anther tissue stained by PAS method. Note the PAS positive starch granules (red in color) in the epidermis (E), endothecium (En), middle layer (M) and pollen grains (P)(indicated by arrow). The cytoplasmic granules of tapetal cells (T) are brown in color, indicating that they are stained by OsO_4 but not PAS. No PAS positive structures are seen in the tapetal cells.

Figure 6. Same specimen preparation as Figure 3 but stained by Coomassie Brilliant Blue R-250. The cytoplasm of pollen grains is densely stained (blue in color), the cytoplasmic granules of tapetal cells (T) are brown, hence, they are not protein bodies. The non-stained granules in the pollen grain represent the location of starch granules.

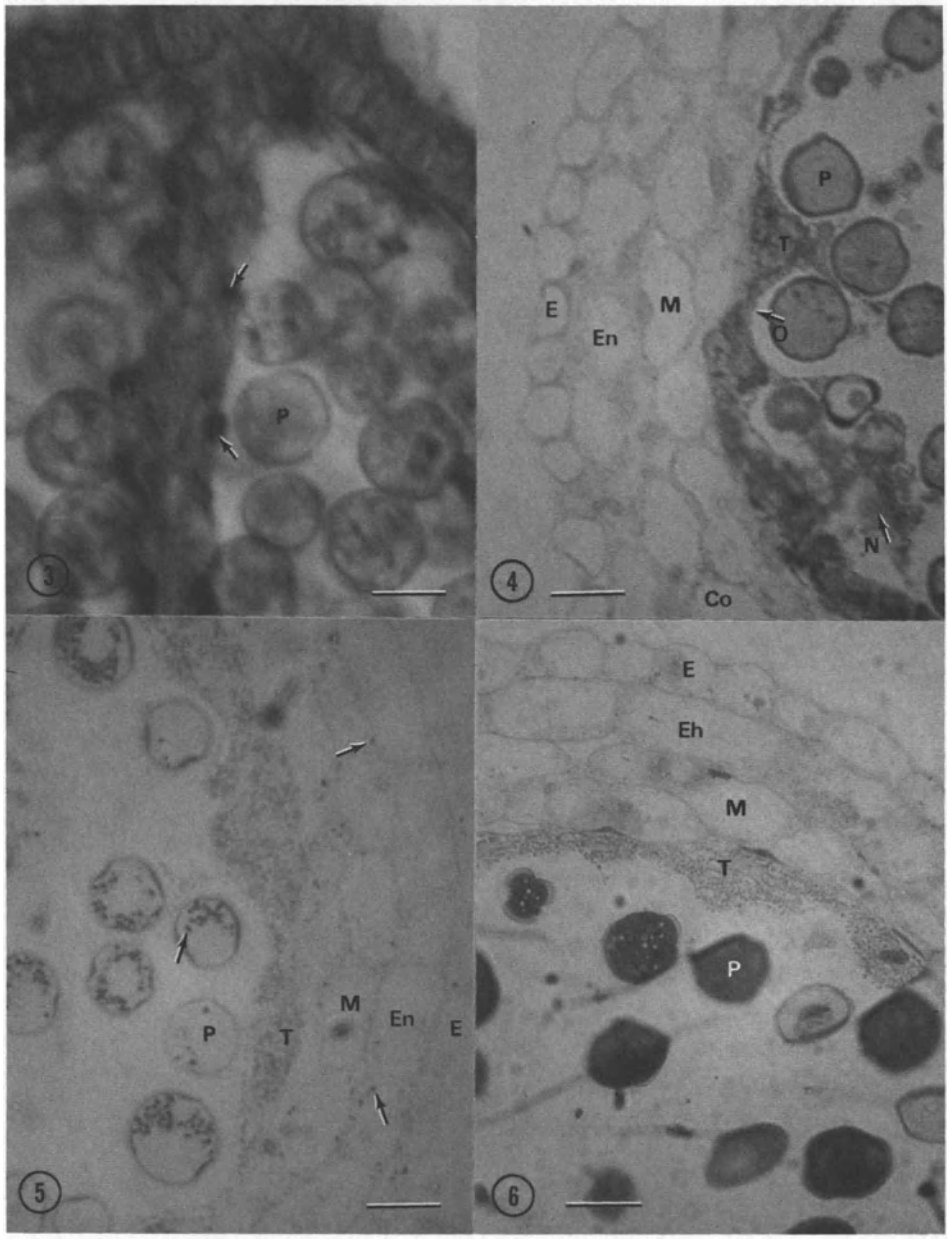
3
P
4
P
T
E
M
En
O
N
Co
5
M
P
T
En
E
6
E
Eh
M
T
P

exine is intine (Fig. 7), whose low absorption most likely is due to the presence of cellulose and small amounts of osmium in the cell wall.

In our studies, the nucleolus exhibits high x-ray absorption at both C *K* (Fig. 11) and Ti *L* (Fig. 2, 7, 10, and 13) energies. Also, clusters of x-ray dense material in the nuclei are observed. Manuelidis *et al.* (1980) have suggested that the interconnected array of x-ray absorption "bumps" in the isolated nuclei may represent meaningful structures; however, in this study, we have been unable to corroborate this observation due to the lack of precise correlation between the TEM images of the specimen and its x-ray images.

Certain very low x-ray absorbing spot(s)(hence a "hole" on the resist) are observed in the anther connective parenchyma cells, epidermis, endothecium, middle layer and young pollen (Fig. 2, 7, 12, and 13). By comparing the replicas with PAS-stained sections (Fig. 5), we conclude that these are starch granules. At high magnification, one can observe a slightly higher x-ray absorbing "rim" surrounding the low absorbing "hole" (Fig. 12 and 13).

Figure 7. SEM-magnified x-ray contact image (Ti *L* replica) of a cross section of *Caltha palustris* L. anther. The four cell layers of the anther wall are clearly visible. The nuclei (N) appear granular with visible nucleoli (No). The tapetal cell cytoplasm has numerous x-ray dense lipid granules (arrows), and orbicules (O) can be clearly seen on their locular surface. Developing pollen is well imaged. Note the pollen exine (Ex) and intine (In); the large vacuoles (V). Starch granules (S) show up as "holes" in the resist, and are seen in the endothecium (En), middle layer (M), epidermal cells (E) and in the young pollen.

Figure 8. Conventional transmission electron microscopic image of tapetal cell. Note the orbicule (O) with a core structure and electron translucent "plate" in the core (see Figure 9). The cytoplasm contains numerous osmiophilic lipid granules (L); few mitochondria (m) are evident. N: nucleus.

Figure 9. High magnification TEM view of an orbicule, the core (Cr) is embedded in a matrix (Mx). Note the electron translucent "plate" (arrow heads) in the core and tubular-like structures (arrows) in the matrix.

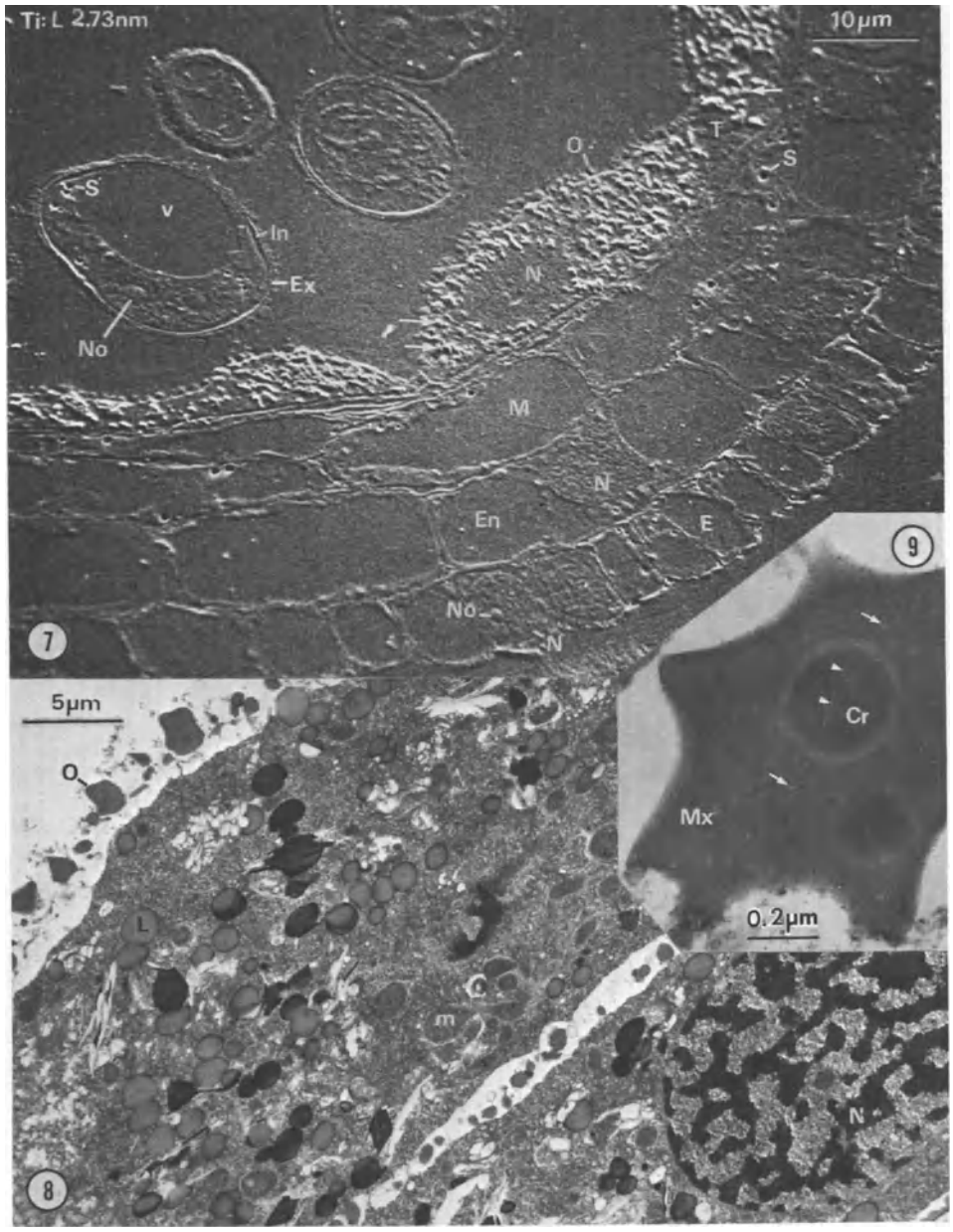
Ti: L 2.73nm
10μm
O
T
S
S
V
In
Ex
No
N
M
N
En
E
No
N
7
9
Cr
Mx
0.2μm
5μm
O
L
m
N
8

The rim is not very pronounced in Fig. 7 because of the viewing angle under the SEM. Starch is composed of carbon, hydrogen and oxygen, and since C *K* radiation is just below the *K* absorption edge of carbon and oxygen an Ti *L* radiation is just below oxygen absorption edge, we expect low absorbance by starch at these two x- ray energies. Since the cytoplasm around them has been permeated by OsO_4 and embedded in Spurr's medium, it will have a relatively higher absorption. The rim around the hole is due to coating of the granules with osmium which penetrate them readily during fixation.

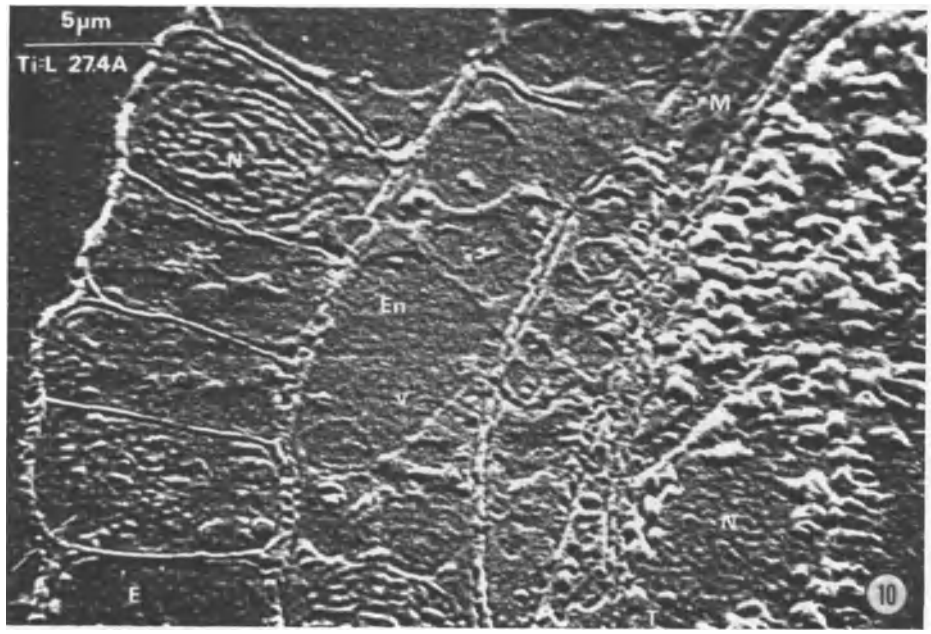

Figure 10. Microsporangia wall of *Caltha palustris*. Note the four layers of cells: epidermis (E); endothecium (En); middle layer (M) and tapetum (T). This image was replicated with Ti *L* radiation. Note the arrows (lower left of the picture) indicate the outer cuticle layer and inner cell wall of the epidermal cell. N: nucleus; No: nucleolus; v: vacuole.

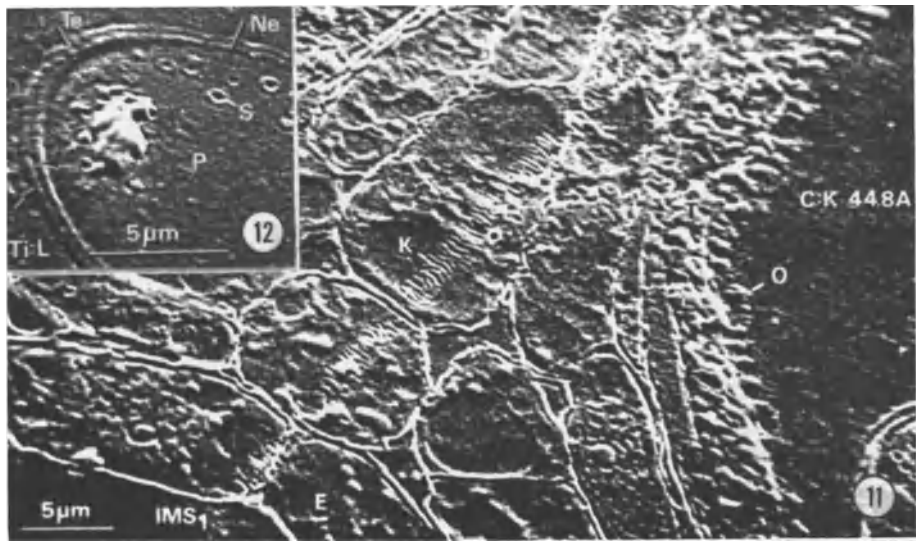

Figure 11. Anther of *Caltha palustris* near the intermicrosporangia stripe 1 (IMS1). knife mark (K); tapetum cell (T); orbicule (O); epidermis (E).

Figure 12. High magnification view of a young pollen (P)(replicated by Ti *L* radiation). Note the tectum (Te) and nexine (Ne) with interconnecting bacula (arrows).

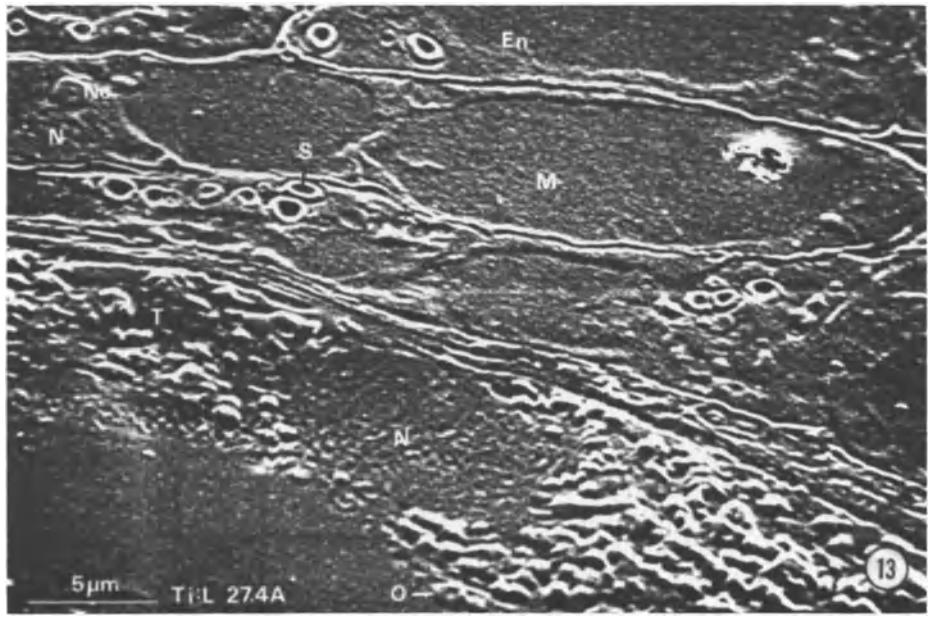

Figure 13. X-ray image (replicated at Ti *L* radiation) of anther wall of *Caltha palustris*. T: tapetal cell; M: middle layer; En: endothecium; N: nucleus; No: nucleolus; O: orbicule. Note the starch granules (S) which have a low x-ray absorbing center and an x-ray dense rim.

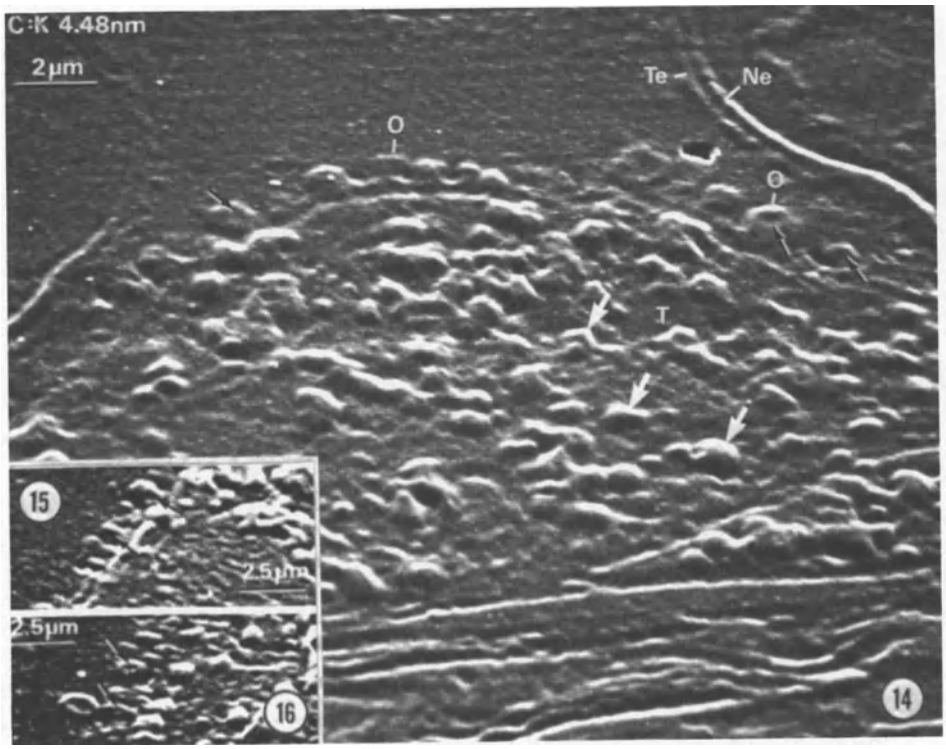

Figure 14. X-ray image (replicated at C *K* radiation) of tapetal cell (T) of *Caltha palustris*. The white arrows indicate x-ray dense cytoplasmic lipid granules. Note the extracellular orbicules (O) with cores (black arrows). The pollen exine consists of an inner nexine (Ne) and an outer tectum (Te).

Figure 15. High magnification of an SEM-magnified contact image showing orbicule and its core (arrows).

Figure 16. Same as Fig. 15

IMAGES OF ANIMAL TISSUE AND CELLS

Two examples are presented in this article to demonstrate the use of x-ray contact microscopy in the study of animal cells.

Cultured cells

Figure 17 shows a TEM image of a *Xenopus laevis* muscle cell. The cell was cultured on a Formvar film, fixed in glutaraldehyde, post-fixed briefly in osmium, dehydrated in ethanol, and critical point dried. For a detailed procedure on cell culture and specimen preparation, refer to Peng *et al*, (1981). The white arrows show the Z-lines of sarcomeres. Filamentous mitochondria (m) are clearly visible. To the right of the myofibril, marked by white arrows, a clear space can be seen. This clear space is caused by electron beam damage during electron microscopic observation. At the lower right of the photo, where a portion of a neighboring cell is evident, note the presence of a thin filament bundle (S) at the margin of the cell. At the upper right of the picture, a portion of a fibroblast (F) can be seen.

In contrast, figure 18 is the x-ray image (C *K*) of the same specimen shown in Fig. 17. The four black arrows indicate the position of Z-lines, and the white arrows indicate the A-band of sarcomeres. High magnification of a similar sarcomere is shown in Fig. 31. A thin filament bundle (S) is evident at the margin of a neighboring cell. This x-ray image was taken before the electron micrograph shown in Fig. 17. Note there is no "clear spot" in the cytoplasm. This demonstrates that x-ray imaging causes less damage than the electron beam.

X-ray contact images can be also viewed by a scanning electron microscope or interference microscope. Figure 19 shows the SEM magnified contact image of the same cell shown in Fig. 17. Note that the regularly spaced sarcomeres of the myofibril are very difficult to recognize. SEM-magnified contact images generally pose some difficulty in image interpretation unless multiple SEM views are obtained. Figure 20 shows the contact image magnified by an interference microscope. The latter method is primarily used for monitoring the resist during chemical development. Note the resulting image is very difficult to interpret. The image density of the interference

microscope-magnified image is solely dependent on the optical path length.

Cells fixed only in aldehyde can produce x-ray images with excellent contrast. Figures 24, 25, and 26 show an x-ray image (C *K*) of mouse 3T3 cells and a muscle cell of *Xenopus laevis*. It is very difficult to study a cell nucleus in a whole-mount specimen with an electron microscope. This is mainly due to the fact that a nucleus is generally very dense and quite thick. However, due to the ability of x-rays to penetrate thicker specimens, the x-ray imaging provides an excellent tool for such studies. Figures 24 and 26 show the images of mouse 3T3 cell's nuclei.

Tissue sections

The newly developed polyethylene glycol (PEG) embedding and sectioning techniques (Wolosewick, 1980) provide a unique method for the preparation of resinless thin sections. We have used this technique for the imaging of bone marrow tissue of rats. Rats were perfused with Hank's buffered saline solution followed by a second perfusion with bone marrow fixative (consisting of 2.5% of glutaraldehyde, 1.5% of paraformaldehyde in 0.1M sodium cacodylate buffer, pH 7.4). Then the tissue was dissected out and fixed in the above fixative. After fixation, the tissue was washed in 0.2M sodium cacodylate buffer (pH 7.4), dehydrated in ethanol, and infiltrated with 1:1 ethanol/polyethylene glycol (EtOH/PEG) for 30 min. at 60 C. Finally, the tissue was embedded in a Beem Capsule, and frozen rapidly in liquid nitrogen. Sectioning was performed on an AO Ultracut microtome with a dry diamond knife. The sections were picked-up in a drop of 40% PEG on a wire loop, then transferred to a polylysine-Formvar coated grid or window. The grids or windows were then soaked in water for 1 hour, dehydrated in ethanol and critical point dried with CO_2.

Figure 21 shows the x-ray image of the resinless bone marrow section taken with zero order synchrotron radiation (Tantalus storage ring). Many cell types are visible. Note the large megakaryocyte (Mk) with an extraordinarily elaborate, multiple lobed nucleus (N), and the uniformly distributed x-ray dense granules in the cytoplasm. Beside the megakaryocyte, an eosinophilic leukocyte (EL), with numerous x-ray-dense cytoplasmic granules (white arrow), is evident.

Figure 17. A whole-mount specimen of *Xenopus laevis* muscle cell imaged by conventional transmission electron microscope. The cell was fixed in glutaraldehyde and osmium. Z-line of sarcomere (white arrows); mitochondria (m); stress fiber (s); fibroblast (F); yolk granule (Y); nucleus (N); nucleolus (No).

Figure 18. The same cell shown in Fig. 17 but imaged by x-rays (C *K*: 4.4 nm) with the contact image magnified by a TEM. m: mitochondria (m); stress fiber (s); z-line of sarcomere (Z and black arrows); yolk granule (Y); nucleus (N); nucleolus (No); fibroblast (F).

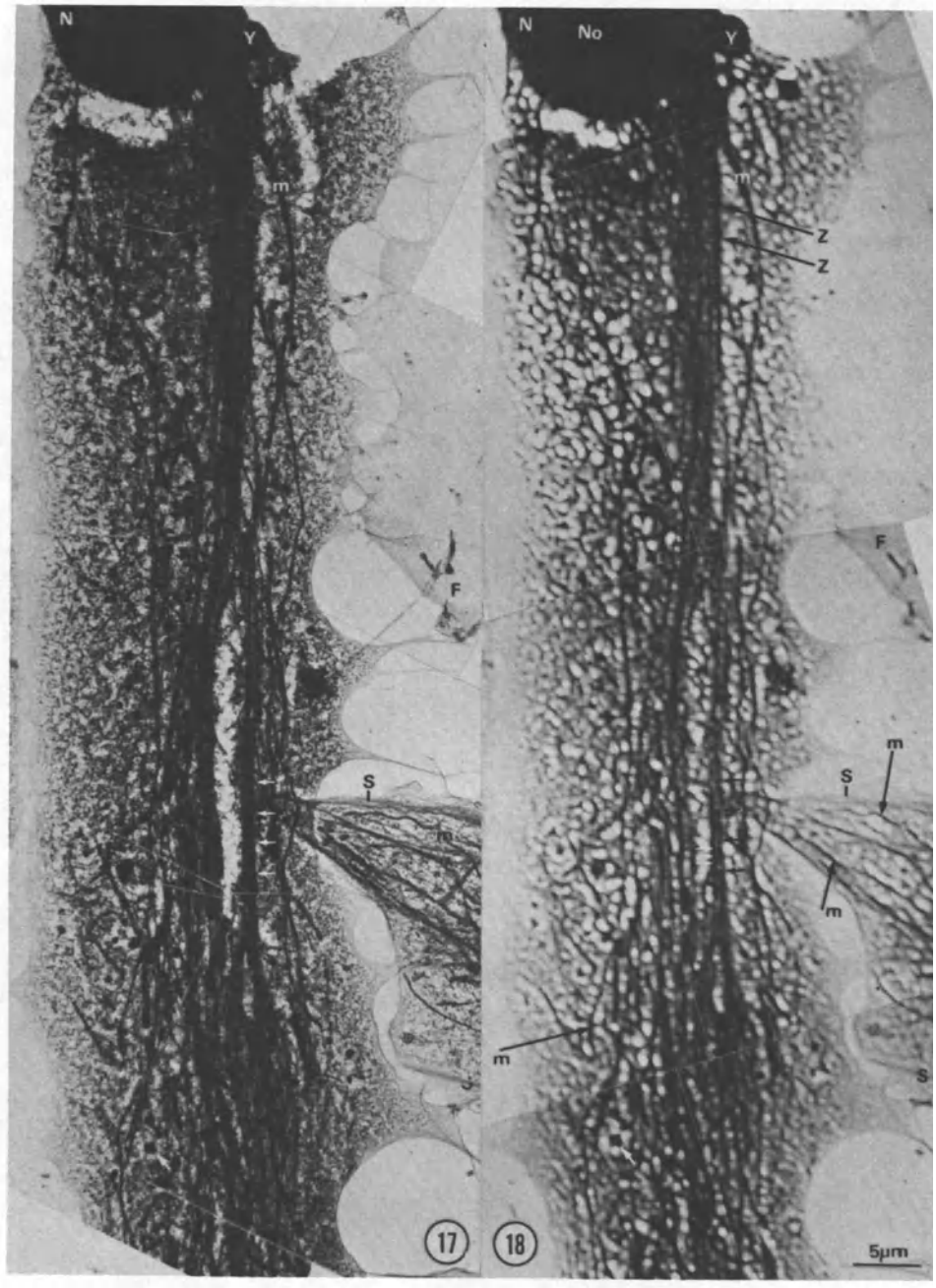
N
Y
m
F
S
I
m
17
N
No
Y
m
Z
Z
F
m
S
I
m
m
m
S
18
5µm

3D IMAGING

It is rare that one can treat a biological specimen as a two dimensional object. In order to obtain 3D structural information about a cell, the general practice is to serial section the cell. Occasionally, if the cell is sufficiently thin (e.g., cultured fibroblasts), stereo image-pairs can be obtained with a TEM. Since soft x-ray microscopy is capable of looking at a much thicker specimen than electron microscopy, 3D image-pairs will also be a useful tool in x-ray microscopy to study cells or tissue sections which are too thick or too dense to be studied using a TEM. Feder *et al.* (1980) have shown x-ray contact images of *Drosophila* giant chromosomes in stereoscopic image pairs. Their work demonstrated that it is possible to produce high resolution 3D image-pairs by contact microscopy. Feder *et al.* (1984) have recently demonstrated that obtaining stereoscopic image-pairs of TEM-magnified contact images is technically possible (due to a publishing error, only the left image of the image-pair is printed in the paper mentioned above).

Figure 19. Same resist as Fig. 18 but magnified by a SEM. The regularly spaced Z-lines are very difficult to visualize.

Figure 20. Same resist as Fig. 18 but magnified by a interference microscope. Note the image is very difficult to interpret. eosinophilic leukocyte (EL), with numerous x-ray-dense cytoplasmic granules (white arrow), is evident.

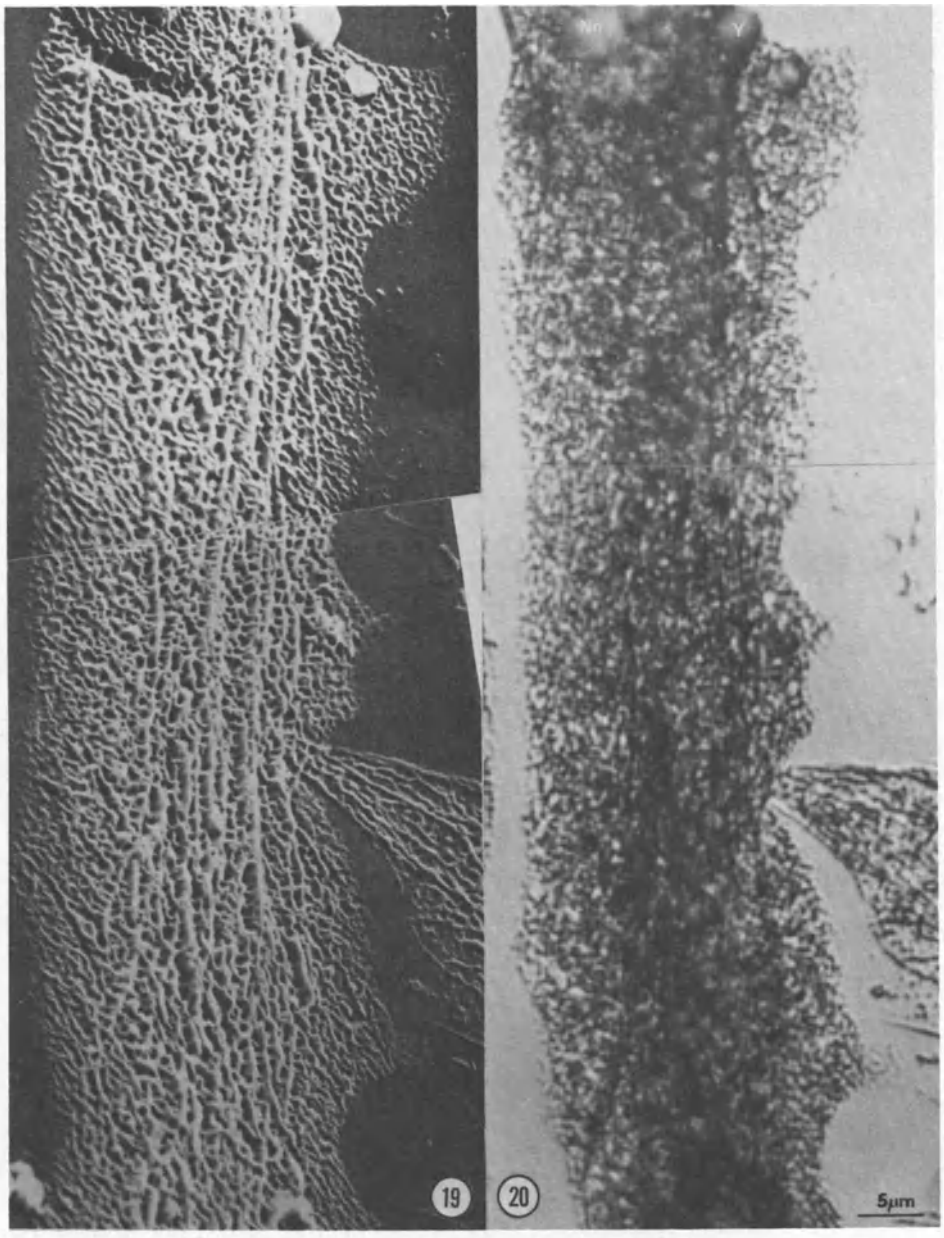
19
20
5µm

For conventional transmission electron microscopy, one can obtain stereo image-pairs by photographing the same specimen at different tilt angles. A similar technique can also be used in x- ray lithography to obtain image-pairs. However, some modification of the imaging procedure is required. A cell-bearing grid is placed in intimate contact with a Si_3N_4-supported x-ray resist, and the exposure is made with the x-ray source positioned at a certain angle (e.g., 30 degrees) with respect to the axis of the grid (Figure 22A). Then, the specimen is reloaded with a new resist and exposed at a different angle (e.g., -30 degrees). It is essential to estimate the final magnification and specimen thickness when the imaging is carried out because the optimum results are dependent on a proper tilt angle. Based on the equation published by Hudson and Makin (1970), one can determine the optimum tilt angle before making an exposure.

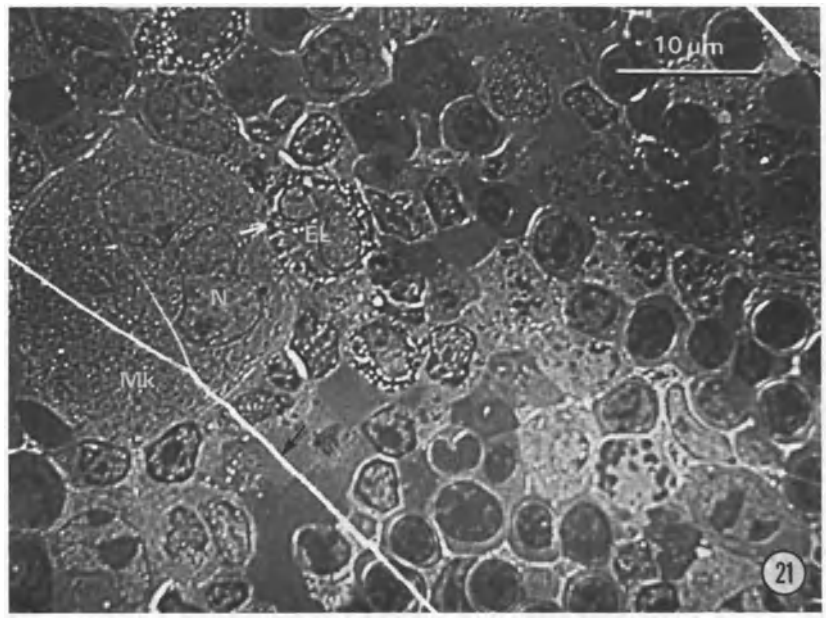

Figure 21. Bone marrow tissue of rats. This image was taken from a Formvar-supported resin-less section. Replicated with zero-order synchrotron radiation on PMMA resist. Note the megakaryocyte (Mk); eosinophilic leukocyte (EL) and developing red blood cells (lower middle of the picture). The black arrow indicates a crack on the Si_3 N_4 supporting window.

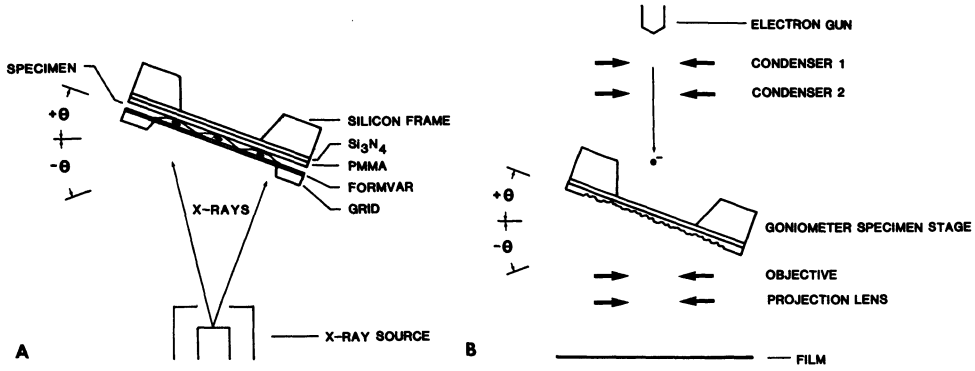

Figure 22. Diagrammatic representation of a 3D imaging set-up. (A) The resist-coated window is placed in intimate contact with a cell bearing grid. Exposures are made while the specimen-window complex is tilted at specific angles (i.e., +20 degrees). (B) TEM viewing of the contact image is done with the resist tilted at the same angle as that at which it has been replicated.

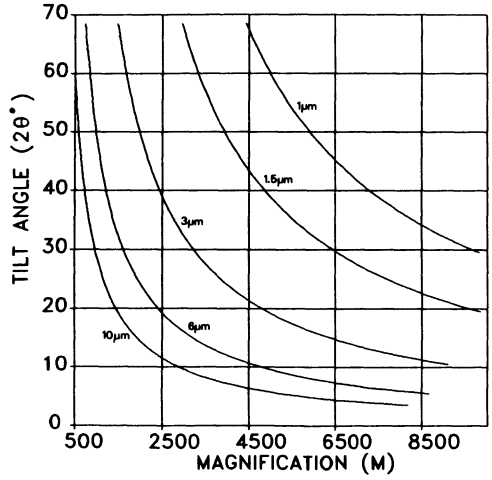

Figure 23. Optimum tilt angle plotted against magnification for various specimen thicknesses from 1 μm to 10 μm. The magnification (M) represent the final magnification of the viewing images, therefore, generally, a microscope magnification of M/2 to M/5 is recommended.

$$\Delta Y = 2\Delta h M \sin \theta$$

where ΔY is the parallax (the difference in the distance between corresponding points in the two images; for optimum result, ΔY is generally fixed at 0.3-0.5 cm), M is the final image magnification, θ is half of the angle of tilt (Fig. 22), and Δh is the vertical separation of points in the object at the angle midway between the two tilts. Figure 23 shows optimum tilt angle against magnification for various specimen thicknesses from 1 μm to 10 μm (ΔY=0.5 cm).

After their exposure, the two resists were then developed identically and viewed under a TEM. A microscope equipped with a goniometer stage is required. In order to facilitate TEM operation, a specially made window holder is used; this device allows the window to be rotated so that proper alignment of the window against the tilt axis can be achieved. The TEM projection images of the x- ray replicas were obtained with the replica positioned at the proper tilt angle which corresponded to the angle at which the replicas were exposed (i.e., projection images at $\pm$30 degrees)(Figure 22B). Stereoscopic image-pairs can then be viewed with the aid of a stereo map viewer. Figure 24 shows a 3D-pair of a mouse 3T3 fibroblast cell. The images were replicated

Figure 24. 3D pair of a mouse 3T3 fibroblast. The cell was grown on the surface of Formvar and fixed in 1% glutaraldehyde and critical point dried. Replicated at $\pm$20 degrees with carbon *K* radiation. Note the nucleoli are suspended in the nucleoplasm. Arrow indicates cell processes which attach to the culture substratum. S: stress fiber. Scale = 10 μm.

Figure 25. 3D image-pair of a *Xenopus laevis* muscle cell. Arrow indicates x-ray dense cytoplasmic arc. The myofibril bundles are clearly visible. The x-ray dense large granules are yolk granules from another cell which have attached to the surface of the cell being viewed. The images were replicated at $\pm$30degree with carbon *K* radiation. The Formvar-supported cell was fixed in 1% glutaraldehyde and critical point dried. Scale=10μm.

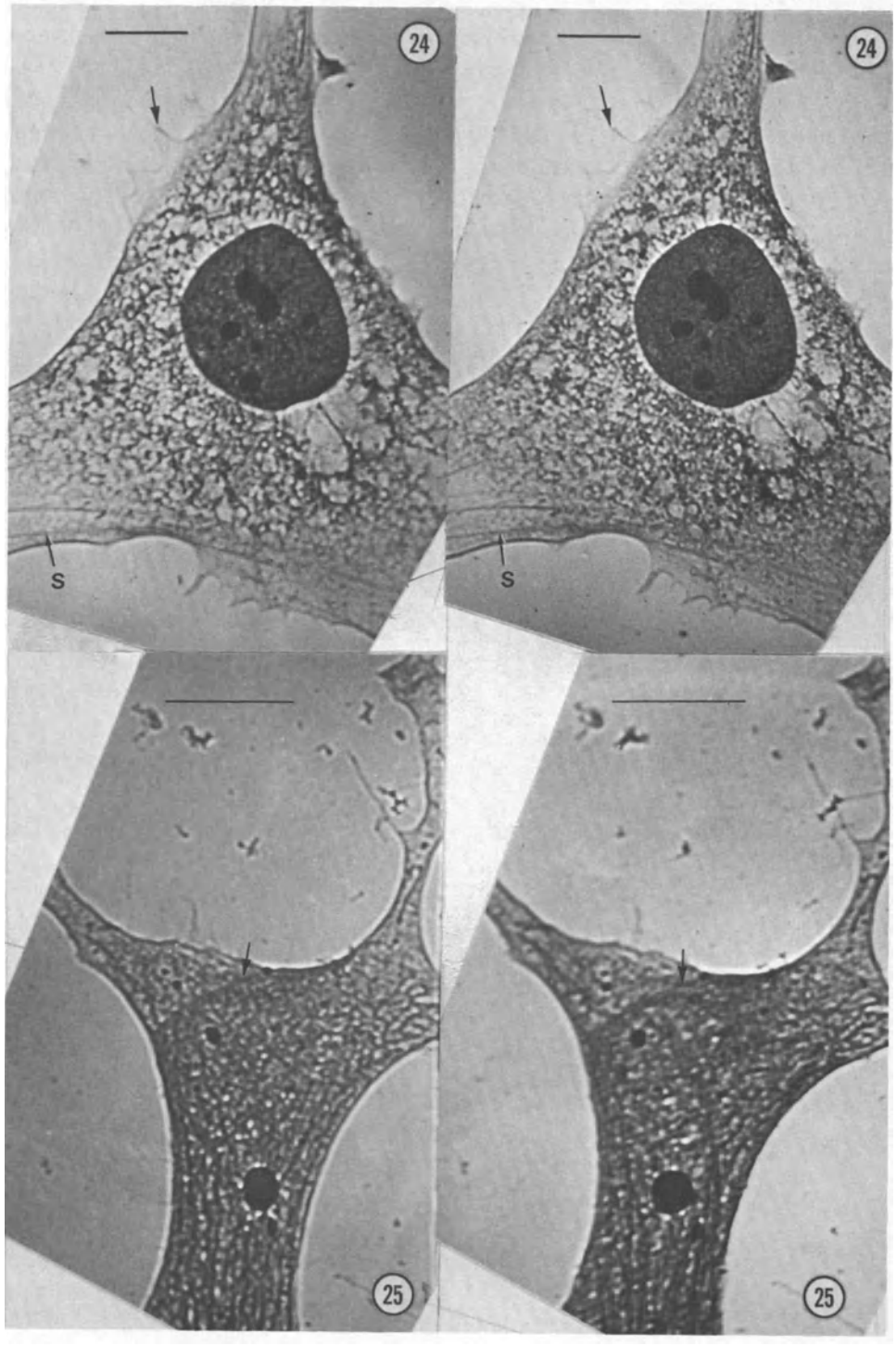
24
S
24
S
25
25

on a PMMA resist at ±20 degrees with carbon *K* radiation. The nucleus with one large and four small nucleoli are evident. Note the nucleoli are suspended in the nucleoplasm at different levels. The edge of the cell (indicated by an arrow) attaches onto the substratum by cytoplasmic projections. At higher magnifications, ±20 degree tilt provides greater depth (Fig. 26). The image is taken from a mouse 3T3 cell in the same way as Fig. 24. Note the three large and one small nucleoli. Close inspection reveals that the large nucleoli consist of two major parts, an x-ray dense portion and a less-dense portion. It seems that the less-dense portion is attached to the nuclear envelope (arrow). At present, we do not know whether the dense portion represents pars amorpha and the less-dense portion represents nucleolonema, as seen in electron microscopy.

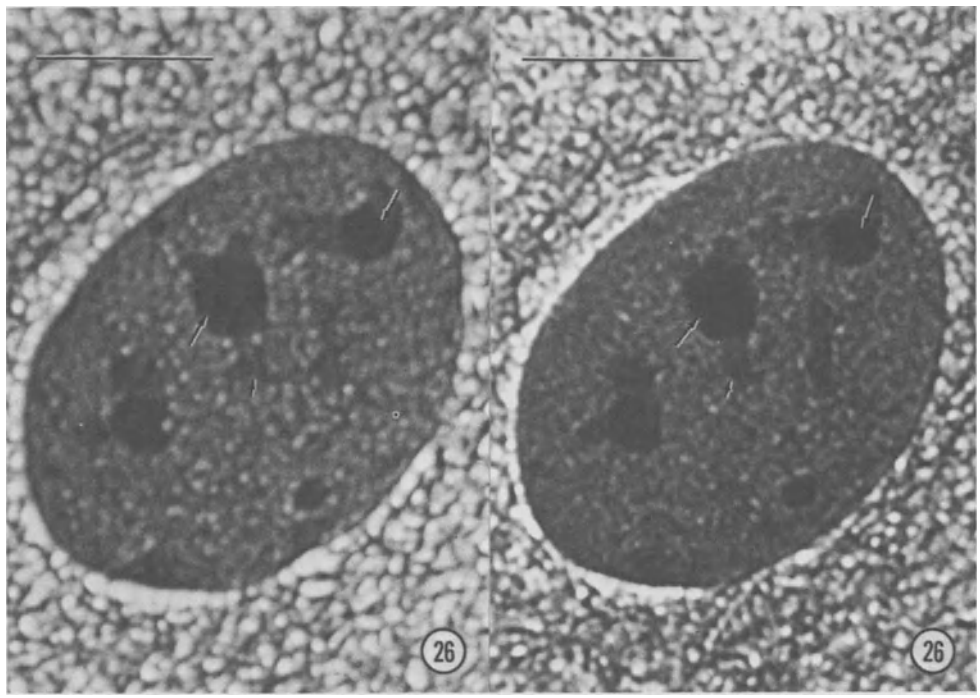

Figure 26. Stereo-pair of a mouse 3T3 fibroblast nucleus. Note the three large nucleoli in the nucleus each consist of two compartments: an x-ray dense portion (pars amorpha?)(long arrow) and a less x-ray dense portion (nucleolonema?)(short arrow). It seems that the less x-ray dense structures attach to the nuclear envelope (short arrow). Replicated at carbon *K* radiation at ±20°. The Formvar-supported cell was fixed in 1% glutaraldehyde and critical point dried. Scale = 10 μm.

Figure 25 shows a *Xenopus laevis* muscle cell. The two paired images were taken at +30 degrees with carbon *K* radiation. The arrow indicates an x-ray dense zone in the cytoplasm. Myofibrils running parallel to the long axis of the cell are evident. The large dark granules are yolk granules from another cell which disintegrated in culture. All the three image-pairs (Fig. 24, 25, and 26) were taken from cells fixed in glutaraldehyde, dehydrated in ethanol, and critical point dried.

IMAGE PROCESSING BY COMPUTERS

With the advance of microcomputers, it became relatively simple to process images digitally. We have used a microcomputer for generating 3D isometric views of the resist surface and perform image subtraction. All the image digitization and subsequent subtraction were done on an IBM 5150 microcomputer, equipped with 320K RAM (random access memory), Tecmar Video Van Gogh image digitizer, and Tecmar Graphic Master (screen control).

Microchemical Analysis and Image Subtraction

Recently, images taken by monochromatic light above and below the phosphorus *L* absorption edge have been reported by Cheng *et al.* (1984). The two images are SEM-magnified contact images of the cytoplasm of a *Xenopus laevis* muscle cell which show significant differences. It is believed that the difference is due to the presence of phosphorous-containing compounds in the cytoplasm.

Biological compounds are carbon-based compounds which show a rapid increase in absorption for wavelengths longer than 4.4 nm. Microchemical analysis becomes more difficult as the background absorption becomes higher. Therefore, for the elements which have absorption edges located in the "window" region such as sulfur and chlorine, microchemical analysis is relatively sensitive and easy. In order to obtain an elemental map from the differences of above and below edge images, the two images have to be digitized and mathematically subtracted by a computer. For proper image subtraction, it is necessary to ensure that the the two images are produced under identical conditions (i.e. equal exposure) and developed equally. Alignment is extremely important for obtaining real information. Figures 27 and 28 show images of mouse 3T3 cells taken at 2.1 nm (Fig. 27) and 2.7 nm (Fig. 28). The difference of the two images (Fig. 27 minus Fig. 26) is shown in Fig. 29.

Fresnel diffraction could contribute significant problems to the subtraction of above- and below-edge images. The diffraction effect (Fig. 30) is clearly visible because of the finite distance between the specimen and resist. For obtaining images above and below a certain absorption edge, it is difficult to ensure that the spacing between the resist and specimen will remain the same between two exposures. Therefore, the diffraction fringe can complicate the image to a point that subtraction becomes very difficult. Because the images used in image subtraction are TEM- magnified contact lithographs, the artifacts (i.e. bubbles, wrinkles, and increased transparency of the resist) created by the electron beam of the microscope are another potential problem in the image subtraction work. Furthermore, the image distoration of the electro-magnetic lens of the microscope can cause difficulty on image alignment.

Computer Generated Resist Topography

There are three major viewing methods to magnify miniature x- ray contact images: (1) magnify the contact image by using an interference microscope (Fig. 20) or a phase contrast microscope; (2) obtain magnified surface topographic views by a scanning electron microscope (Fig. 19); or (3) obtain magnified transmission views by a transmission electron microscope (Fig. 18).

Figure 27. TEM-magnified contact image of mouse 3T3 cell taken at 21 Å monochromatic light. The four corner-marks define the digitized area shown in Figure 29.

Figure 28. TEM-magnified contact image of the same specimen shown in Fig. 27 but taken with 27Å monochromatic light. No: nucleolus.

Figure 29. Resulting image of Fig. 28 minus Fig. 27. The brighter the image, the higher the difference between the two. No: nucleolus.

Figure 30. Fresnel diffraction of the edge of a yolk granule (Y). Note the short black bars mark the position of each intensity maximum of the diffraction fringes. The image was taken at 88.5Å radiation (Tantalus storage ring) on PMMA.

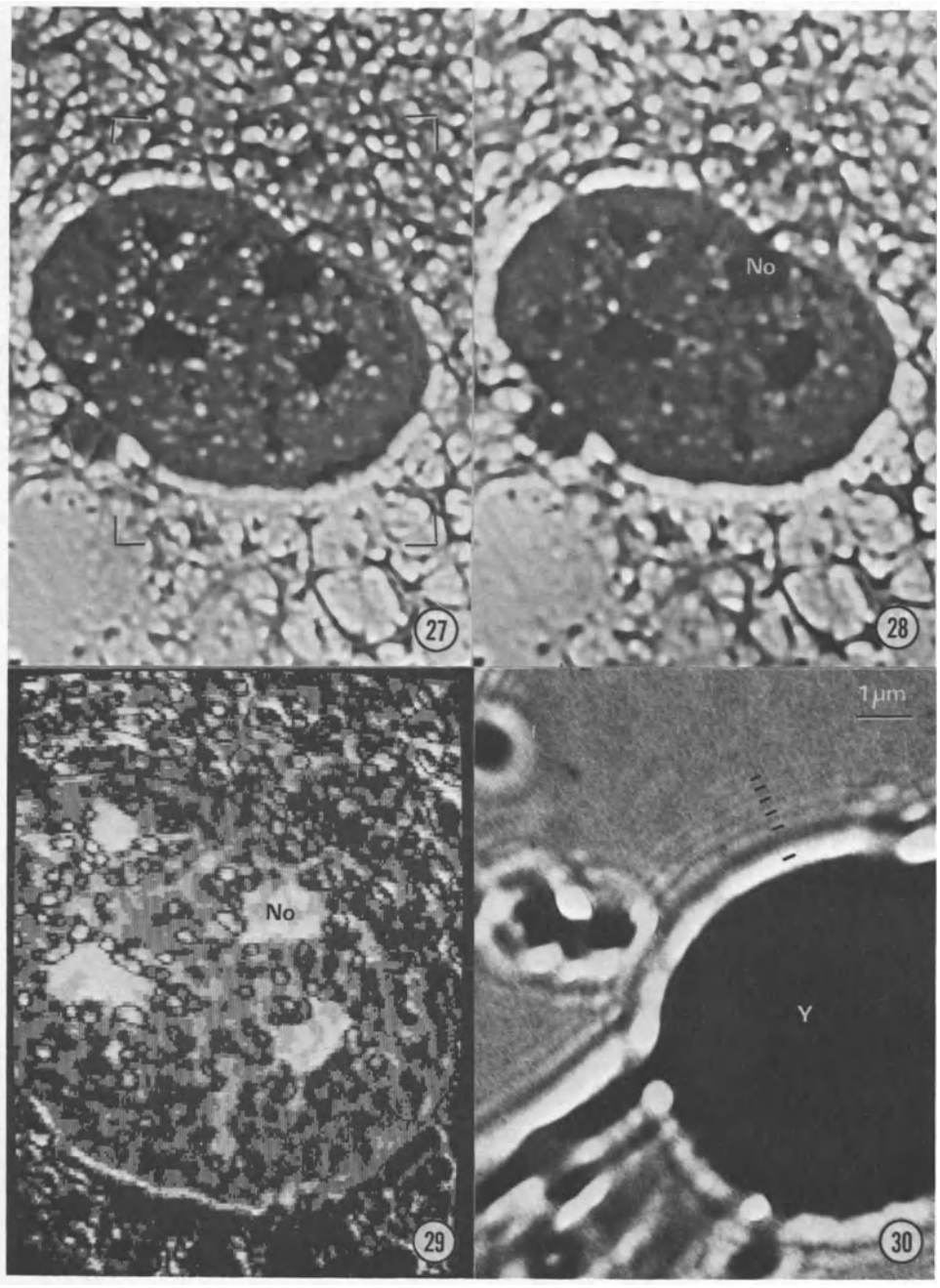
No
27
28
No
29
1 μm
Y
30

Among the three viewing methods, TEM magnified x-ray contact images offer many advantages, such as being suitable for image digitization and readily interpretable. In some instances, the SEM magnified images also provide information useful in image interpretation. However, in order to provide adequate information for image interpretation, it is necessary to obtain multiple SEM images of a lithograph at various viewing angles. Obviously, obtaining multiple SEM images is a time consuming task. Furthermore, x-ray resists are subject to electron beam damage, and prolonged exposure to the energetic electron beam can cause significant damage to the resist under study. Therefore, it is technically difficult to obtain many SEM images at different viewing angles from a replica.

The changes in image density of a TEM magnified lithograph directly represent the thickness variation of the resist. In other words, the degree of image darkness directly reflects the height of surface profiles of the resist. Therefore, it is possible to plot out the resist surface topography by using a computer with a digitized image as the database (Cheng, 1984). Figures 32 - 35 show a set of isometric views of a cultured muscle cell (Fig. 31). The image was taken from a muscle cell which had been fixed in 1% glutaraldehyde and postfixed in osmium briefly, and finally critical-point dried. One can clearly see the x-ray dense Z-line (Z, arrow) and A band (A) of a sarcomere. Please note how the images differ when viewed at different angles. When the resist surface

Figure 31. TEM magnified x-ray contact image (C *K*) of a *Xenopus laevis* muscle cell. The sarcomere demarcated by two Z lines (Z, arrow) is clearly visible. The tissue has been fixed in glutaraldehyde and osmium. The four corner-marks define the digitized area shown in Figure 32-35.

Figure 32. Computer-simulated isometric view of Figure 31 at a high viewing angle.

Figure 33. Similar view as Fig. 32 but at a lower viewing angle.

Figure 34. Isometric view of Figure 31 at a different position from Figure 33.

Figure 35. Same viewing condition as Fig. 34 but the heights of surface profiles are exaggerated to be 1.5X higher.


31
Z
A
Z

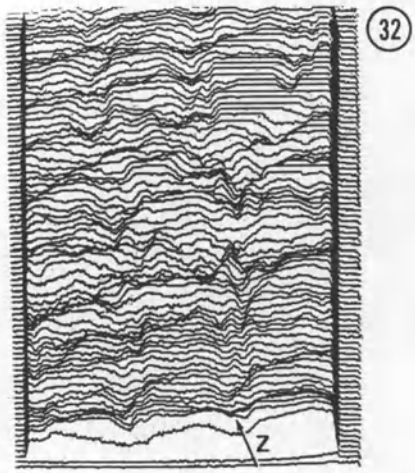
32
Z

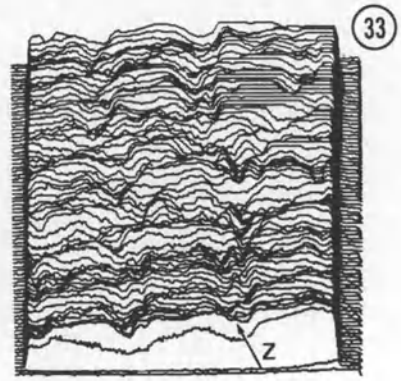
33
Z

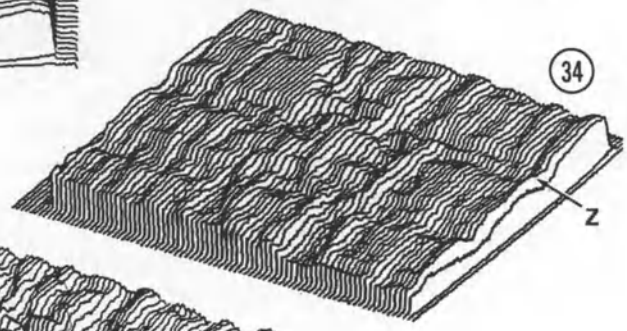
34
Z

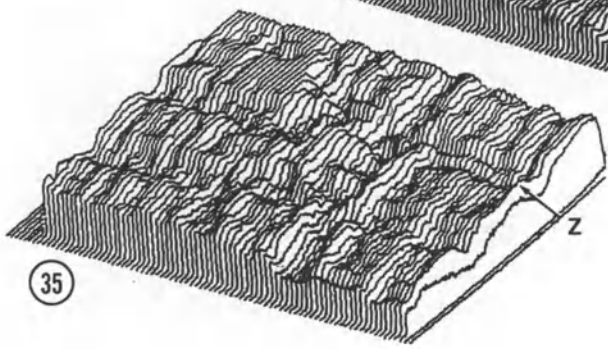
Z
35

is viewed at a high angle (Fig. 32), the Z-lines (arrow) are barely visible. However, when it is viewed at a lower angle (Fig. 33) and at a different viewing location (Fig. 34), the Z- lines become quite conspicuous.

The advantage of using computer-simulated isometric views of resist surfaces is that multiple views can be easily generated and the surface topography can be exaggerated by software for a better visual effect. In Figure 35, the height of surface profiles are exaggerated 1.5X relative to Figure 34. The quality of the simulated image is both hardware and software dependent. All of the computer simulated resist topography shown in this article is generated by an IBM 5150 microcomputer with a simple hidden-line removal algorithm. If a more powerful computer equipped with a high resolution digitizer and advanced image shading software is used, the simulated image can be very "lifelike". By carefully selecting viewing angles, one can easily obtain 3D image-pairs of the resist surface. The above examples demonstrate that computer-generated resist topography is much more than "just another pretty picture." it is a useful tool for image interpretation.

WET CELL IMAGING

Because of the technical limitations of electron microscopes in handling wet samples, our knowledge about cellular ultrastructure is almost entirely based on fixed and dehydrated material. Since water posseses an x-ray transparent window at wavelengths below the oxygen absorption edge (>2.4 nm), and due to the presence of nitrogen and carbon in biological material, the x-ray absorbance of cellular structures is high relative to the water background. Therefore, one of the ultimate goals of x-ray microscopy is the ability to image wet specimens. The major difficulty in wet cell imaging by soft x-rays is the lack of suitable x-ray sources. In order to capture a still frame of a living cell, one has to use a very short exposure, therefore, a very high intensity x-ray source is required. Recently, Feder *et al.* (1984) and Baldini *et al.* (this volume) reported the first successful attempt to image a live human platelet using a gas-puff z-pinch source (LEXIS, Maxwell Laboratories). The source produces x-rays with a pulse length of approximately 200 ns, and the output is on the order of 10 joules per pulse (Feder *et al.*, 1984). Furthermore, a laser generated x-ray source has also been used in wet sample imaging (Rosser, personal communication).

Figure 36 and 37 show the design and dimensions of an enviromental chamber similar to the one described by Feder and Mayne-Banton (this volume). The window used in the environmental chamber was a 100 nm thick Si_3N_4 film. This chamber was particularly designed for handling cultured cells.

The silicon nitride window was glued onto the bottom of a small stainless steel dish where cell culture can be performed. Cells can be cultured directly on the surface of the window providing that the window surface has been coated with a thin layer of carbon.

ABSORPTION PROPERTIES OF BIOLOGICAL SAMPLES

It is important to know the absorption properties of various biological compounds for the precise determination of absorption edges and for understanding general absorption properties. For a given specimen, the transmitted light intensity (I) is governed by the following equation

$$I = I_0 e^{-\mu x}$$

where I_0 is the incident light intensity, μ is the absorption coefficient of the specimen, and x is the thickness of the sample. I and Io can be measured experimentally; therefore, μx can be obtained. If the specimen thickness (x) can be measured, then the absorption coefficient (μ) can be calculated. Due to the difficulties of obtaining thin films from biological compounds with uniform thickness, the absorption spectra in this article are presented as relative absorptions (μx).

A series of studies on the absorption properties of various biological compounds has been conducted at the Canadian Synchrotron Radiation Facility (CSRF) beamline at the Tantalus storage ring (Stoughton, Wisconsin). A Mark IV Grasshopper monochromator (Tan *et al.*, 1982, 1984) was used to obtain monochromatic light, and data acquisition was done with an IBM 5150 computer equipped with a Tecmar A/D converter. Excluding naturally occurring pinhole-free thin films such as the anther surface cuticle of corn, it is very difficult to produce a pinhole-free thin film from biological compounds. At present, only two types of thin film have been successfully produced: gelatin and agar. However, absorption spectra of a few other biologically important compounds have been obtained by mixing the compound in either gelatin or agar (or agarose), and producing thin films.

Protein (gelatin)

Protein is one of the major constituents of cells; therefore, it becomes one of the main elements which contribute to the image density and contrast. Fig-

ure 38 shows the relative absorption spectrum of a pure calf gelatin (Sigma #G-0510 type IV) film. Note the steep carbon *K* edge at 43.1Å. Below the carbon *K* edge, the absorbance reaches its minimum, and begins to increase rapidly as the wavelength increases. In the long wavelength region, gelatin film becomes essentially opaque. As calculated by Feder and Sayre (1980), the optimum resolution for contact microscopy can be achieved with radiation which has a wavelength of about 4nm. Therefore, it is desirable to take ad-

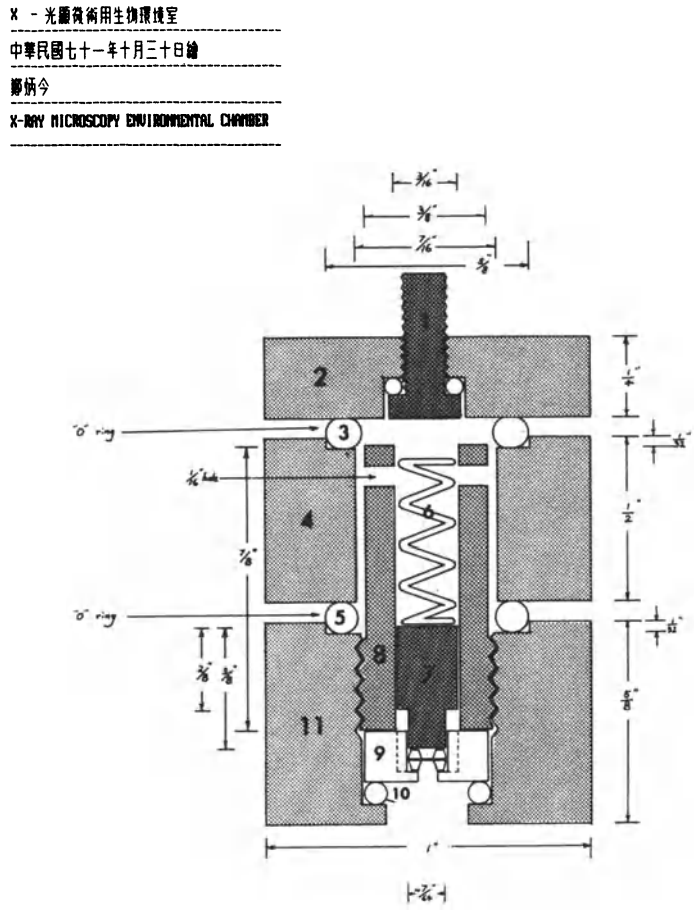

Figure 36. Design of an environmental chamber. A silicon nitride window is glued onto the bottom of a small stainless steel "dish" which allow cells to be cultured directly on the window surface. The screws which hold the three pieces together is not shown.

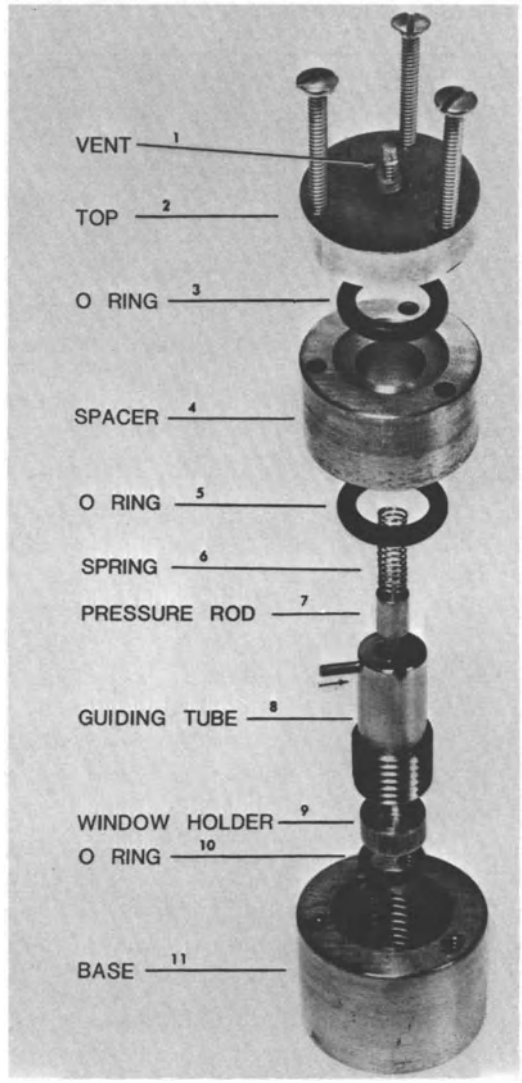

Figure 37. Enviromental chamber for imaging wet specimens. The photograph shows the various parts of the enviromental chamber. The Si_3N_4 window is glued onto a stainless steel "window holder" by high vacuum epoxy glue. Cells can be cultured directly on the surface of the window. The chamber is made of three major pieces: the base, the spacer and the top. The pressure rod and spring keep the resist in intimate contact with the specimen. The top piece consists of a vent hole which is designed to prevent possible build-up of hydrostatic pressure during chamber assembly.

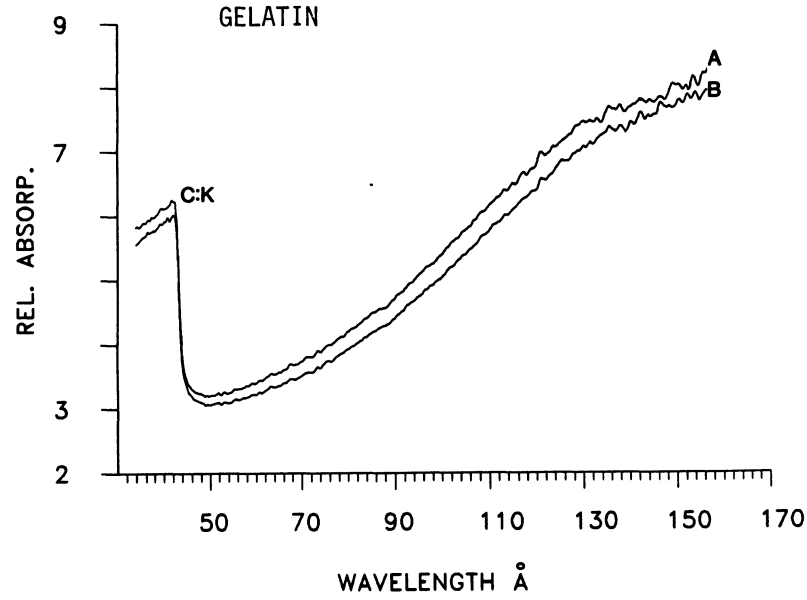

Figure 38. Relative absorption spectra of a gelatin film. Note the pronounced carbon *K* edge (43.1Å). The A spectrum was obtained from undamaged gelatin film, and spectrum B was obtained from the same film irradiated with zero-order white light (3450 units). (1 unit = 1 mA of ring current x min)

vantage of the carbon *K* edge for maximizing the image contrast. Upon high dosage of zero order synchrotron radiation, the gelatin film shows significant mass loss. Fig. 38, spectrum B, shows the resulting spectrum after radiation damage. The damage indicates that upon irradiation there is a significant mass loss. However, the degree of structural alteration which has occurred is not known.

Carbohydrate (Agar)

Agar is a polysaccharide complex extracted from algae *Rhodophyceae*. It is commonly used as a substratum in bacterial cultures, and as a substitute for gelatin in industrial applications. Agar is one of the biological substances from which we have succeeded in preparing thin films. Fig. 39 shows the absorption spectrum of a bacterial culture-grade agar film (carbon *K* edge at 43.3Å). Note the presence of the sulfur $(L)_{II,III}$ at 71.5Å. If one uses electrophoresis-grade agarose (purified agar), the sulfur *L* edge is no longer detectable. Zero-

order synchrotron radiation can cause significant mass loss in agar film. The difference between spectra before (A) and after (B) x-ray irradiation is demonstrated in Fig. 39.

ADP-gelatin mixture

Thin films of adenosine diphosphate (ADP) and gelatin mixture have been made. Figure 40 shows the absorption spectrum of ADP- gelatin film. Note the phosphorus L_I (63.7Å), P $L_{II,III}$ (85.3Å) edges and carbon K edge (43.3Å). The edge just below the P $L_{II,III}$ edge (2° C) is due to the carbon absorption of second order contaminated light. Based on the electron binding energies of the free phosphrous atom published by Lotz (1970), the P L_I is 191 eV (64.9Å), P L_{II} is 135 eV (91.8Å), and P L_{III} is 134 eV (92.5 Å). The shift of L edges from Lotz's result is believed to be due to the chemical bonding of the ADP molecule. Similarly, chemical shift of the carbon K edge in methane and in four fluoromethanes has been demonstrated by Bronn *et al.* (1978).

SUPPORTING MATRIXES FOR BIOLOGICAL SPECIMENS

Besides plastic embedded tissue sections, it is rare to find a biological specimen which is thin enough to be used for high resolution microscopy but which at the same time is self- supporting. For electron microscopy, biological specimens such as resinless tissue sections, micro-organisms and cultured cells, are generally supported by a matrix such as Formvar. For x-ray microscopy, one concern is that the x-ray attenuation by the supporting substratum can vary greatly across the soft x-ray spectrum; this is especially significant near absorption edges. The degree of x-ray attenuation by the substratum also influences the final image contrast: For example, at a certain wavelength, an x-ray dense matrix supporting a relatively transparent specimen will produce a lower contrast image in comparison with the same specimen supported by a less x-ray-dense substratum. While using above- and below-absorption edge imaging, it is necessary to know the degree of x-ray attenuation caused by the substratum so that proper adjustments in exposure can be made. Therefore, obtaining absorption spectra for all supporting substrata becomes essential. Furthermore, it is essential to know to what extent the substrata are subject to x-ray damage. An unstable supporting film could disintegrate during x-ray exposure, or a change in image contrast between two stereo-pair images could result from support film mass loss.

Formvar is the supporting substratum most commonly used in electron microscopy. It is also used intensively in our x-ray imaging work. Formvar, which consists of 70.2% carbon, 9.7% hydrogen and 20.0% oxygen (mass fraction), is a very tough polymer film which can be made very thin (<100 nm). Even though the absorption spectrum (Fig. 41) of Formvar is very similar to many biological specimens (Figs. 38 and 39), its contribution to the decrease in image contrast is generally negligible due to the thinness of the film. However, Formvar's major drawback is that it is subject to x-ray damage. Figure 41 shows the relative absorption spectra of a tilde400 nm thick Formvar film before and after x-ray irradiation. Note the loss of the carbon *K* edge which represents a loss of mass of about 10%. Close examination of the exposed Formvar film reveals physical damage caused by the radiation. Therefore, in obtaining stereo-pairs, significant mass loss of Formvar film between the two exposures can cause a noticeable difference of image contrast. In Fig. 41, the arrow indicates a small chlorine peak (*L* edge) which is contributed by the residual chloroform (chloroform was used to dissolve Formvar for manufacturing the thin film).

In our study, we found that polystyrene is superior to Formvar film. Polystyrene, a polymer consisting of 92% carbon and 8% hydrogen (mass fraction), is a very stable supporting substratum for x-ray irradiation. Figure 42 shows the relative absorption spectrum of a polystyrene film. Note the low absorption "window" region just below the carbon *K* absorption edge (43.5 nm). No noticeable changes in the absorption spectrum occurred when the film was subjected to a high dosage of zero order synchrotron radiation (the two plots shown in Figure 42 represent the spectra taken before exposure to zero order synchrotron radiation and after 1000 unit of irradiation). Furthermore, the absence of oxygen in the polymer makes this film an ideal supporting matrix for x-ray contact microscopy using wavelengths close to the oxygen edge. Thin films (<100 nm) can be easily made in the same way as for Formvar (Cheng and Lin, 1981). Only minor surface treatments (i.e. thin carbon coating or albumin coating) are required to facilitate cell attachment in tissue culture.

Silicon nitride is occasionally used as a supporting matrix. This inorganic substance offers a strong, dimensionally stable but brittle supporting film. Upon x-ray irradiation, it shows no detectable change in absorption properties in the region of 4nm - 17nm. Surface coating with a thin layer of carbon (<100Å) is required to facilitate cell attachment in tissue culture. The relative absorption spectrum is shown in Figure 38. Note the silicon L_I (80Å) and *L*

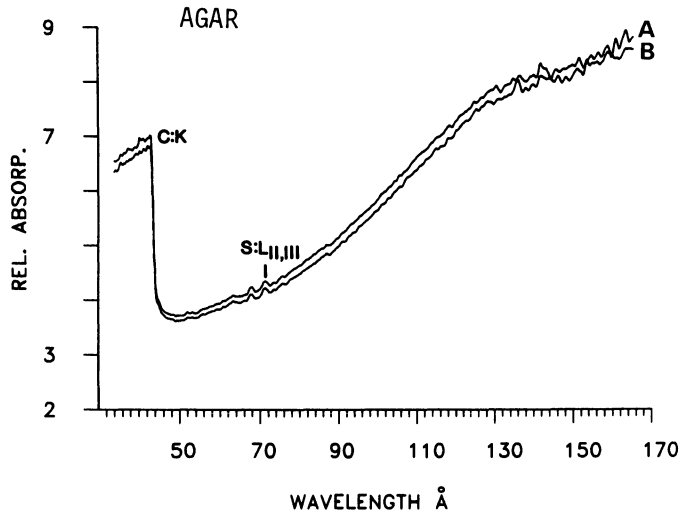

Figure 39. Relative absorption spectra of agar film. The two spectra were taken before (A) and after (B: 535 units) zero-order irradiation. Note the presence of sulfur L edges.

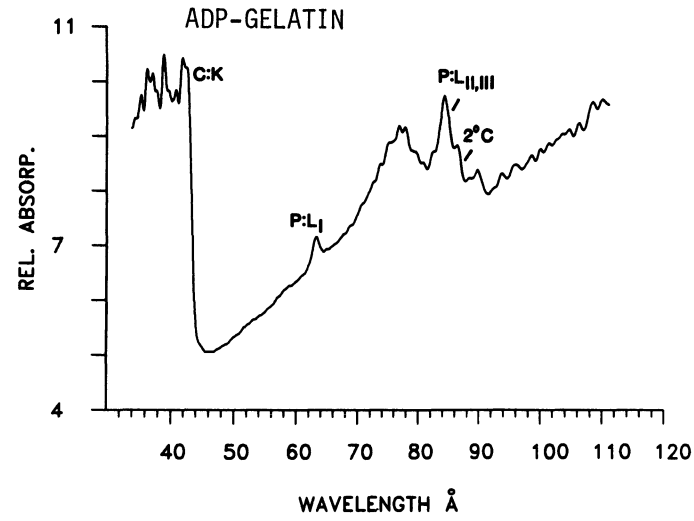

Figure 40. Absorption spectrum of ADP-gelatin mixture. Note the phosphorus L_I, $L_{II,III}$ edges.

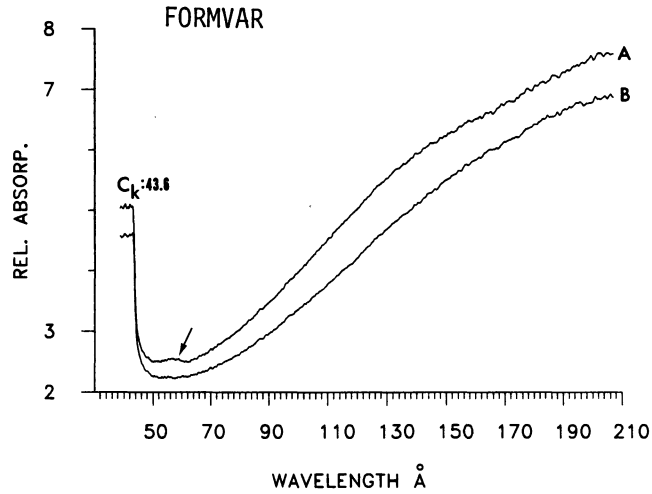

Figure 41. Absorption spectra of Formvar film before and after (1240 units) zero-order white light irradiation. Note the significant loss of the carbon edge.

$_{II,III}$ (118.9Å) edges. It is clear that this supporting film is also an excellent filter material for selecting x-ray energies.

X-RAY ABSORPTION PROPERTIES OF X-RAY RESISTS

Studies of x-ray absorption properties of various x-ray resists have been conducted at the Canadian Synchrotron Radiation Facility (CSRF) beamline (Tan *et al.*, 1984) on the Tantalus storage ring at Stoughton, Wisconsin by Howe (1983). Some of the recent results in this area are being presented in another paper from this Institute (Shinozaki *et al.*). In this article, the relative absorption spectra of PMMA and poly(butene-1-sulfone) (PBS) are shown to illustrate the rate of radiation damage between the two resists.

Figure 44 shows the relative absorption spectrum of a PMMA resist before and after radiation damage. Note that the height of the carbon *K* edge (43.6Å) decreases due to radiation damage. The damage can be visualized on the resist as so-called "self- development".

Because of the poor resolution offered by the PBS resist, it is seldom used in our x-ray contact microscopy. However, its spectrum is shown in Fig. 45 to

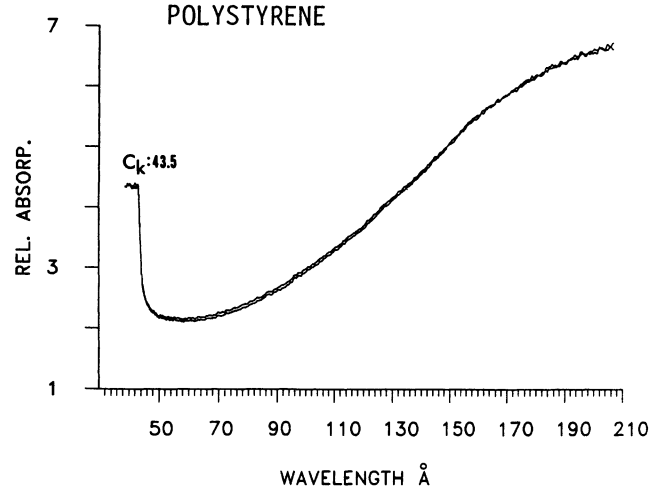

Figure 42. Absorption spectra of polystyrene film. The two nearly identical spectra represent before and after (1000 units) zero- order irradiation.

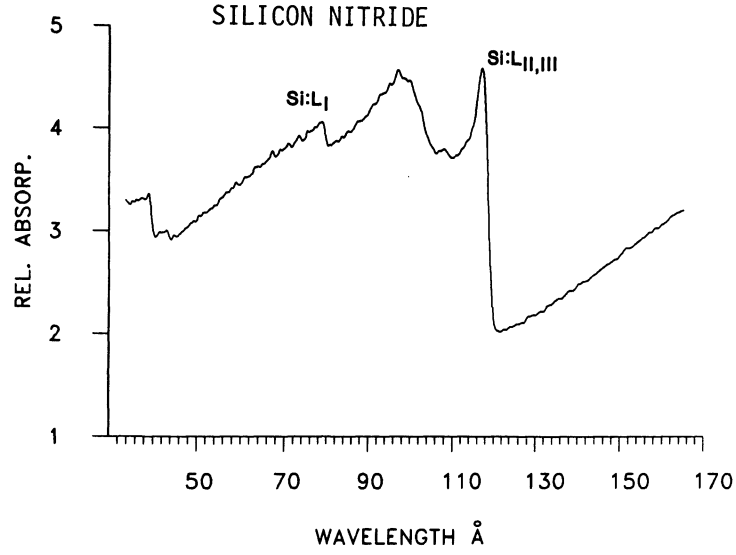

Figure 43. Absorption spectrum of Si_3N_4 window. The Si *L sub I* edge is located at 80Å and the $L_{II,III}$ edges are located at 118.9Å. The small carbon *K* edge is due to contamination on the window.

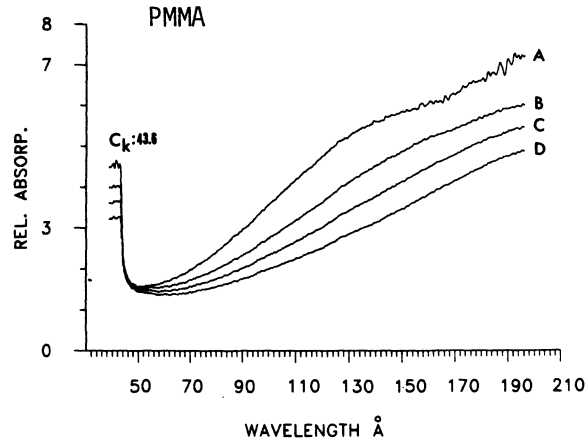

Figure 44. Absorption spectra of PMMA resist. The uppermost spectrum, A, was obtained from nondamaged resist; spectrum B was obtained from the same resist but has been damaged by zero order synchrotron radiation (1650 units); spectrum C and spectrum D are from resist which received 3250 and 6185 units of radiation. Note the changes due to zero order synchrotron radiation damage.

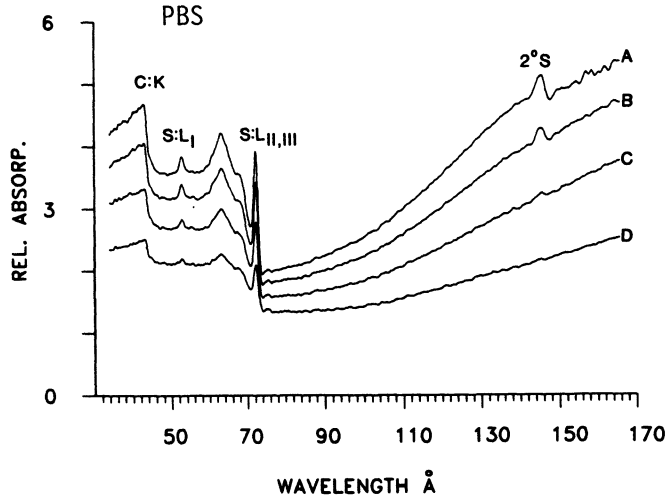

Figure 45. Relative absorption spectra of a PBS resist before and after zero-order synchrotron radiation damage. Spectrum A: before damage. B: 13.8 units. C: 38.3 units. D: 81.3 units. The peak at tilde146 Å is due to the sulfur absorption of the second order radiation from the monochromator grating.

demonstrate the rate of radiation damage and location of the edges. Note the sulfur L_I (53.4Å) and $L_{II,III}$ (72.7 Å) edges and the carbon K edge (43.6Å). The big board peak between S L_I and S $L_{II,III}$ is the result of electron transition from an initial p states to the continuum d states in sulfur (Howe, 1983; Koch *et al.*, 1977).

ELECTRON-BEAM INDUCED DAMAGE ON PMMA RESIST

PMMA resist is subject to electron beam damage. This damage directly affects the final magnified images of contact lithographs. One of the obvious manifestations of electron beam damage is the increased transparency of the resist when viewed in the transmission electron microscope. Figure 48 shows the area where electron transparency has been increased from previous electron beam bombardment. The concentric rings are due to the damage caused by three different beam sizes of the electron microscope. The resist was damaged by the smallest beam spot (double long arrows), second, by intermediate spot size (double short arrows), and then by the largest spot (triple arrows). Under the scanning electron microscope, the damage is characterized by a depression in the resist surface (Fig. 46). This type of electron-induced damage has been studied intensively on various embedding resins for electron microscopy. For instance, Cosslett (1960) has measured a mass loss of 40-60% for methacrylate resins exposed to an electron beam.

If one is working with a thicker resist (>1.5μm), not only does the above mentioned damage occur, but also the resist begins to show secondary damage. Upon electron bombardment, the resist begins to form wrinkles (Fig. 50). This usually occurs in the thick regions of the resist such as those areas under the specimen grid or under dense specimens. Our experiences indicate that resists with thickness less than 1 μm seldom show this type of damage.

After a heavy electron irradiation of a thick resist, tertiary damage, characterized by the formation of bubbles, can be observed. As shown in the SEM image (Fig. 47), the bubbles usually have a dark center and bright peripheral area which are caused by cracking of the metal-coated resist surface; the area which has no surface coating appears dark because of the low secondary

Figure 46. SEM view of a resist surface damaged by the electron beam of a scanning electron microscope. Note the rectangular depression on the resist which represents the area which has been scanned by the electron beam.

Figure 47. SEM view of bubbles formed on the damaged resist. Note a bubble has a dark center and a bright peripheral area, this is due to the fact that the center of the bubble has no metal coating.

Figure 48. TEM view of a Si_3N_4 window-supported resist. Note the electron beam-induced damage on the resist which appears as concentric rings (arrows).

Figure 49. TEM view of a electron beam-induced bubble on the resist. Note the formation of radiating "rays" (arrow).

Figure 50. TEM view of a resist suffering from secondary damage. Note the wrinkles on the resist.

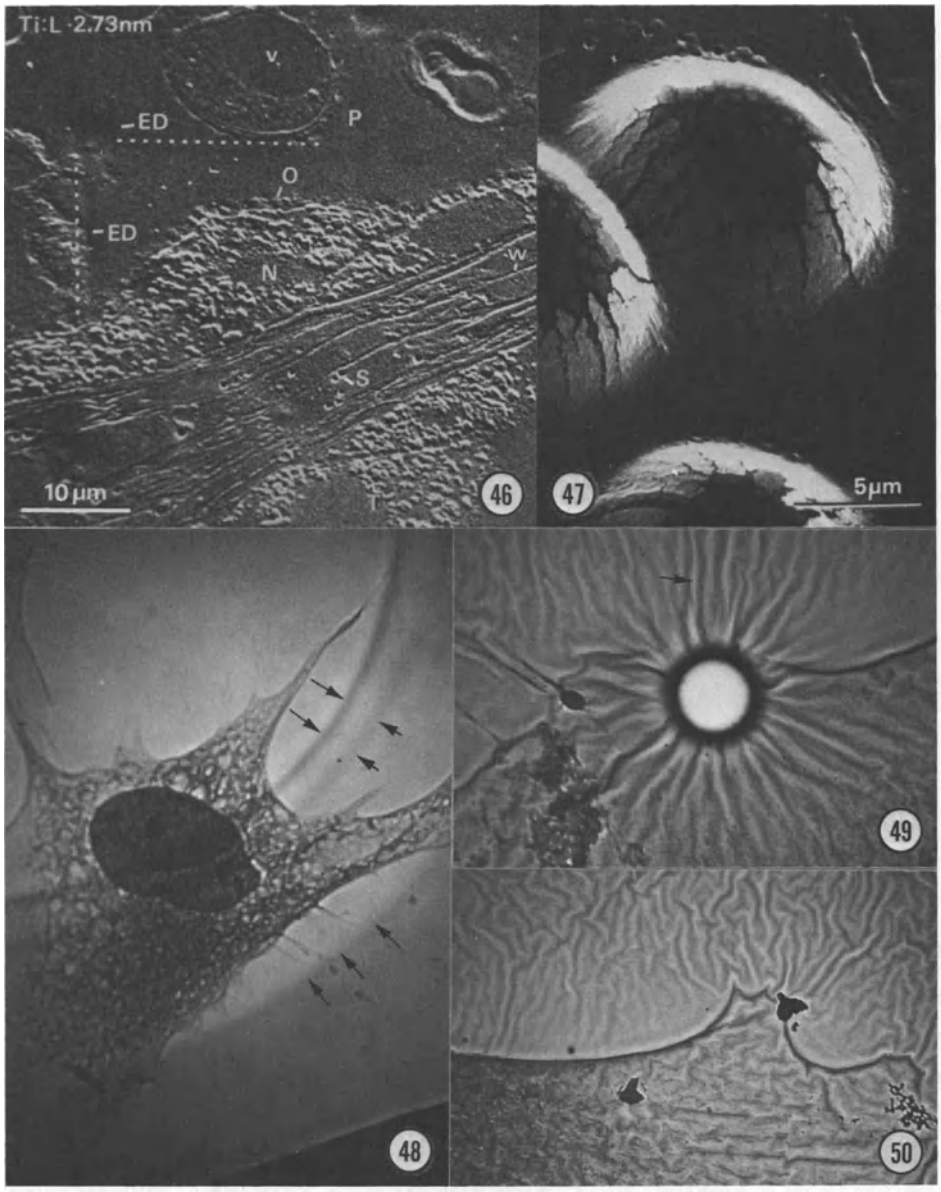
Ti:L 2.73nm
V
ED
P
O
ED
N
W
S
10 µm
T
46
47
5µm
48
49
50

electron emission. Under a transmission electron microscope, this type of damage is characterized by the formation of clear spots with radiating rays (Fig. 49, arrow). We believe that the formation of bubbles is due to localized heating of the resist, which, in turn, generates gases that facilitate the formation of bubbles. If the rate of electron bombardment is kept low, bubble formation would be prevented even in a thick resist. This indicates that the bubble is formed by a sudden burst of gases. Cooling of the resist also tends to reduce the chances of forming bubbles.

SUMMARY

X-ray contact microscopy offers attractive possibilities for the study of biological cells. This is especially true for thick samples or for specimens with high electron density which make transmission electron microscopy very difficult or impossible. Organelles, such as the nuclei of whole-mount cultured cells, can be imaged by x-rays quite easily. The water window below the oxygen absorption edge (2.4 nm) offers potential for wet cell imaging; preliminary results using transmission x-ray microscopy (Schmahl *et al.*, 1980), scanning x-ray microscopy (Kirz, 1984) and contact microscopy (Feder *et al.*, 1984) have shown that imaging wet samples using x-rays is possible. Intensive investigations on the development of specimen preparation methods and imaging techniques are required. We have to keep in mind that many techniques which were developed for electron microscopy may not be suitable for x- ray microscopy. However, the use of vital as well as heavy metal stains should be considered.

With a laser-generated x-ray source and a pulse plasma source, such as LEXIS of Maxwell Laboratory Inc., imaging wet or living cells is possible. These types of x-ray sources provide enough flux and are easy to maintain, therefore, they could become ideal laboratory sources. Further improvements in the environmental chamber and specimen handling methodology are essential, however.

In order to develop x-ray microscopy to be a useful biological research tool, three important areas are worth concentrating on: the continued development of wet cell imaging techniques, the development of proper specimen handling and preparation techniques, and the establishment of basic rules for image interpretation.

ACKNOWLEDGEMENT

We are very grateful to the Canadian Medical Research Council, The Natural Science and Engineering Research Council and the Veeco Fund for financial support. Special thanks to H. B. Peng of the University of Illinois at Chicago for providing *Xenopus laevis* cultures and laboratory facilities. We wish to express our thanks to R. J. Walter and P. K. Gaetano of the University of Illinois at Chicago for providing 3T3 cell cultures and many helpful suggestions. We would like to acknowledge the constant helpful advice of the staff at the Physical Science Laboratory of University of Wisconsin. Special thanks to C. Olson for his kindly providing sample chamber for the synchrotron beamline. Finally, many thanks to Ms. Mai-ing Lin Cheng of Zenith Data System Co., for her superb work in the development of most of the computer programs for this study.

REFERENCES

Baldini, M. G., Kim, B. K., Timmons, S., Feder, R., Sayre, D., and Banton, V., This volume.

Bronn, F. C., Bachrach, R., and Bianconi, A., 1978, Fine structure above the carbon *K* edge in methane and in the fluoromethanes. *Chem. Phys. Lett.*, 54: 425-429.

Cheng, P. C., Greyson, R. I. and Walden, D. B., 1979, Improved plant microtechniques for TEM, SEM and LM specimen preparation. *Natl. Sci. Counc. Monthly, Rep. of China*, 7:1001-1007.

Cheng, P. C. and Lin, M. I., 1980, Cytological studies on the stamen of *Caltha palustris* L.: Anther and filament morphology, ultrastructural studies of their cuticle and orbicule. *Natl. Sci. Counc. Monthly, Rep. of China*, 8:1113- 1140.

Cheng P. C., Findlay, W., McGowan, J. Wm., and Feder, R., 1980, Analysis of plant cells using soft x-ray lithography. *J. Cell Biol.*, 87: 229a.

Cheng, P. C., and Peng, H. B., 1981, Recent development in soft x- ray contact microscopy. *Science Monthly* (Taipei, Rep. of China), 70-9: 11-12.

Cheng P. C., Findlay, W., McGowan, J. Wm., and Feder, R.,1981, Soft x-ray lithography of plant cells. (abstract) 147th National meeting of American Association for Advancement of Science, p. 131.

Cheng, P. C. and Lin, M. I., 1981, Technique and apparatus for serial ultra-thin sectioning. *Natl. Sci. Counc. Monthly, Rep. of China*, 9: 15-22.

Cheng P. C., Peng, H. B., Feder, R., and McGowan, J. Wm., 1982, The use of transmission electron microscope as a viewing tool for high resolution soft x-ray contact microscopy. *Electron Microscopy*, Vol. 1: 461-462.

Cheng, P. C., Peng, H. B., Tan, K. H., McGowan, J. Wm., Feder, R., and Shinozaki, D. M., 1984, Soft x-ray contact microscopy and microchemical analysis of biological specimens, *in*: "Springer Series in Optical Sciences: X-ray microscopy," G. Schmahl and D. Rudolph, eds., Springer-Verlag, Berlin.

Cheng, P. C., 1984, Applications and examples of biological soft x- ray microscopy. *Acta Crystallographica*, A40, Supplement.

Cosslett, A, 1960, Some applications of the ultraviolet and interference microscopes in electron microscopy. *J. Roy. Micr. Soc.*, 79: 263-271.

Cosslett, V. E., and Nixon, W. C., 1960, "X-ray microscopy," University Press, Cambridge, pp. 139-182.

Dauvillier, A., 1927, Sur un tube a rayons X de longueur d'onde effective egale a 8 unites Angstrom. *C. R. Acad. Sci., Paris*, 185, 1460-1462.

Dauvillier, A., 1930, Realisation de la microradiographie integrale. *C. R. Acad. Sci., Paris*, 190, 1287-1289.

Duke, P. J., 1984, X-ray microscopy at the Daresbury Laboratory, *in*: "Springer Series in Optical Sciences: X-ray Microscopy," G. Schmahl and D. Rudolph, eds., Springer-Verlag, Berlin.

Engström, A., 1946, Quantitative micro- and histo-chemical elementary analysis by roentgen absorption spectrography. *Acta Radiol.*, Supp. 63.

Engström, A., 1962, "X-ray Microanalysis in Biology and Medicine," Elsevier Publishing Co., Amsterdam.

Engström, A., 1966, X-ray microscopy and x-ray absorption analysis, *in*: "Physical Techniques in Biological Research", Vol. III, Part A, A. W. Pollister, ed., (2nd edition). Academic Press, New York, pp. 87-171.

Engström, A., 1980, X-ray microscopy, past, present, and future. *Ann. N. Y. Acad. Sci.*, 342: 392-400.

Feder, R., Spiller, E., Topalian, J., Broers, A. N., Gudat, W., Panessa, B. J., Zadunaisky, Z. A., and Sedat, J., 1977, High resolution soft x-ray microscopy. *Science*, 197: 259.

Feder, R., and Sayre, D., 1980, Recent developments in x-ray contact microscopy. *Ann. N. Y. Acad. Sci.*, 342: 213-234.

Feder, R., Costa, J. L., Chaudhari, P., and Sayre, D.,1981, Improved detail in biological soft x-ray microscopy: Study of blood platelets. *Science*, 212: 1398-1400.

Feder, R., Mayne-Banton, V., Sayre, D., Costa, J., Kim, B. K., Baldini, M. G., and Cheng, P. C., 1984, Recent developments in x-ray contact microscopy, *in*: "Springer Series in Optical Sciences: X-ray microscopy," G. Schmahl and D. Rudolph, eds., Springer-Verlag, Berlin.

Feder, R. and Mayne-Banton, V., This volume.

Goby, M. P., 1913, Une application nouvelle des rayons X: la micro-radiographie. *C. R. Acad. Sci., Paris*, 156: 686-688.

Horowitz, P., and Howell, J. A., 1972, A scanning x-ray microscope using synchrotron radiation. *Science*, 178: 606-611.

Howe, R. J., 1983, "Absorption properties of polymers using synchrotron radiation," Master thesis, University of Western Ontario, London, Ontario, Canada.

Hudson, B. and Makin, M. J., 970, The optimum tilt angle for electron stereo-microscopy. *J. Phy. E: Sci. Instru.*, 3: 311.

Kirz, J., 1980, Mapping the distribution of particular atomic species. *Ann. N. Y. Acad. Sci.*, 342: 273-287.

Kirz, J., and Sayre, D., 1980, Soft x-ray microscopy of biological specimens, *in*: "Synchrotron radiation Research," Seb Doniach and Herman Winick, eds., Plenum Press, N. Y..

Kirz, J., and Sayre, D., 1984, Prospects and problems in x-ray microscopy, *in*: "Springer Series in Optical Sciences: X-ray microscopy," G. Schmahl and D. Rudolph, eds., Springer- Verlag, Berlin.

Koch, E. E., Kunz, C., and Sonntag, B., 1977, Electronic states in solids investigated by means of synchrotron radiation. *Physics Reports*, 29: 153-231.

Lamarque, P., 1936, Histologie - Historadiographie. *C. R. Acad. Sci. Paris.*, 202: 684-685.

Lotz, W., 1970, Electron binding energies in free atoms. *J. Opt. Soc. Amer.*, 60: 206-210.

Luft, J. H., 1973, Embedding media - Old and new, *in*: "Advanced Techniques in Biological Electron Microscopy," J. K. Koehler, ed., Springer-Verlag, New York.

Manuelidis, L., Sedat, J., and Feder, R., 1980, Soft x-ray lithographic studies of interphase chromosomes. *Ann. N. Y. Acad. Sci.*, 342: 304-325.

McGowan, J. Wm., Borwein, B., Medeiros, J. A., Beveridge, T., Brown, J. D., Spiller, E., Feder, R., Topalian, J., and Gudat, W., 1979, High resolution microchemical analysis using soft x-ray lithographic techniques. *J. Cell Biol.*, 80, 732-735.

McGowan, J. Wm., and Malachowski, M. J., 1980, Soft x-ray replication of biological material- X-ray microscopy and microchemical analysis of cells. *Ann. N. Y. Acad. Sci.*, 342: 288-303.

Niemann, B., 1984, The Gottingen scanning x-ray microscope, *in*: "Springer Series in Optical Sciences: X-ray Microscopy," G. Schmahl and D. Rudolph, eds., Springer-Verlag, Berlin.

Peng, H. B., Wolosewick, J. J., and Cheng, P. C., 1981, The development of myofibrils in cultured muscle cells: A whole- mount and thin section electron microscopic study. *Develop. Biol.*, 88: 121-136.

Panessa-Warren, B. J., and Warren, J. B., 1980a, Determining biological fine structure by differential absorption of soft x-rays. *Ann. N. Y. Acad. Sci.*, 342: 350-367.

Panessa, B. J., Warren, J. B., Hoffman, P., and Feder, R., 1980b, Imaging unstained proteoglycan aggregates by soft x-ray contact microscopy. *Ultramicroscopy*, 5: 267-274.

Panessa, B. J., Warren, J. B., Feder, R., Sayre, D., and Hoffman, P., 1980c, Ultrastructural and elemental imaging of biological specimens by soft x-ray contact microscopy. *Scanning Electron Microscopy*, II: 107-116.

Panessa-Warren B. J., 1984, Biological applications of x-ray contact microscopy, *in*: "Springer Series in Optical Sciences: X-ray microscopy," G. Schmahl and D. Rudolph, eds., Springer- Verlag, Berlin.

Polack, P., and Lowenthal S., 1984, Photoelectron x-ray microscopy: Recent developments, *in*: "Springer Series in Optical Sciences: X-ray Microscopy," G. Schmahl and D. Rudolph, eds., Springer-Verlag, Berlin.

Rarback, H., Kenney, J. M., Kirz, J., Howell, M. R., Chang, P., Coane, P. J., Feder, R., Houzego, P. J., Kern, D. P. and Sayre, D., 1984, Recent result from the Stony Brook scanning microscope, *in*: "Springer series in Optical Sciences: X-ray microscopy," G. Schmahl and D. Rudolph, eds., Springer- Verlag, Berlin.

Rosser, R. J., 1984, X-ray microscopy at Imperial Collage, *in*: "Springer Series in Optical Sciences: X-ray Microscopy," G. Schmahl and D. Rudolph, eds., Springer-Verlag, Berlin.

Rudolph, D., Niemann, B., Schmahl, G. and Christ, O., 1984, The Göttingen x-ray microscope and x-ray microscopy experiments at the BESSY storage ring, *in*: "Springer Series in Optical Sciences: X-ray microscopy," G. Schmahl and D. Rudolph, eds., Springer-Verlag, Berlin.

Sarafis V., 1984, X-ray microscopy as a possible tool for the investigation of plant cells, *in*: "Springer Series in Optical Sciences: X-ray microscopy," G. Schmahl and D. Rudolph, eds., Springer-Verlag, Berlin.

Sayre, D., 1980, Review of image formation methods with the soft x-ray photon. *Annals N. Y. Academy Sci.*, 342: 387-391.

Sayre, D., and Feder, R., 1980, Additional technical aspects: Wet specimens, thick specimens, and factors affecting convenience. *Annals N. Y. Academy Sci.*, 342: 268-272.

Schmahl, G., Rudolph, D., Niemann, B., and Christ, O., 1980, X-ray microscopy of biological specimens with a zone plate microscope. *Annals of N. Y. Academy Sci.*, 342: 368-386.

Shinozaki, D. M., McGowan, J. Wm., Cheng, P. C., and Tan, K. H., This volume.

Silk, J. K., 1981, A grazing incidence microscope for x-ray imaging applications. *Annals of N. Y. Academy Sci*, 342: 116-129.

Spiller, E., Feder, R., Topalian, J., Eastman, D. E., Gudat, W., and Sayre, D., 1976, X-ray microscopy of biological objects with carbon *K* and with synchrotron radiation. *Science* (Washington D. C.), 191: 1172-1174.

Spiller, E., and Feder, R., 1977, X-ray lithography, *in*: "Topics in Applied Physics.", ed. H. J. Quiesser, Vol. 22: 35-92.

Spiller, E., and Feder, R., 1978, The optics of long-wavelength x- rays. *Scientific American*, 239-5: 70-78.

Spiller, E., 1984, A scanning soft x-ray microscope using normal incidence mirrors, *in*: "Springer Series in Optical Sciences: X-ray Microscopy," G. Schmahl and D. Rudolph, eds., Springer- Verlag, Berlin.

Tan, K. H., Bancroft, G. M., Coatsworth, L. L., and Yates, B. W., 1982, Mark IV "Grasshopper" grazing incidence monochromator for the Canadian Synchrotron Radiation Facility (CSRF). *Can. J. Phys.*, 60: 131-136.

Tan, K. H., Cheng, P. C., Bancroft, G. M., and McGowan, J. Wm., 1984, The Canadian synchrotron radiation facility: Soft x-ray contact microscopy of biological material. *Can. J. Spectrosc.*, 29(5), 134-137.

Wolosewick, J. J., 1980, The application of polyethylene glycol (PEG) to electron microscopy. *J. Cell Biol.*, 86: 675-681.

SOFT X-RAY MICROSCOPY OF ACTIVATED HUMAN PLATELETS

M.G. Baldini, B.K. Kim and S. Timmons

Harvard Medical School at New England Deaconess Hospital (Boston)

R. Feder, D. Sayre and V. Banton

IBM Thomas J. Watson Research Center (N.Y.)

A hundred years ago, in 1882, J. Bizzozero[1] described the blood platelets as they appeared to him under the microscope, unstained and flowing in the mesenteric vessels of rabbits and guinea pigs. His impeccable drawings demonstrated that platelets, the smallest and anucleated cells of the blood, can adhere and aggregate, have a central role in arresting hemorrhage, and an important participation in thrombosis and embolism. Micro-imaging technics have, since then, slowly improved, but progress has been more rapid during the past two decades. Simultaneously, recent studies on the structural physiology of blood platelets have made important strides. We believe that the very recent application of soft x-ray microscopy to platelet studies has offered new possibilities in this important area of research.

This review will include some of our results obtained by soft x-ray microscopy of activated human platelets after a brief description is given of the biophysiological background from which our projects were generated.

PRINCIPLES OF STRUCTURAL PHYSIOLOGY OF ACTIVATED HUMAN PLATELETS

The blood platelets, numbering 1.5 to 3.5 X 10^5 per μl in human subjects, circulate within the vasculature as disc-shaped cells with a mean diameter of 2 to 3.5 μ and a central thickness of 0.5 to 0.75 μ. Being thicker in the center than at the periphery, they resemble pancakes. Non-activated platelets have a discoid shape.

Platelet anatomy is usefully divided into three structural regions[2-5], each grossly related to different aspects of platelet function, a peripheral zone, a sol-gel zone, and an organelle zone. The peripheral zone consists of an exterior coat which contains a number of plasma proteins, clotting factors, and molecules related to fibrinolysis. This is the site which, in the circulation, can sense the presence of vascular injury and transmit the stimuli triggering the platelet response, a complex process called "platelet activation." The platelet peripheral zone also includes the unit membrane and the submembrane area crossed by the ducts of the open canalicular system. The latter is a system of canaliculi lined by invaginations of the plasma membrane and distributed throughout the body of the platelets. Through these channels, exchanges of substances with the environment occurs in both directions.

The sol-gel zone is composed of masses of fibrous elements with different aspects. The most important structures in this zone are the microtubules, the microfilaments, and the submembrane filaments. The circumferential bundle of microtubules (Fig. 1) supports the discoid shape of the resting platelets as the "backbone" of the platelet cytoskeleton. These three fiber systems have the capacity to polymerize and depolymerize depending on the functional state of the cell. They may not be intrinsically different at the molecular level. They may only differ in their state of polymerization or depolymerization, in their degree of coalescence and their location in the cell. Their basic units may possibly be interchangeable. These different fibers in various states of polymerization provide the platelet with a contractile system involved in shape changes, pseudopod extrusion, and in secretion of active substances to the cell environment.

The open canalicular system is not the only one passing through the sol-gel zone of the platelet. The dense tubular system randomly dispersed, also traverses this zone. It consists of internal membranes mostly located underneath the plasma membrane. This system is involved in prostanoid synthesis and Ca^{++} sequestration. When platelets are activated, Ca^{++} is released internally from the dense tubular system probably as the first effect of the stimulus causing activation.

The organelle zone contains a variety of formed particulate structures which are embedded in the sol-gel matrix of the resting platelet. This platelet zone consists mainly of granules, mitochondria, other electron dense bodies, and elements of the dense tubular system. It also contains masses of glycogen particles randomly distributed in the cytoplasm. These are present as a source of energy. Three different types of granules can be distinguished: 1) the dense bodies which are relatively few in number containing primarily ADP, serotonin, Ca^{++} ions, and pyrophosphate, 2) the α-granules (less dense bodies) containing a variety of substances

including platelet factor 4 (a heparin binding protein), a cell growth factor, and some clotting factors (fibrinogen, factor VIII antigen, and factor V), 3) the lysosomes containing hydrolytic enzymes. Platelet mitochondria are few in number. They contribute to the important metabolic pool of ATP for the platelet energy expenditures.

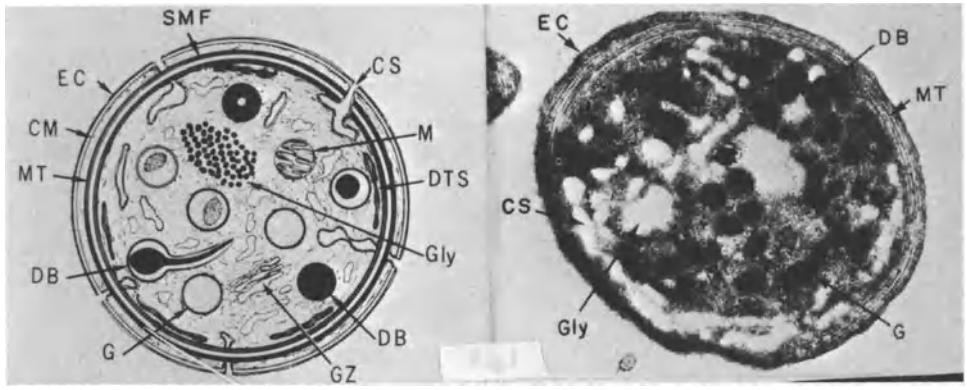

Fig 1: EC:external coat; CM:trilaminar unit membrane; MT:microtubules; DB:dense bodies; G:granules; GZ:Golgi zone; gly:glycogen; DTS:dense tubular system; M:mitochondria; GS:external conalicular system; SMF:submembrane filaments. (From J.G. White[3]).

Platelet activation is a term used to define a group of metabolic and structural changes that are observed in the platelets when they come into contact with an injured blood vessel or a "foreign surface". Activation of blood platelets results in pseudopod formation and may lead to the so-called release reaction. The sequence of events may be as follows: 1) an agonist reacts with a receptor on the platelet membrane, e.g. during platelet adhesion to subendothelial components of a blood vessel (collagen, others). A signal is transferred resulting in a flux of Ca^{++} ions from the dense tubular systems to the cell cytoplasm, 2) this leads to a clustering of platelet granules which is probably mediated by centralization of the bundle of microtubules, 3) contact of the platelet granule membrane with the membrane of the open canalicular system occurs, presumably mediated by Ca^{++} ions, 4) fusion between the granule membrane and the membrane of the open canalicular system follows. Finally, 5) the granule contents are released into the open canalicular system and diffuse to the surrounding medium. ADP is, also, released. Moreover thromboxane A_2 is produced by the activated platelets. Both substances activate and aggregate other platelets.[2-5]

White[2] has pointed out that centralization of platelet granules

during activation is followed by a progressive tightening of the microtubule bundle ending with contraction and fusion of the enclosed platelet granules and other organelles into an apparently amorphous central mass. The significance of this contraction is still obscure. Exocytosis per se has not as yet been seen in the platelets, but it is believed that the platelet release their granule contents through fusion of the granule membrane with the membrane of the open canalicular system.[4] White[2] believes that platelet shape changes stimulated by aggregating agents are highly specific and that a regulated response is essential to the physiologic expression of platelet function in hemostasis.

We must realize that the process of platelet activation and the different intracellular events ocurring during it, appear far more complex today than had previously been appreciated. The two major structural events in platelet activation which, we believe, are: 1) internal cell contraction with tightening of the microtubule bundle around the platelet organelles, and 2)pseudopod formation are not completely understood. Our recent research was devoted to the visualization of platelet structure by different means, namely soft x-ray microscopy, and to the study of platelet activation and pseudopod formation.

RADIATION SOURCES AVAILABLE FOR X-RAY MICROSCOPY

Contact x-ray microscopy using a stationary source is presently developing as an important imaging technic in cell biology. It is a relatively simple method. The specimen, placed on an electron microscope grid, is brought into close contact with a 400 to 800 nm of x-ray resist (polymethylmetacrylate or copolimer) supported by an ultrathin, but strong substrate. The substrate is flat and relatively transparent to soft x-rays and to electrons in the 60 to 100-KeV range. It is a 100-nm film of Si_3N_4 supported by a silicon frame. The mounted specimen is, then, exposed to a soft x-ray source. The exposed resist is, finally, developed and, if necessary, it is coated with a thin (10nm) layer of gold or palladium. It may, however, be examined directly in the electronmicroscope without metal coating. The long exposure time of 10 to 12 hours inhibits examination of well hydrated, living cells (Fig. 2). Contact x-ray microscopy has several advantages over the imaging technics presently in common use. Improved resolution in the order of 5 nm can be obtained even with thick specimens or whole cells. Specimen fixation and staining are not required and sectioning of the specimen in thin layers can be avoided. All these characteristics of the technic can potentially offer a more accurate morphological and functional perception of all cell substructures. The disadvantages are, beside the long exposure time, a loss of resolution with thicker specimens due to blurring of the shadow image by diffraction, and the relatively low efficiency of x-ray photoresists.[6]

The very prolonged exposure in an hypoxic environment required in conventional contact x-ray microscopy with a stationary source has recently given preference to other techniques which are more adaptable for the study of highly hydrated specimens and, especially, living cells. For this purpose, we are presently examining the use of a synchrotron radiation source.[7] It can provide intense photon beams and very short pulses of photon emission in the tens of picoseconds. Storage rings can be ideal sources for x-ray micrography.

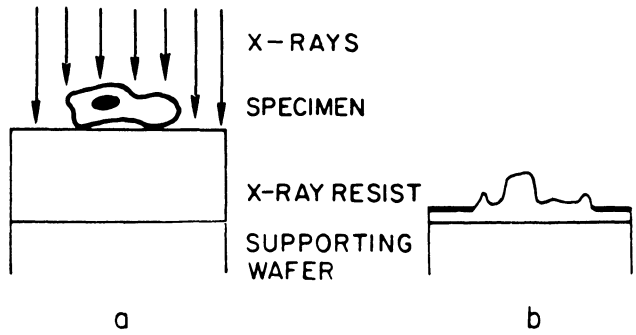

Fig. 2

The advantages presented by this technique are that: 1) storage rings have a higher intensity of soft x-rays, 2) they allow exposure times that are drastically shorter than those obtained with conventional sources, 3) their radiation is highly collimated which eliminates the loss of resolution by blurring, and 4) x-rays are monochromatic and tunable and, therefore, suitable for the identification of elemental compositions in biological samples. By this technique, it should be possible to investigate biological specimens with resolutions near 100 Å. Improvement in x-ray resist should eventually make exposure times much shorter than presently obtainable. However, the synchrotron radiation source generated by high energy electrons in a storage ring is very expensive, highly sophisticated, and rarely available. Also, the microscopy of living cells, a very important goal of all cell biologists, requires x-ray exposures in the nanosecond time frame. Present storage ring sources cannot satisfy the need.[7]

For this reason, we have given preference, in our very recent studies, to a different x-ray source which produces thermal radiation (Fig. 3). This system, the gas puff z pinch, consists of a fast capacitor bank, an array of sparkgaps, and a fast puff valve.[8,9] In

the pinch experiment, gas from a tank (argon, others) is injected through a nozzle in between the discharge electrodes. The switching sparkgaps are fired before the gas has a chance to spread and reach the insulating interface inside the vacuum chamber. By choosing the proper delay between the opening of the puff valve and triggering the sparkgaps, one can control the total gas mass in between the electrodes and tune it to an optimal value. Once this value is reached, the pinch occurs at the peak of the current which usually maximizes the energy delivered to the gas load. The gas puff z pinch is reproducible. Different gases and compounds can be employed.

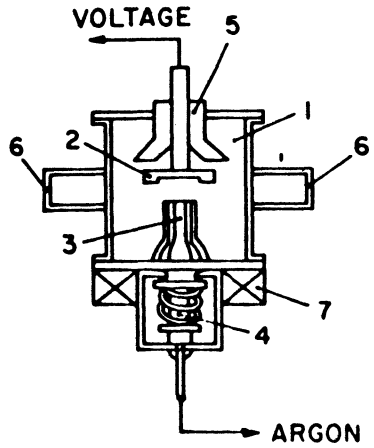

Vacuum chamber geometry. 1--vacuum chamber, 2--anode, 3--nozzle, 4--fast valve, 5--insulator, 6--window, 7--magnetic coil driver for the valve.

Fig. 3

The combination of the gas puff z pinch system as the soft x-ray source, XR-39, a plastic material which was found to be the most sensitive track detector[9], and a scanning electromicroscope for viewing the resist profile is what we have used in our experiments and is very promising. The blood cell sample to pinch distance was 20 cm. Resolution of $\sim$1000 Å was achieved. A 2000-line/inch self-supported nickel mesh was used in these experiments. The samples of blood platelets were placed inside the vacuum chamber and no spectral filtering was used. The x-ray range was 20-100 eV. More efficient radiation was produced by changing the injected gas (argon) to methane.

RESULTS

For the preparation in Fig. 4, the platelet suspension was maintained at room temperature. One volume of platelet suspension was mixed with one volume of 50% Karnovsky's solution. The platelet

suspension was in plasma-buffer (sodium cacodylate buffer 0.2M, pH 7.4). Staining was done by uranylacetate. After dehydration in a series of increasing concentrations of ethanol, the preparation was embedded. Microtome sections of 1,500 Å were, then, placed on grids and were irradiated with carbon K α x-rays (4.4 nm wavelength) as previously described.[11] X-ray resists were, then, examined by transmission electronmicroscopy (TEM) and compared with TEM images of the same cells. Comparison of the two technics, contact x-ray microscopy and TEM was therefore possible. Only human platelets were used.

The two images, TEM picture (left) and TEM picture of the irradiated replica (right) demonstrated striking differences between each other. Some ultrastructural details were not clearly defined in the x-ray exposed replica. On the other hand, other details were new to us. The two main structures seen in the resist exposed to x-rays were: 1) a thick, bilayered contour of the cells, and 2) thick undulating cords inside the platelets alternated with radiolucent spaces of equally curvilinear shape. The cords included several round and more dense areas which, we believe, corresponded to the dense granules and other platelet organelles. In our interpretation, the radiolucent areas may include vesicles of the external canalicular system. Some of the structures which are seen in the TEM pictures (left) appear to be radiolucent, therefore not visible by contact x-ray microscopy (right). It does not seem to be a matter of a defect in resolution, but of the fact that the two technics see different things. Radiodensity does not seem to always correspond to electron density. The external border to the cells appeared of surprising thickness by x-ray microscopy. Although it seemed to follow the course of the platelet plasma membrane, it was too wide to be justified by the carbohydrate layer known to be external to the platelet plasma membrane and only demonstrable by staining with Rubidium or other preparations suitable for the staining of carbohydrates for the TEM technique. Large depositions of uranyl acetate used in staining may have, in part, contributed to the unusual thickness of the platelet outer border seen by contact x-ray microscopy. In essence, the relation of the thick, trilaminar platelet rim seen on contact x-ray microscopy, with the actual cell membrane boundary is not as yet completely apparent.

In Fig. 5 the platelets were prepared differently.[13] They were separated from fresh, human blood and gel filtered, mounted on carbon coated grids, treated with 0.4% Triton X-100, then stained with uranyl acetate. Digestion of the resting platelets in Triton X-100 left the system of microtubules intact. After irradiation of one grid by the contact x-ray method, the x-ray image replica and the E.M. preparation were studied by TEM. A comparison of the two pictures of the same microtubules was possible.

This preparation was supposed to evidence platelet microtubules. When placed on a resist and exposed to soft x-rays, examination of

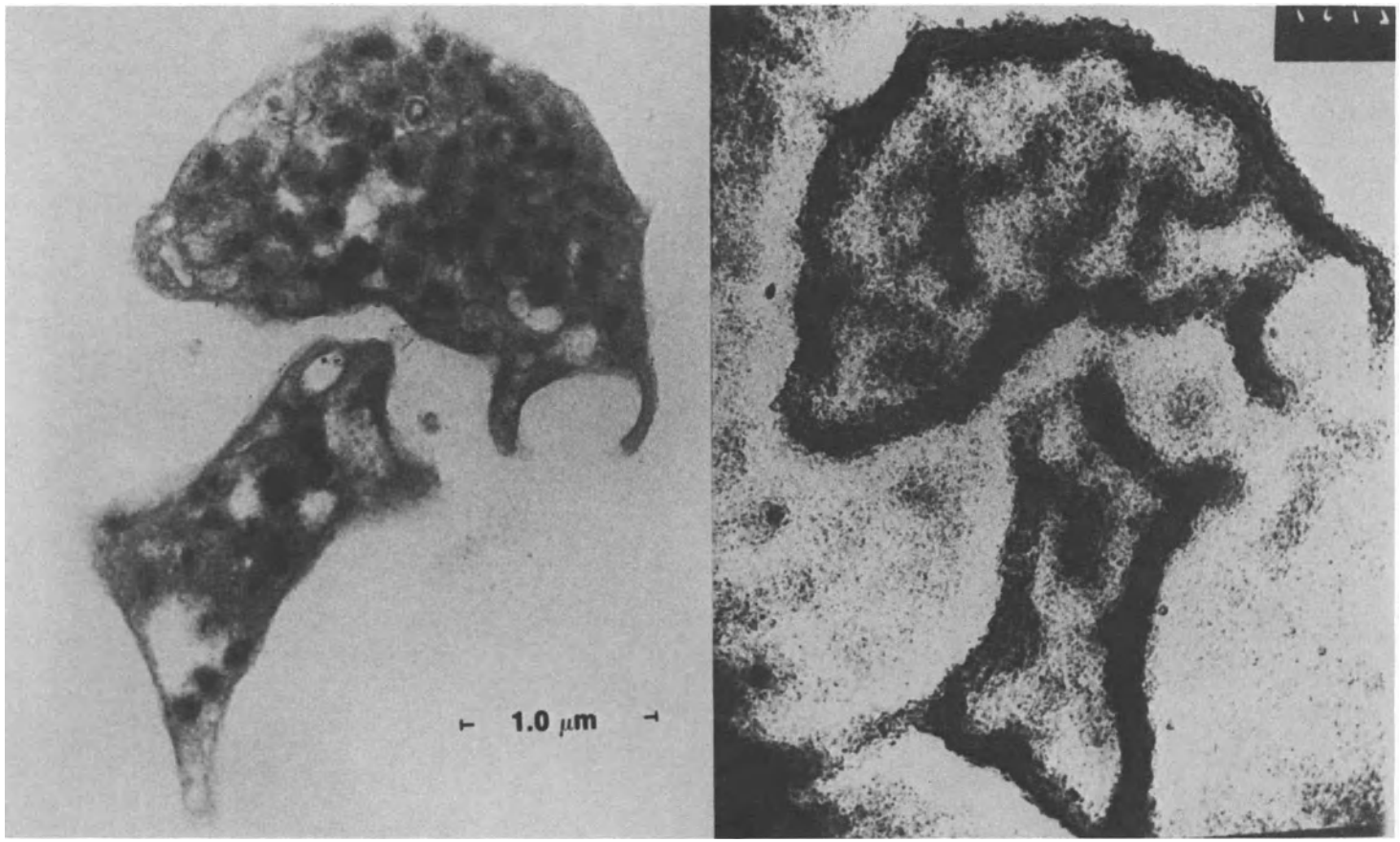

Fig. 4

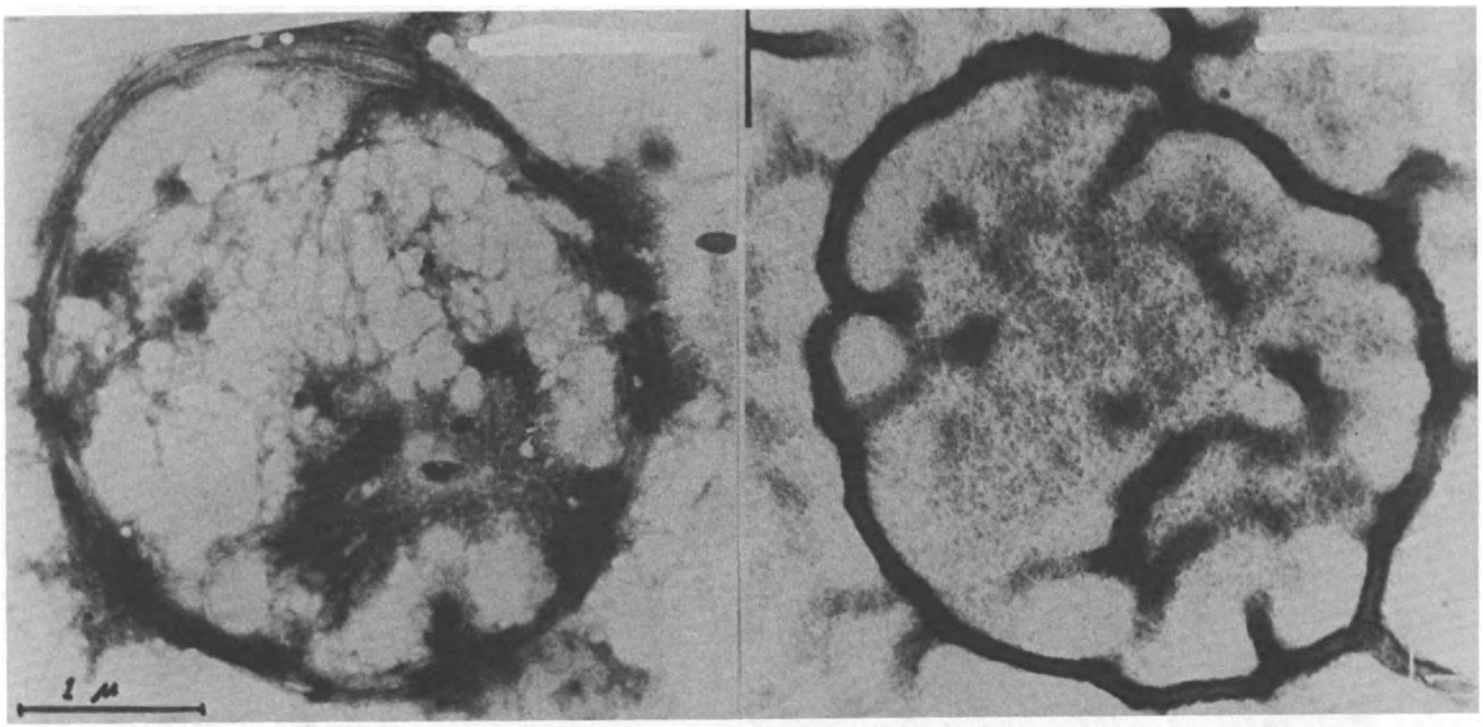

Fig. 5

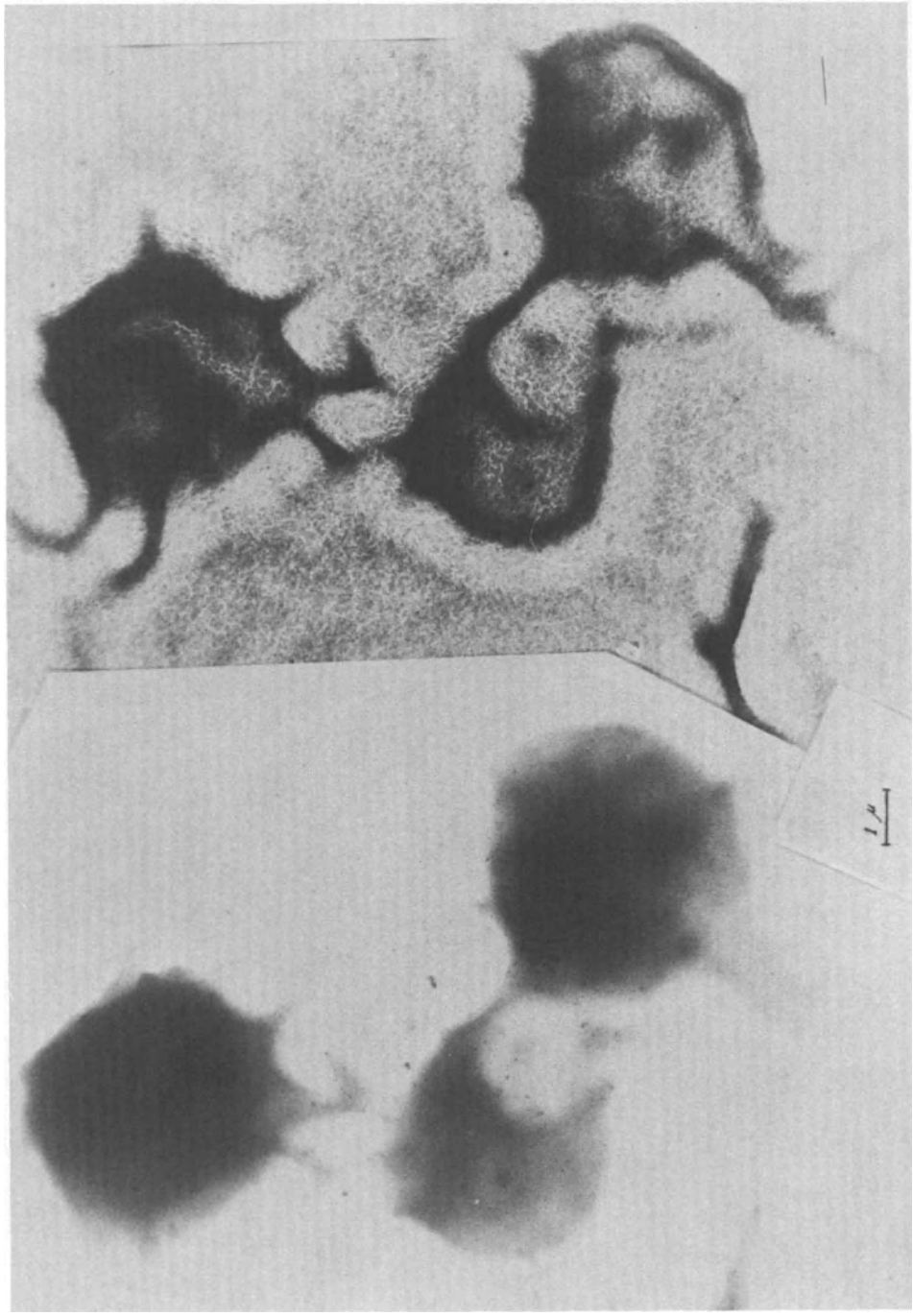

Fig. 6

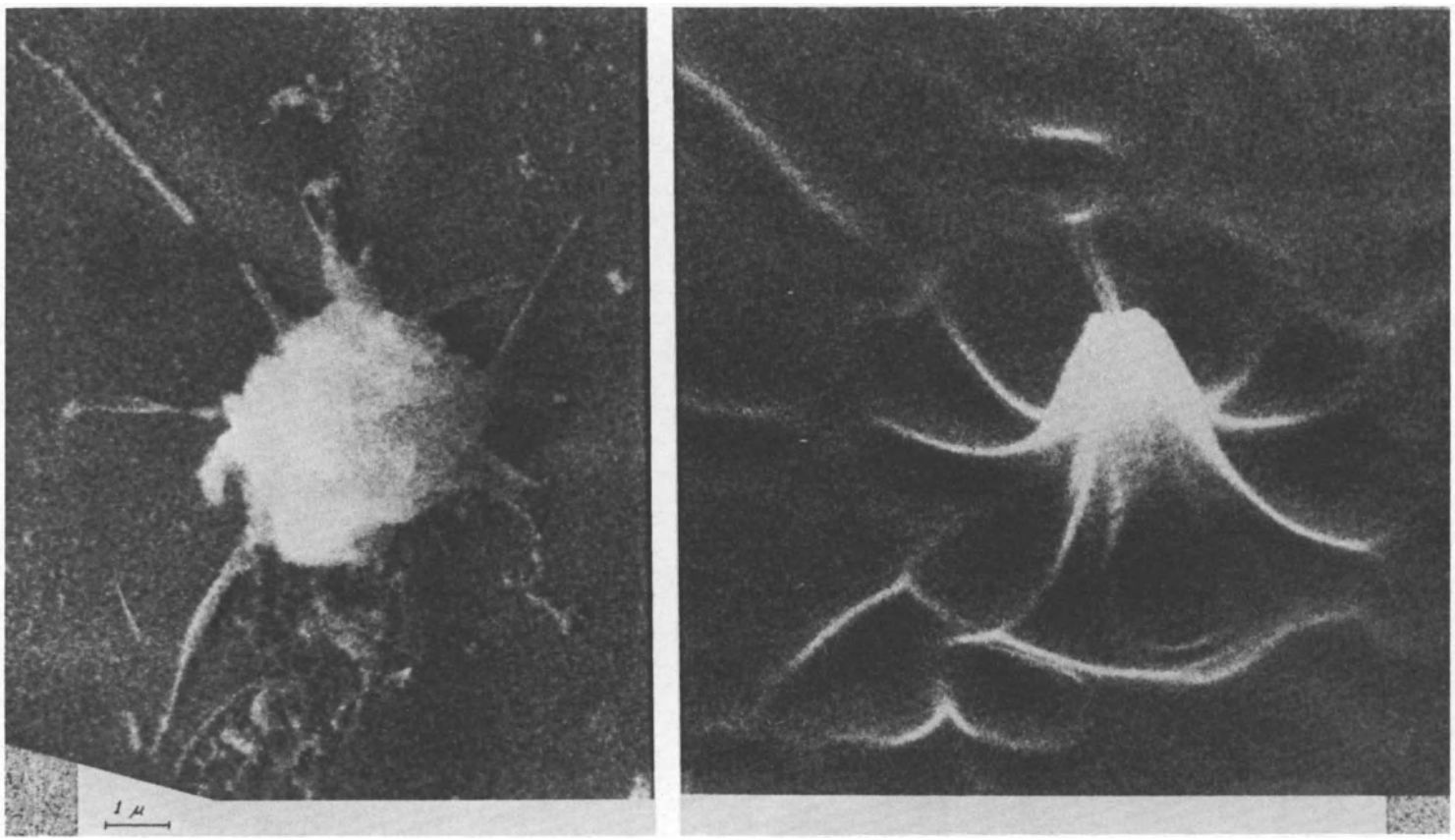

Fig. 7

the replica by TEM clearly demonstrated that microtubules cannot be seen (right). Polymerized tubulin seems, therefore, radiolucent, while its outline is perfectly electrondense (left). In spite of the digestion of the cell body and plasma membrane which seemed almost complete in the TEM image (left), a clearcut and thick structure outlining the outer cell border was still evident on the x-ray image (right). Distribution of the staining material (uranyl acetate) was even throughout the cell seen in the TEM image. This indirectly indicates that the dark, thick cell outline seen in the x-ray image of the same cell does not reproduce concentration points of uranyl acetate.

In the following pictures (Fig. 6 and 7), whole cell mounts of fresh human platelets are presented. The platelets always became partially stimulated by contact with the carbon cotated grids. After fixation with Karnovsky's solution, the preparations were dehydrated with a series of increasing concentrations of ethanol and, finally, air dried (Fig. 6) or critical point dried (Fig. 7). They were, then, exposed to the contact x-ray source. In Fig. 6, replica and grid were examined by TEM. In Fig. 7, the replica and grid were examined by scanning electron microscopy (SEM).

In Fig. 6, two comparable pictures both of the same group of three cells were examined. The TEM image (left) showed clear outlines of the three cells with very dark and less dark areas in the cytosol, but no definition of inner structures. A few faint pseudopods were observed in two of the three cells. Resolution of cell details was much improved in the x-ray image of the same cells (right). The inner body of the platelets showed the usual structure of dense cords and clear zones. Also, the platelet outer rim was, as usual, thickly demarcated. The cell structures which were most clearly defined in the x-ray picture (right) were the pseudopods. Their fine and dark outline could be followed for a long distance from the cell body. Also, their penetration of the cell membrane, into the body of the platelets, could be clearly seen.

In Fig. 7, the grid and the x-ray resist were examined by SEM. The two negatives are here presented. They are hardly recognizable as two pictures of the same cell. The cell was partially activated as demonstrated by the number of pseudopods and the centralization of the platelet organelles. Only the contact x-ray picture (right) can show these details in full. A thick group of centralized and retracted organelles rises high over the plane of the partially spread cell cytoplasm. The shadow of the cell body appears larger on the x-ray image (right) than on the SEM picture (left). The cell skeleton in the x-ray picture (right) has the aspect of tent-like structure with about 8 filaments protruding from the central group of retracted organelles toward the edge of the cell body. Some pseudopods extend for more than one cell radius beyond the thin contour of the cell cytoplasm. The SEM picture (left) shows only

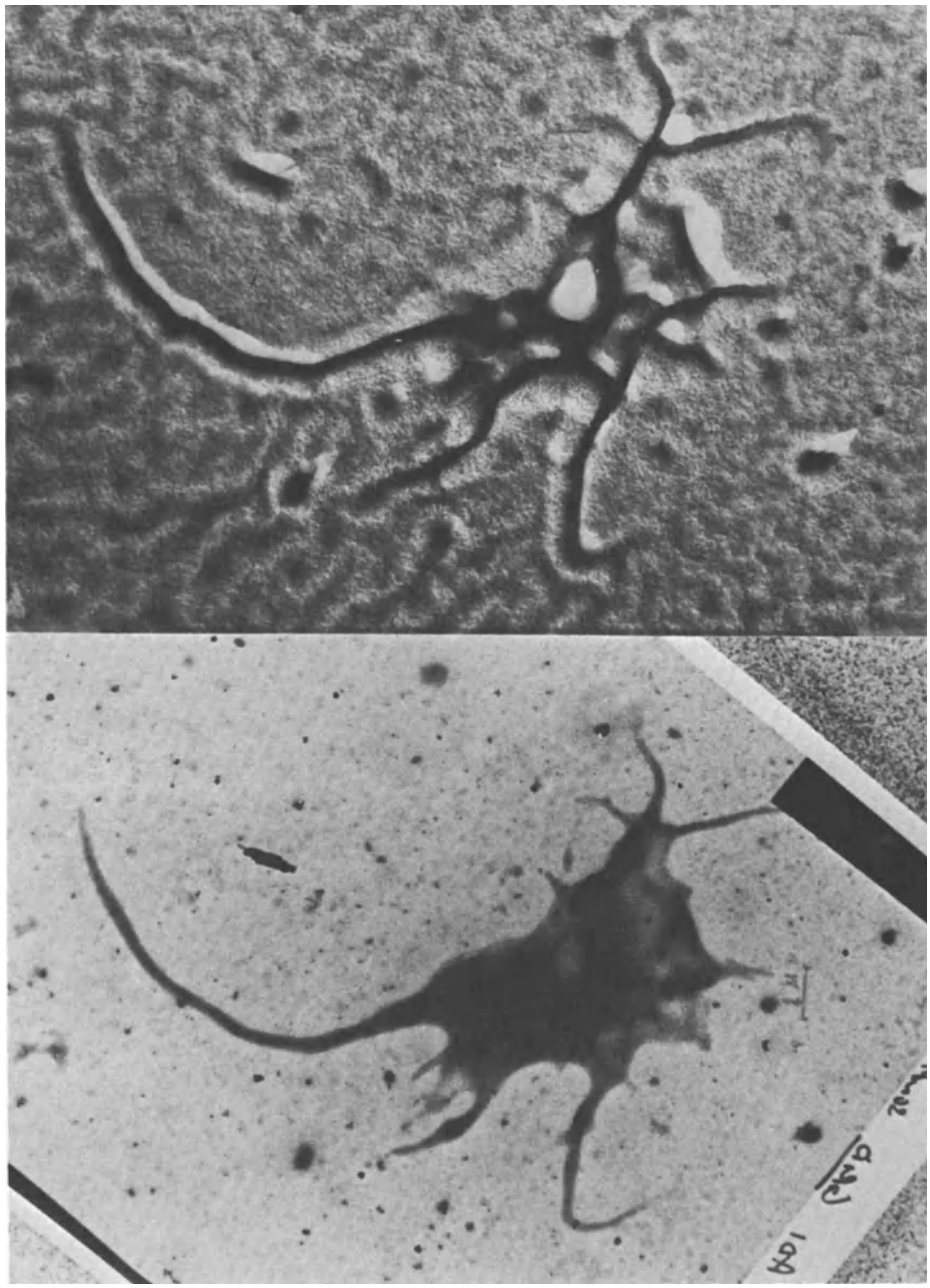

Fig. 8

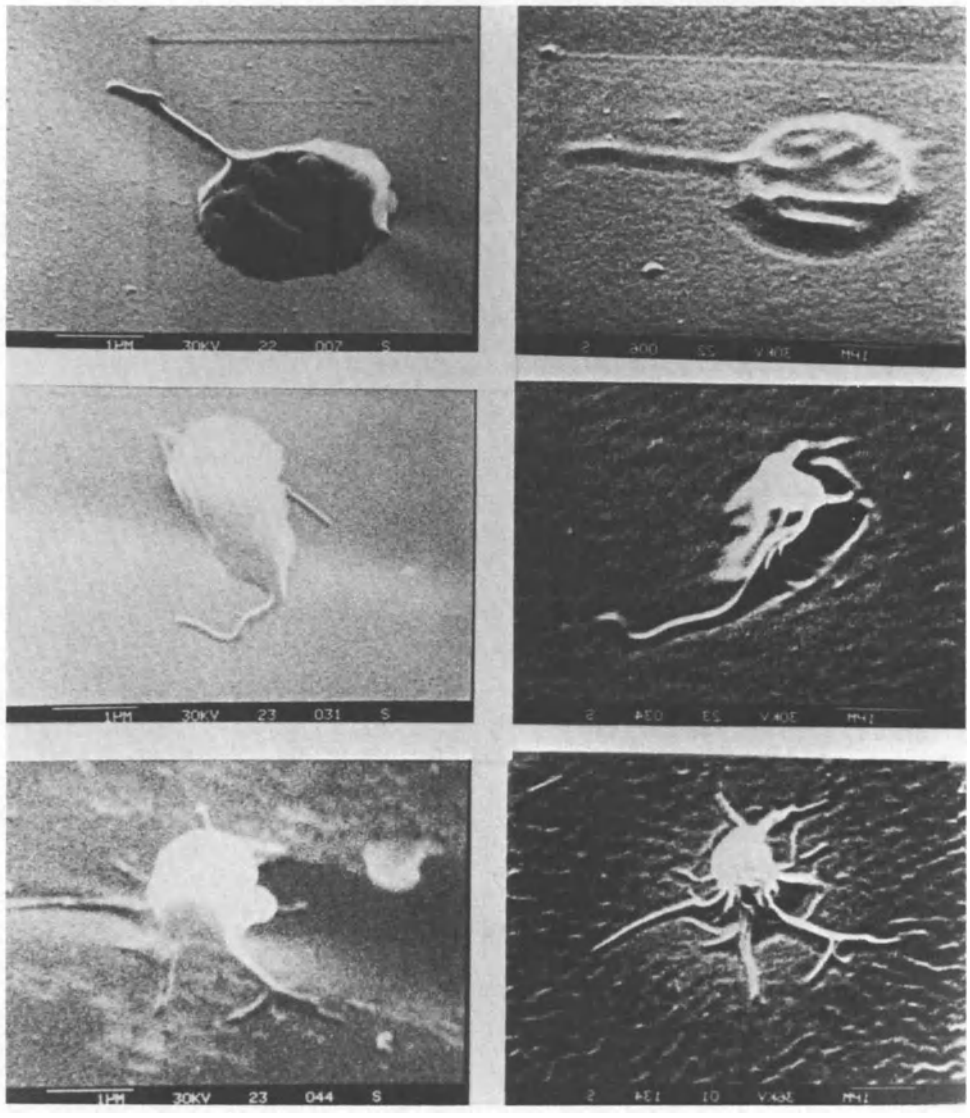

Fig. 9

a thick, white woolen skein which is smaller than the x-ray cell image (left). The pseudopods can be seen in both pictures, but the tent-like filamentous structure reaching the inner core of the cell center is totally blurred in the SEM image (left) while it is very clearly defined in the x-ray image. The functional meaning of the structural morphology of this cell is only evident from the x-ray picture (right) not from its SEM couterpart (left).

In Fig. 8, two images of one platelet in advanced stage of activation are shown. The preparation was arranged as described above for whole cell mount. Exposure of the plasma platelet suspension to the surface of the carbon coated grid was prolonged to 5 minutes rather than the usual 2 minutes. A late stage of activation can be seen. Organelles have fused in the center of the platelet and several long pseudopods can be seen projecting out of the cell contour (left, TEM image). The TEM image of the replica (x-ray picture, on the right) shows that the photon dense material is almost exclusively distributed in the pseudopods. It is perfectly clear in this image, that these do not originate from the cell membrane, nor from the peripheral portion of the cell body, but from an inner, interweaved filamentous structure located at the cell center. The expected, retracted mass of x-ray dense organelles has disappeared to be replaced only by the tracing of a network of x-ray dense filaments. The structural and functional significance of this network is still being debated, but this picture as well as the previous one leave no doubt on the fact that the site of origin of the platelet pseudopods is at the center of the activated platelet body, not at the periphery.

For the following two preparations, (Fig. 9 and 10), a drop of platelet rich plasma was, as usual, deposited on carbon coated electronmicroscope grids. These platelets were at rest, that is, they were stabilized by preincubation with 1 μM PGE_1 at 37 °C for 40 minutes before mounting them.

Fig. 9: The SEM image of a stabilized platelet is seen on the upper left and appears to be of typically discoid shape. The thick and long pseudopod confirms that this cell is, indeed, a platelet. A few protruding zones as well as indentations are seen on the cell surface. The SEM of the x-ray replica of the same cell is seen on the upper right. It shows that the radiodense tracings in the cell body are connected with each other and with the single pseudopod. They correspond to elongated cords of cytoplasmic material protruding from the flat cell surface.

Platelets activated only by contact with the carbon-coated grids for 2 minutes or 7 minutes, respectively, are presented in the middle and the lower portions of the slide. In the SEM pictures on the left, it can be seen that shape changes and pseudopod formation progressed with prolongation of the activation time.

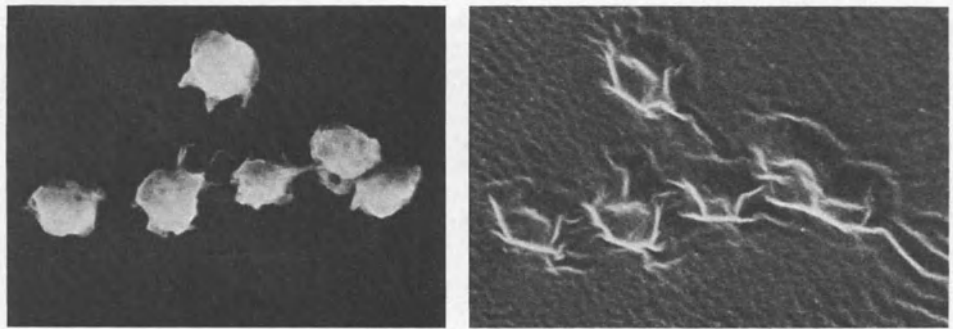

Fig. 10

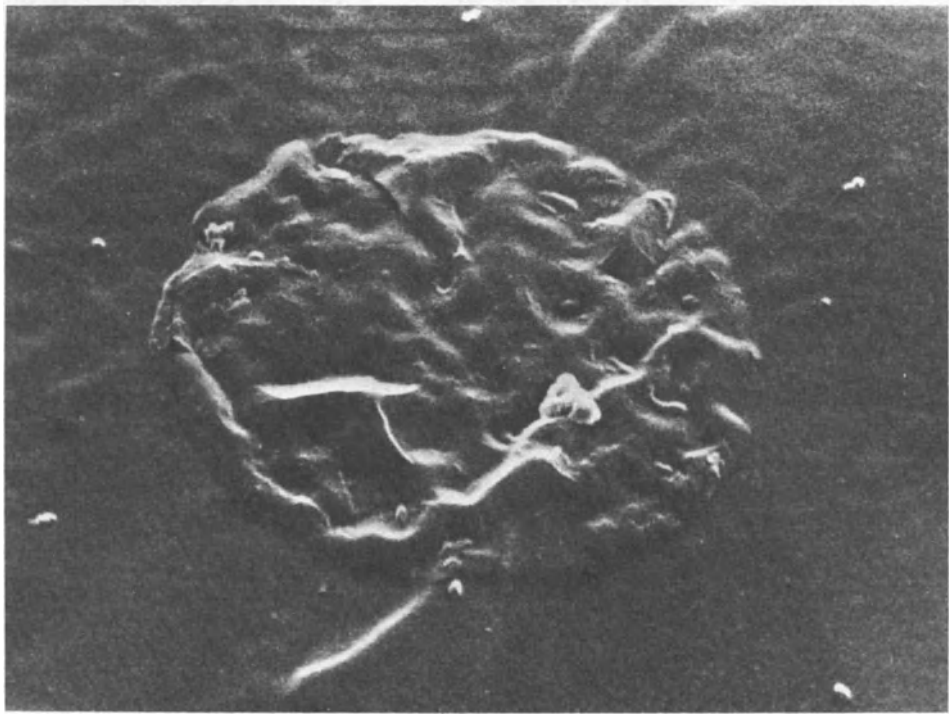

Fig. 11

Intracellular structures in these conventional SEM preparations on the left, cannot be clearly distinguished. On the contrary, the x-ray images on the right, clearly show an intracellular, centralized mass of radiodense material connected with a few long filopodia extending through the cytoplasm and continuing outside of the cell boundary. There are also, numerous, short, intracytoplasmic filopodia originating from the centralized, radiodense mass, most probably representing early or abortive stages of pseudopod formation.

In Fig. 10, three resting, PGE_1 treated platelets are shown which were, then, activated by calcium ionophore (A23187). After mounting the cells on carbon coated grids, these were covered with a drop of plasma containing 40 μM calcium ionophore. The activated specimens were, then, fixed and dehydrated as usual. After one minute of exposure to calcium ionophore, an early stage of platelet activation could be seen. The SEM image on the uppper left, shows a spherical shape of the platelet with an irregular surface and one long filopodium. The x-ray image of the same cell on the upper right shows, again, a contracted and centralized mass of photon dense material from which a tent-like structure of several thick filopodia originates. These filopodia, however, have not yet crossed the cell membrane. As activation advanced, the regular SEM images on the left show an increased number of long pseudopods associated with a diminished size of the cell body. In the x-ray images shown on the right, the contracted and centralized core of photon dense material has become smaller. From it, several long pseudopods depart, cross the cell membrane, then project into the surrounding medium. We have observed similar phenomena, also, when platelet activation was induced by other biological agents including ADP, collagen, epinephrine, or serotonin. These images suggest that during the contracting process of the centralized radiodense mass, the filopodia forming material is projected out of the centralized core, then out of the cell itself. It seems logical to believe that the material of the filopodia is of similar composition and has similar contractile properties as the material forming the central cell core.

In Fig. 11, the preparation utilized human platelets suspended in plasma and placed directly in the vacuum chamber of the gas puff z pinch instrument. After one exposure, the x-ray replica was developed and examined by SEM. The radiodense structure of the live cell is smooth. The outline of the cell boundary is thin with no special concentrations of radiodense material. The cell is partially activated with a centralized and contracted bundle of platelet organelles projecting above the cell boundary. A pseudopod is seen projecting outside the cell. Its origin seems clearly connected with the centralized organelle structure. A cell body structure of undulating cords is clearly apparent with a few craters from which dense granules seem to be released. A small tear in the cell membrane is evident. Cell granules are dispersed in the suspending fluid in the

neighborhood of the cell. The tear in the cell membrane may represent an accidental or a natural event, like a portal for the partial release of platelet granules during the process of the release reaction. This interpretation is still under study.

DISCUSSION

A conclusion which can be derived from our present studies of platelet structure by soft x-ray microscopy is that this new technique, as presently utilized, cannot offer the richness and selectivity of details that transmission and scanning electronmicroscopy have so far made available for cell research. However, cell structures can be seen by soft x-ray microscopy which are not, or not as clearly, identifiable by electronmicroscopy. In other words, electrondensity cannot be equated with photondensity (i.d. radiodensity) and each of the two technics can provide identification of some cell structures which cannot be seen by the other. Therefore, the two methods complement each other with advantage in results. Micro-imaging technics by TEM and SEM have, throughout the years, reached a very high point of sophistication. This high level of resolution with such a variety of materials and structures cannot as yet be achieved by contact x-ray microscopy. In our platelet experiments, intracellular organelles could be better identified by TEM. However, detailed phases of platelet activation with collection and fusion of platelet organelles into a very contracted structure in the center of the cells, and the emission of pseudopods only from this central structure had never appeared as clear before the advent of contact x-ray microscopy.[10] These images may have important meaning for the interpretation of platelet function. We tend to believe that after centralization, the platelet organelles are fused together and transformed into one basic building material which, then, repolarizes into an interwoven, tight net or a closed chamber from which it is propelled towards the periphery and outside the cell, in the form of pseudopods. A logical question is raised here with regard to the nature of the material which is so strikingly radiodense and becomes so prominent during platelet activation. Although this question will presently remain unanswered, an indirect but possible suggestion is that it may represent actin or an actin-like material. More studies, however, are necessary for a definitive demonstration of this hypothesis.[11-13]

Our findings on the early stages of platelet activation have disclosed the advantage of using living cells in ultrastructural studies, a new achievement made possible with soft x-ray microscopy by the gas puff z pinch technic. The presence of platelet granules in surface craters, the dispersion of some of them into the platelet surrounding medium, a tear in the continuity of the cell membrane that we saw during early stages of platelet activation (Fig.11) indicate that the release reaction does not occur only as the ultimate

stage of this phenomenon. It can be seen, also, in early stages, when polarization and contraction of platelet organelles has barely started.

In conclusion, the potential benefits of contact x-ray microscopy in the study of cell biology are evident: resolution in the range of 5 nm is available, staining of specimens is not required, no sectioning is necessary and, above all, living cells can be examined. Also, structures can be seen by x-ray microscopy which cannot be seen by electronmicroscopy. We believe that x-ray microscopy will become an important adjunct to electromicroscopy in future studies of cell biology.

REFERENCES

1. J. Bizzozero, Ueber einen neuen Formbestandteil des Blutes und dessen Rolle bei der Thrombose und der Blutgerinnung, Arch. path. Anat. 90, 261-332, 1882.

2. J.G. White, Combined nephelometric and electron microscopic study of the platelet release reaction. In: Platelet adhesion and aggregation in thrombosis: countermeasures. (E.F. Mammen et al. Eds.), pp. 73-91. Shattauer Verlag, Stuttgart & New York, 1970.

3. J.G. White, Platelet morphology. In: The circulating platelet. (Johnson S., ed.) New York, Academic Press, 1971, pp. 45-121.

4. J.G. White, J.M. Gerrard, Platelet morphology and the ultrastructure of regulatory mechanisms involved in platelet activation. In: Platelets: A Multidisciplinary Approach. G. DeGaetano, S. Garattini, Raven Press, New York, N.Y., 1977, pp. 17-34.

5. J.G. White, G.H.R. Rao, Influence of a microtubule stabilizing agent on platelet structural physiology, Am J Pathol 112: 207-217, 1983.

6. R. Feder, J.L. Costa, P. Chaudari, D. Sayre, Improved detail in biological soft x-ray microscopy: study of blood platelets, Science 212: 1398-1400, 1981.

7. E. Spiller, R. Feder, J. Topalian, D. Eastman, W. Gudat, D. Sayre, X-ray Microscopy of Biological Objects with Carbon K with Synchrotron Radiation, Science 191: 1172-1174, 1976.

8. J.S. Pearlman and J.C. Riordan, X-ray lithography using a pulse plasma source, J. Vac. Sci. Technol 19: 1190-1193, 1981.

9. J. Bailey, Y. Ettinger, A. Fisher, R. Feder, Evaluation of the gas puff z pinch as an x-ray lithography and microscopy source, Appl. Phys. Lett. 40: 33-35, 1982.

10. V.T. Nachmias, Platelet and megakaryocyte shape change: Triggered alterations in cytoskeleton, Sem. Hematol 20: 261-281, 1983.

11. V.T. Nachmias, Cytoskeleton of human platelets at rest and after spreading, J. Cell Biol. 86: 795-802, 1980.

12. R.L. Henry, Platelet function, Sem. Thromb. Haemost 4, 93-122, 1977.

13. D.M. Kenney, Personal communication.

INDEX